

Extra-cardiac Interference in Myocardial Perfusion Imaging
with Rubidium-82 and Positron Emission Tomography

by

Elizabeth J. Orton

A thesis submitted to the Faculty of Graduate and Postdoctoral
Affairs in partial fulfillment of the requirements for the degree of

Doctor of Philosophy

in

Physics: Medical Physics

Ottawa-Carleton Institute for Physics
Department of Physics, Carleton University
Ottawa, Ontario, Canada

© 2015, Elizabeth J. Orton

Abstract

Interpretation of myocardial perfusion images, produced with blood flow tracer rubidium-82 chloride (^{82}Rb) and positron emission tomography (PET), can be affected when high tracer uptake in extra-cardiac organs adjacent to the heart (stomach) interferes with the myocardium. Since extra-cardiac organs are physically spatially distinct from the myocardium, extra-cardiac interference (ECI) in ^{82}Rb PET images arises from limited spatial resolution, and cardiac and respiratory motion.

This thesis aims to provide automated methods that detect and correct ECI. Three algorithms were developed to fulfill these aims: the first detects and ranks severity of ECI, the second attempts ECI correction based on factor analysis of dynamic image series, and the third corrects ECI with a 1D convolution-based method. All algorithms were developed, implemented and evaluated based on sets of clinical images.

The detection and severity classification (DSC) algorithm was developed based on concordance of a 200 image dataset with clinical interpretation. It detected ECI with high accuracy (97% sensitivity and 82% specificity), low failure rate (<1%) and short execution time (<7s). The algorithm was used to estimate prevalence of ECI in a 4920-image dataset and to determine if simple modifications to image processing protocols could reduce ECI prevalence and/or severity. While reduced filtering showed the most promise, none of the available modifications eliminated ECI in the majority of images.

Factor analysis of dynamic image series uses differences in the temporal behaviour of tracer uptake in the myocardium compared to that in the extra-cardiac organ to separate the two structures. Variations of this approach, applied to ^{82}Rb PET images,

were not able to simultaneously correct images with ECI of all severities and avoid reducing myocardial intensity in images without interference prior to correction. The 1D convolution-based correction algorithm modeled the image point spread function, including the effects of motion, as a 1D Gaussian and the underlying myocardial and stomach tracer uptake as simple 1D rectangular functions. This algorithm corrected images with ECI of all severities without reducing myocardial intensity in ECI-free images and >90% of scans examined showed visually acceptable correction. The convolution-based correction algorithm shows promise as a software-based ECI correction.

Acknowledgements

The duration of my degree necessitates I thank many people, all of whom have been a part of my PhD-years. I have the most reason to thank my supervisor, Glenn Wells. His patience, guidance and support have not only helped me arrive at this point but have both directly and indirectly provided me a new set of skills, with which I can approach future intellectual pursuits.

A number of other Carleton medical physics faculty have provided me with particular support that I would like to acknowledge. Thank you to Brenda Clark and Joanna Cygler for support during my initial project, David Rogers for facilitating my transition between supervisors, and Paul Johns for support through the Physics Department during the last few years of this degree.

There are many people who I met through this degree, who I have been encouraged by and learned from, and who I hope will remain my colleges and friends for a long time to come. In particular, thank you to Elsayed Ali, Ran Klein, Amanda Cherpak, Lindsay Beaton and Jared Strydhorst.

I would like to acknowledge the following sources of funding, without which, I would not have been in a position to complete this degree: the Natural Sciences and Engineering Research Council of Canada (NSERC-PGSD2), the Gary S. Duck Graduate Scholarship in Photonics, Mathematics and Physics for Ontario Students, the Queen Elizabeth II - Ontario Graduate Scholarship in Science and Technology, the David and Rachel Epstein Foundation Scholarship, and Carleton Domestic Tuition scholarships. I am particularly grateful for support from the Carleton Physics Department.

Finally, the personals. Anne-Marie Jeffrey was the undergraduate physics secretary at Dalhousie University during my undergraduate degree and was also a force to be reckoned with. She was the person who sent me down the Medical Physics path with a phone call saying 'You've got a Masters supervisor, come meet him', before an MSc had even crossed my mind. In Sept 2008, Anne-Marie died of cancer and I didn't get the chance to thank her. This degree would have made my grandfather Peter particularly proud as he always wanted to be able to tell people *his* granddaughter was a *Dr* but I just couldn't quite get it finished soon enough. Thank you to Hannah because I will never have another friend like you.

The appreciation I want to express to my parents is enormous, they were always on the other end of the phone when I needed to share the good or bad with them. And last but not least, to Rick, who has shown me how to have fun with life and made me realize how important this really is.

Statement of Originality

Chapter 2 of this thesis has been published in the journal *Medical Physics*:

E.J. Orton, I. Al-Harbi, R. Klein, R.S. Beanlands, R.A. deKemp and R.G. Wells, "Detection and severity classification of extra-cardiac interference in ^{82}Rb PET myocardial perfusion imaging", *Med. Phys.* **41**, 102501 (2014)

Preliminary results from this chapter were also published as conference abstracts presented in 2013 at the Society of Nuclear Medicine and Molecular Imaging Annual Meeting, the Imaging Network of Ontario Annual Meeting, the Molecular Function and Imaging Conference, the Cardiovascular Repair using Enhanced Stem cell Therapy (CREST) meeting and the University of Ottawa Heart Institute (UOHI) Research Day:

E.J. Orton, I. Al-Harbi, R. Klein, R.S. Beanlands, R.A. deKemp and R.G. Wells, "Prevalence of extra-cardiac interference in ^{82}Rb PET myocardial perfusion imaging", Society of Nuclear Medicine and Molecular Imaging ASM, Vancouver, June 2013.
Finalist for Best Poster in Clinical Cardiology.
Published in J. Nucl. Med. **54** (Supplement 2):1689 (2013) and also presented at the 6th Annual Molecular Function and Imaging Symposium, June 2013

E.J. Orton, I. Al-Harbi, R. Klein, R.S. Beanlands, R.A. deKemp and R.G. Wells, "Detection of extra-cardiac interference in ^{82}Rb PET myocardial perfusion imaging", 12th Annual Imaging Networks of Ontario Symposium, Toronto, Feb 2013. Poster presentation (P94).
Also presented at the CREST Annual Meeting, March 2013 and UOHI Research Day, May 2013.

Ibraheem al Harbi (MD) provided clinical interpretation of the 200 images used for algorithm development and assessment of concordance. Ran Klein (PhD) and Robert deKemp (PhD) developed and maintain the FlowQuant code, used for LV processing in chapters 2 – 5 of this thesis. All of the scans were drawn from the *Rubidium-82 - An Alternative Radiopharmaceutical for Myocardial Imaging* (Rb-ARMI) trial, for which Robert deKemp and Rob Beanlands (MD) are principle investigators, and images from

these scans were used in chapters 2-5. The concept for this work was suggested by R Glenn Wells (PhD) and developed by Elizabeth Orton (MSc). All algorithm development, implementation of computer code in Matlab, validation, analysis, writing and presenting of articles and abstracts were performed by Elizabeth Orton, under the supervision of R. Glenn Wells.

For Chapters 3 and 5, all algorithm development, implementation of computer code in Matlab, validation, analysis, writing and presenting was performed by Elizabeth Orton, under the supervision of R. Glenn Wells.

For the factor analysis work in Chapter 4, Ran Klein provided Matlab software used to implement the FAMIS algorithm, as well as FlowQuant software components used for kinetic modeling. Chad Hunter provided biodistribution data, collected as part of his Master's thesis, which was used to produce Figure 4-1. All other algorithm development, implementation of computer code in Matlab, validation, analysis, writing and presenting was performed by Elizabeth Orton, under the supervision of R. Glenn Wells.

Table of Contents

Abstract.....	i
Acknowledgements.....	iii
Table of Contents	viii
List of Tables.....	xv
List of Figures.....	xvii
List of Appendices	xxv
Glossary	xxvi
1 Chapter: Introduction.....	1
1.1 Overview.....	1
1.2 Heart disease	2
1.2.1 The heart and coronary arteries	2
1.2.2 Ischemic heart disease (IHD).....	4
1.2.3 Care for IHD.....	5
1.2.4 Myocardial perfusion imaging (MPI).....	6
1.3 Positron emission tomography (PET)	8
1.3.1 Positrons, positron emitting isotopes and annihilation photons.....	8
1.3.2 PET detectors	13
1.3.3 Coincidence detection, lines of response and projections	16
1.3.4 Acquisition: raw data formats and external triggers	17
1.3.5 Data organization	19
1.3.6 Image reconstruction	21
1.3.7 Corrections	25

1.4	Image quality	30
1.4.1	Spatial resolution	30
1.4.2	Noise.....	36
1.5	Motion	39
1.5.1	Cardiac.....	40
1.5.2	Respiratory	41
1.5.3	Gross patient motion	42
1.6	PET Myocardial Perfusion Imaging.....	42
1.6.1	Tracers.....	42
1.6.2	⁸² Rb PET MPI.....	43
1.6.3	UOHI ⁸² Rb PET MPI protocol	45
1.6.4	MPI Interpretation	46
1.6.5	Wall Motion and Kinetic Analysis.....	49
1.7	Extra-cardiac interference (ECI).....	50
1.7.1	ECI in MPI	51
1.7.2	ECI in ⁸² Rb PET MPI.....	57
1.7.3	Solutions proposed to date.....	59
1.8	Thesis summary.....	60
1.8.1	Objectives.....	60
1.8.2	Hypotheses.....	60
2	Chapter: Detection and severity classification of extra-cardiac interference in ⁸²Rb PET myocardial perfusion imaging	62
2.1	Introduction.....	62
2.2	Methods and Materials	66

2.2.1	Scan acquisition and image reconstruction	66
2.2.2	Datasets.....	66
2.2.3	Algorithm summary.....	71
2.2.4	Parameters and thresholds.....	72
2.2.5	Population failure rate	76
2.2.6	Algorithm-based prevalence estimate.....	76
2.3	Results	76
2.3.1	Datasets.....	76
2.3.2	Parameters and thresholds.....	77
2.3.3	Algorithm accuracy	78
2.3.4	Failure rate, manual intervention rate and execution speed	81
2.3.5	Prevalence of interference in Jan 2011 – Dec 2012 population	82
2.4	Discussion	83
2.5	Conclusion	90
3	Chapter: Simple approaches to ECI compensation	91
3.1	Introduction.....	91
3.2	Cardiac gating.....	93
3.2.1	Introduction	93
3.2.2	Methods and materials.....	94
3.2.3	Results.....	96
3.2.4	Discussion.....	98
3.2.5	Conclusion.....	101
3.3	Respiratory gating	102
3.3.1	Introduction	102

3.3.2	Methods and materials	102
3.3.3	Results	104
3.3.4	Discussion.....	106
3.3.5	Conclusion	108
3.4	Filtering.....	109
3.4.1	Introduction	109
3.4.2	Methods and materials	109
3.4.3	Results	111
3.4.4	Discussion.....	116
3.4.5	Conclusion	118
3.5	Time-of-flight (TOF) reconstruction and reduced filtering.....	118
3.5.1	Introduction	118
3.5.2	Methods and materials	119
3.5.3	Results	120
3.5.4	Discussion.....	123
3.5.5	Conclusion	123
3.6	Summary.....	124
4	Chapter: Dynamic-data based correction.....	125
4.1	Introduction.....	125
4.2	Methods and materials	131
4.2.1	Correction algorithm summary.....	131
4.2.2	Image acquisition and reconstruction.....	133
4.2.3	Estimation of Basis Functions.....	133
4.2.4	Estimation of coefficients.....	138

4.2.5	Interference-free normal databases	139
4.2.6	Correction algorithm development	140
4.2.7	Correction algorithm evaluation	143
4.3	Results	146
4.3.1	Manual VOI TACs.....	146
4.3.2	FAMIS factors as basis functions and structures as coefficients.....	147
4.3.3	FAMIS myocardium and blood basis functions and VOI-TAC stomach basis function 151	
4.3.4	Reducing noise in basis functions	153
4.3.5	Evaluation of stomach fall-off conditions	156
4.3.6	Interference-free normal databases	156
4.3.7	Correction algorithm development	157
4.3.8	Correction algorithm evaluation	159
4.3.9	Using a kinetic model to define mean and variance of blood-free myocardial and stomach basis functions.....	165
4.4	Discussion	166
4.5	Conclusion	172
5	Chapter: 1D convolution-based correction	173
5.1	Introduction.....	173
5.2	Methods and materials	174
5.2.1	Scan acquisition, image reconstruction, LV processing and 1D profile extraction	175
5.2.2	Datasets.....	176
5.2.3	Algorithm summary.....	176
5.2.4	Myocardium-only model in the interference-free region.....	180

5.2.5	Myocardium-only and myocardium-stomach models in the interference search region	181
5.2.6	Parameter smoothing, voxel-specific interpolation and corrected images.....	189
5.2.7	Correction algorithm evaluation	189
5.2.8	Failure criteria, population failure rate and algorithm execution time	190
5.3	Results	190
5.3.1	Algorithm evaluation.....	190
5.3.2	Population failure rate and algorithm execution time	200
5.4	Discussion	200
5.5	Conclusion	206
6	Chapter: Summary and future directions	207
6.1	Introduction.....	207
6.2	Directions for improving algorithm performance	207
6.2.1	Expanding 1D convolution algorithm to 2D/3D	207
6.2.2	Optimizing the input to the convolution algorithm	208
6.2.3	Defining scan-specific interference search region	209
6.3	Impact on the quality of care derived from ⁸² Rb PET MPI	210
6.3.1	Clinical implementation of ECI correction	210
6.3.2	Clinically relevant versus physical ECI	214
6.3.3	Clinical impact of ECI	215
6.4	Extended application	216
6.5	Conclusion	217
	Appendices	219
	Appendix A Permission for use of material from Medical Physics.....	219

Appendix B Ottawa Health Research Ethics Board (OHREB) Application.....	221
B.1 OHREB Approval Letter	222
B.2 PhD Supervisory Committee Approval.....	223
B.3 Annual Renewal Report	224
B.4 OHREB ethics protocol, final version 8 May 2013.....	226
References	231

List of Tables

Table 1-1. Properties of some positron emitting nuclides used for medical imaging. β^+ ranges are in water and the effective FWHM = 2.35*root mean square (rms) range. (Cherry <i>et al</i> 2012, Lecomte 2004)	10
Table 1-2. Ratio of the photoelectric ($\mu_{\text{photoelectric}}$) to the Compton scattering (μ_{Compton}) linear attenuation coefficient, and the total (μ) linear attenuation coefficient values for 511 keV photons in materials relevant to medical imaging (Berger <i>et al</i> 2010, ICRP 2002 [†] , Cherry <i>et al</i> 2012 [‡] , Pepin <i>et al</i> 2004 [*])	12
Table 1-3. Characteristics of some typical crystals used in PET: bismuth germanate (BGO), lutetium oxyorthosilicate (LSO) and sodium iodide (NaI) (Tarantola <i>et al</i> 2003). 14	
Table 1-4. Properties of PET blood flow tracers (Klein <i>et al</i> 2010a, Machac 2005). ¹⁵ O-water is not a trapped tracer and is therefore mainly used for dynamic myocardial blood flow (MBF) quantification, not generating myocardial perfusion images (MPI). NH ₃ : ammonia. NA: not applicable. ¹⁸ F-mitochondrial inhibitors (18F-MC-1) are an emerging blood flow tracer.(-): data not available.	43
Table 2-1. Demographics for the truth dataset and the Jan 2011-Dec 2012 dataset. The Jan 2011-Dec 2012 dataset does not contain the Truth dataset. The Truth dataset contains 200 images (i.e. 100 paired rest/stress studies). [†] denotes a significant difference between Truth dataset and Jan 2011 – Dec 2012 dataset, p = 0.05. BMI = body mass index. Continuous variables are expressed as mean \pm standard deviation (range); categorical variables are expressed as % (number).	69
Table 2-2. Demographics for the Truth dataset by interference severity class, as per the clinician’s interference severity classification, broken down into Rest and Stress images. [‡] denotes a significant difference between Absent Rest (Stress) severity class and other Rest (Stress) severity classes, p = 0.017. BMI = body mass index. Continuous variables are expressed as mean \pm standard deviation (range); categorical variables are expressed as % (number).	70
Table 2-3. The parameters used by the algorithm, their units and values tested during optimization. A notation of A: B: C indicates a range of A to C inclusive at intervals of B. SA = short axis; CW = clockwise; MMI = maximum myocardial intensity.	73
Table 2-4. The threshold values and mean and 95% confidence interval on the mean [95%CI] of the accuracy measures of the final algorithm. Columns two and three give the size (N) and the known positive truth fraction (n) of the image population used for evaluation at the given threshold.	80

Table 2-5. Accuracy measures versus interference severity class. The mean and 95% confidence interval on the mean [95%CI] were evaluated on all images from the truth dataset for which the algorithm successfully completed (column three) during TFSCV for overall Kappa. Column 2 gives the distribution of the known truth interference severity classes. 81

Table 2-6. Prevalence of interference (p) in Jan 2011 – Dec 2012 dataset as evaluated by the proposed algorithm. Rest and stress image prevalence are shown separately; prevalence is not corrected for sensitivity or specificity of the algorithm and the uncertainty is the 95% confidence interval on prevalence, [95%CI]..... 83

Table 3-1. Summary of ECI reduction and removal results versus the alternate forms of image processing examined in Chapter 3..... 124

Table 4-1. Comparing the difference in myocardial segment values after minus before correction (delta) for the dynamic-based correction algorithm applied to the evaluation dataset. 162

Table 4-2. Revised category D delta values and comparisons for the dynamic-based correction algorithm applied to the evaluation dataset after exclusion of one category D scan exhibiting a non-physiologic myocardial basis function..... 165

Table 5-1. Initialization and bounds of myocardial-only model parameters, applied when fitting profiles from the interference-free region. r = profile radial location; $r = 0$ at the FlowQuant-determined LV myocardium, $r < 0$ inwards (blood pool), $r > 0$ outwards. .. 181

Table 5-2. Bounds of myocardial-stomach model parameters. N_i is used to denote the initialization value of the parameter N ; r = profile radial location; $r = 0$ at the FlowQuant-determined LV myocardium, $r < 0$ inwards (blood pool), $r > 0$ outwards..... 186

Table 5-3. Delta values and comparisons for the 1D convolution-based correction algorithm (Ch5) applied to the evaluation dataset, including additional comparisons to the dynamic-based algorithm (Ch4) in categories C and D. Delta is the difference in myocardial segment values after minus before correction. 192

Table 5-4. Revised category D delta values and comparisons for the 1D convolution-based correction algorithm applied to the evaluation dataset, after exclusion of the category D scan exhibiting a non-physiologic myocardial basis function in Chapter 4. 195

List of Figures

- Figure 1-1. (a) Heart anatomy and blood flow: deoxygenated blood is denoted in blue, oxygenated, in pink. The four chambers of the heart are labeled and the walls, composed of heart muscle a.k.a. *myocardium*, are shown in grey². Heart diagram source: (Lynch 2006), modified to add labels.(b) The coronary arteries are located on the surface of the heart. The aorta is the artery through which blood exits of the left ventricle, at the base of the heart. The right and left coronary arteries (RCA and LCA respectively) originate at the aorta: the left branches to become the left anterior descending (LAD), and the left circumflex, (LCX). Counter intuitively, the base of the heart is located at the top, at its widest point, near the origin of the aorta; the apex of the heart is the bottom tip, near the end of the LAD. Figure source: www.texasheart.org/HIC/images/coronill.gif (last accessed 17 July, 2015)..... 3
- Figure 1-2. The three states of myocardial perfusion interpreted via comparison of stress versus rest images from a PET MPI study with the tracer 82-rubidium chloride, (⁸²Rb). The images are oriented to show a slice through the left ventricle, in the plane orthogonal to the long axis of the ventricle and are displayed on a scale of 0 (no tracer uptake) to 1 (maximum myocardial tracer uptake). 7
- Figure 1-3. Differential cross-section versus Compton scattering angle for 511 keV photons 12
- Figure 1-4. PET scanner components and geometry for a scanner using a block design. PMTs: photomultiplier tubes; LOR: line of response. Labeling of the 2x2 PMT array is used in Equations 1-3a and b..... 13
- Figure 1-5. Line of response (LOR) data spatially binned into projections: (a) a sample projection within a single detector ring is a function of radial distance (r) and transaxial angle (θ), and (b) projections between rings also require a non-zero azimuthal angle (ϕ) to fully describe the projection..... 18
- Figure 1-6. Temporal binning of coincidence events to produce a series of sinograms: all or a portion of the acquisition data is selected and then divided via (a) dynamic binning based on acquisition time which produces sinograms for each time frame or (b) gated binning based on an external, periodic trigger produces sinograms for all phases of the cycle. ECG: electro-cardiogram..... 20

Figure 1-7. Four types of coincidence events that occur in PET detection: (a) true, (b) attenuation, (c) scatter and (d) random. The pink semi-transparent lines indicate the detected LOR resulting from the coincidence event. No coincidence events are detected as a result of attenuation but the photon reaching the detector may be recorded as a singles event. 26

Figure 1-8. Illustration of the partial volume effect, PVE, due to a system with a 14 mm FWHM Gaussian PSF imaging a 10 mm wide rectangular function of amplitude 1.0. The rectangular function represents the true underlying structure, (True). When the true underlying structure is imaged, convolution with the system PSF causes the intensity of the true underlying structure to spread. Subsequent digitization of this signal demonstrates the PVE. *is used to denote convolution in the figure legend..... 33

Figure 1-9. 1D analytic model of the myocardial wall. Above the 1D rectangular function (left), the orientation of the profile that this function represents is shown on an image of a slice through the LV cavity in the plane perpendicular to the cavity axis (the short axis orientation, Figure 1-10b, section 1.6.4). The Gaussian function, $f(x)$, representing the scanner PSF, is shown on the right. A_{myo} , A_b , and A_{bkgd} denote the activity concentration in the myocardium, the blood inside the LV cavity and the background, respectively. R and w are the location of the inner boundary of the myocardial wall and the width of the wall, respectively, while \otimes denotes the convolution operator, σ is the standard deviation of the Gaussian distribution and x is the radial position along the profile. 34

Figure 1-10. Our centre's (UOHI) ^{82}Rb PET MPI protocol. ^{82}Rb bolus duration is 30 s; bolus infusion and PET acquisition begin simultaneously. Aminophylline begins 4 mins after start of stress PET acquisition. 45

Figure 1-11. Scanner reference frame (a) versus the left-ventricle (LV) reference frame (b). PET reconstruction produces a series of trans-axially oriented image slices, image processing is then used to re-orient cardiac images to the LV reference frame. Heart diagram source: (Lynch 2006)..... 47

Figure 1-12. 3D representation of the left ventricle (a) and corresponding polarmap (b) extracted from a ^{82}Rb PET MPI scan using FlowQuant software (Klein *et al* 2006). (c) shows the American Heart Association (AHA) 17 segment polarmap model (Cerqueira *et al* 2002) and demonstrates the territories attributed to each of the three main coronary arteries. The concentric rings of this polarmap represent, from the outside ring inwards, the basal, mid, apical, and apex regions of the LV, respectively. FlowQuant images are displayed on a scale normalized the maximum myocardial intensity (MMI)..... 48

Figure 1-13. Short-axis (SA) image slices from ^{82}Rb PET MPI scans showing (a) normal myocardial perfusion, (b) abnormal myocardial perfusion and (c) unknown perfusion in the inferior myocardial wall due to extra-cardiac interference (ECI). SA slices are displayed using the 10-step colour-scale and are normalized to the maximum myocardial intensity (MMI). 51

Figure 1-14. The organs and structures that surround the left ventricle (LV): (a) coronal view and b) short axis (SA) view. The SA view can be thought of as looking, from the front of the subject’s left hip towards the back of their right shoulder, with the head tilted so that the upper left corner of the SA view corresponds to the centre of the subject’s chest. The diaphragm is 3D and so can appear planar in both the coronal and SA views 52

Figure 1-15. Cardiac contraction of the left ventricle (LV) versus location of wall centre and wall width: systole is maximum contraction, diastole maximum dilation (relaxation). A diaphragm-like structure is shown below the LV to help visualize the relative separation between it and the wall centre, at systole versus diastole. 56

Figure 2-1. Example SA slices of clinician’s extra-cardiac interference severity classifications. Images are scaled independently to show relative uptake with the maximum myocardial intensity (MMI) shown as pink (1) and absent tracer uptake shown as black (0). 68

Figure 2-2. Processed image showing automated software detection of the left ventricle (LV) myocardium. Pseudo-short axis (SA) slices are shown on the left, with slice numbers located in the upper left corners (1-8 conical and 9-24 planar slicing); the larger images on the right show Horizontal and Vertical long axis views (HLA and VLA, respectively). The right ventricle (left side of SA/HLA views) and stomach wall (inferior region of SA and VLA views) are also visible. 71

Figure 2-3. Representative samples of the parameters used by the algorithm and the range of values searched during optimization. Table 2-3 lists all values of parameters and thresholds tested during optimization. 74

Figure 2-4. Mean receiver operating characteristic (ROC) curves (solid, blue) and Kappa (dotted, red) versus false positive ratio (FPR) for S1, S2 and S3 thresholds; produced with ten-fold stratified cross-validation of the optimal combination of parameters. The points of maximum Kappa are marked and Table 4 lists the threshold values and accuracy measures for these points. TPR = true positive ratio. Error bars show 95% confidence intervals..... 79

Figure 3-1. Example short axis (SA) image slices of the reference image and systolic and diastolic cardiac-gated frames for a scan with moderate interference in the reference image that is reduced to mild in the systolic cardiac gated frame but which increases in the diastolic frame. The centre of the myocardial wall is shown with a thin white line; the interference search region is outlined with heavy white lines and the region where interference was detected is delineated in black. The clinical 10-step colour scale is used with units of % maximum myocardial intensity (%MMI). 96

Figure 3-2. Example short axis (SA) image slices of the respiratory frames exhibiting minimum and maximum interference compared to the reference image, for the scan with mild interference in the reference image that is removed in the minimum interference respiratory gated frame. The centre of the myocardial wall is shown with a thin white line in SA slice images; the interference search region is outlined with heavy white lines and the region where interference was detected is delineated in black. The SA slice images are shown with the clinical 10-step colour scale, in units of % maximum myocardial intensity (%MMI)..... 105

Figure 3-3. Two examples showing SA slices of scans with reductions in interference severity in static 8 mm Hann filtered images relative to that in the reference images: severe interference in the reference image, reduced to moderate in the 8 mm filtered image (first row) and mild interference in the reference image removed in the 8 mm filtered image (second row). Colour scale units are %MMI. 112

Figure 3-4. Example scan with mild interference in the reference image demonstrating interference severity as a function of filter width in static images: 12 mm Hann (reference), 8 mm Hann, 4.3 mm Hann and unfiltered images. 113

Figure 3-5. Example scan where removing filtering does not remove interference but the increased image noise causes the DSC algorithm to incorrectly classify interference as absent. 114

Figure 3-6. Two example scans demonstrating the effect of combining cardiac gating with reduced filtering. (a) shows a scan with ECI in the reference image that is reduced to mild in the systolic (ES) cardiac gated image frame when an 8 mm Hann filter is applied, but not when 16 mm or 12 mm filters are applied to the same gated frame; (b) shows a scan where mild ECI in the reference image is unchanged by the combination of cardiac gating and filtering. Colour scale units are %MMI. 115

Figure 3-7. Two examples showing SA slices of scans with reductions in interference severity in TOF 4 mm Hann filtered images relative to that in the reference images: severe interference in the reference image, reduced to mild in the TOF 4 mm filtered image (left) and mild interference in the reference image removed in the TOF 4 mm filtered image (right). Colour scale units are %MMI. 121

Figure 3-8. Example SA slices from the reference image and the TOF 4 mm filtered image for a scans showing mild interference in the reference image, which is not eliminated in the TOF 4 mm filtered image where noise levels are higher than those in the reference image. Colour scale units are %MMI. 122

Figure 4-1. Mean region of interest (ROI)-based time activity curves (TACs) for the stomach and the heart wall from the dynamic image series of 30 ⁸²Rb PET MPI scans. Data provided by C. Hunter, (Hunter 2010). 130

Figure 4-2. Manually sampled region of interest (VOI)-based time activity curves (TACs) for 3 example dynamic image series, all with visible stomach uptake. In the upper row, TACs are expressed as a function of dynamic frame number; in the lower row, as a function of the frame’s central acquisition time. LV = left ventricle; RV = right ventricle. 147

Figure 4-3. Implementation of FAMIS-MSO with an automatically determined number of factors on six example scans with visible stomach uptake. The first column shows the FAMIS VOI on pseudo-static SA image slices; columns 2 – 4 show the product of the pseudo-static images and structures, {S1, S2 and S3}, corresponding to the factor curves, {F1, F2 and F3}, shown in column 5. Ex2 and Ex6 are the no-interference, visible stomach and severe interference scans shown in Figure 4-2, respectively. 149

Figure 4-4. Implementation of FAMIS-MSO with four factors on example scans of Figure 4-3. The first column shows the FAMIS VOI on pseudo-static SA image slices; column 2 shows the ‘corrected image’: the product of the pseudo-static images and the sum of all structures except that attributed to the stomach (denoted *); columns 3 – 6 show the product of the pseudo-static images and structures, {S1, S2, S3 and S4}, corresponding to the factor curves, {F1, F2, F3 and F4}, plotted in column 5. 150

Figure 4-5. Application of FAMIS-MSO with 3 factors and a VOI excluding the stomach and interference regions to Figure 4-3 example scans. Pseudo-static SA image slices with the VOI delineated are shown in column 1, followed by structure images (columns 2 – 4) and corresponding factor curves (column 5). 152

Figure 4-6. Basis functions derived using a combination of FAMIS with 3-factors and a VOI excluding stomach and VOI-TAC derived stomach basis function, shown for examples from the categories A, B and C development images. Column 1 shows pseudo-static SA image slices with the FAMIS VOI excluding stomach (upper dotted), the stomach search region (solid) and the stomach TAC-VOI delineated (lower dotted); column 2, myocardium, LV and RV blood factor curves from application of FAMIS-MSO with 3 factors and the VOI from column 1. Column 3 shows stomach VOI-TACs and TACs fit with a 1-compartment model using the LV blood factor curve and column 4 shows all four basis functions together. The category A and category C examples are the no

interference, visible stomach and mild interference scans shown in Figure 4-2, respectively.....	153
Figure 4-7. The four methods of fitting factor curves and the TAC-derived stomach function to remove noise and produce physiologically realistic basis functions.....	154
Figure 4-8. The results of four variations in the correction method for the three development image examples of Figure 4-6. The VOIs in column 1 show the area of the image selected for correction; the two additional VOIs in column 4 show the pure stomach region for the $T = 0.7$ and $T = 0.4$ thresholds. The correction methods which produced images in columns 2 and 3 did not constrain stomach fall-off and used the basis function fitting methods given; the correction methods which produced images in columns 5 and 6 constrained stomach fall-off to $\leq pc10$ (less than or equal to the upper 10% of coefficients of voxels closer to pure stomach) and used the basis function fitting and pure stomach threshold values given.....	155
Figure 4-9. Interference-free physiological normal perfusion rest and stress databases, NDBINT-free; units are maximum myocardial intensity, MMI.....	156
Figure 4-10. Histograms of delta values for the $N = 22$ category D evaluation dataset scans.....	163
Figure 4-11. Examples demonstrating the two types of correction algorithm failure on category D images. Type (a), first row, is the more common failure where factor curves appear physiologically realistic but myocardial intensity is unchanged by correction; while type (b), second row, is the isolated case where factor curves and resulting basis function fits are non-physiologic and myocardial intensity is greatly reduced by correction.....	164
Figure 4-12. FlowQuant (Klein <i>et al</i> 2006) voxel-based 1-compartment kinetic modeling of measured TACs to evaluate uncertainty on resulting basis functions (AUC-normalized KM-predicted curves). The examples shown are the {No interference, visible stomach; mild interference; and severe interference} scans from Figure 4-2.....	167
Figure 5-1. The interference-free (ECI-free) and interference-search (ECI-search) regions along with example 1D profiles as extracted from each region. The vertical line on the profiles demonstrates the inwards extent where profiles will be truncated during initialization prior to modeling (section 5.2.4).	176
Figure 5-2. Myocardium-only model and parameters, where: A_b , A_{myo} , and A_{bkgd} are the blood, myocardium and background amplitudes, respectively, and c_{myo} and w_{myo} are the myocardium centre location and width and FWHM is the full width at half maximum of a 1D normalized Gaussian PSF.....	179

Figure 5-3. Development of the mean and 95% confidence myocardium-only model from the interference-free region of a SA slice: (a) interference-free profiles and (b) mean \pm 95% myocardium-only model. 179

Figure 5-4. Myocardium-stomach model and parameters, where: A_b , A_{myo} , and A_{bkgd} are the blood, myocardium and background amplitudes, c_{myo} and w_{myo} are the myocardium centre location and width, FWHM is the full width at half maximum of a 1D normalized Gaussian PSF, A_{stom} and w_{stom} are the stomach amplitude and width and $sep_{myo-stom}$ is the radial separation/distance between the outer wall of the myocardium and the inner wall of the stomach. 180

Figure 5-5. Example of information used to visually evaluate the appropriate value for the coefficient of determination (R^2) when the myocardium-only model is applied in the interference-search region. The locations of the two profiles (b, no interference, white profile and c, with interference, blue profile) as well as the results of the DSC algorithm are displayed on the SA slice (a). 182

Figure 5-6. A selection of the observed profile shapes that must be fit by the myocardium-stomach model: (a) bi-modal with high stomach amplitude; (b) indistinct separation with high stomach amplitude; (c) bimodal with low stomach amplitude; (d) indistinct separation with gradually decreasing but detectable, low amplitude stomach; (e) constant, low amplitude background. Note the difference in vertical scale used in (b); the vertical dotted line on each plot marks the outer boundary of the myocardium. For initialization of the stomach parameters, profile values outside (right) of this boundary are considered. 184

Figure 5-7. Sequential process used to decide the initialization method used for stomach parameters based on characteristics of the profile shape. Profile shapes are illustrated in Figure 5-6; A is the amplitude of the profile and r is the radial coordinates of A . r_{myo} outer is the location of the outer myocardial wall, \exists indicates 'there exists', $|$ indicates 'such that' and Lagrange's notation is used to represent derivatives. 185

Figure 5-8. Examples of the information used to visually evaluate the appropriate values for the coefficient of determination (R^2) and maximum allowable difference between measured and fit profiles values, $dmaxmyo$, when the myocardium-stomach model is applied in the interference-search region. (a) shows successful fitting; (b) shows failure and (c) shows success due to incorporation of $dmaxmyo$ and relaxing R^2 188

Figure 5-9. Examples of the two types of incorrect myocardial intensity found during visual review of corrected images from the evaluation dataset: (a) shows where excess myocardial intensity was removed and (b) shows where insufficient stomach was removed. 197

Figure 5-10. Demonstration of the 1D convolution-based correction algorithm results on an image from each category in the algorithm development dataset. Scans are the same as those used in Figure 4-9. 198

Figure 5-11. The difference between correction algorithm results for the dynamic-based versus the 1D convolution-based algorithm , on the two scans used in Figure 4-11 to demonstrate failure of the dynamic-based algorithm in category D images..... 199

List of Appendices

Appendix A. Permission for use of material from Medical Physics.....	232
Appendix B. Ottawa Health Research Ethics Board (OHREB) Application.....	234
B.1 OHREB Approval Letter	235
B.2 PhD Supervisory Committee Approval.....	236
B.3 Annual Renewal Report.....	237
B.4 OHREB ethics protocol, final version 8 May 2013.....	239

Glossary

AUC	area under curve
CA	coronary angiography
CRC	clinically relevant change
CT-AC	computed tomography based attenuation correction
CW	clockwise
CCW	counter-clockwise
DCS	detection and severity classification
dixel	voxel in a dynamic image series
ECI	extra cardiac interference
FA	factor analysis
FADS	factor analysis of dynamic sequences
FAMIS	factor analysis of medical image sequences
FOV	field of view
IHD	ischemic heart disease
KM	kinetic modeling
LVEF	left ventricle ejection fraction
MBF	myocardial blood flow
MFR	myocardial flow reserve
MLEM	maximum likelihood expectation maximization
MMI	maximum myocardial intensity
MPI	myocardial perfusion imaging
MSO	minimum spatial overlap
NDB	normal database

NF	no filtering
OSEM	ordered subset expectation maximization
PCA	principle component analysis
PI	potential interference
PLS-FADS	penalized least-squares FADS
PSF	point spread function
PVE	partial volume effect
RC	recovery coefficient
rms	root mean square
RPM	Real-time Position Management system (Varian Medical)
SRS	sum of perfusion defect scores at rest
SSS	sum of perfusion defect scores at stress
SS-sim	single scatter simulation
SVD	singular value decomposition
TAC	time activity curve
TBV	total blood volume
TFSCV	ten-fold stratified cross validation
UOHI	University of Ottawa Heart Institute
VOI	volume of interest

1 Chapter: **Introduction**

1.1 **Overview**

Heart disease affects a large fraction of the human population (Finegold *et al* 2013). Effective management of this disease, including methods for diagnosis and monitoring, is therefore important to many people. One non-invasive method for tracking heart disease uses positron emission tomography (PET). PET permits visual evaluation of the heart muscle's blood supply and allows nuclear cardiologists to accurately determine the degree and effect of blocked arteries with good sensitivity (the ability to detect disease when present) and specificity (the ability to rule out disease when absent). In some patients, PET images of cardiac blood supply are affected by signal from organs nearby the heart. Signal from these organs can mix with that of the heart, filling in signal deficits in the heart and masking areas inadequately supplied with blood due to a blocked artery. This poses a problem and reduces the efficacy of the PET images. Signal mixing in PET images arises from limited spatial resolution combined with motion during imaging. This thesis presents methods to detect, quantify, and compensate for the extra-cardiac interference (ECI) in cardiac PET imaging. The remainder of this chapter supplies the background necessary for understanding: why imaging cardiac blood supply with PET is important, the physics behind PET, the cardiac blood supply signal and how images of this signal are interpreted, and finally, the present state of knowledge on ECI and the goals of this thesis.

1.2 Heart disease

Cardiovascular diseases encompass diseases of the heart and circulatory system¹. The most recent data, from 2008, stated that cardiovascular disease was responsible for 29% of deaths in Canada, heart disease was one of the 3 leading causes of death and 4.8% of Canadians reported living with heart disease (Statistics Canada 2011).

1.2.1 The heart and coronary arteries

The heart is a muscle whose shape forms four chambers (Figure 1-1a), which contract to pump de-oxygenated blood from the body into the lungs (blue, right side of the heart²), then pumps the newly oxygenated blood from the lungs back out to the rest of the body (pink, left side of heart²). The chamber which pumps oxygenated blood out to the body is the left ventricle (LV). Since this action requires the most pressure, the LV wall is the thickest and most powerful of the heart walls. Although proper function of all chambers is important for overall heart health, some cardiac tests focus mainly on the LV.

The heart muscle, or *myocardium*, requires a blood supply of its own to obtain the oxygen and nutrients it requires to beat continuously. Blood is delivered to the myocardium via the coronary arteries: large vessels that run over the outer surface of the heart, branching and penetrating the myocardium like the roots of a tree into the ground³. The three main coronary arteries are the left anterior descending (LAD), left circumflex (LCX) and right coronary artery (RCA) Figure 1-1b.

¹ The major components of which are heart disease and stroke

² Right and left are reversed in the display of most medical images to represent the point of view of the doctor, facing the patient.

³ Note however that the direction of the flow of nutrients is opposite to the tree analogy: in the myocardium, it's like the tree is supplying nutrients to the soil

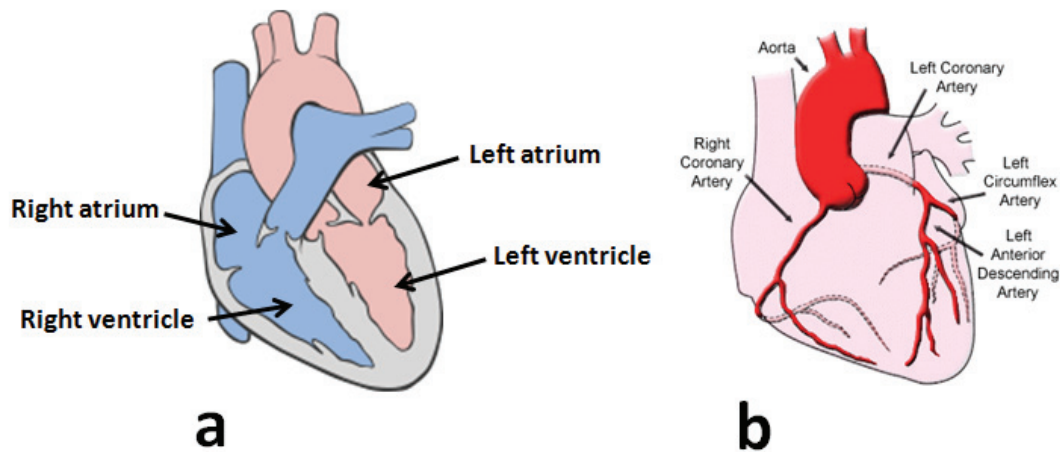


Figure 1-1. (a) Heart anatomy and blood flow: deoxygenated blood is denoted in blue, oxygenated, in pink. The four chambers of the heart are labeled and the walls, composed of heart muscle a.k.a. *myocardium*, are shown in grey². Heart diagram source: (Lynch 2006), modified to add labels.(b) The coronary arteries are located on the surface of the heart. The aorta is the artery through which blood exits of the left ventricle, at the base of the heart. The right and left coronary arteries (RCA and LCA respectively) originate at the aorta: the left branches to become the left anterior descending (LAD), and the left circumflex, (LCX). Counter intuitively, the base of the heart is located at the top, at its widest point, near the origin of the aorta; the apex of the heart is the bottom tip, near the end of the LAD. Figure source: www.texasheart.org/HIC/images/coronill.gif (last accessed 17 July, 2015)

These arteries branch off the aorta at the base (superior end) of the LV and trace their way down to the apex (the lower tip of the LV which lies caudal/inferior and anterior of base). The heart sits to the left of centre in the chest cavity and its axis, if pictured as an upright cone, is rotated approximately 50° counter clockwise (CCW), (towards the patient left) in the coronal plane and 20° clockwise (CW), (towards the anterior) in the

sagittal plane. The average human heart is approximately the size of a fist and the RV sits on the right, anterior surface of the LV. Maximal cardiac contraction is referred to as systole, at which time the LV cavity has its smallest volume and LV walls are at their thickest. Cardiac relaxation or dilation, known as diastole, is when the LV cavity is at its largest volume and LV walls are most thin. The thickness of the LV wall in humans falls within the range of 0.8 – 1.5 cm (Kaul *et al* 1986, Johnson *et al* 2011, Erlandsson *et al* 2012).

1.2.2 Ischemic heart disease (IHD)

Ischemic heart disease (IHD)⁴ contributes significantly to mortality but also, due to medical advances, many more people are surviving their first cardiac event (e.g. heart attack) and therefore continue to live chronically with IHD. IHD is a type of cardiovascular disease where plaque (fat and cholesterol) builds up inside the arteries of the heart in a process known as *atherosclerosis*. Plaque can block the arteries, stiffen their walls and, if sufficiently severe, it can limit the amount of blood delivered to the myocardium by the artery. If the amount of blood required by the myocardium is greater than the artery can supply, a condition known as *ischemia* results. Myocardium can be chronically or acutely ischemic. If the blood deficit is chronic but not severe, or if it is severe and acute (blocked only for limited period of time), ischemic myocardium can recover if necessary blood supply is restored; however, if severe ischemia persists, the myocardium fed by the blocked artery will die, a process known as *infarction*, leaving behind scar tissue. Once scarred, tissue cannot recover even if blood supply is

⁴ Ischemic heart disease has a number of names, including: coronary artery disease, CAD, coronary heart disease, CHD, atherosclerotic heart disease and atherosclerotic coronary disease

restored. The medical term for heart attack is *myocardial infarction* (MI) and is characterized as heart tissue death, typically as a result of acute, severe ischemia. In 2008, 54% of cardiovascular death in Canada was attributed to IHD and an additional 23% to heart attack (which can result from IHD)(Statistics Canada 2011). In 2010, IHD was the leading source of disease adjusted life years worldwide (Murray *et al* 2012) and Finegold *et al.*, having reported IHD as the leading cause of death worldwide for both men and women, notes that methodology for early diagnosis is especially important from a universal healthcare standpoint due to the fact that ‘... the susceptibility of IHD to prevention and treatment is exquisite’(Finegold *et al* 2013).

1.2.3 Care for IHD

The symptoms of IHD (e.g. chest pain, shortness of breath) are not always apparent (Zellweger *et al* 2009) and even the occurrence of cardiac events (e.g. heart attack) can be ambiguous, making early stage diagnosis difficult as the process of plaque accumulation in the arteries is gradual.

Simple lifestyle changes (diet and exercise) and medications (statins, a cholesterol-lowering class of drugs) can be effective for treating early stage disease (Kereiakes *et al* 2007). When plaque accumulation becomes functionally significant (defined as resulting in downstream ischemic tissue) invasive re-perfusion surgery known as percutaneous intervention (PCI) can use a stent (wire mesh cylinder) or a balloon to push open the blocked artery. PCI is considered minimally invasive but surgical intervention is both expensive and incurs additional patient risk, as disturbing atherosclerotic arteries can dislodge or disrupt plaque and cause stroke. Studies show that the benefits outweigh

the risks for reperfusion surgery if $\geq 10\%$ of the LV is ischemic (Hachamovitch *et al* 2003). Surgery, such as a coronary artery bypass graft (CABG), is an alternative treatment to PCI. CABG allows reperfusion without significant disruption of the blocked arteries and, in the limit of heart failure (where enough of the LV tissue is infarcted or scarred that the heart is prevented from pumping blood out to the body effectively) the only remaining solution is heart transplant. It is important to note that if the end tissue supplied by a blocked artery is scarred and not ischemic, then reperfusion is not useful.

1.2.4 Myocardial perfusion imaging (MPI)

Myocardial perfusion imaging uses intravenously injected, radioactive atoms or radioactively-labeled molecules, known as *tracers*, and nuclear tomographic imaging to non-invasively show the relative, regional blood supply to the LV myocardium. Also referred to as a *nuclear stress test*, MPI studies focus on the LV and include two sets of data: one acquired in the resting state and one after exercise or pharmacologic stress. Acquiring data at rest and at stress reflects the 'stress-test' concept employed in many cardiac diagnostic tests. At stress (e.g. exercise) the demand for blood by the body and the myocardium increases, often bringing to light deficiencies not apparent under resting conditions. When transitioning from rest to stress, the healthy heart's characteristic electrical depolarization-repolarization signal should remain unchanged, contractile wall motion should not develop regional abnormalities and the coronary arteries should all dilate to maintain uniform blood supply (*perfusion*). Abnormal signs at stress that return to normal at rest indicate ischemia, while abnormalities that persist at rest indicate scarred or infarcted tissue.

MPI can therefore be used to differentiate between normal perfusion, ischemia and scar and can indicate the location and fraction of the LV myocardium affected by abnormalities, Figure 1-2. The artery experiencing a functionally significant blockage can be inferred from the location of the segment of the myocardium showing decreased perfusion and the ischemic versus scarred fraction of the LV can be used to assess risk of future cardiac events and direct therapy (medication versus reperfusion versus invasive surgery) (Hachamovitch *et al* 2003). Many consider the gold standard for performing MPI to be positron emission tomography (PET) (Bengel *et al* 2009, Loong and Anagnostopoulos 2004). Since MPI focuses on the LV, from this point onwards, *myocardium* will be used to refer to *LV myocardium* unless otherwise stated.

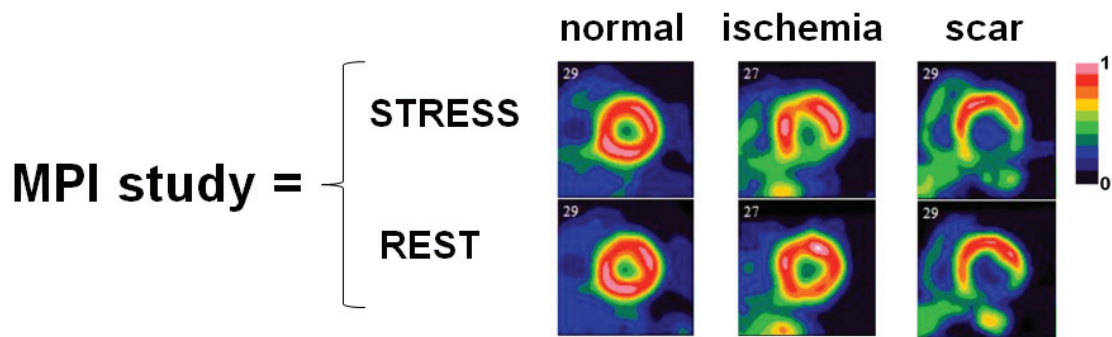


Figure 1-2. The three states of myocardial perfusion interpreted via comparison of stress versus rest images from a PET MPI study with the tracer 82-rubidium chloride, (⁸²Rb). The images are oriented to show a slice through the left ventricle, in the plane orthogonal to the long axis of the ventricle and are displayed on a scale of 0 (no tracer uptake) to 1 (maximum myocardial tracer uptake).

1.3 Positron emission tomography (PET)

Positron emission tomography (PET) is a medical technology that creates 3-dimensional (3D) images of the distribution of radioactively-labeled tracers that have been injected into a patient and subsequently decay through the emission of positrons.

1.3.1 Positrons, positron emitting isotopes and annihilation photons

Positrons and decay by positron emission

Positrons are elementary, anti-matter particles with the same mass and charge as electrons but their charge is positive. Radioactive isotopes which decay via positron emission (*beta plus decay*) are used as the source for PET. Isotopes with excess protons in the nucleus, relative to their stable atomic state, decay by either positron emission or electron capture. Decay can be fully positron, fully electron capture or a mixture of both, as dictated by the isotope's *branching ratio*; and may also involve the emission of secondary gamma photons if the positron emission or electron capture transition leaves the nucleus in an excited state. Decay by positron emission changes a proton, from the nucleus of the unstable parent, into a neutron in the daughter nucleus, emits a positron and a neutrino from the atom, each with some kinetic energy and, since the positive charge on the nucleus has now decreased by one, an orbital electron is also released. The combined kinetic energy of the positron and the neutrino is equal to the net change in rest mass before versus after decay and can be calculated using the atomic mass-energy balance equation. If decay results in an excited state, the energy of secondary gamma photons must also be included in the mass-energy balance equation. Positron emitters are typically produced by proton bombardment in a cyclotron; however, they

can also be decay products, e.g. 82-strontium (^{82}Sr), with a half life ($t_{1/2}$) of 25.5 days, decays by electron capture to 82-rubidium (^{82}Rb), a positron emitter. When the positron emitter is produced via a decay process with a suitably long half-life, it can be supplied by a generator thus avoiding the cost of an onsite cyclotron.

Positron interactions with matter and annihilation

When interacting with matter, positrons in motion behave as electrons do, experiencing collisional and radiative energy losses. As anti-matter, when positrons have little to no remaining kinetic energy, they encounter a nearby electron and annihilate. With annihilation, the rest mass energy of the positron and electron is converted into two gamma photons which have equal energies (511 keV). If the positron undergoes annihilation at rest, the resulting photons are emitted in opposite directions, conserving momentum. If the positron has some residual kinetic energy at annihilation, termed *in-flight annihilation*, the emission angle will no longer be exactly 180 degrees between the two photons. Positron range, the distance traveled from the point of emission to the point of annihilation, can be reported in a number of ways. The extrapolated range reflects the maximum possible distance that a positron, emitted with maximum energy and traveling a straight path (i.e. not scattering), could obtain. Since positrons are emitted with a range of energies and typically do scatter multiple times prior to annihilation, the average range is much less than this and the distribution of distances from emission to annihilation is 'inverse cusp' shaped with a narrow centre and long tails (Levin and Hoffman 1999). The FWHM can be evaluated for this distribution; however, for the purposes of estimating its effect on PET spatial resolution, the most

appropriate measure of range is the effective FWHM. Range is also a function of the electron density of the material through which the positron travels. The positron ranges for some typical isotopes used in PET for medical imaging are given in Table 1-1.

Typical isotopes used in PET

Isotopes chosen for use in PET ideally have a suitable half-life relative to the process being imaged, branching ratios that are heavily positron decay weighted with little to no secondary gamma emissions, low positron energy and energy of secondary gammas far from that of positron annihilations photons (511 keV). Table 1-1 gives the values of some of these properties for typical isotopes used in medical imaging of blood flow with PET.

Table 1-1. Properties of some positron emitting nuclides used for medical imaging. β^+ ranges are in water and the effective FWHM = 2.35*root mean square (rms) range. (Cherry *et al* 2012, Lecomte 2004)

Radio-nuclide	Half-life	β^+ fraction	Max β^+ energy, [MeV]	β^+ range, [mm]			Production method
				extrapolated	FWHM	effective FWHM	
¹¹ C	20.4 min	0.99	0.96	3.9	0.13	0.92	Cyclotron
¹³ N	9.96 min	1.00	1.19	5.1	0.17	1.35	Cyclotron
¹⁵ O	123 s	1.00	1.72	8	0.28	2.4	Cyclotron
¹⁸ F	110 min	0.97	0.635	2.3	0.13	0.54	Cyclotron
⁸² Rb	76 s	0.95	3.35	16.5	0.42	6.1	Generator (⁸² Sr)

Photon interactions in matter at 511 keV

At 511 keV annihilation photons interact by coherent scatter, photoelectric interaction or Compton scattering.

Interaction cross sections are based on photon energy and atomic number (Z) of the material. The dominant form of interaction for 511 keV photons in biological materials and scintillator materials is Compton scatter. The amount of energy transferred from the incident annihilation photon to the scattered electron in a Compton scattering interaction as a function of scattering angle, α , is given by Equation 1-1:

Equation 1-1.
$$hv' = \frac{511}{2 - \cos(\alpha)}$$

where α is defined relative to the direction of the incident photon prior to scattering,

and h

$h\nu'$ is the final energy of the scattered photon

The probability of Compton scatter at a given angle is dictated by the Klein-Nishina differential cross-section $d_e\sigma/d\Omega_\alpha$, Equation 1-2. At 511 keV, this is forward peaked with minimum probability of scatter orthogonal to the original direction of the photon, ($\alpha = 90^\circ$), Figure 1-3.

Equation 1-2.
$$\frac{d_e\sigma}{d\Omega_\alpha} = \frac{r_0^2}{2} \left(\frac{hv'}{hv}\right)^2 \left(\frac{hv}{hv'} + \frac{hv'}{hv} - \sin^2\alpha\right)$$

where $d_e\sigma/d\Omega_\alpha$ is the differential cross section per unit solid angle and per electron at photon scattering angle α , r_0 is $e^2/m_0c^2 = 2.818 \times 10^{-13}$ cm (the 'classical electron radius'), $hv = 511$ keV is the original photon energy.

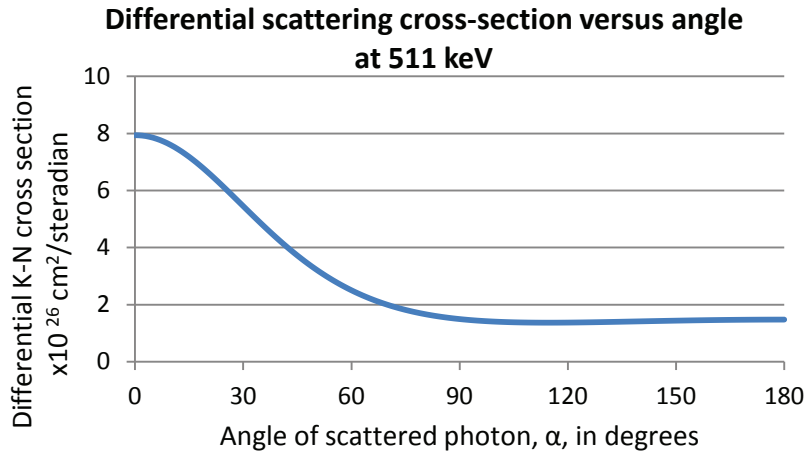


Figure 1-3. Differential cross-section versus Compton scattering angle for 511 keV photons

Table 1-2 gives the relative contribution of the photoelectric effect versus Compton scattering to the overall linear attenuation coefficient (μ) for some materials relevant to medical imaging.

Table 1-2. Ratio of the photoelectric ($\mu_{\text{photoelectric}}$) to the Compton scattering (μ_{Compton}) linear attenuation coefficient, and the total (μ) linear attenuation coefficient values for 511 keV photons in materials relevant to medical imaging (Berger *et al* 2010, ICRP 2002†, Cherry *et al* 2012‡, Pepin *et al* 2004*).

Material	$\mu_{\text{photoelectric}} / \mu_{\text{Compton}}$	μ [cm^{-1}]	density [g/cm^3]
ICRP Skeletal muscle (composition†)	0.0002	0.10	1.04
ICRP Bone (composition†)	0.0020	0.17	1.85
Bismuth germinate (BGO, $\text{Bi}_3\text{Ge}_4\text{O}_{15}$ ‡)	0.651	0.85	7.13*
Lutetium oxyorthosilicate (LSO, Lu_2SiO_5 ‡)	0.521	0.81	7.35*

1.3.2 PET detectors

PET detectors are built to interact with the collinear 511 keV annihilation photons and are typically composed of scintillation crystals backed by photomultiplier tubes (PMTs) as shown in Figure 1-4. When the annihilation photons interact with the scintillation crystals, the energy deposited in the crystals is converted into a burst of visible light photons. These photons then travel through the remainder of the scintillator to reach the photomultiplier tubes, where they are converted into an electrical pulse.

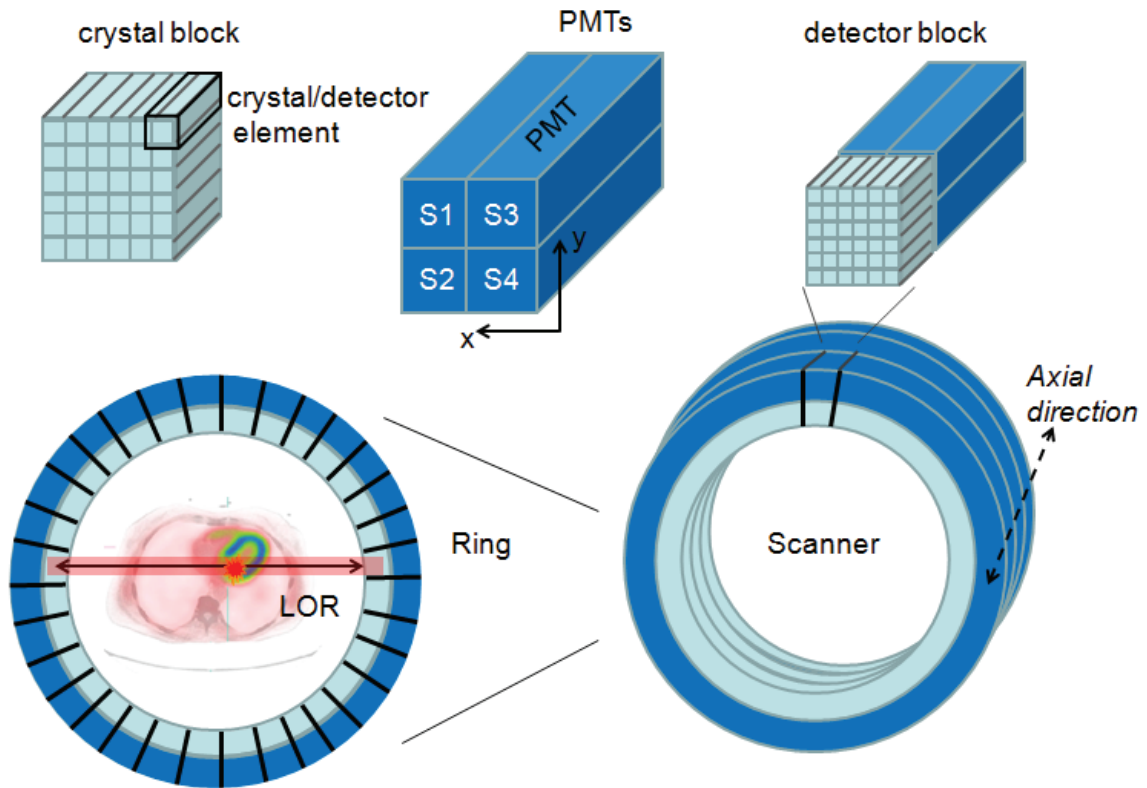


Figure 1-4. PET scanner components and geometry for a scanner using a block design. PMTs: photomultiplier tubes; LOR: line of response. Labeling of the 2x2 PMT array is used in Equations 1-3a and b.

Scintillation Crystals

Scintillators are characterized by their density, light output (number of visible light photons emitted per unit energy from high energy photon interaction) and decay time constant (rate at which light escapes the crystal). Ideal scintillators are dense to maximize the probability of 511 keV photon interactions, have high light output and short decay time to maximize both spatial and temporal precision of the subsequent electronic signal, are non-hydroscopic to avoid complications in packaging, and are easily cut into detector-element-sized pieces. Historically, bismuth germanate (BGO) was the most commonly used PET detector crystal but, although it remains in use for many commercial scanners, lutetium oxyorthosilicate (LSO) is now considered the crystal of choice due to its superior characteristics for PET imaging (in particular its short decay time). The characteristics of some typical crystals used in PET are given in Table 1-3.

Table 1-3. Characteristics of some typical crystals used in PET: bismuth germanate (BGO), lutetium oxyorthosilicate (LSO) and sodium iodide (NaI) (Tarantola *et al* 2003).

Scintillation crystal	Relative light output	Decay time constant (ns)	Density (g/cm ³)	Effective atomic number (Z)	Energy resolution at 511 keV
BGO	0.15	300	7.1	73	0.12
LSO	0.50 – 0.80	40	7.4	65	0.10
NaI	1	230	3.7	50	0.08

Block detectors

Most commercially produced PET scanners incorporate a block detector design: where multiple crystal elements are grouped together and read out by a smaller number of PMTs, Figure 1-3. The detector element configuration will contribute to determining the spatial resolution limit of the scanner.

A single PMT with multiple anodes or multiple PMTs is/are arranged backing onto the crystal block. The pattern of light sharing that then occurs between the anodes or separate PMTs creates a signature characteristic of a 511 keV photon interaction in a single detector element. The visible light emitted from a gamma interaction is spread amongst the PMT array and Equations 1-2a and 1-2b (Phelps 2004) are used to produce an (x,y) position for the event, assuming the 2x2 configuration of PMTs/PMT anodes given in Figure 1-3.

$$\text{Equation 1-3a.} \quad x = (S1 + S2 - S3 - S4)/(S1 + S2 + S3 + S4)$$

$$\text{Equation 1-3b.} \quad y = (S1 + S3 - S2 - S4)/(S1 + S2 + S3 + S4)$$

This (x,y) position is typically distorted relative to the actual position of the event in the scintillator block due to non-uniform light sharing to the PMTs/PMT anodes. To convert (x,y) position to the crystal element where the annihilation photon interaction occurred, the position is compared to a flood histogram calibration for the block. This flood histogram is derived from uniformly irradiating the block surface and represents the likelihood of an event with calculated position (x,y) having originated in each detector element (Phelps 2004).

PET scanners

To provide full angular coverage of a given plane, PET scanners typically consist of detector elements arranged in a ring. When blocks are arranged in this configuration, multiple rings are formed, giving the PET scanner field of view (FOV) some axial extent, Figure 1-4.

The commercial scanner used to acquire the data for this thesis was a Discovery 690 PET/CT (GE Healthcare), which couples a PET scanner with an x-ray CT scanner. The PET scanner portion of the Discovery 690 packages 9 (transaxial) x 6 (axial) individually cut LYSO scintillation crystals together which back onto a single four-anode PMT. 64 detector blocks are arranged to form a 70 cm diameter ring. Each rings is 4 blocks deep in the axial dimension, giving 4 blocks x 6 crystals/block = 24 individual crystal detector elements axially. The crystal size is 4.2 mm (trans-axial) x 6.3 mm (axial) x 25 mm (depth, radial). When inter-crystal and inter-block spacing is included, this results in a net axial span of 157 mm (Bettinardi *et al* 2011).

1.3.3 Coincidence detection, lines of response and projections

Two fundamental physical characteristics of annihilation photon emission differentiate PET from other forms of gamma photon imaging: emission is 1) simultaneous and 2) back-to-back (co-linear). Simultaneous emissions permit us to assume that two photons originate from a single annihilation event if they arrive at the scanner and are detected within a very short *coincidence timing window*; this is known as the principle of *coincidence detection*. The coincidence timing window is typically 0.5 – 20 ns (Phelps 2004) and its duration is determined by the scanner bore diameter, scintillator decay

constant and variations in electronic signal processing time. Knowing further that the two photons are co-linear allows a line to be drawn between the two detector elements which register the coincidence event and the assumption made that the annihilation must then have occurred somewhere along this *line of response* (LOR), Figure 1-4. The PET scanner geometry determines the LORs available and the imaging FOV within the scanner rings determines the set of useful LORs. Coincidence events can be spatially binned by radial position from the centre of the scanner versus angle to produce one-dimensional *projections*, Figure 1-5. Historically, only coincidence events from LORs within the same ring of the scanner were accepted and projections were described by radial position, transaxial angle (θ) and ring number. The current standard for PET coincidence acquisition is now '3D mode' which accepts coincidence events from LORs between all rings of the scanner, significantly increasing scanner sensitivity. When LORs between rings are used, projections are now also a function of the azimuthal angle (ϕ), Figure 1-5b.

1.3.4 Acquisition: raw data formats and external triggers

Raw data formats

Raw PET data are typically acquired in list-mode format (LMF) which records each coincidence event in a time-stamped list providing the two detectors in coincidence and the energy deposited. This format requires large amounts of memory (~2.5 GB for a 60-80 million coincidence event clinical scan) but allows post-acquisition division of the data; enabling multiple images to be produced from a single acquisition, or *scan* (section 1.3.5).

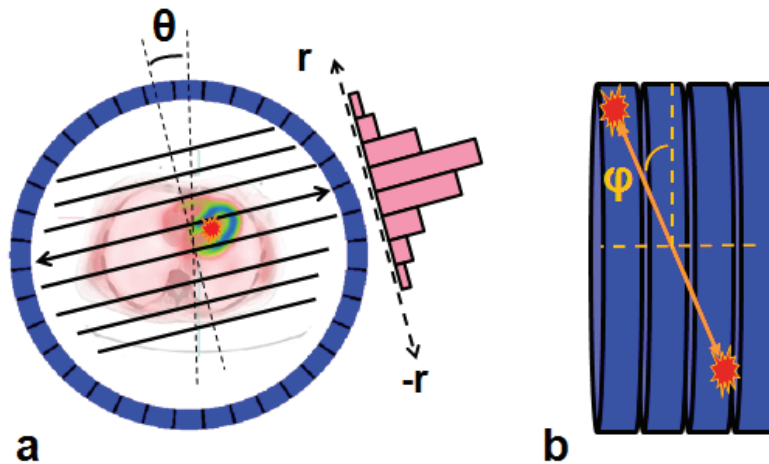


Figure 1-5. Line of response (LOR) data spatially binned into projections: (a) a sample projection within a single detector ring is a function of radial distance (r) and transaxial angle (θ), and (b) projections between rings also require a non-zero azimuthal angle (ϕ) to fully describe the projection.

External triggers

If external devices are used to monitor the subject during PET data acquisition, their information can be included in the list-mode data and integrated into PET image processing. Such devices can monitor time dependent behaviour and produce trigger events that are incorporated into LMF files and are then used post-acquisition to subdivide data. For this work, two external devices were used: an electrocardiogram (ECG) to monitor the cardiac cycle and the Real-Time Position Management (RPM) system (Varian Medical) to track respiratory motion.

1.3.5 Data organization

Spatial binning: Sinogram format

As introduced above, a projection contains the number of events detected by each LOR at a given angle, for the set of parallel lines spanning the FOV of the scanner. When the combination of projections from the scanner are arranged as an (r,θ) matrix, this is referred to as a 2D *sinogram*. During fully 3D acquisition, as is used for scans in this work, LORs between all axial scanner rings (*oblique planes*) are accepted and LMF files are spatially binned into 3D sinograms, now a function of (r,θ,ϕ) . Most image reconstruction algorithms take sinogram format data as input. Sinogram format greatly reduces storage requirements over LMF.

Temporal binning

Temporal binning divides acquired LMF data into pieces from which multiple sinograms, and subsequently multiple images, can be produced. For the purposes of MPI, temporal binning is based either on coincidence event time or on periodic external trigger signals. Coincidence time based binning can be used to select a single, continuous period of acquisition and produce a *static* sinogram and image, or it can select sequential periods of time to produce a *dynamic* series of sinograms and images, Figure 1-6a.

Binning based on external triggers from a device monitoring a periodic process that occurs during PET data acquisition (such as cardiac contraction or respiration) divides up the data from the LMF file like dealing a hand of cards. Triggers are used to label each coincidence event with the phase of the cycle in which it was acquired. All events from

each phase can then be grouped and a *gated* series of sinograms and images produced, Figure 1-6b.

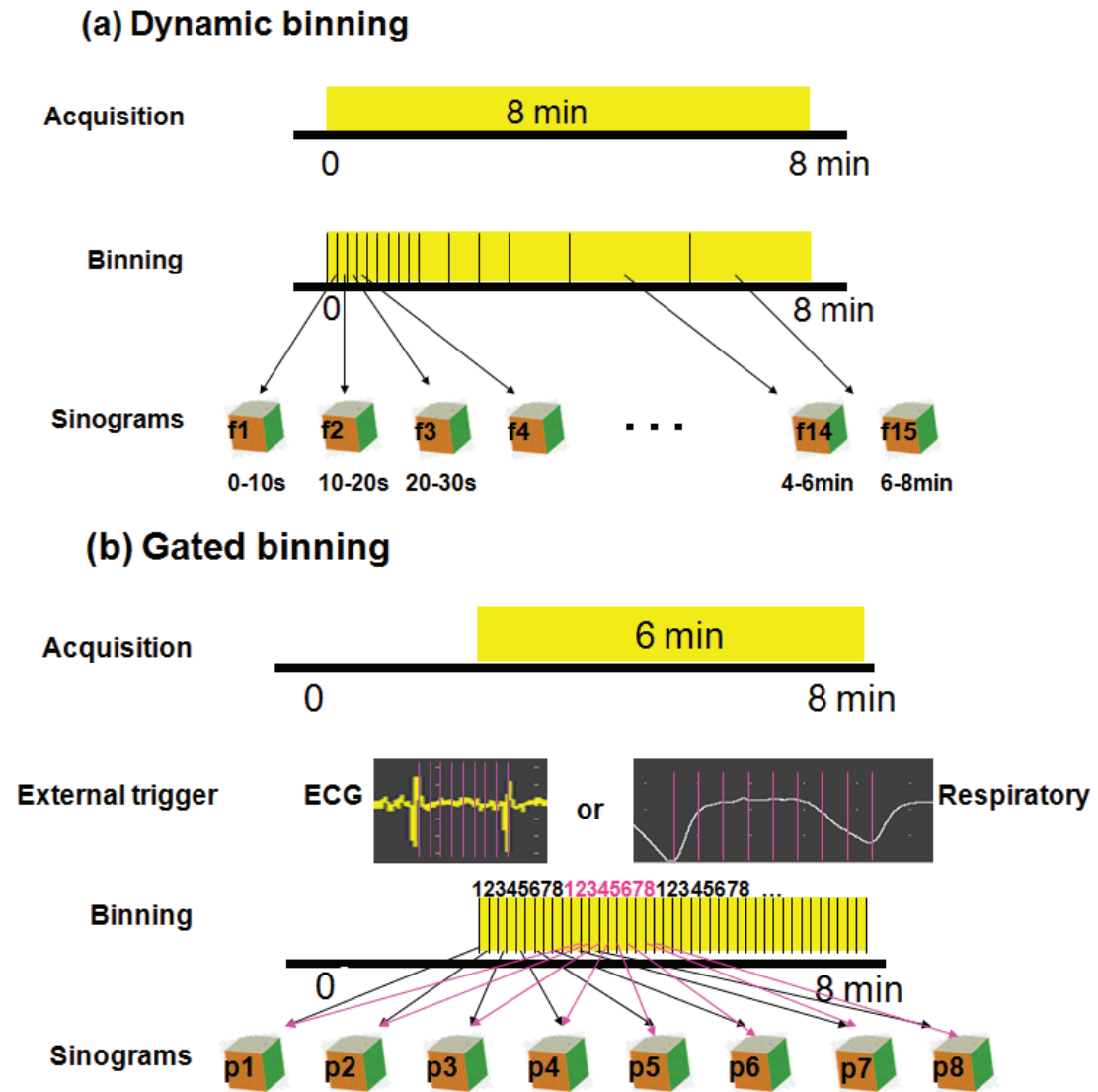


Figure 1-6. Temporal binning of coincidence events to produce a series of sinograms: all or a portion of the acquisition data is selected and then divided via (a) dynamic binning based on acquisition time which produces sinograms for each time frame or (b) gated binning based on an external, periodic trigger produces sinograms for all phases of the cycle. ECG: electro-cardiogram.

1.3.6 Image reconstruction

Projections and sinogram data represent Radon transforms of the distribution of activity in the detector's FOV. Reconstruction is the process by which projection data are converted into cross-sectional images using the algorithms of computed tomography. There are two main types of algorithm in current clinical use: filtered back-projection and iterative reconstruction. The principles behind these types of algorithm are outlined below, followed by a brief description of how time of flight information (TOF) can aid reconstruction.

Filtered back-projection (FBP)

Filtered back-projection (FBP) (Radon and Parks 1986) is the most commonly used analytical form of image reconstruction. Originating from simple back-projection (where the intensity recorded for each LOR is simply 'smeared' back into all image pixels along the LOR and the image produced as a summation of the smeared lines), filtered back-projection improves this by using the Fourier transform and a ramp filter to correct the inherent $1/r$ blurring effect present in simple back-projection. FBP can be performed in either 2D or 3D but requires minimum linear sampling below which streaking artifacts occur. FBP also requires data with full coverage, i.e. 3D FBP requires a method to produce a full 'sphere' of projections. Because it is analytic, FBP is computationally fast but assumes noise-free projection data, ignores the effects of the system point-spread function (section 1.4.1), and corrections (section 1.3.7) such as for scatter are typically applied to the projection data prior to reconstruction and may not provide as accurate a correction as can be achieved by including scatter estimation within an iterative

algorithm. Although iterative reconstruction overcomes these limitations, FBP continues to be used for reconstruction of data series with many sinogram frames (e.g. typical dynamic series with >10 frames) in the interest of minimizing computation time.

Iterative reconstruction

Iterative reconstruction (Shepp and Vardi 1982, Hudson and Larkin 1994, Qi and Leahy 2006) uses a model of the PET camera (the *system model*) to calculate projection data from an estimate of the activity distribution (i.e. the image). The calculated projections are then compared to measured projections (i.e. the sinogram) and the estimated activity distribution updated. This process is repeated until calculated projection data reflect measured projection data. The system model can incorporate information about the statistical nature of the projection data and include estimates of the effects of degrading influences such as attenuation, scatter, randoms and the system point spread function (PSF) (section 1.4.1). In these ways, information unaccounted for in FBP is incorporated into iterative reconstruction and, depending on the nature of the projection data, can result in higher quality images (better spatial resolution and lower noise) produced by iterative reconstruction compared to those produced by FBP.

Maximum likelihood expectation maximization (MLEM) is a frequently used form of iterative reconstruction (Shepp and Vardi 1982), and ordered subset expectation maximization (OSEM) is a variation of the MLEM algorithm that divides the full set of measured projections into a number of equal sized subsets (n) and updates the image estimate based on each subset in turn (Hudson and Larkin 1994, Qi and Leahy 2006).

OSEM is advantageous since forward projection (calculating projections from the

activity distribution estimate through the system model) is the most time consuming part of the iterative process and the time to complete forward projection is proportional to the number of projections that must be calculated. Because of this, and the fact that one iteration is considered to have occurred when all projections have been used once, the computation time for one OSEM iteration is comparable to that for one MLEM iteration. However, since OSEM provides n subset updates to the image estimate per iteration, images resulting from k iterations of OSEM have been shown of similar quality to those produced by $k*n$ iterations of MLEM (Qi and Leahy 2006).

Time of flight information

Time of flight (TOF) refers to the interval between creation of an annihilation photon and its interaction in a detector element. Up to this point, the principles of coincidence detection and co-linearity have been combined to place annihilation events on the LOR joining two detectors in coincidence. If the timing resolution of the system is reduced below the transit time of a photon across the LOR then the difference in detection times between two photons arriving within the coincidence timing window can be used to better locate the position of the annihilation along the LOR. This is the principle behind TOF, which, in the limit of ideal timing resolution, could be used to avoid image reconstruction entirely as the difference in detector arrival times would dictate the exact location of the annihilation event on the LOR.

The timing resolution values currently achieved with commercially available detectors are 500-600 ps which provides the location of annihilation to within 10-15 cm. Timing resolution is a function of: scintillator light output and decay time and electronic

processing speed and reliability (Cherry and Dahlbom 2006). Since typical PET scanners used for medical imaging have ring diameters on the order of 80-100 cm, TOF information can be integrated into reconstruction algorithms by representing annihilation event location as a Gaussian probability distribution along the LOR, centered on the location dictated by the difference in arrival times and with FWHM dictated by the timing resolution of the LOR detector pair. TOF information can be incorporated into both FBP and iterative reconstruction and, for consistency, should also be incorporated into corrections (in particular scatter correction) (Conti 2009). The main effect of TOF information on reconstructed images is reduced noise correlation length (i.e. spatial range, relative to a signal source, over which noise originating from that source affects the image) which leads to increased signal to noise ratio (SNR). Increased SNR can then be translated into decreased post-reconstruction filter width (section 1.2.4). Because TOF adds information to the reconstruction, it increases computational complexity and, without modifying processing techniques, will increase the computation time required for reconstruction. It has; however, been shown that for a single iteration, adding TOF information can accelerate convergence (Wang *et al* 2006). Overall, the benefit of TOF information is reported to be greatest where there is the most ambiguity in source location, i.e. in cases of limited count statistics and where corrections (scatter, randoms, normalization, section 1.3.7) may be inaccurate (Conti 2011). In this work, TOF information is used in Chapter 3 within VUE Point FX (GE-Healthcare 2009) iterative TOF reconstruction of static images. The VUE Point FX algorithm takes 3D sinograms as input and performs fully 3D, iterative reconstruction

which includes corrections for randoms, normalization, scatter and attenuation within the forward projector (system matrix). TOF information is fully incorporated into the model, including model-based scatter correction (GE-Healthcare 2009).

1.3.7 Corrections

There are multiple factors which can degrade the quantitative accuracy of the PET image. Four of the most important corrections to make in ^{82}Rb PET are for the effects of attenuation, scatter, random coincidences and dead-time, all of which aim to restore the validity of the assumption that all emitted annihilation photons result in true coincidence events (Figure 1-7a).

Attenuation

Attenuation results from the interaction of one or both annihilation photons with the intervening medium before reaching the detector (Figure 1-7b) and is reflected in the projection data as missing true coincidence events. The magnitude of attenuation for a given LOR is the integral of the linear attenuation coefficient for 511 keV photons across the materials in the FOV.

PET originally used radio-isotope transmission scans for attenuation correction; however, x-ray computed tomography (CT) based attenuation correction (CT-AC) has now been the dominant form for more than a decade. Attenuation maps are produced by a CT scanner coupled to the PET scanner, forming the single-bed PET-CT unit and avoiding the motion and deformation associated with transferring subjects between two scanners. CT-AC acquisition is fast and attenuation maps contain very little noise compared to the PET data. CT uses an x-ray beam, typically of energy 100 – 140 kVp, and

because attenuation coefficients are energy dependent, the CT-AC attenuation factors must be adjusted through segmentation (division of the image into regions of uniform attenuation coefficient) and/or scaling (Kinahan *et al* 2003) to reflect those at 511 keV. The fraction of the radiation dose, received by the patient, from the CT-AC portion of a PET-CT scan is not negligible. Methods to reduce CT dose have been implemented clinically, including increased axial pitch and modulating the photon fluence (via x-ray tube current, in milli-amperes, mAs) and energy (via x-ray tube voltage, in kilovolt potential, kVp) (McCollough *et al* 2006, Bruesewitz *et al* 2008).

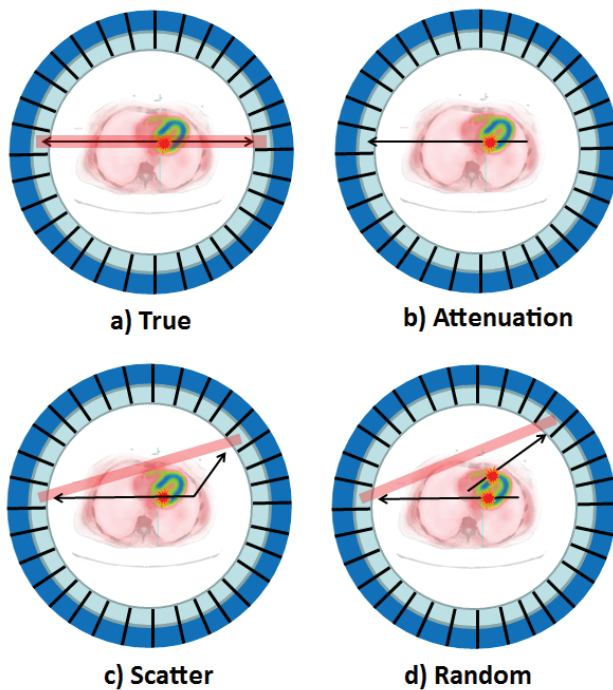


Figure 1-7. Four types of coincidence events that occur in PET detection: (a) true, (b) attenuation, (c) scatter and (d) random. The pink semi-transparent lines indicate the detected LOR resulting from the coincidence event. No coincidence events are detected as a result of attenuation but the photon reaching the detector may be recorded as a singles event.

Finally, differences in acquisition duration between x-ray CT (1-5 s) and PET (minutes) can lead to co-registration problems in the presence of patient motion (Gould *et al* 2007). Images for this work were visually assessed for 3D CT-AC alignment by the PET technologists using online tools prior to final reconstruction; misalignments ≥ 3 mm were manually corrected by 3D linear transformations.

Scatter

Scatter also arises from the interaction of 511 keV photons before reaching the detector; however, scattered photons lose only a fraction of their energy and are redirected instead of being absorbed, Figure 1-7c. Scattered photons are therefore reflected in projection data as mis-positioned coincidence events. Compton scatter is the dominant form of interaction for 511 keV photons in materials relevant to medical imaging with PET, Table 1-2 (Cherry *et al* 2012). Scatter contamination in 3D PET is typically 30 -50%, for cardiac imaging with our scanner, the scatter fraction is 50-80% (Teras *et al* 2007). Poor energy resolution prevents complete exclusion of scattered photons from the PET detector photopeak and thus additional forms of scatter correction are needed. A full discussion of scatter correction in PET imaging is beyond the scope of this thesis, but Zaidi (2000) provides a good review on the topic.

The single scatter simulation (SS-sim) (Watson *et al* 1996, Ollinger 1996) method is currently the most frequently used scatter correction method for PET (Polycarpou *et al* 2011) and is the method used with our scanner for this work. The SS-sim model reconstructs uncorrected projection data to estimate of the activity distribution and

uses the CT-AC attenuation map as an interaction probability distribution. From these two pieces of information, the detected scatter distribution is estimated. The SS-sim model can be incorporated into iterative or FBP reconstruction techniques and multiple scattering events are corrected using a blurred version of the single scatter distribution. Because even analytic-model based scatter correction can prove time consuming when placed inside the iterative reconstruction loop, the version of SS-sim implemented on our scanner reduces the axial and trans-axial resolution of the activity and attenuation distributions into 'super slices' and uses an analytic simulation method to minimize computation time (GE-Healthcare 2008, Wollenweber 2002).

Randoms

Random coincidences occur when two photons from separate annihilation events are detected in coincidence, Figure 1-7d. The rate at which this occurs for any detector pair is related to the photon fluence seen by each detector and the length of the coincidence timing window. The random coincidence rate can be estimated using two different techniques: a delayed coincidence window or detector singles rates. The delayed window technique uses an additional coincidence timing window, for one of the two detector elements in coincidence, which is sufficiently offset in time to ensure it cannot detect any true coincidences. The number of delayed window coincidences can then be subtracted from the number of true coincidence window events; correcting for the presence of randoms. The detector singles rate technique is based on probability: given the width of the accepted coincidence timing window (Δt) and the event rate at each of

the detector elements in the pair forming the LOR (N_{det1} and N_{det2}) the randoms rate (N_{rand}) experienced by that LOR is given by Equation 1-4 (Phelps 2004):

Equation 1-4.
$$N_{rand} = d\tau^2 N_{det1} N_{det2}$$

The singles rate technique results in far less noise in the randoms correction when compared to the delayed window technique because detectors record a much higher number of singles events than coincidences (approximately 90% of events detected are singles (Phelps 2004)). In images, uncorrected random coincidences appear as uniformly increased background and noise across the image which reduces contrast. In this work, the detector singles rate technique is used to correct for randoms inside the iterative reconstruction.

Dead-time

Dead-time is primarily a result of the timing resolution of the PET detector system which, in turn, is determined by the light output, rise time and decay time constant of the scintillation crystal and electronic components used to subsequently process and measure the signal. Electronic triggering is based on these properties and dictates the uncertainty and interval between sequential events. Another factor that can contribute to timing circuit uncertainty is inconsistency in the propagation time required for analog PMTs signals to reach the digitizer (Phelps 2004). The manufacturer of the scanner used for this work reduces this source of uncertainty by placing multiple digitization units around the detector ring. Dead-time correction becomes necessary when the count rate seen by a detector element results in multiple annihilation photon interactions within a period less than the recovery time of the detector. The recovery time of a detector

element is mostly a function of the scintillation crystal decay constant but can also be affected by signal integration time in the electronics or processing and storage of the coincidence event. Dead-time correction is performed using a look-up table and the result of large dead-time corrections is increased uncertainty in the acquired data. The *dynamic range* of a scanner reflects the range of count rates over which the scanner is able to accurately measure activity.

1.4 Image quality

Image quality is described using a set of image properties known or expected to influence the knowledge to be extracted from the image. A number of properties influence physicians' ability to interpret medical images. The two most important image properties for this work are spatial resolution and image noise.

1.4.1 Spatial resolution

Spatial resolution is typically characterized by the full width at half-maximum (FWHM) of the point spread function (PSF) which estimates the smoothing effect of the system on the image of a point source. The physical characteristics of both the scanner and the isotope contribute to the spatial resolution in PET projection data. The spatial resolution in the final PET image is then a function of the resolution in the projection data as well as the type of reconstruction and any post-reconstruction filtering that is used to reduce image noise. Equation 1-5 (Moses and Derenzo 1993) describes the spatial resolution of images produced with PET detectors that use a block design. This equation includes terms quantifying the effects of detector crystal size, positron range, annihilation photon non-collinearity (caused by in-flight annihilation) and position de-coding

uncertainty within the detector block. These components are summed in quadrature and then a scaling factor is used to incorporate the effect of reconstruction.

Equation 1-5.
$$FWHM = A\sqrt{\left(\frac{d}{2}\right)^2 + R_{\beta}^2 + 0.0022D^2 + R_B^2}$$

where d is the crystal size, R_{β} is the effective FWHM related to the positron range, D is the bore diameter of the scanner, and R_B is the effect of the detector block (Moses and Derenzo 1993). The scaling factor, A , represents the effect of reconstruction and is 1-1.3 (Lecomte 2009). For the scanner used in this work, $d = 4.2$ mm (transaxially) x 6.3 mm (axially) resulting in $(d/2)^2 = 4.4$ mm² (transaxial) x 9.9 mm² (axial); $D = 700$ mm results in $(0.0022D)^2 = 2.4$ mm². With ⁸²Rb as the positron emitter, $R_{\beta+Rb} = 6.1$ mm and $R_{\beta}^2 = 37.2$ mm². The block position de-coding factor, R_B^2 has a value of approximately 4 mm² (Lecomte 2004, Moses 2011). This demonstrates the largest contributions arise from positron range and then crystal size for ⁸²Rb.

The effect of depth of interaction (of the 511 keV photons in the detector crystals) and decreased sampling density, with increasing radial distance from the central axis of the ring (transaxially) and from the central axial plane of the scanner, reduce resolution outside the central region of the scanner FOV. Spatial resolution in the PET scanner varies with position (Phelps 2004), but this can be measured and compensated for through incorporation into an iterative reconstruction algorithm.

The reconstruction algorithm can also influence the spatial resolution. The maximum spatial frequency recoverable is dictated by how finely the projection data are sampled. In addition, for images reconstructed using iterative methods, spatial resolution increases with iteration number and maximum resolution is achieved only once the

algorithm converges. Iterating to convergence is never done in clinical practice due to the computation time required, but as convergence is asymptotic, the loss in resolution is small for the typical number of iterations used in clinical imaging.

The final factor which contributes to spatial resolution, and which dominates ^{82}Rb PET MPI image resolution, is the smoothing filter used to reduce noise levels in reconstructed images. The choice of filter is discussed further in section 1.4.2.

Partial volume effect and spillover

The partial volume effect (PVE) is caused by a combination of the finite spatial resolution of the imaging system and the subsequent discretization when images are displayed digitally. PVE is apparent when the boundaries of structures being imaged do not align with the pixel boundaries of the image (Figure 1-8).

When the spatial extent of the object being imaged is less than twice the PSF FWHM, the true activity concentration in the object will not be recovered, as the PVE causes counts to 'spillover' into adjacent pixels. Integration over the area of the image surrounding the object can recover the total counts and then, if the dimensions of the object are known, the true activity concentration can be calculated. This correction becomes more complicated when multiple objects are imaged and the PVE spillover causes their signals to mix. Many methods have been developed for PVE correction in PET (Rousset *et al* 2007). The majority rely on the ability to accurately model or measure the overall imaging PSF (e.g. via measurements or simulations) and to independently define the structures in the imaging FOV with uniform uptake (e.g. via co-registered anatomical imaging). In PET cardiac imaging, because the thickness of the myocardial

wall is often less than twice the FWHM of the spatial resolution in the images, the myocardial image intensity is affected by PVE.

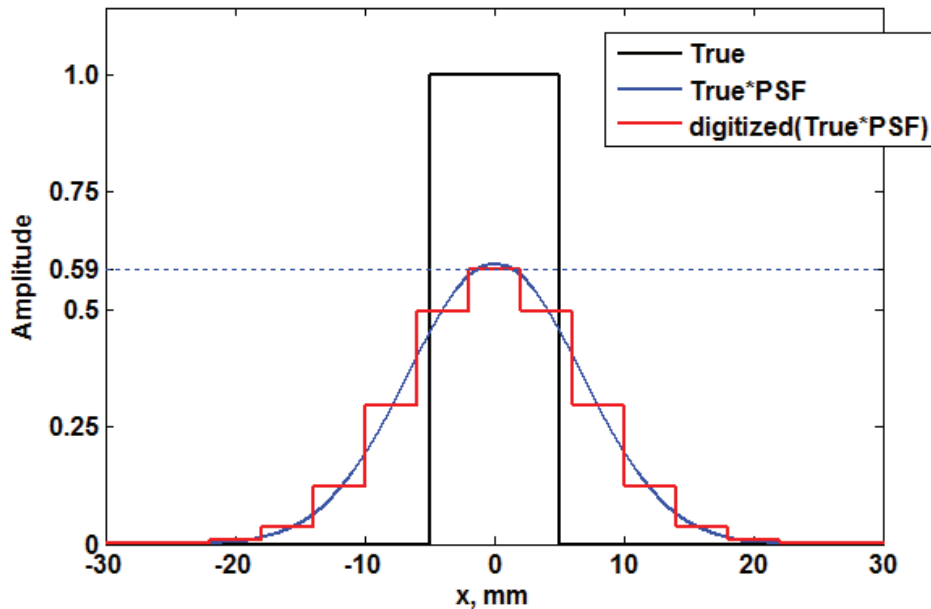


Figure 1-8. Illustration of the partial volume effect, PVE, due to a system with a 14 mm FWHM Gaussian PSF imaging a 10 mm wide rectangular function of amplitude 1.0. The rectangular function represents the true underlying structure, (True). When the true underlying structure is imaged, convolution with the system PSF causes the intensity of the true underlying structure to spread. Subsequent digitization of this signal demonstrates the PVE. *is used to denote convolution in the figure legend.

In his 1992 PhD thesis, Gambhir proposes a 1D analytic model for partial volume correction of cardiac PET images. This model fits 1D profiles, measured radially through the LV myocardial wall, to the convolution of a rectangular function with a Gaussian function, Figure 1-9. The values for the rectangular function parameters are derived from the fit and represent the spatial location {inner radius, R, and width, w, of the

myocardial wall} and activity concentrations of the myocardium, blood inside the LV cavity, and background $\{A_{\text{myo}}, A_{\text{b}}, A_{\text{bkgd}}\}$.

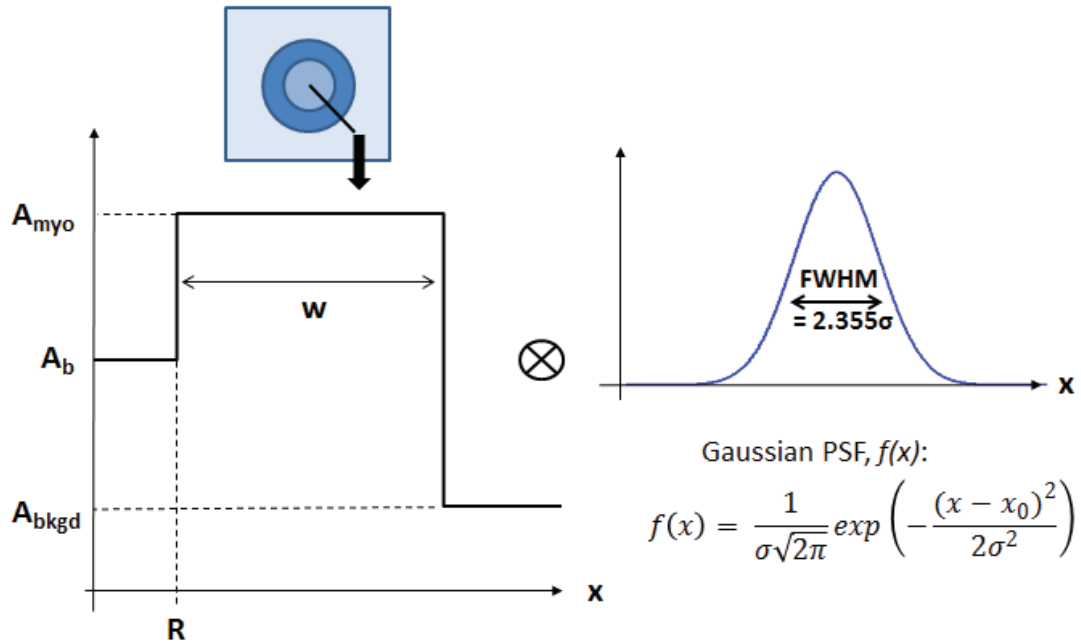


Figure 1-9. 1D analytic model of the myocardial wall. Above the 1D rectangular function (left), the orientation of the profile that this function represents is shown on an image of a slice through the LV cavity in the plane perpendicular to the cavity axis (the short axis orientation, Figure 1-10b, section 1.6.4). The Gaussian function, $f(x)$, representing the scanner PSF, is shown on the right. A_{myo} , A_{b} , and A_{bkgd} denote the activity concentration in the myocardium, the blood inside the LV cavity and the background, respectively. R and w are the location of the inner boundary of the myocardial wall and the width of the wall, respectively, while \otimes denotes the convolution operator, σ is the standard deviation of the Gaussian distribution and x is the radial position along the profile.

The Gaussian PSF is input to the fit and represents the spatial resolution of the imaging system. In Gambhir's model, this function is determined from fitting measurements or simulations of the PET scanner's spatial resolution. Since measurements of the PET scanner's spatial resolution do not account for cardiac motion and neither does modeling the underlying activity distribution with a rectangular function, cardiac gated images are used and all other sources of motion assumed negligible. The model parameters are therefore a function of cardiac gate, g , and of the angle, θ , of the profile when extracted from a short axis (SA, Figure 1.10b, section 1.6.4) image slice.

The convolution is given by Equation 1-6:

Equation 1-6.

conv(rect, Gaussian)

$$\begin{aligned}
&= \frac{1}{2} A_{bkgd}(\theta, g) + \frac{1}{2} A_b(\theta, g) + \frac{1}{2} A_{myo}(\theta, g) \operatorname{erf}\left(\frac{x - R(\theta, g)}{\sqrt{2}\sigma}\right) \\
&\quad - \frac{1}{2} A_{myo}(\theta, g) \operatorname{erf}\left(\frac{x - R(\theta, g) - w(\theta, g)}{\sqrt{2}\sigma}\right) \\
&\quad - \frac{1}{2} A_b(\theta, g) \operatorname{erf}\left(\frac{x - R(\theta, g)}{\sqrt{2}\sigma}\right) \\
&\quad + \frac{1}{2} A_{bkgd}(\theta, g) \operatorname{erf}\left(\frac{x - R(\theta, g) - w(\theta, g)}{\sqrt{2}\sigma}\right)
\end{aligned}$$

where erf is the error function:

$$\operatorname{erf}(u) = \frac{2}{\sqrt{\pi}} \int_0^u \exp(-t^2) dt$$

$A_{\text{myo}}(\theta, g)$ represents the PVE corrected myocardial activity concentration. This model has also been successfully used to evaluate contractile function and LV geometry in human cardiac PET (Porenta *et al* 1995, Khorsand *et al* 2003, Bartlett *et al* 1996).

1.4.2 Noise

Noise can cause spatially distinct signals to become indistinguishable when imaged. The dominant sources of noise in PET arise from stochastic processes which can be represented by the Poisson distribution and therefore require only the number of counts to estimate uncertainty. Positron emission and annihilation photon interactions, both in the FOV and in the detector scintillator, are stochastic processes, and while noise in electronics can introduce both offset and bias, noise in projection data is largely accepted to be white noise. The method used for reconstruction affects image noise, as do the corrections applied. Iterative reconstruction incorporates a noise model that appropriately weights the contribution of each projection datum according to the expected uncertainty in that measurement. This results in correlation of the local magnitude of noise with the magnitude of the local, underlying activity unlike FBP where noise magnitude is uniform throughout the image. In FBP, scatter correction is applied to projection data prior to reconstruction and this can amplify noise. In iterative reconstruction, projections are not altered and scatter is incorporated into the forward projection of the iterative reconstruction loop, mitigating the effect seen in FBP (Qi and Leahy 2006). Noise contributions from CT-based attenuation (Kinahan *et al* 2003) and singles randoms corrections (Phelps 2004) are small since the statistics in their measured values are much better than the coincidence event data. In iterative

reconstruction, noise in the images is often regularized by limiting the number of iterations and not iterating to convergence. For both iterative and FBP reconstruction, noise is also commonly regularized by applying low-pass filtering post-reconstruction. Therefore, although many factors can modulate its magnitude and distribution, for a given type of reconstruction and implementation of corrections, noise in reconstructed images is primarily determined by the number of the coincidence events per LOR in the sinogram(s) used for the reconstruction.

The overall goals of an imaging test will dictate the acquisition protocol, and subsequently, the number of coincidence events obtained per LOR in sinograms, with a specific tracer and scanner. Most frequently, the goal of a MPI study is to produce static images of the tracer taken up and retained in the myocardium. Often however, an additional goal of a MPI study is measurement of myocardial blood flow, MBF (Klein *et al* 2010a). MBF requires a quantitatively accurate dynamic image series, beginning at the time of tracer injection. Achieving these two goals without excessive noise in the static images is challenging when ^{82}Rb is used as the tracer (positron emitter) due to the isotope's short half life and the physiology of tracer delivery and accumulation.

Immediately following injection of the tracer, its activity is in a concentrated bolus and so the entire injected amount can be inside the PET FOV at once, generating very high count rates in the detectors. To avoid detector saturation and inaccuracy in the acquired data due to large dead-time corrections, the amount of injected activity (tracer) must be limited. Once injected, a period of time is required for the tracer to clear from the blood and accumulate in the myocardium before static images are acquired. This delay period

increases with decreased heart function. According to clinical guidelines, the coincidence events used to produce static perfusion images are those acquired beginning anywhere from 70 – 130 s after infusion of the tracer ^{82}Rb is initiated (Dilsizian *et al* 2009). At our centre static imaging in ^{82}Rb myocardial PET begins somewhat later, at 150 s (2.5 minutes) after injection to ensure full clearance of tracer from the LV cavity blood pool. Since ^{82}Rb 's half-life is 76 s, 120 s after injection just 35% of the injected activity remains. The amount of activity available to contribute coincidence events to static MPI sinograms is then further reduced by the fact that tracer accumulation *in the myocardium* plateaus at 2 – 4% of the injected activity (Heller *et al* 2009) after 90 – 120 s following the injection (Klein *et al* 2010a). The ability to accurately measure MBF with ^{82}Rb , therefore, leads to static MPI sinograms which have very low numbers of counts and so produce images with high noise levels. As indicated in section 1.4.1, to mitigate the high noise levels, a larger width post-reconstruction smoothing filter is then often applied.

The upper bound to the PET scanner's dynamic range combined with Rb's rapid decay also limits the total counts that can be acquired: at our center, an injection of 10 MBq/kg of ^{82}Rb is used with a total acquisition period of 8 minutes, producing scans with 60-80 million counts. This count level is much less than, for example, our centre's $^{13}\text{N-NH}_3$ (ammonia) studies which use an injected activity of 3 MBq/kg but due to the longer half-life (10 min) and longer acquisition duration (20 min) produce 400 - 500 million counts.

Because temporal binning involves subdivision of the acquired data, the number of events per image in dynamic or gated series is less than the total acquired. This leads to increased noise and, as a result, a need for increased post-reconstruction filter sizes. The choice of filter is somewhat subjective and will vary from centre to centre depending on the preferences of the reviewing clinicians. In this work, we use the same as are used clinically at our centre for dynamic and gated images. Gated images use 1/8 of the static image data and a 16 mm Hann filter is applied, whereas for static images, a 12 mm Hann filter is applied.

1.5 Motion

Temporal averaging in the presence of motion reduces the sharpness of boundaries and contrast between adjacent regions. It changes the distribution of signal strength within the area occupied by the object and can also allow structures known to be physically separate to appear to overlap in the images. If motion results in deformation, changes in the thickness of structures can alter the magnitude of PVE they experience. Temporal binning is a standard method used to reduce or eliminate motion. If temporally averaged motion is periodic or random, the resulting spatial smoothing can be approximated by a Gaussian function and it becomes possible to incorporate motion into the overall spatial resolution of the image. In cardiac imaging, three sources of potentially significant motion are: respiratory motion and cardiac contraction (both of which are periodic) and gross patient motion (spontaneous, translational movement).

1.5.1 Cardiac

Cardiac contraction involves a complex wringing motion which reduces the inner volume of the LV cavity. Contractile motion of the LV has components along the long axis (base towards apex), radially inwards, and circumferentially clockwise (CW) at the base and counter-clockwise (CCW) towards the apex, when viewed from the base. It is periodic (period is on the order of 1 s, i.e. a minimum heart rate of 60 beats per minute) and in images that temporally average cardiac contraction, sharpness of the inner and outer myocardial walls is reduced by the radial component of contraction. The amplitude of radial contraction of the outer LV surface is position dependent: on the order of 6.7 ± 1 mm in the lateral wall (the wall opposite to that coupling the LV to the RV) and decreasing to virtually no motion approaching the wall coupling the LV to the RV (the septal wall); this is known as the crescent effect (Riordan and Kovács 2006). Grid-tagged MRI has shown that cardiac contractile motion can cause the portion of liver, that is only separated from the myocardial wall by the diaphragm, to move in-phase with cardiac contraction, with a net displacement of up to 4.5 mm (Chung *et al* 2011).

Innervation of the heart controls cardiac contraction and the electrical signal from depolarization of cardiac cells can be measured using an ECG. The largest deflection of the ECG signal, the *R-wave*, occurs at the end of diastole (beginning of systole) when ventricular contraction begins. The R-wave is easily identifiable and is recorded as an external periodic trigger. Division of the time interval between R-waves into phases allows temporal binning (section 1.3.5) to produce a cardiac gated image series with

reduced motion in each gated frame. For this work, the cardiac cycle was divided into 8 gated image frames.

1.5.2 Respiratory

Respiratory motion results from contraction of the diaphragm, mainly in the superior-inferior direction, and simultaneous expansion of the chest cavity, in both the lateral and anterior-posterior directions. The heart on one side of the diaphragm, and the stomach, liver and spleen, on the other side experience mainly superior-inferior translational motion with amplitudes proportional to their distance from the diaphragm. In a study of 187 ^{82}Rb PET MPI images, the displacement of the LV due to respiratory motion was found to be 2.9 ± 1.0 mm left-right, 2.3 ± 0.9 mm anterior-posterior and 4.4 ± 2.0 mm superior-inferior, resulting in a net displacement 5.4 ± 2.0 mm (29% of images had net displacement > 6 mm) (Wells *et al* 2010). The amplitude and pattern of respiratory motion can be highly variable but this variation can be minimized with coaching (Cervino *et al* 2009). The typical period of the respiratory cycle is 3 - 5 s. In this work, the respiratory cycle is tracked using the RPM (Varian Medical) external monitoring system. The system detects motion of infrared reflectors on a block placed on the patient's chest and generates an amplitude-based trigger signal. Creation of an 8-frame respiratory-gated image series from amplitude-based triggers is then analogous to the production of cardiac gated image series from R-wave ECG triggers described in the previous section.

1.5.3 Gross patient motion

Gross patient motion (shifts due to coughing, sneezing, adjusting position) can be identified using a visual tracking system. With tracking information it is possible to correct for this motion in cardiac perfusion imaging (King *et al* 2013, Mukherjee *et al* 2013) and in PET brain imaging gross motion is corrected for routinely. Recent work suggests that gross patient motion may be a more significant problem in ^{82}Rb PET cardiac imaging than previously thought, especially when dynamic image sequences are reconstructed for myocardial blood flow (MBF) assessment (Klein *et al* 2011). At our centre, visual tracking of gross motion is not currently available and so is not corrected and instead accepted as an additional but not interpretation-limiting loss of resolution.

1.6 PET Myocardial Perfusion Imaging

1.6.1 Tracers

As noted in section 1.2.4, tracers are radioactive atoms or radioactively-labeled molecules which, when administered at trace (very low) concentrations in-vivo (in a living organism), can follow a biological process of interest without disturbing it. When choosing a tracer for imaging myocardial perfusion, many factors must be considered, from biological and physiological, through physical and practical (e.g. economical). Myocardial blood flow and perfusion studies aim to produce 3D images of the regional distribution of blood supplied to the myocardium with sufficient image quality for clinical interpretation and an acquisition time short enough to allow sequential rest and stress imaging without significant patient motion or discomfort. Costs and radiation

dose must be kept low (as the fraction of population with IHD is large) and good diagnostic and prognostic accuracy for IHD are essential. Table 1-4 lists some of the important properties of four PET myocardial blood flow tracers.

Table 1-4. Properties of PET blood flow tracers (Klein et al 2010a, Machac 2005). ¹⁵O-water is not a trapped tracer and is therefore mainly used for dynamic myocardial blood flow (MBF) quantification, not generating myocardial perfusion images (MPI). NH₃: ammonia. NA: not applicable. ¹⁸F-mitochondrial inhibitors (18F-MC-1) are an emerging blood flow tracer.(-): data not available.

	¹⁵ O-water	¹³ N-NH ₃	⁸² Rb	¹⁸ F-MC-1
Extraction fraction (%)	~100	>90	~40	>90
Retention fraction (%)	NA	55 - 65	25 - 30	-
Isotope half-life (min)	2.03	9.97	1.27	109.8
Injected activity for 3D PET (MBq)	700 - 900	370 - 550	750-1000	150-300
Rest + stress total dose for 3D PET (mSv)	1.6 – 2.0	1.5 – 2.2	1.1 – 2.2	7 - 10
Radiation dose-limiting organ	Heart	Bladder	Kidneys	Bladder
Extra-cardiac organ(s) with high uptake during MPI scan acquisition period	NA	Liver	Stomach, spleen	Liver
Rest-stress interval (min)	0	20 - 40	0	-
MPI(MBF) Scan-time (min)	NA(6)	10(2 – 20)	6(2 – 8)	-(2 – 10)
Reconstructed image resolution (mm)	8 - 12	6 - 10	8 - 12	4 - 8
Production method	On-site cyclotron	On-site cyclotron	Generator	Regional cyclotron

1.6.2 ⁸²Rb PET MPI

⁸²Rb-RbCl, rubidium chloride, is used as an MPI tracer. ⁸²Rb is a cation that resembles potassium and can therefore be taken up into myocardial cells by active transport using

the transmembrane transport enzyme ATP-ase, also known as the sodium-potassium pump. Due to its short radiological half life (76 s), ^{82}Rb is administered using a custom infusion system (Klein *et al* 2007). 50-60% of the administered dose is extracted from the blood during the tracer's first pass through the vasculature (Mullani *et al* 1983) and blood clearance is typically quick, with the recommended time for perfusion imaging beginning 70 – 90s after infusion for patients without impaired ventricular function (Machac *et al* 2006). Excretion is renal. In healthy myocardium, uptake plateaus at 2 - 4% of the injected activity by 1.5 - 3 minutes after completion of the injection. Uptake is linearly proportional to blood flow up to flow rates of 2.5 – 3 times the resting rate (Heller *et al* 2009, Klein *et al* 2010a). Once inside myocardial cells, ^{82}Rb behaves as a trapped tracer with a small washout rate constant. Due to ^{82}Rb 's short half life, whole body and individual organ doses are low ($1.26 \pm 0.20 \mu\text{Sv}/\text{MBq}$ whole body and maximum organ dose (kidneys) of $5.81 \mu\text{Gy}/\text{MBq}$ (Senthamizhchelvan *et al* 2010)). ^{82}Rb is the most commonly used PET MPI tracer (Heller *et al* 2009) as it is generator-produced. Generators are relatively expensive but can be eluted every 10mins, making them a cost-effective option for centers with high throughput: \$60-85 tracer cost/patient, with 6-8 patients/day on an 8-week generator (deKemp, Robert 2013). Spatial resolution in ^{82}Rb PET MPI is typically 8 – 12 mm FWHM; however, the principle images used for MPI interpretation at our centre are more heavily filtered and have a 12 mm FWHM resolution.

1.6.3 UOHI ^{82}Rb PET MPI protocol

The acquisition protocol for ^{82}Rb PET MPI at our centre, the University of Ottawa Heart Institute (UOHI), is demonstrated in Figure 1-10.

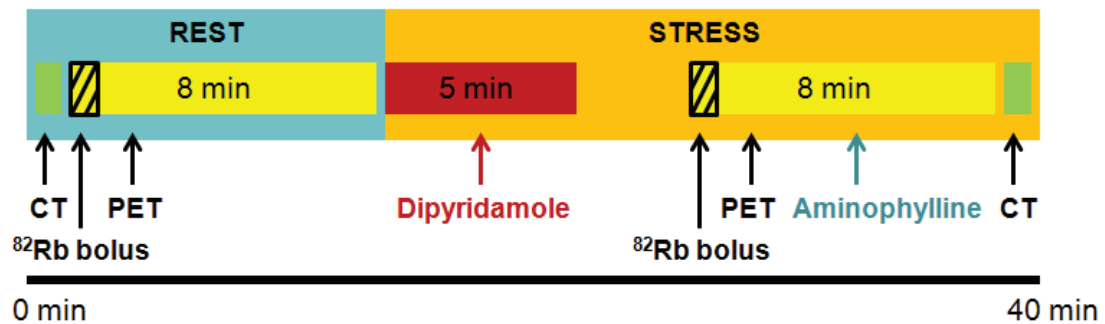


Figure 1-10. Our centre's (UOHI) ^{82}Rb PET MPI protocol. ^{82}Rb bolus duration is 30 s; bolus infusion and PET acquisition begin simultaneously. Aminophylline begins 4 mins after start of stress PET acquisition.

ECG leads and RPM respiratory system monitors are placed on the patient followed acquisition of the rest state CT attenuation scan, recorded during free-breathing near end-expiration (64-slice CT, 20 – 210 mA, 140 kVp, 0.4 s duration, dose <1 mSv). 30 seconds of continuous tracer bolus administered from the ^{82}Rb infusion system (activity 10 MBq/kg) and a fully 3D PET LMF acquisition are then begun simultaneously. Signals from the ECG and RPM system are recorded throughout the 8 min PET acquisition. The ^{82}Rb generator can be eluted at 10 minute intervals and, within this amount of time, the amount of activity left in the patient has decayed to background levels. The pharmacologic stress agent dipyridamole is administered over the course of 5 mins. A second 30 s ^{82}Rb bolus and stress state PET acquisition commence 3 min after the end of

pharmacologic stress infusion. The stress PET acquisition is the same as the rest acquisition. An antidote to the pharmacologic stress agent (aminophylline) is administered beginning 4 minutes after the PET stress acquisition begins. The CT attenuation scan for the stress state is then acquired. LMF files are binned into multiple sinograms at the PET console and saved in the following formats: static, ECG gated, dynamic, and respiratory gated (stress only).

1.6.4 MPI Interpretation

Image Evaluation

The principle images in an MPI study are the static rest and stress images. To display images for interpretation, the LV myocardium is located in the reconstructed images and the image volume reoriented from the scanner reference frame (transverse, sagittal, and coronal planes) to the LV reference frame (Figure 1-9a), typically using standard semi-automated software packages. The LV reference frame is comprised of three orthogonal planes: the short axis (SA) planes are orthogonal to the long axis, the horizontal long axis (HLA) planes are parallel to the long axis and perpendicular to the septal wall, the vertical long axis (VLA) planes are parallel to the heart long axis and parallel to the septal wall.

Images are normalized to their maximum LV myocardium intensity (MMI) and rest and stress images are displayed simultaneously to facilitate comparison. At our centre, MPI images are typically displayed for clinical evaluation using a ten-step colour scale where each colour represents a 10% increment of the MMI (Figure 1-2). The clinical evaluation includes an assessment of whether a perfusion defect exists (scan is normal or

abnormal) and, if so a specification of its location and a categorization of its size and severity as mild, moderate or severe. Based on location, the coronary artery causing the perfusion defect may also be inferred. Defect severity classifications are loosely based on the colour scale.

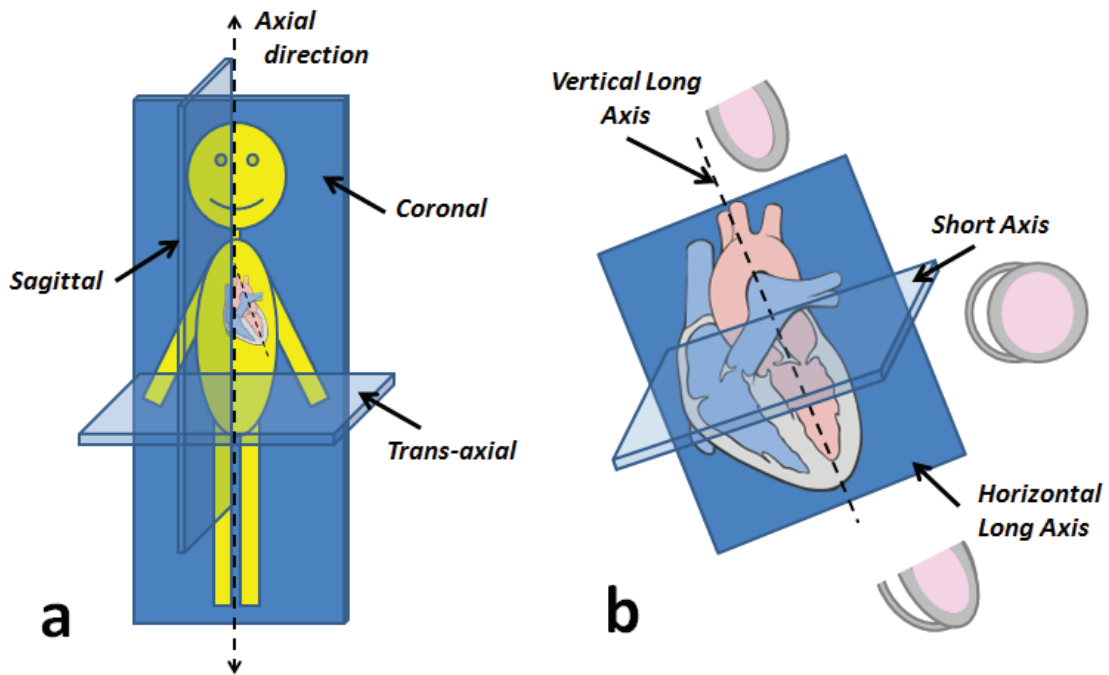


Figure 1-11. Scanner reference frame (a) versus the left-ventricle (LV) reference frame (b). PET reconstruction produces a series of trans-axially oriented image slices, image processing is then used to re-orient cardiac images to the LV reference frame. Heart diagram source: (Lynch 2006)

Polarmaps

Polarmaps are 2D representations of the image intensity inside the 3D myocardium and can be thought of as collapsing the bullet-like shape of the LV down on its end then

redistributing the area so that each increment of long axis surface is equally represented, Figure 1-12a and 1-12b.

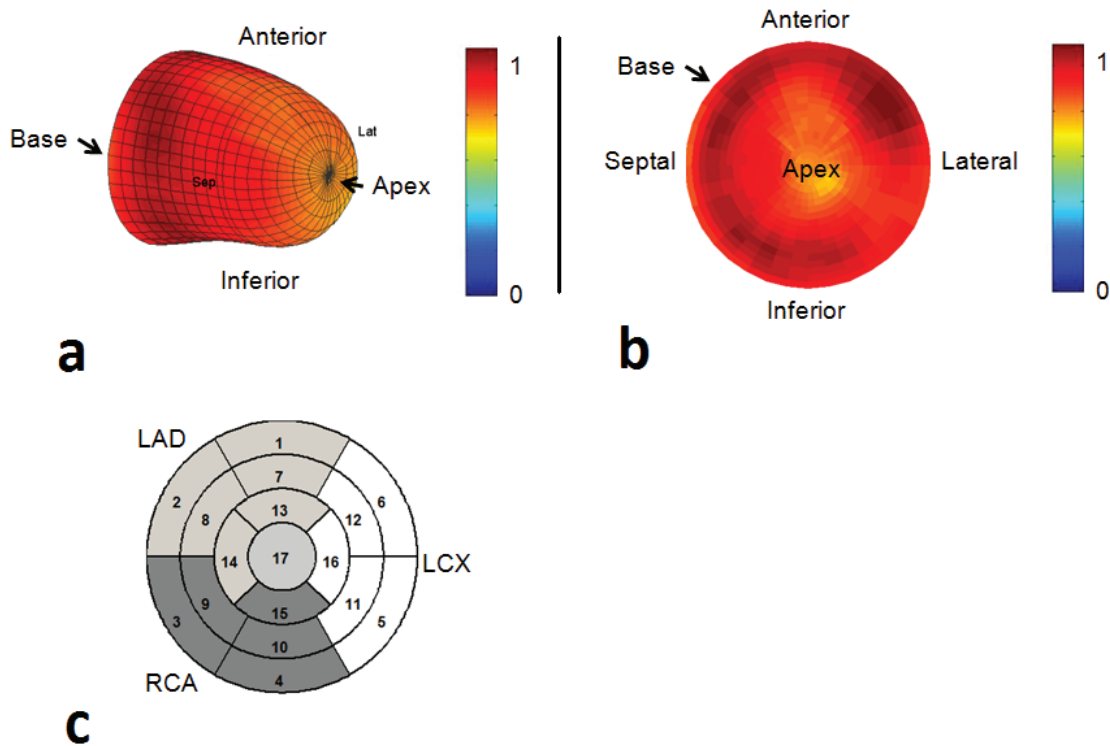


Figure 1-12. 3D representation of the left ventricle (a) and corresponding polarmap (b) extracted from a ^{82}Rb PET MPI scan using FlowQuant software (Klein *et al* 2006). (c) shows the American Heart Association (AHA) 17 segment polarmap model (Cerqueira *et al* 2002) and demonstrates the territories attributed to each of the three main coronary arteries. The concentric rings of this polarmap represent, from the outside ring inwards, the basal, mid, apical, and apex regions of the LV, respectively. FlowQuant images are displayed on a scale normalized the maximum myocardial intensity (MMI).

Polarmaps are also commonly divided into 17 segments when measures of regional perfusion are desired. Figure 1-12c shows the three coronary artery territories

superimposed on a 17-segment polarmap: the LAD supplies the anterior and anterior aspects of the septal and lateral walls; the LCX supplies the lateral wall and the lateral aspect of the inferior wall and the RCA supplies the inferior wall and the septal aspect of the inferior wall.

Segmental defect scoring and summed scores

Perfusion can be ranked (*scored*) in each segment, on a five-point, ordinal scale representing defect severity (0 – no defect to 3 – severe defect, and 4 - absent perfusion) and the sum of scores at stress (SSS) and rest (SRS) are used as measures of the overall reduction in perfusion for the scan.

Normal databases and automated segmental defect scoring

Perfusion scores can be generated automatically by comparing the mean (MMI-normalized) segmental perfusion for the image to the segmental perfusion in a population of normal studies. The score is a function of the difference from the mean expressed in units of population standard deviation (Kaster *et al* 2012). Estimates of mean normal segmental perfusion and physiological variability are referred to as a *normal database*, (NBD). A normal database is typically built from a group of myocardial perfusion images from individuals with a low likelihood of disease (i.e. with all other clinical values indicating no reason to suspect perfusion defects).

1.6.5 Wall Motion and Kinetic Analysis

In addition to static images of relative perfusion, interpretation of LV wall motion (cardiac contractile function) and cardiac output (Abidov *et al* 2006, Lertsburapa *et al* 2008) provide incremental prognostic and diagnostic value to MPI studies. To evaluate

wall motion, cardiac gated image series are typically produced for stress scans and sometimes for rest as well. Images in each series are re-oriented to the LV reference frame and displayed in a cine loop. Image intensity in each gated frame is normalized to the maximum MMI of all images in the series. Thickening of the LV wall with contraction causes increased myocardial image intensity due to reduced PVE. Automated contouring of the LV myocardium at systole and diastole allows the LV ejection fraction (LVEF) to be calculated as a measure of cardiac output.

Incremental prognostic and diagnostic information is also provided by quantitative assessment of myocardial blood flow (MBF) and flow reserve (MFR) (Gould *et al* 2013, Murthy *et al* 2014). MBF is measured by applying kinetic modeling to a dynamic image (Bailey *et al* 2005) and MFR is defined as the ratio of MBF at stress over that at rest (Klein *et al* 2007). Dynamic imaging places the greatest demand on the performance of the PET scanner due to the need for accurate measurements during the early acquisition phase of the scan, at times when the scanner is experiencing maximum count rates and subsequent dead-time correction.

1.7 Extra-cardiac interference (ECI)

Extra-cardiac interference (ECI) refers to tracer accumulation in an organ or structure outside the heart which, when imaged, obscures or results in decreased certainty when evaluating the true regional LV myocardial uptake.

1.7.1 ECI in MPI

ECI occurs in MPI when an extra-cardiac organ is located within the motion and image resolution margin of part of the LV myocardial surface and the organ has higher uptake than the extra-cardiac background within that margin over the remainder of the myocardial surface. This locally elevated uptake causes otherwise uniform PVE spillover to become non-uniform, changing the apparent relative myocardial image intensity and impacting interpretation (Figure 1-13).

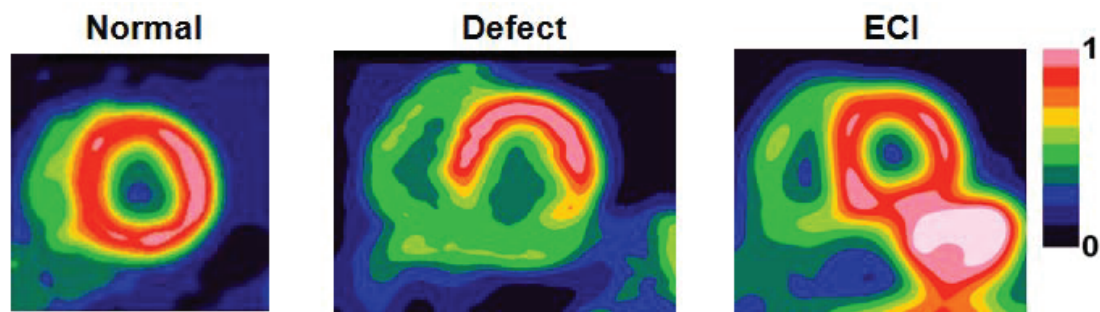


Figure 1-13. Short-axis (SA) image slices from ^{82}Rb PET MPI scans showing (a) normal myocardial perfusion, (b) abnormal myocardial perfusion and (c) unknown perfusion in the inferior myocardial wall due to extra-cardiac interference (ECI). SA slices are displayed using the 10-step colour-scale and are normalized to the maximum myocardial intensity (MMI).

Extra-cardiac organs and tracer uptake

All organs surrounding the LV are shown in Figure 1-14a and include: lungs, RV, diaphragm, liver, stomach, and spleen. Figure 1-14b demonstrates the relative position of the liver, stomach, spleen and lungs versus the LV myocardium in a SA slice approximately mid-long axis.

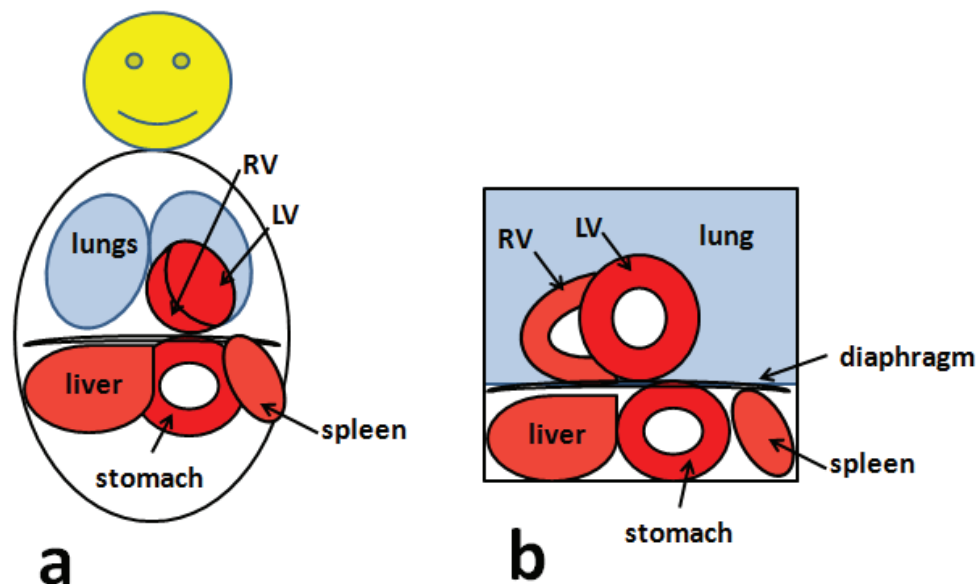


Figure 1-14. The organs and structures that surround the left ventricle (LV): (a) coronal view and b) short axis (SA) view. The SA view can be thought of as looking, from the front of the subject's left hip towards the back of their right shoulder, with the head tilted so that the upper left corner of the SA view corresponds to the centre of the subject's chest. The diaphragm is 3D and so can appear planar in both the coronal and SA views

Non-zero but low and uniform extra-cardiac background uptake (low noise relative to its contrast with normally perfused myocardium) in MPI does not affect relative myocardial image intensity and is therefore not considered ECI. For all MPI tracers in current clinical use, lung uptake is low and relatively uniform during the static image acquisition period (Dilsizian *et al* 2009). In addition, of all the organs surrounding the LV, the lungs span the largest fraction of LV outer surface and therefore, for the purposes of this work, lung uptake constitutes an acceptable extra-cardiac background uptake, i.e. whose spillover is *not* considered ECI. Some fraction of MPI scans with all currently used tracers show

accumulation significantly greater than lung in at least one other organ facing the LV: $^{13}\text{N-NH}_3$ is taken up by the liver, ^{82}Rb is taken up in the stomach, bowel and spleen and ^{18}F -mitochondrial inhibitors are also taken up in the liver (Klein *et al* 2010a). The RV spans the septal wall of the LV and RV tracer uptake above that of lung is common with all MPI tracers as the mechanisms of tracer uptake apply to RV and LV myocardium alike. The RV is within the motion and image resolution margin of the LV at the location where the two structures join, along the *RV insertion*. Here the effect on relative LV myocardial intensity can be viewed as either a true increase in thickness of the myocardium, and therefore a reduction in PVE, or as spillover from an extra-cardiac structure abutting the LV myocardium with a similar magnitude tracer uptake. For the purposes of this work, the RV and its effect on the relative LV myocardial image intensity are not considered ECI. It is assumed desirable to leave the RV and its effects on the LV myocardium intact.

Geometry and spatial resolution

Anatomically, all of the organs which exhibit elevated extra-cardiac MPI tracer uptake have boundaries and are physically distinct from the myocardium; however, as explained in sections 1.4 and 1.6, the spatial resolution and motion combine to result in a margin where distinct structures, separated by less than the margin, will overlap in the images. The liver, stomach, bowels and spleen are all abdominal organs and are separated from the heart by the diaphragm. The diaphragm thickness is a function of respiratory phase and ranges between 1.7 ± 0.2 mm (exhale) and 4.5 ± 0.9 mm (inhale)(Ueki *et al* 1995). Signal overlap due to spatial resolution occurs with separations

less than twice the PSF FWHM and for the principle images from PET MPI studies using the two most common tracers, $^{13}\text{N-NH}_3$ and ^{82}Rb , the resolution is 6 - 10 mm and 8 - 12 mm, respectively (Table 1-4) (Klein *et al* 2010a).

Motion

Motion induced signal overlap with the myocardium originates mainly from components of motion orthogonal to the LV wall. While cardiac contractile motion is naturally given in the LV reference frame, respiratory motion is typically described using the scanner (body) reference frame. The LV axis is typically parallel to a line connecting the front of the left hip to the back of the right shoulder (Marieb 2012) and is frequently simulated angled at approximately 50° coronal and 20° sagittal rotation relative to the axial direction of the body reference frame (Figure 1-11) (Segars *et al* 2010). Wells *et al.* (Wells *et al* 2010) found that the mean cardiac displacement due to respiratory motion in the body reference frame was 5.4 mm and the maximum displacement was 15.1 mm when ^{187}Rb PET MPI scans were examined. The majority of motion was in the axial direction (Figure 1-11a, a.k.a. cranial-caudal direction), accounting for 62% - 95% of the displacement, and no significant difference was found when this component of motion was compared between rest and stress scans. Respiratory motion appears in LV-oriented images as widening and smoothing of the anterior and inferior walls. The effect of motion due to cardiac contraction on ECI is limited since the extra-cardiac organs involved in ECI are typically located below the inferior and inferior-septal regions of the myocardial wall, where contractile displacement of the outer surface is minimal (Riordan and Kovács 2006). Although there is evidence that extra-cardiac organ motion

can be induced by cardiac contraction, if present, this motion is in-phase and low amplitude, likely resulting in smoothing of the extra-cardiac organ boundaries (Chung *et al* 2011).

Motion summary

The information above suggests that even if motion is negligible then in regions where the diaphragm alone separates the myocardium and abdominal organs there is insufficient separation to avoid signal overlap due to limited spatial resolution. When motion is present, the overlap may prove more severe and increase to involve cases where the myocardium and/or abdominal organs need only be near, not in contact with, the diaphragm.

Cardiac contraction

When considering the impact of cardiac contraction on ECI in MPI, motion may not be the most important factor. Cardiac contractile motion causes deformation: the inward displacement of the myocardial inner surface is greater than that of the outer surface increasing wall thickness. Increased wall thickness produced in this manner both shifts the centre of the myocardial wall inwards and increases the thickness of myocardium between the centre of the wall and the outer surface. Increased wall thickness can reduce the PVE experienced by the myocardium and, assuming the structure of the extra-cardiac organ does not change as a function of cardiac contraction, this will increase myocardial to extra-cardiac contrast. In addition, if we assume there is no significant extra-cardiac organ motion as a function of cardiac contraction, the location where myocardial uptake is sampled for polarmaps (the centre of the wall) is shifted

away from the ECI with contraction and therefore ECI may be reduced at systole (Figure 1-15).

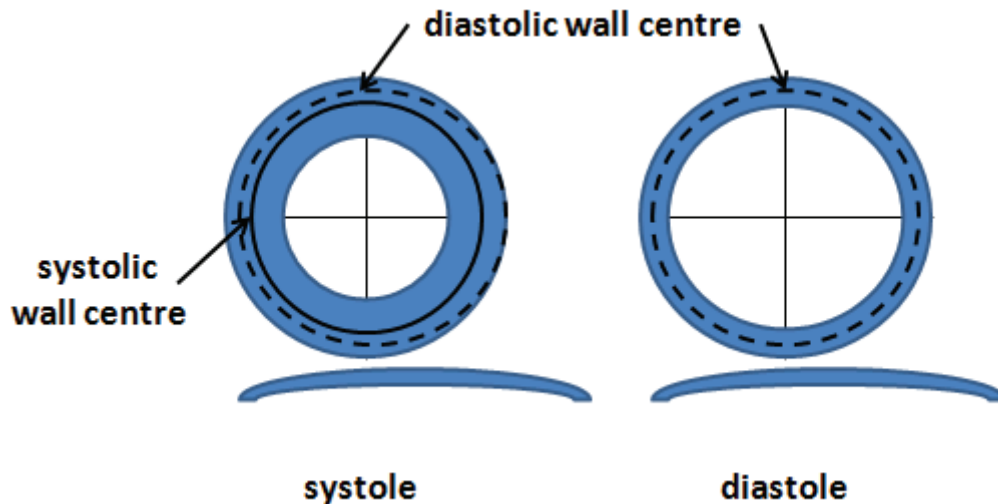


Figure 1-15. Cardiac contraction of the left ventricle (LV) versus location of wall centre and wall width: systole is maximum contraction, diastole maximum dilation (relaxation). A diaphragm-like structure is shown below the LV to help visualize the relative separation between it and the wall centre, at systole versus diastole.

The stress state increases perfusion of the coronary arteries, which increases the fraction of injected tracer taken up by the myocardium over that seen at rest. If extra-cardiac organ uptake does not also increase at stress, the myocardium to extra-cardiac organ contrast will be higher in stress images than rest images, decreasing the observed severity of ECI.

PVE correction as ECI correction

PVE correction methods are difficult to apply to MPI since patient specific, spatially-variant motion complicates the definition of the overall imaging PSF and, although CT-AC provides co-registered (aligned) anatomical images, lack of soft tissue contrast prevents accurate definition of the myocardium and extra-cardiac organ boundaries. To overcome these difficulties, cardiac-gated image series can be used to minimize motion and PET-MR is an emerging technology in nuclear perfusion imaging (Bailey *et al* 2015) which would enable better delineation of soft tissues. In images exhibiting ECI, it is generally unclear if the problem originates from a single factor or a combination of spatial resolution, cardiac and respiratory motion.

1.7.2 ECI in ^{82}Rb PET MPI

Physiology of extra-cardiac ^{82}Rb uptake

Physiologically, Rb^+ cations are treated as K^+ and taken into myocardial cells via active transport by the P-type Na^+/K^+ enzyme pump. Cells in the wall of the upper stomach (gastric fundus), contain another P-type pump responsible for stomach acidity (H^+/K^+ pump) (Goodsell 2009). It is hypothesized that Rb^+ substitutes for K^+ in the same way here, resulting in elevated tracer concentration in the stomach wall.

The ratio of stomach: myocardial ^{82}Rb uptake can change between rest and stress states. Myocardial uptake at rest is approximately 2% and doubles at stress. While this difference is small in terms of the amount of tracer available to the rest of the body, (96% versus 98%); the body's response to stress diverts blood flow from digestive

organs, e.g. stomach, to action organs, e.g. muscles, reducing the availability of tracer to the stomach.

Stomach anatomy, appearance in images and motion

Figure 1-14 shows the general shape and location of the stomach. The stomach wall is composed of smooth muscle, it is less rigid than the myocardium, is collapsible and distensible and therefore its shape and thickness vary (Pickhardt and Asher 2003). The stomach appears in perfusion images as either a walled or solid structure, often, but not always approximately dome-shaped, adjacent to but below the inferior LV wall in SA slice views of the LV.

In terms of x-ray attenuation, the stomach wall falls into the soft tissue category, unfortunately along with much of its surroundings. In CT-AC images, there is little contrast between the stomach wall, the stomach contents (with the exception of gas bubbles), the liver, the diaphragm, the LV wall and even the LV blood pool, making delineation difficult. The stomach experiences respiratory motion and may also experience cardiac contraction-induced motion.

^{82}Rb specific imaging considerations affecting ECI

As discussed at the end of sections 1.4.1 and 1.4.2, when the acquisition protocol for ^{82}Rb perfusion scans aims to produce accurate dynamic and static images, the static image data are count starved, leading to post-reconstruction filter widths that dominate the spatial resolution in these images. The 10 mm LV wall thickness, when imaged with 14 mm FWHM ^{82}Rb PET static image spatial resolution, experiences significant PVEs

(Figure 1-8). Filter width can be reduced to gain spatial resolution and gating used to reduce the effects of motion, both at the expense of increasing image noise.

Prevalence

Prevalence of ECI in ^{82}Rb PET MPI has not been thoroughly examined to date. Although multiple studies have cited ECI as having a detrimental impact on ^{82}Rb PET MPI (Thompson 2008, Shkvorets *et al* 2007, Abraham *et al* 2010) and quantification of MBF (Klein *et al* 2010a), only one study was found quantifying the prevalence. (Bateman *et al* 2006) used visual interpretation of a set of 110 images and estimated prevalence of ECI in ^{82}Rb PET MPI as approximately 10%.

1.7.3 Solutions proposed to date

Initial approaches to reducing ECI in MPI used adaptations to patient preparation, including eating and/or drinking prior to scan acquisition, in the hopes of modifying extra-cardiac organ anatomy (stomach distension), location or physiological uptake (tracer affinity for non-myocardial cells). Only modest reductions in prevalence of extra-cardiac interference were found (Thompson 2008).

The only image-analysis-based ECI correction proposed to date was based on factor analysis of dynamic image sequences (FADS) and was shown to have some potential for correction of ECI in 99m-technetium ($^{99\text{m}}\text{Tc}$) teboroxime MPI with dynamic single photon emission computed tomography (SPECT) (Sitek *et al* 2002a). Dynamic SPECT, however, is not typically available as a clinical option and, as a result, this method was not adopted and no software is currently clinically available for either detection or correction of ECI.

In the clinic, technologists typically identify the most severe cases of ECI when reviewing image quality immediately following scan acquisition while additional cases are identified by clinicians reviewing the images. Clinical image review potentially occurs prior to the patient leaving the hospital but often not until hours after acquisition. Rapid detection of ECI cases may allow same-day rescanning of the patient; however, this does not guarantee improvement and delayed identification generally means that the patient will have left the hospital. The present clinical solution requires the clinician to 'read around the problem' as best they can or to request the patient return for repeat image acquisition at a later date. Repeat imaging reduces efficiency by imposing an additional burden on the medical system and patient (rebooking, time, cost, radiation dose).

1.8 Thesis summary

1.8.1 Objectives

The objective of this thesis is to provide a method that significantly reduces ECI in ^{82}Rb PET MPI. The objective was broken into three steps: 1) detection, 2) simple sources of improvement and 3) correction. These are detailed in chapters 2 – 5.

1.8.2 Hypotheses

Chapter 2 examines the hypothesis that an automated method for ECI detection and severity ranking can be developed with high sensitivity and specificity for detection. With this automated method of detection and classification, it becomes possible to more accurately assess the prevalence of ECI by applying the method to the large database of patient studies available at UOHI.

Simple methods, if they are effective, would be the easiest to implement in the clinic and so Chapter 3 evaluates several simple approaches to ECI compensation: reducing post-reconstruction filtering, using a single phase from cardiac or respiratory gated image series, and using TOF reconstruction combined with reduced post-reconstruction filtering. We hypothesize that simple methods can reduce ECI but are unlikely to be sufficient to remove ECI in the most severe cases.

Chapter 4 evaluates the hypothesis that the temporal pattern of tracer uptake in the stomach is different enough from the myocardium to provide the basis for a dynamic approach to ECI correction in ^{82}Rb PET MPI, similar to that proposed by Sitek et al. for SPECT MPI (Sitek *et al* 2002a). Using dynamic image series, acquired for kinetic analysis of MBF, we hypothesized that factor analysis of dynamic sequences, (FADS), could extract temporal basis functions allowing us to separate the myocardial, blood pool, and ECI signals and thereby remove the ECI.

Chapter 5 develops a 1D convolution-based method for estimating the ECI signal in principal static images and it is hypothesized that this method provides sufficient accuracy that it can be used for correction.

2 Chapter: **Detection and severity classification of extra-cardiac interference in ^{82}Rb PET myocardial perfusion imaging**

Results for the work presented in this chapter were published in Medical Physics (Orton et al. 2014). © 2014 Medical Physics. Reprinted with permission (Appendix A), from E. Orton, I. Al-Harbi, R. Klein, R. deKemp, R.S.B. Beanlands and R.G. Wells, Detection and severity classification of extra-cardiac interference in ^{82}Rb PET myocardial perfusion imaging, Medical Physics, October 2014. This paper has been reformatted and the tables, figures and references have been edited to conform to the thesis format. A section of the introduction has been removed to avoid repetition from section 1.7.3. The first paragraph of the introduction has been added to provide the reader with context for this chapter.

2.1 Introduction

Previous evaluation of extra-cardiac interference in MPI has been performed by clinical interpretation; there did not exist any automated methods for identifying interference. Clinical interpretation is a time consuming process and therefore typically limits both the number of scans evaluated and feasibility of repeat evaluation. This is compounded by the fact that low prevalence of extra-cardiac interference translated to interpretation of a large number of scans to yield just a few with ECI. This chapter develops an automated algorithm using concordance with a clinically-interpreted 200-image dataset to quantify the level of interference based on physical parameters (levels of relative perfusion associated with ECI and amount of involved LV surface area). The algorithm can then be used to provide an estimate of prevalence from a much larger dataset and to identify a set of scans with extra-cardiac interference which might benefit from the application of correction algorithms.

Myocardial perfusion imaging (MPI) is widely used for non-invasive diagnosis and prognosis of coronary artery disease (CAD) (Loong and Anagnostopoulos 2004, Bourque

and Beller 2011, Beller and Zaret 2000, Yoshinaga *et al* 2006) and positron emission tomography (PET) is the gold standard for MPI (Loong and Anagnostopoulos 2004). However, despite the superior performance of PET (Bourque and Beller 2011, Beanlands and Youssef 2010), traditionally single photon emission computed tomography (SPECT) MPI with ^{99m}Tc -labelled perfusion agents has dominated clinical use. More recently, this has started to change: growth in the number of available PET cameras, increased availability of the generator produced PET perfusion tracer rubidium-82 chloride (^{82}Rb), combined with ongoing concern over the supply of ^{99m}Tc (Beanlands and Youssef 2010, Morrison 2010, Branswell 2013) have generated increasing interest in clinical cardiac PET.

Though less prevalent than in its SPECT counterparts, ^{82}Rb -PET MPI is also prone to interference from tracer accumulation in structures outside the heart (Bateman *et al* 2006). Extra-cardiac interference is a problem that has been noted qualitatively in multiple ^{82}Rb -PET studies (Thompson 2008, Shkvorets *et al* 2007, Abraham *et al* 2010) and, although its prevalence has not been extensively studied, extra-cardiac interference has been estimated to occur in 10% of ^{82}Rb PET MPI studies (Bateman *et al* 2006). Elevated radiotracer uptake in organs and/or structures near the myocardial wall, when combined with respiratory and cardiac motion and limited spatial resolution, can contribute an unknown amount of activity to the region of the image occupied by the myocardial wall. Elevated ^{82}Rb uptake is observed in the stomach wall and spleen (Senthamizhchelvan *et al* 2010) and these structures lie adjacent to the inferior-, infero-lateral wall of the left ventricle (LV) in the basal, mid and distal regions.

Extra-cardiac interference can decrease interpretive confidence or even preclude study interpretation if sufficiently severe (Bateman *et al* 2006, Thompson 2008). While observed in a fraction of MPI studies performed with all current clinically-used SPECT and PET perfusion tracers (Thompson 2008); extra-cardiac interference has been investigated most thoroughly for ^{99m}Tc - based SPECT MPI tracers. Previous studies found that adaptations to patient preparation protocols (eating or drinking prior to image acquisition) provided only modest reductions in prevalence of extra-cardiac interference (Thompson 2008) and did not wholly eliminate the problem. Factor analysis-based correction of dynamic image sequences was shown to have some potential but was developed for dynamic SPECT, an acquisition option that is not typically clinically available (Sitek *et al* 2002a). As a result, this method has not been translated to the clinic and no software is currently clinically available for either detection or correction of extra-cardiac interference.

At present, the most severe cases of extra-cardiac interference are typically detected by technologists reviewing image quality immediately following acquisition. Additional cases are identified by clinicians when reviewing the images, potentially prior to the patient leaving the hospital but often hours after acquisition. Furthermore, delayed identification increases the odds that the raw data will have been discarded due to memory limitations, eliminating the availability of that data for software-based correction methods.

Acknowledging that reprocessing and corrective methods will increase computing time, routine application of these steps to all images is not practical, especially when the

prevalence of extra-cardiac interference is relatively low, as in the case of ^{82}Rb PET. This provides good motivation for developing a fast, simple method capable of detecting the presence of extra-cardiac interference in images immediately after reconstruction, while the patient is still present and the raw data are still available. While no correction methods currently exist for extra-cardiac interference in ^{82}Rb PET MPI, dynamic ^{82}Rb PET image sequences are currently acquired to quantify myocardial blood flow (El Fakhri *et al* 2005, Klein *et al* 2010a), providing the necessary data for testing correction methods based on factor-analysis of dynamic image sequences, such as that developed by Sitek *et al.* for dynamic SPECT (Sitek *et al* 2002a). The algorithm developed here may be used in future studies to both detect images requiring correction and then evaluate the effectiveness of the correction method. In addition, retrospective application of this automated measure of interference severity to a large database, for which additional demographic, risk factor and outcome data are available, will enable refinement of previously reported extra-cardiac interference prevalence estimates, development of a pre-test probability measure for extra-cardiac interference and allow quantification of this problem's impact on downstream testing costs. An automated measure of interference severity may also allow clinicians to provide more consistent reporting of the problem's clinical relevance.

This work develops an algorithm that quickly and consistently detects and classifies the severity of extra-cardiac interference in ^{82}Rb PET MPI rest and stress images. The algorithm accuracy is evaluated against the expert classification of 200 images by a

trained nuclear cardiologist and the failure rate of the algorithm is assessed using a large set of 4920 clinical images.

2.2 Methods and Materials

2.2.1 Scan acquisition and image reconstruction

Images were acquired on a Discovery 690 PET/CT (GE Healthcare), using the ^{82}Rb -ARMI UOHI protocol (Kaster *et al* 2012). Briefly, 10 MBq/kg of ^{82}Rb was infused over 30s and static images reconstructed from data acquired from 2.5 to 8 minutes after the start of injection. Image reconstruction was performed using vendor supplied VUE Point HD; a fully 3D, iterative algorithm, combined with a 12mm post-reconstruction Hann filter (GE-Healthcare 2008). Reconstructed images were then analyzed off-line.

2.2.2 Datasets

Datasets for this work were retrospectively taken from the University of Ottawa Heart Institute (UOHI) ^{82}Rb PET MPI rest-stress perfusion database acquired between Jan 2011 and Dec 2012 (University of Ottawa Research Ethics Board consent via ^{82}Rb -ARMI Group A, HI protocols 2009872-01H & 20130268-01H, (Appendix B)).

A *truth dataset* of 100 ^{82}Rb PET MPI studies, including both the rest and the stress images, was selected to be read by a clinician for the presence and severity of extra-cardiac interference. This *truth dataset* of images was used for algorithm development and evaluation of its accuracy. Selection of studies for the truth dataset was not random due to the low estimated prevalence of extra-cardiac interference and knowledge that when classification algorithms are trained mainly from the majority class (images

without interference), the minority classes (images with extra-cardiac interference) experience poor prediction performance (Chawla 2005, Weiss and Provost 2003). With the aim of achieving a truth dataset that was evenly populated across all levels of extra-cardiac interference severity, 80 of the 100 studies were selected based on the visual assessment of at least minimal interference in either the rest or stress image and the remaining 20 studies were chosen to have minimal to no interference in both the rest and stress images. The study set was also chosen to include a broad range of perfusion defects and anatomical variability. The objective of this biased selection was to identify interference characteristics upon which the algorithm could be robustly based through use of an approximately equal number of representative samples in each interference severity class. A cardiologist trained in nuclear imaging (IAH) reviewed the 100 studies and reported the presence and severity of extra-cardiac interference and its general location in the rest and the stress images separately. Studies were viewed with Corridor 4DM (Invia) as per our clinical protocol and interference severity classified based on the maximum uptake in the region of overlapping myocardial and extra-cardiac uptake (Figure 2-1), according to the following criteria:

<i>Interference severity</i>	<i>Relative uptake</i>
<i>Absent</i>	<i>0 – 0.4</i>
<i>Mild*</i>	<i>0.4 – 0.6</i>
<i>Moderate*</i>	<i>0.6 – 0.7</i>
<i>Severe*</i>	<i>≥ 0.7</i>

**with angular coverage of $\geq \sim 20^\circ$ in $\geq \sim 5$*

short axis (SA) slices (Figure 2-2).

where relative uptake is expressed as a fraction of the maximum myocardial uptake (MMI) and can be judged visually by normalizing image intensity to the MMI prior to display with a 10-step colour scale, Figure 2-1. These criteria formed the basis of algorithm development and are therefore analogous to the methodology described below (section 2.2.3).

In addition to the truth dataset, a larger set of images was obtained: N = 4920 images from a population of N = 2533 patients imaged between January 2011 and December 2012, excluding the truth dataset images. This set of images was used to represent the general population for demographic comparison with the truth dataset, for better definition of the algorithm failure rate (section 2.2.5) and for assessment of algorithm-based prevalence of extra-cardiac interference. The demographics for the truth dataset and the Jan 2011 – Dec 2012 dataset are given in Table 2-1.

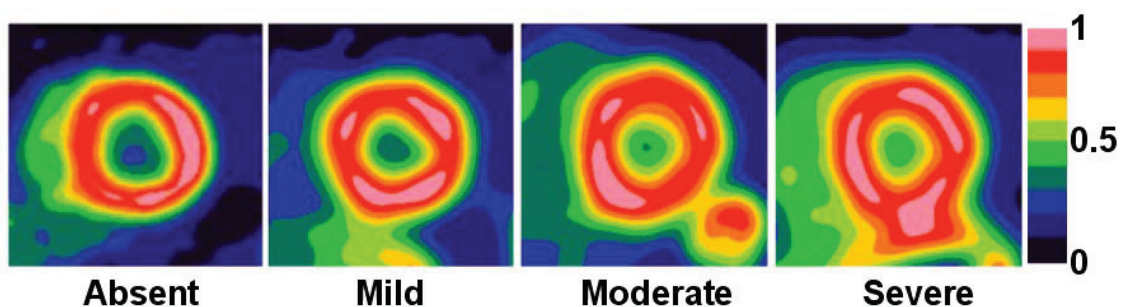


Figure 2-1. Example SA slices of clinician’s extra-cardiac interference severity classifications. Images are scaled independently to show relative uptake with the maximum myocardial intensity (MMI) shown as pink (1) and absent tracer uptake shown as black (0).

The truth dataset is reported as a whole in Table 2-1 and also subdivided by interference severity class as per the known truth classification, broken down into rest and stress images, in Table 2-2. Comparisons were made between the Jan 2011-Dec 2012 dataset and the truth dataset populations; and separately between the Absent subset and each of the Mild, Moderate and Severe interference severity subsets for both Rest and Stress. Wilcoxon rank-sums tests were used for continuous variables and Fisher Exact tests for categorical variables; significance was reported at the $p = 0.05$ level and Bonferroni corrected when multiple comparisons were performed (i.e. between interference severity subsets, $p = 0.05/3 = 0.017$).

Table 2-1. Demographics for the truth dataset and the Jan 2011-Dec 2012 dataset. The Jan 2011-Dec 2012 dataset does not contain the Truth dataset. The Truth dataset contains 200 images (i.e. 100 paired rest/stress studies). †denotes a significant difference between Truth dataset and Jan 2011 – Dec 2012 dataset, $p = 0.05$. BMI = body mass index. Continuous variables are expressed as mean \pm standard deviation (range); categorical variables are expressed as % (number).

	Truth dataset (whole)	Jan 2011 – Dec 2012 dataset
N images	200	4920
N patients	100	2533
Age	62.6 \pm 12 (18 – 87)	63.7 \pm 11.3 (20 - 94)
Male (%)	51 (51)	1433 (57)
BMI	29.7 \pm 7.4 (18 – 63) [†]	31.2 \pm 7.6 (15-67)
Diabetes (%)	28 (28)	796 (31)
Smoker, current or past (%)	52 (52) [†]	1633 (65)
Hypertension (%)	71 (71)	1870 (74)
Hyperlipidemia (%)	70 (70)	1864 (74)
Family history (%)	51 (51)	1384 (55)

Table 2-2. Demographics for the Truth dataset by interference severity class, as per the clinician’s interference severity classification, broken down into Rest and Stress images. ‡ denotes a significant difference between Absent Rest (Stress) severity class and other Rest (Stress) severity classes, p = 0.017. BMI = body mass index. Continuous variables are expressed as mean ± standard deviation (range); categorical variables are expressed as % (number).

	Interference severity classes from Truth dataset							
	Absent		Mild		Moderate		Severe	
	Rest	Stress	Rest	Stress	Rest	Stress	Rest	Stress
N images	14	33	38	37	22	20	26	10
Age	60.9 ± 14.2 (28 – 85)	62.4 ± 13.5 (18 – 85)	64.2 ± 12.2 (18-87)	63.6 ± 12.1 (30 – 87)	59.0 ± 10.9 (30-79)	58.9 ± 8.0 (37 – 75)	64.3 ± 11.2 (37-85)	66.6 ± 12.1 (45-85)
Male (%)	7 (50)	14 (42)	16 (42)	20 (53)	11 (50)	10 (53)	17 (65)	7 (70)
BMI	34.8 ± 7.6 (25 – 51)	31.8 ± 7.0 (18 – 51)	30.6 ± 9.2 (18-63)	29.0 ± 8.7 (18 – 63)	27.5 ± 4.7 (18-36)‡	28.9 ± 6.0 (21-48)	27.6 ± 4.3 (21 – 39)‡	27.1 ± 4.2 (21-34)
Diabetes (%)	4 (29)	9 (27)	15 (40)	12 (32)	3 (14)	3 (16)	6 (23)	4 (40)
Smoker (%)	7 (50)	14 (42)	18 (47)	20 (53)	12 (55)	11 (58)	15 (58)	7 (70)
Hypertension (%)	6 (43)	17 (52)	31 (82)‡	31 (82)	12 (55)	14 (74)	22 (85)‡	9 (90)
Hyperlipidemia (%)	9 (64)	20 (61)	27 (71)	26 (68)	15 (68)	14 (74)	19 (73)	10 (100)
Family history (%)	7 (50)	16 (48)	18 (47)	20 (53)	9 (41)	10 (53)	17 (65)	5 (50)

2.2.3 Algorithm summary

Images were processed off-line using subroutines from the semi-automated FlowQuant software (Klein *et al* 2010b) to locate the left ventricle (LV) of the myocardium and divided it into 24 pseudo-short axis (SA) slices spanning from the apex (slice #1) to the basal valve plane (slice #24), where slices 1-8 were conical slices and 9-24 were planar slices. The software used a deformable 13-point spline model to fine tune the LV location in SA slices, defined in spherical-cylindrical coordinates (Figure 2-2).

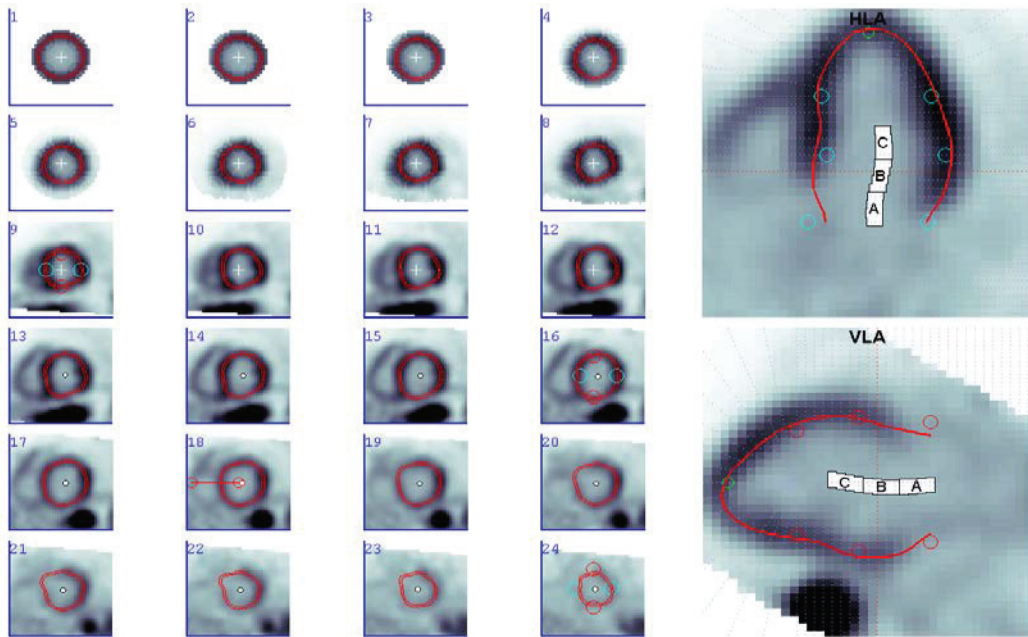


Figure 2-2. Processed image showing automated software detection of the left ventricle (LV) myocardium. Pseudo-short axis (SA) slices are shown on the left, with slice numbers located in the upper left corners (1-8 conical and 9-24 planar slicing); the larger images on the right show Horizontal and Vertical long axis views (HLA and VLA, respectively). The right ventricle (left side of SA/HLA views) and stomach wall (inferior region of SA and VLA views) are also visible.

The algorithm then sampled the MMI-normalized uptake at a constant radial distance from the LV myocardium. Samples were taken at five degree intervals over a truncated SA-slice and angular search range corresponding to the portion of the myocardium facing the stomach wall and spleen. The samples were classified as having interference or no interference based on whether they were above or below a predetermined uptake threshold. An image was then classified as having interference if the total number of samples exceeded a minimum value corresponding to a non-negligible area of interference (i.e. sufficient extent). The process was repeated for each of three severity thresholds (S1, S2, and S3, separating Absent - \geq Mild, Mild - \geq Moderate and Moderate-Severe severity classes respectively) to find the maximum severity at which the scan exceeded the minimum threshold and area requirements. Images whose reconstructed FOV did not encompass all sample locations were flagged and caused the algorithm to fail.

2.2.4 Parameters and thresholds

In addition to the three threshold values, S1-S3, the algorithm also uses seven parameters. These parameters define the search region (apical and basal SA slice limits, and lateral and septal angular limits), the radial sampling distance, and the minimum area requirements (minimum number of SA slices and minimum angular coverage per SA slice). The search region *apical* SA slice and *lateral* angular limits (SA slice 5 and 90° CW from vertical, respectively) were defined outright based on the fact that no apical or anterior interference was reported in the truth dataset by the clinician. For the five remaining parameters and the three thresholds, multiple values of each were

investigated in order to find the combination that maximized concordance with the truth dataset and minimized the failure rate of the algorithm. The parameter and threshold values were therefore defined as truth-population based constants. The range of values investigated for the parameters and threshold values are listed in Table 2-3 and illustrated in Figure 2-3.

Table 2-3. The parameters used by the algorithm, their units and values tested during optimization. A notation of A: B: C indicates a range of A to C inclusive at intervals of B. SA = short axis; CW = clockwise; MMI = maximum myocardial intensity.

Description	Parameter (units)	Values tested
Radial sampling distance	r (mm from myocardium, i.e. r_{myo})	8, 11:1:17,20
Search region	apical SA slice limit (SA slice number /24)	5
	basal SA slice limit (SA slice number /24)	18, 21, 24
	lateral angular limit (degrees CW from vertical)	90
	septal angular limit (degrees CW from vertical)	180,200,220
Minimum area requirements	SA slice coverage (number of slices)	1, 3, 5, 7
	angular coverage (number of 5-degree samples)	1, 3, 5, 7
Thresholds	S1 (MMI)	0:0.01:1
	S2 (MMI)	0:0.01:1; S2>S1
	S3 (MMI)	0:0.01:1; S3>S2

Parameter optimization was performed using the truth dataset and ten-fold stratified cross-validation (TFSCV) (Kohavi 1995). For all possible combinations of the parameter values listed in Table 2-3, the failure rate of the algorithm was determined and a receiver operating characteristic (ROC) curve analysis was performed with respect to S1

by calculating the sensitivity and specificity over the full range of S1 threshold values given in Table 2-3.

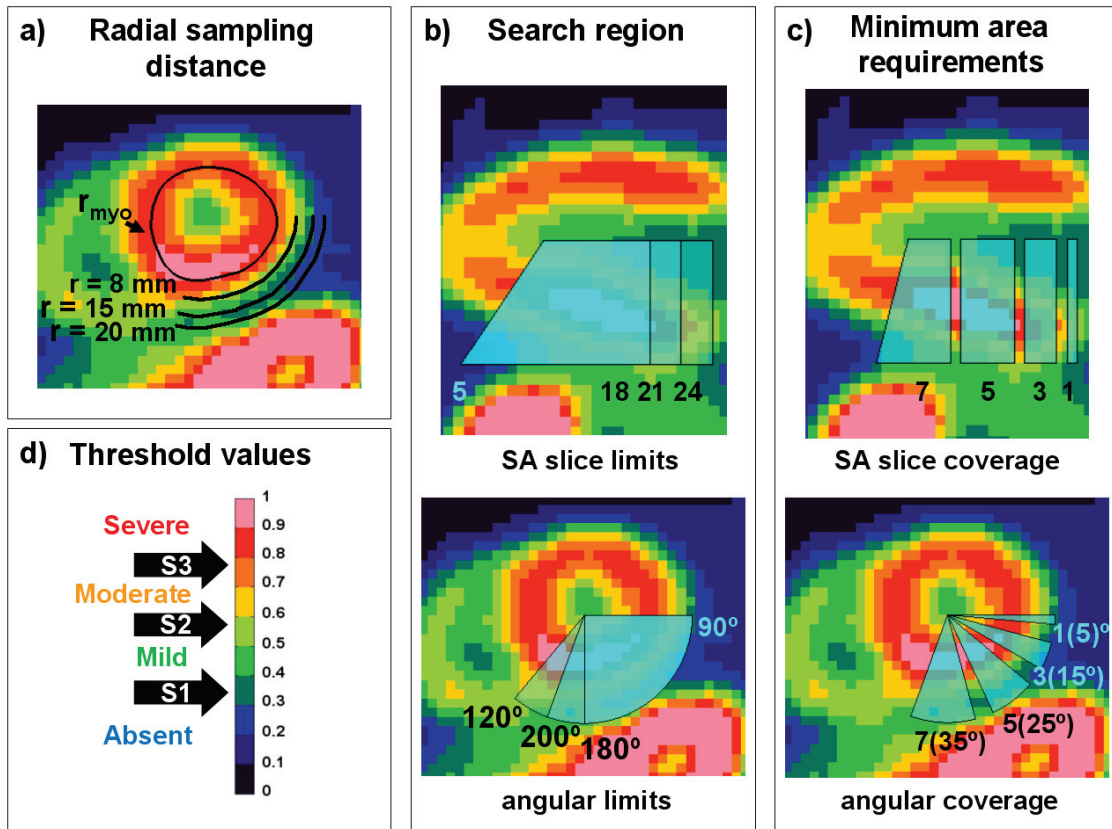


Figure 2-3. Representative samples of the parameters used by the algorithm and the range of values searched during optimization. Table 2-3 lists all values of parameters and thresholds tested during optimization.

TFSCV was used to provide the most efficient use of truth dataset images without circular reference; allowing optimal algorithm threshold values to be found (training) and algorithm accuracy measures reported (validation) based on independent sets of images. The algorithm was considered to have failed if it was unable to obtain samples from the full search region specified by the chosen parameter set. From the ROC

analysis, the area under the curve (AUC) and maximum Cohen's Kappa (Cohen 1960) value, along with the corresponding S1 threshold, sensitivity, and specificity, for that Kappa value, were calculated.

The S1 threshold value that maximized the Kappa value was chosen for each combination of parameters. A one-sided Student's t-test was performed to determine the combinations of parameters, along with their corresponding Kappa-maximized S1 threshold values, that yielded significantly ($p \geq 0.05$) higher failure rates or lower Kappa values than the respective maximums over all possible combinations of the parameters. To improve classification of interference severity, these combinations were then eliminated from further consideration before evaluating S2 and S3 to ensure the failure rate and separation of absent from present interference was not degraded.

With the remaining combinations of parameters, the Kappa analysis was repeated for S2 and S3 and TFSCV used again to obtain the means and standard errors of thresholds and accuracy measures. Note that the population of images used for TFSCV at each threshold was defined by having sequentially implemented the algorithm with all previously evaluated, lower mean threshold values and advancing only the images positive for less severe interference for testing at the next highest severity level (section 2.2.3). Once all three threshold values had been found, the full algorithm was applied and the overall concordance (via a 4x4 cell contingency table, non-weighted overall Kappa value), along with the Kappa, sensitivity and specificity for each severity class was calculated, using TFSCV. The optimal combination of parameter and threshold values was chosen as that with the maximum overall Kappa value.

2.2.5 Population failure rate

There were very few images in the truth dataset whose reconstructed FOV caused the algorithm to fail. A more statistically meaningful measure of the failure rate was therefore obtained by running the algorithm on ten subsets of $N = 492/4920$ images from the Jan 2011 – Dec 2012 dataset. From these ten measurements, the mean failure rate and its standard error were calculated.

2.2.6 Algorithm-based prevalence estimate

Having run the algorithm on all images in the Jan 2011 – Dec 2012 dataset, the results were used to estimate the prevalence of extra-cardiac interference in each severity class, for both rest and stress images, in the general population.

2.3 Results

2.3.1 Datasets

The number of images falling into each interference severity class, as interpreted by the clinician, for both rest and stress images, is given in Table 2-2. Note that while initial visual assessment for selection of studies aimed to obtain an approximately equal size image populations for each interference severity class, inclusion of both the rest and the stress image from each study combined with uncertainty in the visual assessment of absent versus mild interference lead to slightly greater than 20% of images classified as absent and an elevated number of mild interference cases. When the number of rest images and the number of stress images, interpreted by the clinician to fall into each interference severity class, are combined, the fraction of the truth dataset belonging to

each interference severity class other than mild was close to balanced (Table 2-5, ~20%). When comparing demographics, significant differences were found between the truth and the Jan 2011 – Dec 2012 database populations in mean BMI ($p = 0.025$) and the proportion of current or past smoker ($p = 0.017$) categories. Using a Bonferroni-corrected level of significance ($p = 0.017$), and significant differences were found in mean BMI for the Rest images between Absent and Moderate ($p = 0.007$) and Absent and Severe ($p = 0.004$), and in the proportion of patients with hypertension between Absent and Mild ($p = 0.013$) and Absent and Severe ($p = 0.011$), also for the Rest images.

2.3.2 Parameters and thresholds

In the first step for finding the optimal combination of parameter and threshold values, the maximum mean S1 Kappa value was 0.79 [0.65, 0.93] and the minimum mean failure rate was 0.01 [+ 0.07, -0.01]. Of the 1296 combinations of parameters evaluated for optimal S1 threshold via TFSCV versus S1 Kappa, 81 were found to have both no significant decrease in S1 Kappa from the maximum over all combinations of parameters and no significant increase in failure rate from the minimum over all combinations of parameters. Elimination of parameter combinations with S1 Kappa values significantly less than the maximum resulted in exclusion of all combinations with radial sampling distance (r) < 12 mm; while elimination of parameter combinations with failure rates significantly more than the minimum removed all combinations with $r > 15$ mm (see Figure 2-3a).

The optimal combination of parameter and threshold values, found to give the maximum overall Kappa within TFSCV, was: $r = 14$ mm, SA slice search limits = slices

5:21, angular search limits = 90°: 200° CW from vertical and minimum area requirements of 3 SA slices and 5 5-degree samples (25°) per SA slice; along with optimal threshold values of $S1 = 0.490 \pm 0.005$, $S2 = 0.648 \pm 0.005$ and $S3 = 0.762 \pm 0.005$ (as shown in Figure 2-4 for all thresholds). Together this combination of parameters and thresholds gave an overall Kappa value of 0.72 [0.64, 0.81]. 61 of the 81 combinations of parameters, when combined with their optimized threshold values, were found to give overall Kappa values not significantly lower than the optimal combination's overall Kappa ($p \geq 0.05$). The overall Kappa was significantly decreased by any change in the septal angular limit but not significantly decreased by any of the tested basal SA slice limit values, when the optimum minimum area requirements were used with a radial sampling distance of either 14 or 15 mm. The overall Kappa was also significantly decreased by increases in either the SA slice or angular coverage but not significantly decreased by decreased SA slice or angular coverage, when all other parameters had their optimal values. Within the other parameters sets showing no significant decrease in overall Kappa, few contained angular coverage of 7 and those that did, did not contain the smallest angular search limit (180°); also few contained SA slice coverage of 7 slices and those that did, did not contain the smallest basal SA slice search limit (18).

2.3.3 Algorithm accuracy

Figure 2-4 shows the mean ROC curves for each threshold with the optimal combination of parameters and Table 2-4 gives all measures of accuracy for the final algorithm, using the optimal combination of parameter and threshold values. Also given in Table 2-4 are

the size and composition of the image populations used to evaluate accuracy measures at each threshold.

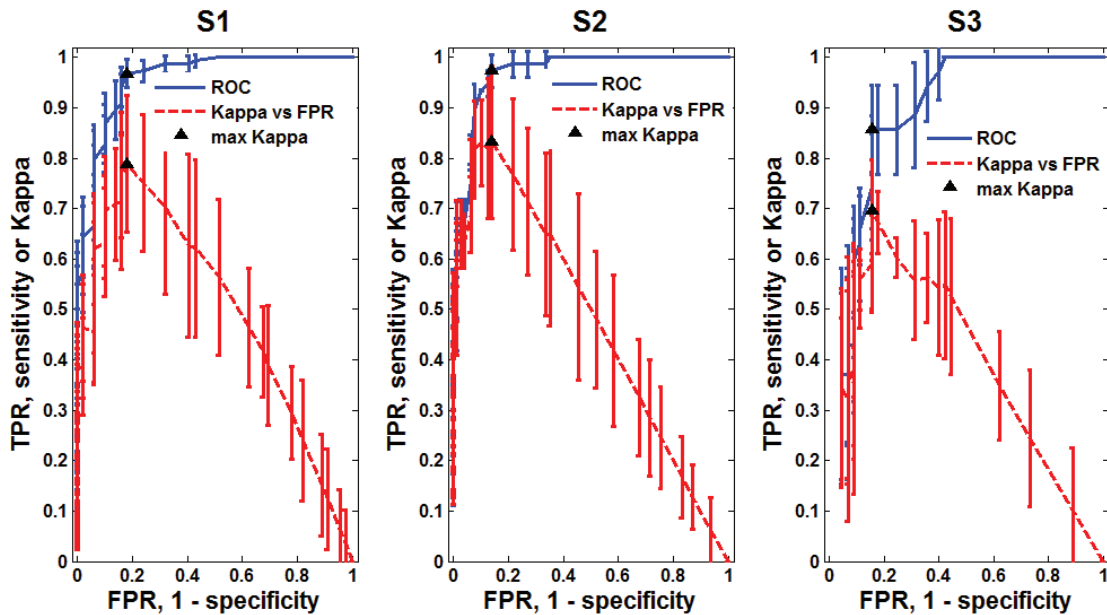


Figure 2-4. Mean receiver operating characteristic (ROC) curves (solid, blue) and Kappa (dotted, red) versus false positive ratio (FPR) for S1, S2 and S3 thresholds; produced with ten-fold stratified cross-validation of the optimal combination of parameters. The points of maximum Kappa are marked and Table 4 lists the threshold values and accuracy measures for these points. TPR = true positive ratio. Error bars show 95% confidence intervals.

Table 2-5 gives the range of Kappa, sensitivity and specificity for the four classes of interference severity as determined using all images from the truth dataset for which the algorithm successfully completed. Note that in calculating the sensitivity in Table 2-4, positives are defined as all images where the truth interference severity class is greater than the separation made by the current threshold (i.e. for S1, negatives are

images with truth classification ‘absent’, while positives are images with truth classification ‘mild’, ‘moderate’ and ‘severe’), while in Table 2-5, positives are only those images with the current truth interference severity class (i.e. to assess ‘absent’ sensitivity, negatives are images with truth classification ‘mild’, ‘moderate’ and ‘severe’ and positives, only those with truth classification ‘absent’).

Table 2-4. The threshold values and mean and 95% confidence interval on the mean [95%CI] of the accuracy measures of the final algorithm. Columns two and three give the size (N) and the known positive truth fraction (n) of the image population used for evaluation at the given threshold.

Threshold	N	n (%) positive truth	Threshold value (MMI)	Kappa μ [95%CI]	sensitivity μ [95%CI]	specificity μ [95%CI]	AUC μ [95%CI]
S1	198	151 (76.3)	0.490±0.005	0.79 [0.65, 0.92]	0.97 [0.94, 1.00]	0.82 [0.66, 0.98]	0.954 [0.951, 0.958]
S2	150	77 (51.3)	0.648±0.005	0.78 [0.64, 0.92]	0.92 [0.86, 0.99]	0.86 [0.71, 1.00]	0.969 [0.961, 0.976]
S3	83	35 (42.2)	0.762±0.005	0.65 [0.60, 0.70]	0.83 [0.77, 0.88]	0.82 [0.77, 0.88]	0.878 [0.869, 0.887]

Table 2-5. Accuracy measures versus interference severity class. The mean and 95% confidence interval on the mean [95%CI] were evaluated on all images from the truth dataset for which the algorithm successfully completed (column three) during TFSCV for overall Kappa. Column 2 gives the distribution of the known truth interference severity classes.

Interference severity class	n known truth	n successfully completed	Kappa μ [95%CI]	sensitivity μ [95%CI]	specificity μ [95%CI]
Absent	47	47	0.79 [0.71, 0.89]	0.80 [0.74, 0.88]	0.97 [0.93, 1.00]
Mild	78	77	0.70 [0.60, 0.81]	0.82 [0.75, 0.90]	0.88 [0.84, 0.94]
Moderate	39	39	0.61 [0.45, 0.77]	0.71 [0.55, 0.87]	0.92 [0.86, 0.97]
Severe	36	35	0.78 [0.70, 0.88]	0.85 [0.73, 0.97]	0.96 [0.92, 0.99]
Total	200	198	-	-	-

2.3.4 Failure rate, manual intervention rate and execution speed

Only 2 of the 200 truth dataset images had insufficient reconstructed FOV outside the myocardium, thereby causing the algorithm to fail and giving an estimated failure rate from the truth dataset of 1%. The incompatible images were a pair of rest and stress images from the same study classified as having mild and severe interference, respectively, by the clinician (column 2 vs. 3, Table 2-5). Once the algorithm search region parameters and radial sampling distance were chosen, the failure rate, which itself does not require clinician input, was evaluated on the Jan 2011-Dec 2012 dataset and was found to be $1.0 \pm 0.2\%$ (55/4920 images).

The software used to locate the LV myocardium (Klein *et al* 2010b) did not always accurately complete in fully automated mode. The frequency of manual intervention required during this step, evaluated on the Jan 2011-Dec 2012 dataset, was $5.9\pm 0.4\%$ (290/4920 images). The algorithm's execution time was ~ 40 seconds in total, with interference classification contributing only 6.6 ± 0.1 s. All code was run in MATLAB version 7.12.0 (R2011a) using a 1.86GHz Intel® Core™ 2 CPU, 6300 processor with 2.00 GB RAM. Manual intervention during location of the LV added 30 – 60 seconds to the execution time.

2.3.5 Prevalence of interference in Jan 2011 – Dec 2012 population

Table 2-6 gives the prevalence of interference as evaluated by the algorithm on the Jan 2011 – Dec 2012 dataset, broken into rest and stress image subsets. Prevalence decreases with increasing interference severity for stress images; while for rest images, the prevalence of moderate and severe interference are similar and only approximately one third are absent of interference. Prevalence of mild interference is equal for rest and stress images, while severe interference occurs more frequently in rest than in stress images and absent interference is more frequent in stress than rest images.

Table 2-6. Prevalence of interference (p) in Jan 2011 – Dec 2012 dataset as evaluated by the proposed algorithm. Rest and stress image prevalence are shown separately; prevalence is not corrected for sensitivity or specificity of the algorithm and the uncertainty is the 95% confidence interval on prevalence, [95%CI].

	Rest p [95%CI]	Stress p [95%CI]
Absent	0.28 [0.26, 0.30]	0.41 [0.39, 0.42]
Mild	0.38 [0.36, 0.40]	0.39 [0.38, 0.41]
Moderate	0.15 [0.14, 0.17]	0.11 [0.10, 0.13]
Severe	0.18 [0.16, 0.19]	0.08 [0.07, 0.09]

2.4 Discussion

To our knowledge this is the first automated algorithm for detection of extra-cardiac interference in the myocardium in nuclear imaging. The algorithm has good accuracy for detecting extra-cardiac interference and classifying interference as mild versus moderate-or-greater interference. It also predicts the level of interference severity with good specificity for each interference severity class. Execution time was less than one minute per image and, once the LV myocardium was located, classifying interference severity added less than 7 seconds to the processing time. However, the accuracy of the algorithm for separating moderate versus severe interference (S3 threshold) was not as good as absent versus present or mild versus moderate-or-greater (Figure 2-4c and Table 2-4, row 4).

The differences in sensitivity and specificity between the thresholds (Table 2-4) and the interference severity classes (Table 2-5) can be explained by the definition of positive

versus negative images in each case. The higher threshold sensitivities define positive images as those from *all* severity classes above the threshold while lower severity class sensitivities define positives as *only* those in the class currently investigated. Similarly, lower threshold specificities define negatives as primarily *only* those images from the severity class below the threshold while higher severity class specificities define negatives as images from *all* severity classes not equal to the class currently investigated.

Manual review of all falsely classified images showed that at the S1 threshold the main cause of false positives was a radial sampling distance that was too small. However, the review also indicated that increasing this distance would result in more false positives at both the S2 and S3 thresholds. This suggests threshold-specific radial sampling distance may improve accuracy over the single value used here. Classification of the inferior right ventricle (RV) insertion as mild interference also caused false positives while false negatives resulted from search limits (basal SA slice or septal angular coverage) and, at the S1 threshold, extra-cardiac uptake below the threshold but with clearly visible stomach wall structure. Individualized search limits may also increase algorithm accuracy. Overall, falsely classified images demonstrated the limitations of single-valued, population-based parameter definitions. Manual review of images on which the interference algorithm failed to complete showed that failure was primarily due to images of very large left ventricles or those not centred properly on the left ventricle, limiting the reconstructed FOV within the search region.

The main effect of the first step of parameter optimization proved to be reducing the range of potential radial sampling distances: the detection accuracy restriction (S1 Kappa) limited the minimum possible, and the failure rate restriction, the maximum possible, radial sampling distance going into the second step of optimization. The second step of parameter optimization demonstrated that the algorithm's overall concordance was least sensitive to the basal SA slice search limit, moderately sensitive to radial sampling distance, SA slice coverage and angular coverage and most sensitive to the angular search limit and optimized threshold values, as demonstrated by the alternate parameter combinations that produced no significant decrease in overall concordance over the optimal combination of parameters and the ROC curves for threshold values.

Table 2-2 shows that severe interference was reported by the clinician more frequently in rest than stress images and more stress than rest images had no interference (absent), while mild and moderate interference occurred with approximately equal frequencies in rest and stress images. The frequency of interference was observed to increase with decreasing BMI: the truth dataset was enriched with interference cases relative to the general population and had a significantly lower mean BMI than the large Jan 2011 – Dec 2012 dataset; as did the moderate and severe interference class subsets of the truth dataset relative to the absent class, for rest images. The odds ratio (OR) of extra-cardiac interference in the lowest ($22.6 \pm 0.4 \text{ kg/m}^2$, range = 18-25 kg/m^2) versus the highest ($40 \pm 1 \text{ kg/m}^2$, range = 32-63 kg/m^2) BMI quartiles is 1.3 in the rest images and 1.4 in the stress images. The odds ratio was observed generally to increase with

increasing interference severity: the OR for moderate and severe interference was 1.8 (rest images) and 1.2 (stress images), and the OR for severe interference was 2.0 (rest) and 1.5 (stress). All odds ratios were assessed with the truth dataset. The purpose of comparing the truth dataset demographics with those of the Jan 2011 – Dec 2012 dataset was to demonstrate which variables are potentially linked to presence of interference (show significant differences) as well as to identify the potential limitations when generalizing the conclusions from the truth dataset-developed algorithm to the overall population. The significant differences in the proportion of smokers in the truth dataset versus the large Jan 2011 – Dec 2012 dataset and the proportion of hypertensive patients in the mild versus absent and absent versus severe truth dataset rest image populations are suspected to be due to chance and not correlated with the presence of interference; however, further investigation is required.

The thresholds found during the optimization had values $S1 = 0.490$; $S2 = 0.648$ and $S3 = 0.762$ and the minimum area requirements were found to be 25° angular coverage and 3 SA slices. These values deviate from those set out in the clinician's criteria: the thresholds and angular coverage values are higher while the SA slice coverage is lower. The increased thresholds and minimum angular coverage are likely compensating for the use of population-based search region parameters which, alone, proved insufficient to exclude all regions of RV and basal background uptake and simultaneously include all regions of extra-cardiac interference. The difference in minimum area SA slice coverage may result from small differences in the average SA slice thickness between the

software used for clinical study display (4DM) and that used within the first stage of the algorithm to locate the LV (FlowQuant).

The optimal thresholds fall close to the guideline database thresholds differentiating between perfusion defect severity scores in the ^{82}Rb -ARMI standardized interpretation and scoring guidelines (Renaud *et al* 2014). Perfusion defect severities are: None (Normal) ≥ 0.75 , Mild (Equivocal) $0.60 - 0.75$, Moderate (Abnormal) $0.45 - 0.60$, Severe $0.30 - 0.45$ and Absent $0 - 0.30$. This indicates that if extra-cardiac interference is able to contribute the amount of uptake equivalent of Normal perfusion, to the myocardium, it is a severe interference problem. If extra-cardiac interference is only contributing uptake equivalent of a Moderate perfusion defect, it constitutes only mild interference. The sensitivity and specificity values determined in this study are specific to the truth dataset used here. While we do not consider the number of cases in the truth dataset to have been prohibitively small, and considering effort was made to ensure that the images in each interference severity class of the truth dataset were approximately representative of the characteristics seen in the general population, limited sample size means that the images in the truth dataset are not guaranteed to be representative of those in the general population. Caution should therefore be used when applying the algorithm results (prevalence) and accuracy measures (algorithm sensitivity and specificity) directly to the general population. If the population differs from that used in this study, the prevalence, sensitivity and specificity may also change.

If the algorithm-based prevalence is assessed in the Jan 2011 – Dec 2012 dataset, trends are similar to those observed in the truth dataset: higher prevalence of interference in

rest versus stress images caused by a larger fraction of rest images with severe interference and a larger fraction of stress images without interference (absent), and relatively large mild interference prevalence in rest and stress images. More severe interference in rest images can be explained by the difference in myocardial perfusion between rest and stress states. The rest state reflects perfusion of the myocardium by the coronary vessels in their normal, everyday state; while the stress state is achieved by selectively, pharmacologically, dilating the coronary vessels to increase perfusion of the myocardium. Within the range of interest, myocardial tracer uptake increases with perfusion. Lower myocardial perfusion in the rest state, relative to the stress state, results in lower myocardium : extra-cardiac contrast and therefore more severe interference rest images. Comparing row 2 of Table 2-2 with Table 2-6 shows that non-random truth dataset selection appears to have enriched the truth dataset, relative to the general population, in moderate and severe rest images and moderate stress images; which appears to have resulted in a deficit in absent rest and stress images. It is important to note that interference severity, as defined by this algorithm, does not include any measure of how extra-cardiac interference affects clinical study interpretation. It defines the physical severity of interference on a single image basis. This differs from the definition used by Bateman et al. (Bateman *et al* 2006) who reported interference on a per study basis (rest image + stress image) and included the effect of interference on clinical study interpretation in the definition of their classes. Although these differences preclude direct comparison of prevalence results, the frequency of interference observed in this study is much higher than that reported by

Bateman et al. suggesting that only a small fraction of the interference reported in this work affects clinical study interpretation, that prevalence of interference may be higher than that reported by Bateman et al., or some combination of the two.

When reporting extra-cardiac interference severity for studies in the truth dataset, the clinician also indicated generally whether the interference was likely to affect their overall clinical interpretation of perfusion defects for the study. While higher interference severity, in either the rest or stress image, appears to increase the probability of affecting clinical interpretation, the trend is not sufficient to be an independent predictor. For example, approximately one third of studies with absent interference at stress and only mild interference at rest were reported as potentially clinically relevant and not all studies with severe interference at both rest and stress were reported as clinically relevant. Therefore, while some cases of interference are easily identified at the time of acquisition; the clinical relevance of many cases, and subsequent need to correct for interference or rescan the patient, is more difficult to determine. It is in these cases where an algorithm may prove beneficial. Although the current algorithm does not indicate clinical relevance; it does form a good basis for incorporation of additional clinical parameters (e.g. location of suspected perfusion defects) which could potentially provide accurate and objective prediction of clinically relevant extra-cardiac interference.

2.5 Conclusion

An automated algorithm was produced that successfully detects extra-cardiac interference with 97% sensitivity, 82% specificity compared to visual scoring, and a failure rate of 1% in ^{82}Rb PET MPI. It adds < 7 s to the normal LV modeling software execution time and is able to classify interference severity. This algorithm provides a good measure for screening: it can be used to reliably rule out images without extra-cardiac interference and thereby assess the prevalence of extra-cardiac interference.

3 Chapter: **Simple approaches to ECI compensation**

3.1 Introduction

Extra-cardiac interference is caused by a combination of motion and limited spatial resolution. Cardiac gating and respiratory gating reduce motion. Reduced post-reconstruction filter width and time-of-flight information increase spatial resolution. This chapter demonstrates how much change can be expected in ECI severity when the degree of motion present in the image is reduced, by cardiac or respiratory gating, and when spatial resolution is improved, by reducing filter width and including TOF information. ECI severity is evaluated using the algorithm developed in Chapter 2 and changes are expressed relative to ECI in images produced with standard (un-gated, non-TOF) MPI processing (section 2.2.1). Reductions in ECI severity were found when using TOF information, reducing post-reconstruction filter width and, to a lesser extent, using cardiac and respiratory gating. All of these alternate forms of image processing were able to remove ECI from some scans that showed mild ECI with standard MPI processing, but were not able to remove ECI from any scans that initially showed moderate-severe ECI. This chapter shows that simple, alternate methods for image processing can reduce the appearance of MPI but that they alone do not provide a solution for scans where ECI is more severe.

Simple modifications to the acquisition and processing protocols, such as gating and changing the degree of filtering, can improve the overall spatial resolution in images and thus may reduce ECI. Simple changes, if effective, have the advantage of being readily

applied to existing systems and are therefore more likely to find clinical utilization. This chapter explores the degree to which simple protocol modifications can produce images with reduced ECI relative to that in the principle images used for MPI interpretation, i.e. the static images used in Chapter 2 and referred to throughout this chapter as *reference images*. In addition to the reference images, MPI studies typically also contain cardiac gated image series to assess contractile motion (Dilsizian *et al* 2009). Respiratory gated image series are also becoming more commonly available and were obtained for a subset of stress scans at our centre. As our centre also retains raw sinograms for static and gated series, it was possible to reprocess and evaluate images with different levels of filtering. Finally, our scanner is capable of time-of-flight (TOF) imaging, allowing the benefit of this technique to be assessed.

In this chapter, the detection and severity classification algorithm of Chapter 2 (DSC algorithm) was applied to images created using modified forms of processing to compare their interference severity to that in the reference images. The scans used in this chapter are those from Chapter 2's truth dataset where interference was present in the reference image and was correctly classified by the DSC algorithm.

Unlike normalization for cine display of gated image series, where each frame is normalized to the maximum MMI over all frames, in this chapter, each gated or filtered frame was treated as a separate image and used its own MMI value for normalization. In addition, since true myocardial uptake is obscured within the region of the myocardium affected by ECI, the DSC algorithm was modified to ensure that the MMI position was not co-located with ECI (section 3.2.2).

3.2 Cardiac gating

3.2.1 Introduction

Thickening of the myocardial wall inwards at systole does two things that can potentially reduce the effect of ECI: i) it reduces the partial volume effect (PVE) which, assuming no change in stomach thickness at systole, increases myocardium-to-stomach contrast, and ii) it shifts the centre of the myocardium inwards which increases the mean separation between the myocardium and the stomach compared to diastole when the wall is thinner. The cardiac gated image series used to produce systolic images also minimize the loss of spatial resolution caused by cardiac motion averaging and, if motion of the outer surface of myocardial wall is present, the location of the outer surface would be closest to the LV axis (farthest from extra-cardiac uptake) at systole. While all of these factors may contribute to reduced ECI severity at systole, the effect of increased myocardium-to-stomach contrast is thought to be the dominant source of change. The filter width used for gated series is greater than that used for the reference images; this increased smoothing will counteract the benefits in PVE and spatial resolution produced by cardiac gating, potentially limiting reductions in interference severity.

The hypothesis of this section was that the systolic frame of the cardiac gated image series will exhibit less severe interference than the diastolic frame and the static reference image. If the systolic frame of the cardiac gated image series has less interference, then it could be displayed alongside the reference image to aid MPI interpretation.

3.2.2 Methods and materials

Modification of DSC algorithm to ensure normalization is independent of ECI

An iterative loop was added to the DSC algorithm from Chapter 2 to ensure that the normalization (MMI) position does not coincide with ECI. Inside the loop, the MMI is taken from the myocardial polarmap and then the DSC algorithm evaluates presence and location of interference, as per Chapter 2. Following this, if the MMI location falls within a 2 SA slice, 20 degree buffer of interference, the myocardial polarmap is zeroed within this region and input to the next iteration of the loop. The process stops when the MMI location is outside of the ECI + buffer region.

Scan acquisition, data organization, reconstruction and LV image processing

Cardiac gated image series use data acquired between 2 and 8 minutes after the ^{82}Rb bolus injection begins. The data are gated into an 8-frame, 3D sinogram series triggered by the ECG R-wave. Image frames are produced from sinograms using VUE Point HD (GE-Healthcare 2008) iterative OSEM reconstruction with 24 subsets, 4 iterations and a 16 mm post-reconstruction Hann filter. The filter width used to produce gated images is larger than that used for the static reference images (12 mm Hann) due to the increased noise in the gated reconstruction frames. The 16 mm Hann filter is used clinically in our centre and is therefore chosen to reduce noise to an acceptable level in the gated images. Images are then brought off-line and processed to locate and re-orient the LV myocardium using FlowQuant software. FlowQuant uses an image summed over all gated frames to locate the LV axis, followed by spline fitting performed separately on

each gated frame to locate the myocardium. Once complete, the systolic frame is identified as that with the smallest LV volume and the diastolic frame as that with the largest LV volume.

Population and interference severity classification

All of the 200 truth dataset scans (Chapter 2) had cardiac gating information and 108 had ECI in their reference image which was correctly classified by the DSC algorithm (53 mild, 23 moderate and 32 severe; 63 rest scans and 45 stress scans).

Interference severity was classified using the DSC algorithm on each cardiac gated frame independently. The frames exhibiting the minimum and maximum interference severity were identified and their interference compared to that in the reference image and to one another. The proportion of scans was calculated that showed: i) no interference in their minimum interference severity image frame, ii) reduced interference in their minimum interference frame relative to that in their reference image, iii) increased interference in their minimum interference frame relative to that in their reference image, iv) minimum interference severity in the systolic frame, v) maximum interference severity in the diastolic frame, and vi) a difference in interference severity class within the gated image series. The proportion of scans for which the difference in interference severity class within the gated image series was 2 interference severity classes was also evaluated.

The ratio of the normalization value (MMI) for each gated image frame relative to that of the reference image was calculated and was compared for frames showing a reduction in interference versus those that did not, as well as for the systolic frames

versus the diastolic frames. The ratio of the maximum MMI over the minimum MMI within each gated image series was also calculated and was compared for scans showing no change in interference severity versus cardiac gated frame, those showing a change and for those showing a change of two interference severity classes. Student's t-tests were used to perform comparisons.

3.2.3 Results

Figure 3-1 shows the DSC algorithm evaluated on a SA slice of the reference image, as well as the systolic and diastolic cardiac gated image frames, for a scan with moderate interference in the reference image that is reduced but not eliminated in the systolic frame and increases in the diastolic frame.

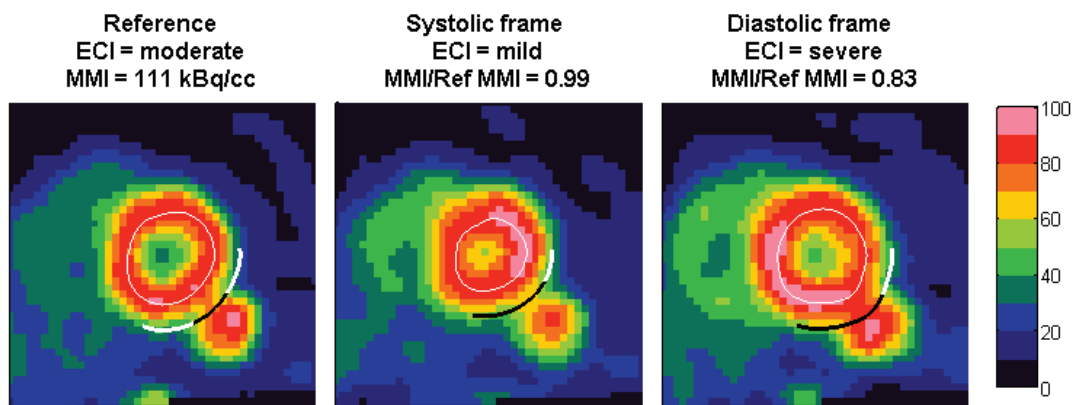


Figure 3-1. Example short axis (SA) image slices of the reference image and systolic and diastolic cardiac-gated frames for a scan with moderate interference in the reference image that is reduced to mild in the systolic cardiac gated frame but which increases in the diastolic frame. The centre of the myocardial wall is shown with a thin white line; the interference search region is outlined with heavy white lines and the region where interference was detected is delineated in black. The clinical 10-step colour scale is used with units of % maximum myocardial intensity (%MMI).

Two percent (2/108) of scans produced a cardiac gated image frame which eliminated interference. The scans for which interference was eliminated both exhibited mild interference in their reference images; no scans with moderate or severe interference in their reference images produced a cardiac gated frame without interference. 17% (18/108) of scans produced a cardiac gated image frame with interference severity less than that in the reference image: 4% (2/53), 35% (8/23) and 25% (8/32) of scans with mild, moderate and severe interference, respectively, in their reference images. The reduction was never by more than one interference severity class. 4% (4/108) of scans showed increased interference severity in their minimum interference cardiac gated image frame relative to their reference image, leaving 79% of scans with interference severity in their minimum interference cardiac gated image frame equal to that in their reference image. In the majority of scans, the systolic frame was classified as having the least interference within the cardiac gated series (87%) while the diastolic frame was classified as having the most (90%). 69% of scans showed a change in interference severity versus cardiac gated frame and 13% showed a change of 2 interference severity classes.

The mean ratio of the cardiac gated frame MMI to the reference MMI was 0.9 ± 0.2 , (max 1.0 ± 0.2 ; min 0.8 ± 0.2). When all cardiac gated frames from all scans were considered, 33/831 frames had interference reduced compared to that in the reference image and had a mean ratio of gated-frame to reference MMI = 0.98 ± 0.05 . The remaining frames which showed no reduction, had a mean ratio of gated-frame to

reference MMI = 0.9 ± 0.2 , which was significantly different from that of frames showing a reduction, ($p < 1 \times 10^{-4}$).

The mean ratio of systolic-frame to reference MMI was 1.0 ± 0.2 and was significantly different ($p < 1 \times 10^{-4}$) from the mean ratio of diastolic-frame to reference MMI (0.8 ± 0.2). The ratio of maximum over minimum MMI for all scans was 1.25 ± 0.08 and for scans showing no change in interference severity versus cardiac gated frame was 1.23 ± 0.07 . The ratio of maximum over minimum MMI for scans showing no change was not significantly different than that for scans showing a change of one interference severity class (1.25 ± 0.08), ($p = 0.24$); but was significantly different from that of scans showing a change of two classes (1.30 ± 0.09), ($p = 0.01$).

3.2.4 Discussion

While approximately two thirds of the scans examined showed changes in ECI severity large enough to be identified with the DSC algorithm, interference severity was reduced relative to that in reference images in less than one fifth of the scans.

If the change in intensity of the myocardium over the cardiac cycle is the dominant factor behind changes in ECI severity for cardiac gated image series, and it is assumed that changes in intensity are uniform over the myocardium, then the ratio of normalization values (MMI) can be used to explain changes in ECI. Neither the mean nor the maximum ratios of cardiac-gated-frame to reference MMI were found to be greater than one. This suggests that reductions in PVE in systolic cardiac gated frames were offset by spatial resolution losses due to increased filtering of the gated image series (16 mm) relative to the reference image (12 mm). Since little increase in intensity of the

myocardium is seen over reference images, few scans showed reductions in interference relative to reference images. However, ratios of the maximum over minimum MMI within the gated series showed values greater than one and a significant difference was seen between the mean ratio of systolic-frame to reference MMI and the mean ratio of diastolic-frame to reference MMI, which demonstrate that the magnitude of the PVE does change over the cardiac cycle. This shows that the magnitude of the PVE and, therefore, myocardial intensity is changing over the cardiac cycle and explains why the majority of scans showed changes in interference severity versus cardiac gated frame. Significantly larger maximum over minimum MMI ratios were seen for scans showing changes of 2 interference severity classes within their cardiac gated series versus that for scans showing no change in interference severity class over their cardiac gated series. This observation supports the hypothesis that the magnitude of the PVE is correlated with ECI severity, as does the observation that the mean ratio of cardiac-gated-frame to reference MMI for scans showing reductions in interference severity is significantly larger than the ratio for scans showing no reductions.

The fact that there was no significant difference in the maximum over minimum MMI ratio (MMI_{max}/MMI_{min}) for scans showing a change of one interference severity classes over their cardiac gated series versus the same ratio for scans showing no change in interference severity class, may indicate that myocardial intensity is not the only factor affecting interference severity. The magnitude of the maximum over minimum MMI ratios are on the same order as the ratio between the DSC algorithm thresholds (S1, S2 and S3) separating each interference severity class from its neighbouring classes:

$\mu(\text{MMI}_{\text{max}}/\text{MMI}_{\text{min}}) = 1.25 - 1.30$, $S3/S2 = 1.18$, $S2/S1 = 1.32$; but is not quite as large as the ratio of thresholds separating moderate-severe and absent-mild interference severity classes, $S3/S1 = 1.56 > \mu(\text{MMI}_{\text{max}}/\text{MMI}_{\text{min}})$. This observation also supports a conclusion that the overall interference severity is the product of changes in myocardial intensity combined with other factors, such as the change in myocardial centre location and myocardium-stomach separation.

A limited number of scans had cardiac gated series where interference in all frames was greater than that in the reference images. Review of the DSC algorithm results for these image series showed that the gated-frame to reference MMI ratios were all less than one and indicated that increased filtering of these images, relative to reference images, reduced the overall spatial resolution, increasing spillover and ECI severity.

The DSC algorithm uses a constant radial sampling distance relative to the centre location of the myocardium to estimate interference. Thickening of the myocardial wall during contraction will reduce the distance between the outer myocardial surface and the interference sampling points, potentially increasing the myocardial contribution to the sampling points and falsely increasing interference severity. This problem could mask reductions in interference severity at systole and could be resolved by allowing radial sampling distance to vary as a function of cardiac contractile phase. However, visual review of systolic frames from image series without interference suggests that for images correctly classified by the DSC algorithm, this effect does not alter classification. Because MPI is a relative form of imaging, using MMI normalization, and because the DSC algorithm uses the normalization of the image as the scale against which

interference is measured, interpretation of the images and results of the algorithm assume that the magnitude of PVE effects experienced throughout the myocardial wall is uniform and equal to that at the point of normalization (MMI location). This assumption holds for normal myocardium where wall thickness, wall thickening and radial motion as a result of contraction can be assumed to be relatively uniform. The assumption may be compromised in abnormal or diseased myocardium where the wall can be thinner and does not experience as much wall thickening or motion during contraction (Heller *et al* 2009). The impact of this assumption on DSC algorithm results is that, if the myocardium underlying interference is abnormal and therefore the reduction in PVE it experiences at systole is less than that experienced at the location of normalization (MMI location), the myocardium-stomach contrast in the interference region will not be increased and the algorithm will overestimate the reduction in interference at systole. Since estimates of local myocardial PVE are not typically available in MPI, this is a limitation of the present method.

3.2.5 Conclusion

Although systolic image frames exhibit the least severe interference over all gated frames for the majority of scans, their interference severity is less than that in reference images in less than one fifth of the scans examined. The ratio of normalization values, from systolic image frames relative to those from reference images, suggests that the increased filtering used on the gated image series may cancel gains in spatial resolution and contrast produced by increased myocardial wall thickening and reduced cardiac motion. A large proportion of scans showed a variation in interference severity versus

cardiac gated frame which indicates that, while not the sole cause, cardiac motion likely contributes to overall ECI. We conclude that cardiac gating alone does not provide a solution for ECI.

3.3 Respiratory gating

3.3.1 Introduction

Respiratory motion can introduce spatial overlap between the myocardium and adjacent stomach in respiratory-averaged reference images. Large amplitude respiratory motion is infrequent, for example Wells et al. (Wells *et al* 2010) showed that only 20% of scans had axial motion >6mm, but low amplitude respiratory motion occurs more frequently in the MPI population and can contribute to ECI. The hypothesis of this section is that low amplitude respiratory motion contributes to ECI and that respiratory gating will result in reduced effective interference severity relative to the static reference image. Respiratory motion is not suspected to change myocardial wall thickness and therefore, unlike cardiac gated images, reductions in ECI in respiratory-gated images are likely due to improved spatial resolution resulting from decreased translational-motion averaging and increased maximum physical separation.

3.3.2 Methods and materials

Scan acquisition, data organization, reconstruction and LV image processing

Scan acquisition, data organization, reconstruction and LV image processing were performed as described in section 3.2.2; however, instead of basing the gating on the R-wave from the ECG signal, the gating was triggered based on the amplitude of the signal

from the RPM motion-detection system (Varian Medical). FlowQuant was used to locate and re-orient the image frames as described in 3.2.2.

Population and interference severity classification

Patient positioning did not always permit acquisition of a respiratory signal with sufficient quality for respiratory gating and therefore respiratory-gated image series were produced less frequently than the other types of images in our clinical ^{82}Rb PET MPI database. In addition, respiratory-gated series were only produced for stress scans. Of the 100 truth dataset stress scans, respiratory-gated image series were produced for 63 scans, of which 21 had interference in their reference image that was correctly classified by the DSC algorithm (12 mild, 8 moderate and 1 severe).

Similar to the approach used in section 3.2, interference severity was classified using the DSC algorithm for each respiratory gated frame independently. The frames exhibiting the minimum and maximum interference severity were identified and their interference compared to that in the reference image and to one another. The proportion of scans was calculated that showed: i) no interference in their minimum interference severity image frame, ii) reduced interference in their minimum interference frame relative to that in their reference image, iii) increased interference in their minimum interference frame relative to that in their reference image, and iv) a difference in interference severity class within the gated image series. The proportion of scans for which the difference in interference severity class within the gated image series was 2 interference severity classes was also determined.

The ratio of the normalization value (MMI) for each image frame relative to the reference image MMI and the ratio of the maximum to minimum MMI within each gated image series were calculated and the same comparisons were made as for the cardiac gated series, described in section 3.2.2 above. Student's t-tests were used to perform comparisons. In addition, paired t-tests were used to compare the MMI ratios of the cardiac versus respiratory gated series for the 21 scans of the respiratory dataset. The ratio of the maximum MMI within each gated series to the reference MMI, the ratio of the minimum MMI per gated series to the reference MMI ratio and the maximum versus minimum MMI per gated series ratio were compared.

3.3.3 Results

Figure 3-2 demonstrates the results of the DSC algorithm on an example SA slice of a reference image and the corresponding maximum and minimum interference severity respiratory-gated frames, for the scan showing mild interference in the reference image and absent of interference in the minimum interference respiratory frame.

Only 1 of the 21 scans examined (5%) was able to produce a respiratory gated frame without interference and it had mild interference in its reference image, Figure 3-2. 14% (3/21) of the scans examined produced a respiratory gated frame with reduced interference relative to that in their reference image. Interference in the scan whose reference image was classified as severe remained classified as severe in all respiratory gated frames.

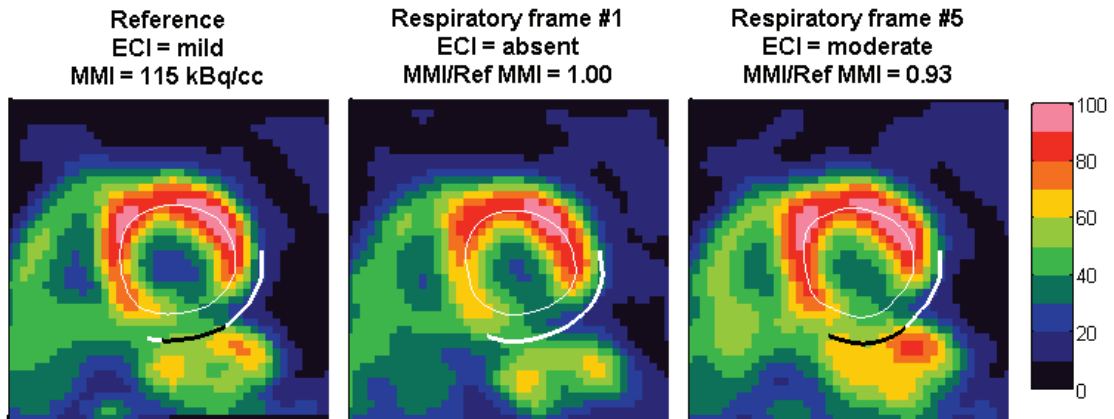


Figure 3-2. Example short axis (SA) image slices of the respiratory frames exhibiting minimum and maximum interference compared to the reference image, for the scan with mild interference in the reference image that is removed in the minimum interference respiratory gated frame. The centre of the myocardial wall is shown with a thin white line in SA slice images; the interference search region is outlined with heavy white lines and the region where interference was detected is delineated in black. The SA slice images are shown with the clinical 10-step colour scale, in units of % maximum myocardial intensity (%MMI).

No scans showed increased interference severity in their minimum-interference respiratory-gated image-frame relative to their reference image. 71% (15/21) of scans showed a difference in interference severity class between the maximum and minimum interference respiratory gated frame. In 14% (3/21) of scans, the difference between maximum and minimum frames was 2 interference severity classes. In 71% of scans, there was increased interference severity in their maximum interference cardiac gated image relative to their reference image.

The mean ratio of the respiratory-gated-frame to reference MMI was 0.94 ± 0.09 (max 0.96 ± 0.21 ; min 0.85 ± 0.18). When all respiratory gated frames from all scans were

considered, only 3/168 had reduced interference severity compared to that in the reference image and they had a mean ratio of gated-frame to reference MMI = 1.0 ± 0.2 . The remaining frames which showed no reduction, had a mean ratio of gated-frame to reference MMI = 0.93 ± 0.09 , which was not significantly different from that of frames showing a reduction, ($p = 0.12$).

The ratio of maximum over minimum MMI for all scans was 1.13 ± 0.05 and for scans showing no change in interference severity versus respiratory-gated frame was 1.12 ± 0.03 . The ratio of maximum over minimum MMI for scans showing no change was not significantly different than that for scans showing a change of one interference severity class (1.13 ± 0.06), ($p = 0.73$), or a change of two classes (1.13 ± 0.04), ($p = 0.60$).

A paired t-test comparing the ratio of the maximum MMI over all gated frames to the reference MMI for respiratory gated series, $\mu = 1.0 \pm 0.2$ ($0.96/0.21$), to that for cardiac gated series, $\mu = 1.0 \pm 0.2$ ($0.98/0.20$), for the 21 scans for which both cardiac and respiratory gated series were available, showed no significant difference, ($p = 0.34 > 0.05$). However, the ratio of maximum over minimum MMI (cardiac 1.25 ± 0.08 , respiratory 1.13 ± 0.05), showed a significant difference ($p < 0.0001$).

3.3.4 Discussion

While the proportion of scans showing changes in interference severity versus respiratory-gated frame suggests that respiratory motion affects ECI in more than two thirds of scans, the proportion for which interference was eliminated indicates it is rarely the sole cause of ECI. Like cardiac gating, values of the mean (and max) ratio of the respiratory-gated-frame to reference MMI being less than one suggest that the

gains in spatial resolution due to gating are offset by the effects of increased filtering. Unlike cardiac-gated image series, respiratory-gated frames show translation not deformation of the myocardium, which is reflected by a significantly smaller ratio of maximum over minimum MMI in the respiratory-gated series versus the cardiac-gated series. This difference can be observed by comparing Figures 3-1 and 3-2. Translation of the myocardium is evident in Figure 3-2, but absent in Figure 3-1. By contrast, the myocardium is very similar in the two respiratory frames, but shows increased thickness – and consequently changing intensity relative to the stomach – in the systolic versus diastolic frames.

Although large (>8 mm) amplitude respiratory motion is infrequent (Wells *et al* 2010), by using only scans for which reference-image interference was correctly classified by the DSC algorithm, scans with large-amplitude respiratory motion may have been excluded. If the motion averaging present in reference images increased the effective width of the myocardial wall sufficiently that the radial sampling distance used by the algorithm was no longer applicable, incorrect classification by the algorithm could result. Respiratory motion occurs mainly in the superior-inferior direction. Large (>8 mm) amplitude superior-inferior motion is easily visually identified in reference images as paired apparent widening of the anterior and inferior myocardial walls. The cause of large amplitude superior-inferior motion can be attributed to respiration if, in the respiratory-gated image series, motion averaging is reduced and physical translation is visible. There were 18 additional scans from the truth dataset for which respiratory information was available and interference was present in the reference image but was

incorrectly classified. Visual review of the DSC algorithm results for the reference images from these scans was used to determine if large amplitude superior-inferior motion caused them to be incorrectly classified. Only one such scan was found and review of the respiratory gated image series showed no change in motion averaging indicating gross patient motion, not respiration, was the cause. It is likely that reductions in ECI may be achieved by the respiratory gating of scans with large amplitude respiratory motion will exceed that shown here for small amplitude motion; however, caution should be exerted during interpretation of such images as they may also suffer from uncertainty in other corrections (i.e. CT-AC alignment).

All scans examined in this section were stress scans; the impact of respiratory gating on ECI in rest scans is expected to be equal to or less than that seen here as the amplitude and frequency of respiratory motion at rest is comparable to that at stress (Wells *et al* 2010) and the severity of interference is similar or higher.

3.3.5 Conclusion

In the majority of scans examined, although the amplitude of respiratory motion is sufficient to change ECI severity within the gated image series, respiratory-gating was unable to reduce or resolve the apparent overlap between the myocardium and the stomach when gated images are processed with a 16 mm Hann filter. The scans examined here were all stress scans; however, the corresponding results for rest scans are expected to be similar. While use of respiratory-gated image frames may enable improved interpretation in some scans with mild interference, respiratory gated series do not provide a full correction for ECI.

3.4 Filtering

3.4.1 Introduction

Post-reconstruction low-pass filtering is often applied to PET images to mitigate the effects of image noise. These filters also reduce spatial resolution and thereby contribute to the interference of extra-cardiac activity with the myocardial signal. There are three main hypotheses for this section: 1) that there exists a lower limit to filter width below which images will exhibit noise levels that prohibit confident definition of myocardium and stomach boundaries; 2) that this limiting filter width is less than the standard width used for reference images (12 mm); and 3) that reducing filter width for static images can reduce the degree of myocardial-stomach signal overlap and therefore reduce severity of interference. If, through reduced filtering, myocardium-stomach boundary could be accurately delineated, activity outside the myocardium could be removed prior to final (clinical) filtering to produce corrected images that are free of ECI. An anecdotal assessment of the combined effect of gating and reduced filtering is presented through an example cardiac gated image series.

3.4.2 Methods and materials

Scan acquisition, data organization, reconstruction and LV image processing

Scan acquisition, data organization, reconstruction and LV image processing were performed as described in section 2.2.1 for reference images, with the exception that the post-reconstruction filter width was reduced. Hann filter widths of 0 (no filter, NF), 4 mm and 8 mm were used. All reconstructions were performed using VUE Point HD (GE-Healthcare 2008) iterative OSEM reconstruction with 24 subsets, 4 iterations. The

FlowQuant software was used to locate the LV and re-orient the reference image and then this orientation and sampling was applied to all other static images with alternate filter widths produced for that scan. This was done because there is no change in the underlying static acquisition data - the location and distribution of the myocardium are the same - and this method results in a more consistent definition of the MMI location in those images with increased noise levels.

For the scans used to demonstrate the effect of reduced filtering on a gated image series, the scan acquisition, data organization, reconstruction and LV image processing were performed as described in sections 3.2.2 and 3.3.2, with the exception that the Hann filter widths were reduced from 16 mm to 12 mm and 8 mm. The LV location and re-orientation of all images was based on the FlowQuant software applied to the gated images with 16 mm filtering.

Population, interference severity classification and filter width versus interference and noise

The 108 scans from the truth dataset (Chapter 2) with ECI correctly classified in their reference images were smoothed with 8 mm Hann filters (53 mild, 23 moderate and 32 severe; 63 rest scans and 45 stress scans). The interference severity was classified using the DSC algorithm and the ratio of the normalization value (MMI) relative to the reference image MMI was calculated for these images. The proportions of scans showing elimination of interference, and showing a reduction in ECI severity relative to that in the reference image, were evaluated. The mean MMI/reference MMI for scans showing a reduction in interference severity was compared to that for scans showing no

reduction using a Student's t-test. A subset of scans was selected for further evaluation of images produced with 4.3 mm Hann filters and no filtering. These images were visually reviewed to determine the lower limit to filter width which allowed confident delineation of myocardial and stomach boundaries or classification of interference by the DSC algorithm.

Cardiac gated image series were produced with reduced filter widths for a set of 5 scans. Interference severity was classified using the DSC algorithm and images were visually reviewed to determine the lower limit to filter width which allowed confident delineation of myocardial and stomach boundaries or classification of interference by the DSC algorithm.

3.4.3 Results

Interference severity classification

Figure 3-3 demonstrates the results of the DSC algorithm on SA slices evaluated at the DSC algorithm radial sampling distance, for the reference image and static 8 mm Hann filtered images for two scans: one showing severe interference in the reference image reduced to moderate in the 8 mm filtered image, the other showing the scan with mild interference in the reference image that was eliminated in the 8 mm filtered image.

With an 8 mm filter, interference was removed in 15% (16/108) of scans (all of which had mild interference in their reference images); while 32% (35/108) of scans had interference reduced relative to that in their reference image. Scans with reduced interference severity consisted of the scans where mild interference in the reference image was eliminated, as well as 52% (12/23) and 22% (7/32) of scans with moderate

and severe interference in their reference images, respectively. None of the scans showed a reduction in interference severity by more than one interference severity class and, as expected, there were no scans for which interference severity in the 8 mm filtered images exceeded that in the reference images.

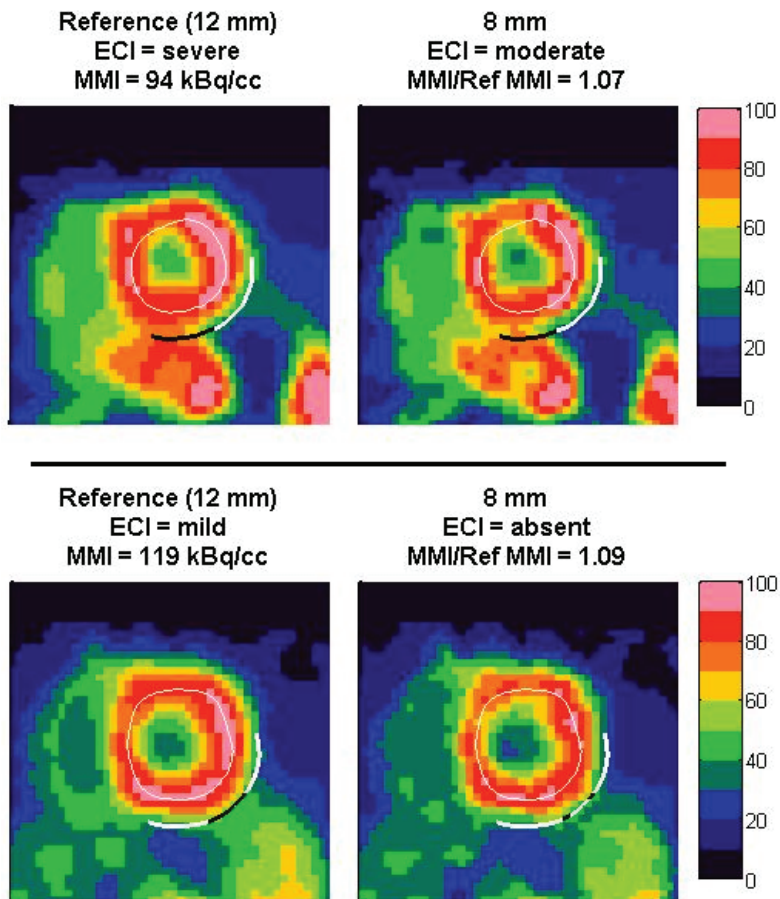


Figure 3-3. Two examples showing SA slices of scans with reductions in interference severity in static 8 mm Hann filtered images relative to that in the reference images: severe interference in the reference image, reduced to moderate in the 8 mm filtered image (first row) and mild interference in the reference image removed in the 8 mm filtered image (second row). Colour scale units are %MMI.

The mean ratio of 8-mm-filtered-image to reference MMI for all scans was 1.07 ± 0.02 ; for scans with reduced interference severity relative to that in the reference image, the ratio was 1.08 ± 0.03 and for scans without reduced interference severity, it was 1.07 ± 0.02 . The difference between scans with and without reduction was (almost but) not significant (unpaired t-test, $p = 0.053$).

Filter width versus interference and noise

Figure 3-4 demonstrates the results of the DSC algorithm on a single SA slice from an example scan where images were produced with Hann filter widths of 0 (unfiltered), 4.3 mm, 8 mm and 12 mm. Interference severity is mild in the reference image, remains mild in the 8 mm filtered image and is reduced to absent in both the 4.3 mm filtered and unfiltered images. Noise becomes apparent in the 4.3 mm filtered image and increases slightly in the unfiltered image.

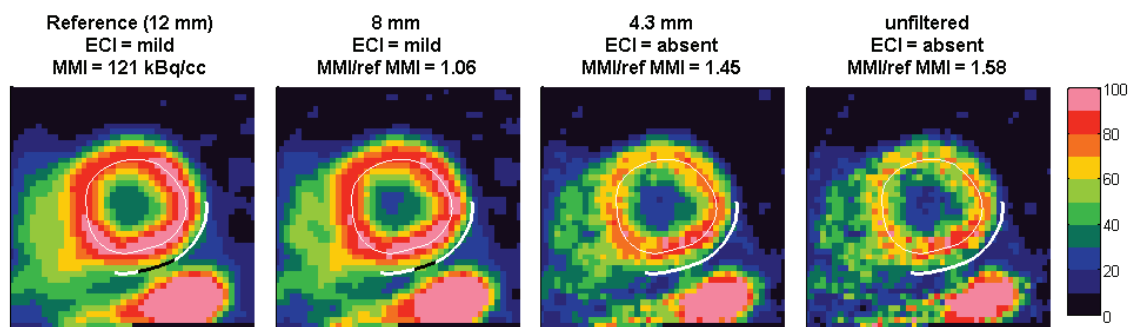


Figure 3-4. Example scan with mild interference in the reference image demonstrating interference severity as a function of filter width in static images: 12 mm Hann (reference), 8 mm Hann, 4.3 mm Hann and unfiltered images.

Figure 3-5 demonstrates a scan where removing filtering does not provide confident definition of the boundary between the myocardium and stomach. The appearance of elevated intensity in the inferior myocardial wall, combined with increased noise and lack of separation, indicates that interference is still present in the unfiltered image despite being classified by the DSC algorithm as absent of interference. This shows that there remains a population of scans for which even completely removing filtering cannot resolve interference and that, in images with noise levels exceeding those in images for which the DSC algorithm was developed (reference images), the classification produced by the algorithm may not be reliable.

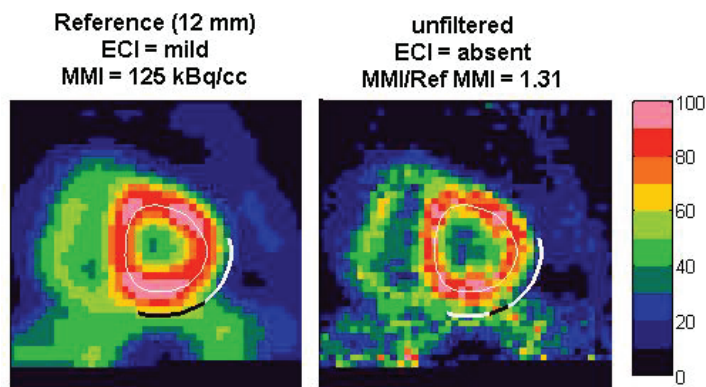


Figure 3-5. Example scan where removing filtering does not remove interference but the increased image noise causes the DSC algorithm to incorrectly classify interference as absent.

Visual review of images produced with the filter widths demonstrated in Figure 3-4, from a select subset of 5 scans, found that reliable classification of interference severity or delineation of myocardial and stomach boundaries in the interference region for all

SA slices within the image was possible in the majority of 8 mm filtered images, in some 4 mm filtered and very few of the unfiltered images.

Filter width versus interference and noise with gated image series

Figure 3-6 demonstrates the results of the DSC algorithm on example SA slices for the reference image and the systolic frame of the 16 mm, 12 mm and 8 mm filtered cardiac gated image series for two scans: one showing moderate interference in the reference image that is reduced to mild in the systolic (ES) frame of the 8 mm filtered, cardiac gated series, and the other showing mild interference in the reference image that does not change as a function of combined gating and reduced filtering.

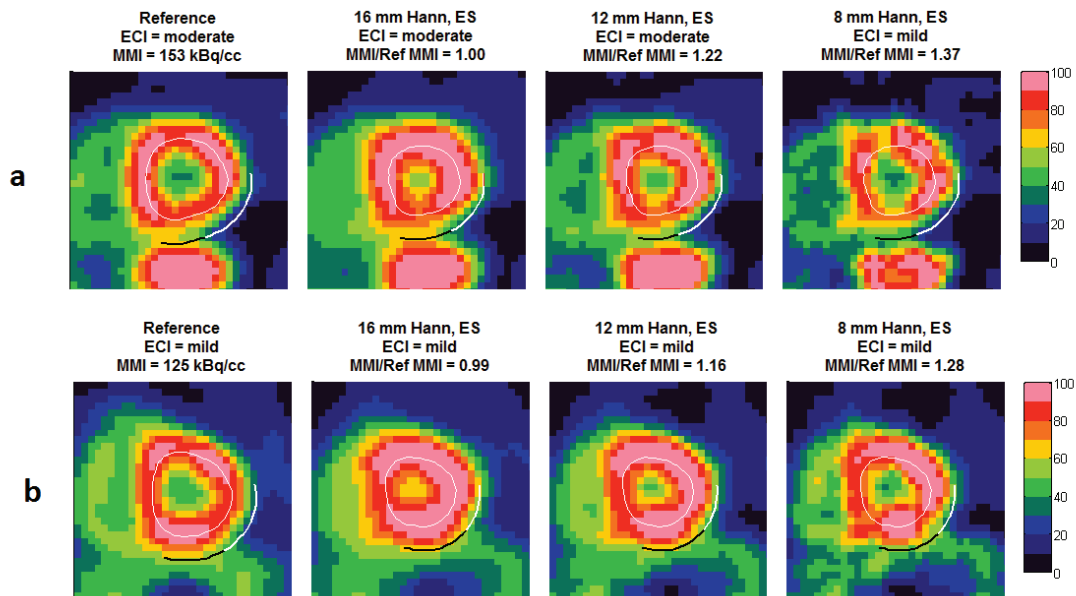


Figure 3-6. Two example scans demonstrating the effect of combining cardiac gating with reduced filtering. (a) shows a scan with ECI in the reference image that is reduced to mild in the systolic (ES) cardiac gated image frame when an 8 mm Hann filter is applied, but not when 16 mm or 12 mm filters are applied to the same gated frame; (b) shows a scan where mild ECI in the reference image is unchanged by the combination of cardiac gating and filtering. Colour scale units are %MMI.

The static images from both of these scans were also analyzed with reduced filtering and it was found that gating provided no additional benefit. The level of noise in the 8 mm filtered, systolic frame appears to fall between that seen in 8 mm and 4.3 mm filtered static images.

3.4.4 Discussion

The results found here support the hypotheses in the section's introduction: the lower limit of the filter width, below which image noise prohibits confident definition of boundaries, was found to be between 4 mm and 8 mm for Hann filtering applied to iteratively reconstructed, static images. This width is less than that used in reference images and was found to reduce interference severity relative to reference images for approximately one third of the scans examined. Based on the select set of scans examined, combining reduced filtering with cardiac gating does not appear to provide additional benefit over filtering alone. However, examination of a larger population may prove that, while this method is not effective for the majority, it still might provide improvements in a small fraction of scans. 8 mm is predicted to be the approximate lower limit of the Hann filter width, below which noise proves prohibitive to accurate DSC classification and stomach-heart boundary delineation, when applied to iteratively-reconstructed cardiac-gated images.

Reduced filtering improves spatial resolution which both reduces the amplitude of spillover at a given distance from each structure and increases the peak intensity in structures small enough to be influenced by PVE. In terms of ECI, this will mean less stomach signal at any given distance from the stomach. Increased intensity at the

location of normalization in the myocardium will then amplify gains in myocardial-stomach contrast caused by better localization of stomach and myocardial signals.

The ability to reduce filtering further was limited by image noise. As the amplitude of noise in the image approached that of the myocardial and stomach signals, the boundary between the heart and stomach could not be confidently defined. Noise in the images limited the accuracy of the DSC algorithm in assessing interference severity because the sampling points, from which interference was derived by the algorithm, were simple interpolations of neighbouring voxels without regional averaging to compensate for noise.

Since image noise in ^{82}Rb PET MPI is mainly statistical, increasing the number of coincidence events would allow images to be produced with less filtering and achieve the same level of image noise. Because of ^{82}Rb 's short half life, increasing acquisition time will not significantly increase the number of coincidence events in a scan.

Increasing the injected dose, while feasible from a patient-dose stand point (both whole body and organ doses for ^{82}Rb PET MPI are well below acceptable limits), is not an option with current generation scanners as dose is currently limited to maintain reasonable uncertainty in dead-time corrections caused by the high count rates seen in early acquisition (also a product of ^{82}Rb 's short half life). The number of coincidence events per image could however, be doubled, by simply repeating scan acquisition and summing the data prior to reconstruction. This is a practical solution but would double the scan costs to the clinic (equipment, dose and personnel time) and also comes with the potential for additional patient motion and alignment problems associated with

increased scan durations. At the current noise levels, alternative methods to improve image quality are to apply motion correction (sections 3.2 and 3.3) or to use TOF information during reconstruction (section 3.5).

3.4.5 Conclusion

Reducing the width of the Hann filter applied to static images from 12 mm to 8mm reduced interference severity in one third of the scans examined, removed interference in 15% of scans having mild interference in their reference images but was unable to remove interference from any scans with moderate or severe interference in their reference images. Although it appears further gains may be available as filter width is further decreased, confident delineation of structure boundaries and accurate evaluation of interference severity by the DSC algorithm was compromised due to increasing image noise. Similarly, reduced filtering of gated image series may provide some improvement in a fraction of scans but is not able to eliminate interference in the majority of scans before reductions in filtering leads to prohibitive levels of image noise. It was concluded that both filtering alone and the combination of gating and filtering, are insufficient to correct ECI.

3.5 Time-of-flight (TOF) reconstruction and reduced filtering

3.5.1 Introduction

As introduced in section 1.3.6, current timing resolution allows time-of-flight (TOF) measurement of the difference in arrival time of the two annihilation photons and thereby permits positioning of an annihilation event along a LOR to be improved from a

uniform probability to a Gaussian probability distribution. This improvement better localizes image signal as well as image noise and, overall, results in the ability to use smaller filter sizes while maintaining acceptable levels of image noise. The hypothesis of this section is that a greater proportion of scans will show reduced interference severity relative to reference images when TOF information is combined with reduced filter width compared to what was seen with reduced filter width alone (section 3.4, 8 mm filtered images).

3.5.2 Methods and materials

Scan acquisition, data organization, reconstruction and LV image processing

Scan acquisition, data organization, reconstruction and LV image processing were performed as described in section 2.2.1 for static images, with the following differences: reconstruction was performed with FX VUE Point HD (GE-Healthcare 2009) iterative OSEM reconstruction which incorporates TOF information into all steps, and post-reconstruction filtering used a 4 mm Hann filter. OSEM reconstruction used 24 subsets and 4 iterations. FlowQuant image processing for LV location and re-orientation from the reference images was applied.

Population, interference severity classification and filter cut-off versus interference and noise

Three of the 108 truth dataset scans (Chapter 2), with ECI in their reference image correctly classified by the DSC algorithm, did not have TOF information available; images were produced from the remaining 105 scans incorporating TOF information and 4 mm Hann filtering (51 mild, 23 moderate and 31 severe; 62 rest scans and 43 stress scans).

The interference severity was classified using the DSC algorithm and the ratio of the normalization value (MMI) relative to the reference image MMI was calculated. The proportions of scans showing elimination of interference, and showing a reduction in ECI severity relative to that in the reference image, were evaluated. The mean ratio of TOF MMI to reference MMI for scans showing a reduction in interference severity was compared to that for scans showing no reduction using a Student's t-test. A subset of scans was visually reviewed to determine if TOF-4 mm filtered images permit confident delineation of myocardial and stomach boundaries and classification of interference by the DSC algorithm.

3.5.3 Results

Figure 3-7 shows example scans where moderate interference in the reference image is reduced but not eliminated in the 4 mm TOF image and where mild interference in the reference image is removed in the 4 mm TOF image. Figure 3-8 shows a scan where the 4 mm filtered TOF image is noise limited, making confident delineation of myocardial and stomach boundaries difficult and reducing the accuracy of the DSC algorithm.

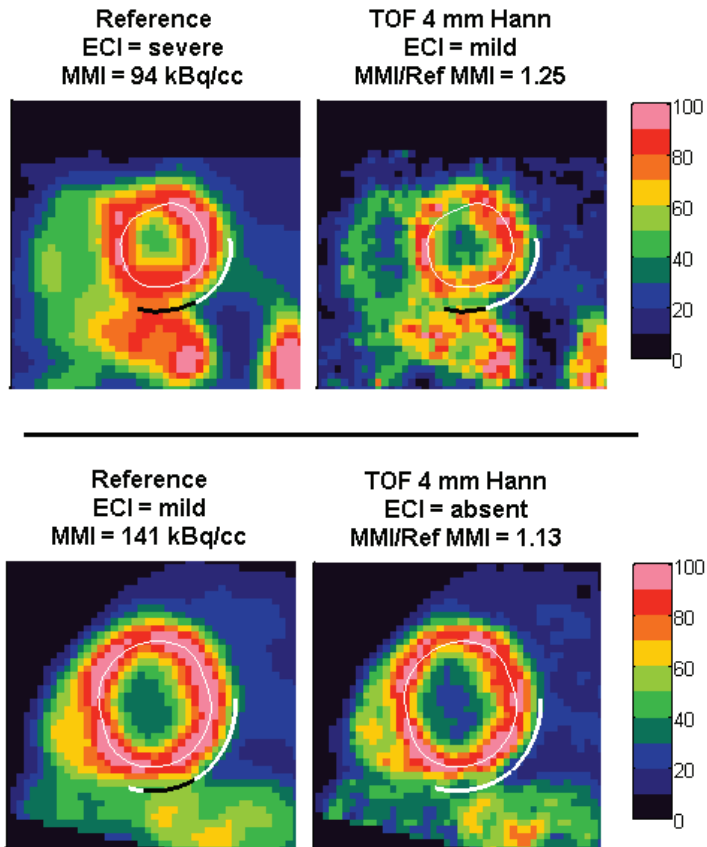


Figure 3-7. Two examples showing SA slices of scans with reductions in interference severity in TOF 4 mm Hann filtered images relative to that in the reference images: severe interference in the reference image, reduced to mild in the TOF 4 mm filtered image (left) and mild interference in the reference image removed in the TOF 4 mm filtered image (right). Colour scale units are %MMI.

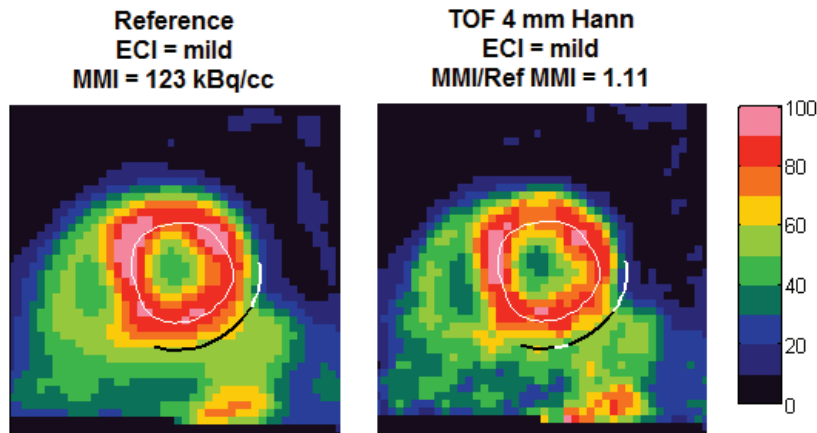


Figure 3-8. Example SA slices from the reference image and the TOF 4 mm filtered image for a scans showing mild interference in the reference image, which is not eliminated in the TOF 4 mm filtered image where noise levels are higher than those in the reference image. Colour scale units are %MMI.

Using TOF and 4mm filtering, 30% (35/105) of the scans produced images without interference (all of which had mild interference in their reference images); while 58% (61/108) of scans produced TOF-4 mm filtered images with interference reduced relative to that in their reference image. Scans with reduced interference severity consisted of the scans where mild interference in the reference image was eliminated, as well as 91% (21/23) and 25% (8/32) of scans with moderate and severe interference in their reference images, respectively. As expected, there were no scans for which interference severity in the TOF-4 mm filtered images exceeded that in the reference images. Only one scan, showing severe interference in its reference image, had interference severity reduced by 2 severity classes in the 4 mm filtered TOF image.

The mean ratio of TOF-4 mm filtered MMI to reference MMI over all scans was 1.15 ± 0.04 ; for scans with reduced interference severity relative to that in the reference image, the ratio was 1.16 ± 0.05 and for scans without reduced interference severity, it was 1.14 ± 0.04 . The difference between scans with and without reduction was (almost but) not significant (unpaired t-test, $p = 0.0545$). The mean ratio of the TOF-4 mm filtered MMI to reference MMI was significantly different than the mean ratio of the 8 mm filtered MMI to reference MMI, ($p < 0.0001$).

3.5.4 Discussion

Results of the DSC algorithm suggest that the combination of incorporating TOF information into iterative reconstruction and reducing Hann filter width to 4 mm approximately doubles the proportion of static images whose mild reference image interference is eliminated relative to non-TOF reconstructed 8 mm filtered static images and also doubles the proportion of scans where interference severity was reduced. However, interference remained in the majority of TOF-4mm filtered images and confidence in the results of the DSC algorithm is reduced in 4 mm filtered TOF images due to increased noise, Figure 3-8.

3.5.5 Conclusion

While TOF 4 mm Hann filtered images provide a reduction in interference severity in the majority of scans, this method of image processing still cannot eliminate interference classified as moderate or severe in reference images and approaches the lower limit of the filter width where noise in the images prevents confident boundary delineation and interference classification in some images.

3.6 Summary

Table 3-1 presents summarizes the results of Chapter 3. This chapter evaluates the reduction in ECI severity achieved with images produced by a number of simple modifications to image processing, all of which were clinically available. Although some reductions in interference were observed, none of the alternate approaches were able to eliminate severe interference before reduced filtering rendered them noise-limited and the results in this chapter suggest that more advanced methods – such as those proposed in Chapters 4 and 5 – are needed to fully remove extra-cardiac interference.

Table 3-1. Summary of ECI reduction and removal results versus the alternate forms of image processing examined in Chapter 3.

	% ECI removed		% ECI reduced
	MILD	MOD - SEV	
Cardiac gating	4%	0%	17%
Respiratory gating	8%	0%	14%
8 mm Hann filter	30%	0%	32%
TOF with 4 mm Hann filter	63%	0%	58%

4 Chapter: **Dynamic-data based correction**

4.1 Introduction

This chapter explores the possibility that extra-cardiac interference (ECI) can be distinguished from myocardial activity based on differences in the temporal behaviour of radiotracer uptake in the stomach versus that in the myocardium. This approach is motivated by the fact that differences in uptake kinetics between the liver and the myocardium were the foundation for the only previously published software-based ECI correction method (Sitek *et al* 2002a). Intravenously administered radioactive tracer is supplied to tissue/organs via the local vasculature and since the blood supply to extra-cardiac organs is downstream of the coronary arteries, a slight time delay is expected between myocardial and extra-cardiac uptake. By using dynamic binning (Figure 1-5, section 1.3.5), PET data can be reconstructed into a series of time frames (a dynamic image series) that show the temporal behaviour of radiotracer uptake. Factor decomposition and kinetic modeling are two methods that can be used to determine the functional form of the dominant temporal signals in dynamic image series. When the dominant temporal signals are determined, a coefficient for each temporal signal is assigned to each dynamic voxel in the image. Zeroing the coefficients corresponding to the stomach's temporal signal can then provide a corrected image. A variety of approaches to factor decomposition were examined in this chapter but none were found to be capable of both preserving myocardial uptake when ECI was not present in the scan, and also providing correction of ECI. Using a kinetic modeling approach, it was

demonstrated that, when variance was taken into account, there was no measurable difference between the temporal behaviour stomach and myocardial uptake.

The previously proposed dynamic-image-based correction algorithm (Sitek *et al* 2002a) used a factor decomposition method (PLS-FADS,(Sitek *et al* 2002b)) to derive four temporal basis functions from a dynamic series of ^{99m}Tc-teboroxime SPECT MPI images.

Factor decomposition seeks to represent dynamic data, **D**, as a linear combination of factors, **F**, (temporal basis functions) and structures, **S**, (factor coefficients) with an error term, ϵ , which encompasses variance unaccounted for by **SF**:

Equation 4-1.
$$\mathbf{D} = \widehat{\mathbf{S}}\widehat{\mathbf{F}} + \epsilon$$

To implement decomposition methods, dynamic image series are rearranged into a matrix **D** with size N x M where N is the number of voxels in the image and M is the number of images in the dynamic series (time frames). Then, the size of the factor matrix **F** is K x M, where K is the number of factors, and the size of the structure matrix **S** is N x K.

The most direct way to perform factor decomposition is by orthogonal or principal component analysis (PCA). This can be accomplished by eigenvalue or singular value decomposition (SVD) and produces a set of orthogonal (independent) factors, that when placed in descending order by their eigenvalues, account for progressively less of the overall variance in the dynamic data. Orthogonal analysis is simple and robust but may not yield physically realistic factor-structure pairs (e.g. negative amplitude) (Rummel 1988). In addition, when dynamic data comes from a physiological system, the desired temporal functions may not be completely independent, e.g. uptake of MPI tracers in

the myocardium relies on the availability of tracer, as supplied by the LV blood. Since the factors produced by PCA are orthogonal, they are often referred to as basis functions.

Factor analysis (FA) is a term used to describe a wide variety of methods that typically perform PCA followed by derivation of a rotation matrix (either orthogonal or oblique via minimization of an objective function) and application of this rotation matrix to the factors (basis functions) (Rummel 1988). The most common constraint incorporated into the rotation matrix's objective function is non-negativity. However, this alone does not guarantee a unique solution (Houston 1984) and can therefore also be accompanied by other application-specific constraints (to ensure uniqueness). The term FADS usually refers to performing SVD, followed by imposing the non-negativity constraint (Barber 1980, Paola *et al* 1982). Despite the fact that rotation matrices may result in non-orthogonal factors, the terminology from PCA is sometimes carried over and the terms *basis function* and *factor* are used synonymously within FA.

The method used by Sitek *et al.* (2002a&b), termed 'PLS-FADS', does not include PCA or SVD and instead of the traditional two-step FA approach, performs the factor decomposition in a single step using a multi-objective minimization. The objective function includes a least squares term, f_{LS} , a substitute for the orthogonal analysis, Equation 4-2:

$$\text{Equation 4-2.} \quad f_{LS}(\hat{\mathbf{S}}, \hat{\mathbf{F}}) = \sum_{i=1}^N \sum_{t=1}^M \left(\sum_{p=1}^P \hat{S}_{ip} \hat{F}_{pt} - D_{it} \right)^2$$

where: \hat{F}_{pt} is the estimate of the p^{th} factor and t is the index in time. \hat{S}_{ip} is the i^{th} pixel of the estimate of the p^{th} structure (factor coefficient image). D_{it} is the value of the measurement data from the dynamic sequence at the i^{th} pixel of the t^{th} index in time. The other two terms in the PLS-FADS objective are for non-negativity and uniqueness. The non-negativity constraint is given by Equation 4-3:

$$\text{Equation 4-3.} \quad f_{neg}(\hat{\mathbf{S}}, \hat{\mathbf{F}}) = \sum_{i,p=1}^{N,P} H(\hat{S}_{ip}) + \sum_{t,p=1}^{K,P} H(\hat{F}_{pt})$$

where $(x) = \begin{cases} ax^2 & x < 0 \\ 0 & x \geq 0 \end{cases}$, and a is a penalty constant. The final objective, f_{uni} , is implemented as an additional constraint and represents the amount of spatial overlap between the structure images of each of the factors, Equation 4-4:

$$\text{Equation 4-4.} \quad f_{uni}(\hat{\mathbf{S}}) = b \sum_{p=1}^P \sum_{q=p+1}^P \sum_{i=1}^N \frac{\hat{S}_{ip}}{\sqrt{\sum_{j=1}^N \hat{S}_{jp}^2}} \cdot \frac{\hat{S}_{iq}}{\sqrt{\sum_{j=1}^N \hat{S}_{jq}^2}}$$

b is the relative weighting constant and was adjusted every few iterations of the minimization to ensure the ratio $f_{uni} / (f_{LS} + f_{neg}) = 0.1$

The total penalized LS (PLS-FADS) objective function is given by Equation 4-5:

$$\text{Equation 4-5.} \quad f_{PLS} = f_{LS} + f_{neg} + f_{uni}$$

and is minimized using the conjugate gradient method. Sitek et al (2000) compared the results of factor decomposition using the least-squares (LS-FADS) method versus the more traditional SVD-based (FADS) approach and found that, when equal constraints for non-uniqueness were applied, the two approaches provided similar, accurate results. In this chapter, factor analysis is accomplished using the Factor Analysis of Medical Image Sequences (FAMIS) software package (Frouin et al 1992), which performs

decomposition using the FADS algorithm. FAMIS allows different methods of constraint to be added to non-negativity when rotating basis functions and provides an automated method for defining the image volume (VOI) that is input to FADS. The minimal spatial overlap (MSO) constraint available in the FAMIS software has the same objective as PLS-FADS's f_{uni} . The Matlab software used to execute all instances of the FAMIS code in this chapter was developed and supplied by Ran Klein (Klein 2010).

In their ECI correction algorithm, the four basis functions derived by Sitek et al. (2002a) represented the RV and LV blood, the myocardium and the extra-cardiac (liver) uptake. Images corrected for liver ECI were then produced by summing the structures corresponding to all basis functions except that of the extra-cardiac uptake.

Comparison of population mean, region of interest (ROI)-sampled time activity curves (TACs) from rubidium-82 chloride (^{82}Rb) PET MPI (Figure 4-1) (Hunter 2010) with ROI-sampled TACs presented by Sitek et al. suggests that the myocardium-stomach differences in ^{82}Rb PET MPI are of the same order as the myocardium-liver differences in $^{99\text{m}}\text{Tc}$ -teboroxime SPECT MPI.

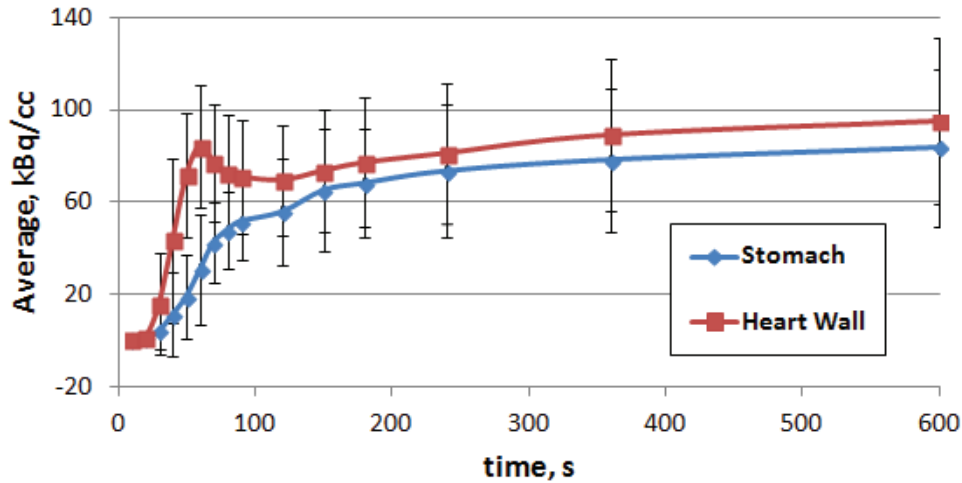


Figure 4-1. Mean region of interest (ROI)-based time activity curves (TACs) for the stomach and the heart wall from the dynamic image series of 30 ^{82}Rb PET MPI scans. Data provided by C. Hunter, (Hunter 2010).

The TAC from a voxel in a dynamic image series (a *dixel*) represents the tracer concentration in that volume as a function of time. Since spatial resolution and motion are known to cause spatially distinct sources of tracer uptake to overlap in images, the TAC may be a superposition of the temporal behaviour of radiotracer uptake in different organs. In addition to overlap caused by spatial resolution and motion, structures in the image with different uptake kinetics may truly coexist in a given dixel (*partial occupancy*). For example, myocardium is a highly vascularized tissue which leads to co-location of myocardium and blood; however, physiologically, myocardium and blood are separate structures with different uptake kinetics. Kinetic modeling (KM) is a technique that makes *a priori* assumptions about the temporal behaviour of radiotracer uptake in physiologic structures by modeling the behaviour of each physiologic structure with a parameterized function (Bailey *et al* 2005). KM fits TACs as a combination of the

parameterized basis functions which together form a model of the underlying physiology. Physiological models for MPI tracers have been developed and validated. They predict expected, physiologically realistic shapes of the parameterized basis functions. Factor analysis and factor decomposition are other techniques that seek to accomplish the same goal but without making *a priori* assumptions about the form of the underlying physiologic basis functions.

The hypothesis of this chapter is that factor analysis of dynamic image series from ^{82}Rb PET MPI can be used to separate extra-cardiac uptake from uptake in the myocardium and blood, and can then be used to produce static images corrected for ECI. A correction method was developed and evaluated based on dynamic image series from clinical ^{82}Rb PET MPI studies.

4.2 Methods and materials

4.2.1 Correction algorithm summary

The dynamic-based correction algorithm proposed here mimics that of Sitek et al. in that it derives a set of basis functions, fits coefficients for each basis function to each image voxel and then produces the corrected image as the product of the uncorrected image with the summation of all coefficients except that corresponding to the extra-cardiac (stomach) uptake. A number of different methods for estimating basis functions were investigated in an effort to obtain functions that were both physiologically representative and produced separated myocardial and stomach uptake structures. In addition, constraints were applied to enforce a priori information in an effort to improve

algorithm performance: i) stomach coefficient values were constrained to not-increase as a function of distance from voxels known to contain only stomach uptake (fall-off) and ii) the threshold used to dictate the set of voxels assumed to contain only stomach uptake was varied.

The dynamic-based correction algorithm was executed on transaxially-oriented image dixels to avoid blending of adjacent dixel values due to interpolation when reorienting images to the LV-reference frame. Because of differences in reconstruction and filtering between the reference images and the dynamic image series, the corrected image was based on the dynamic image series's pseudo-static image (section 4.2.2). As such, the region of the image to be corrected was selected as a sub-volume of the transaxially-oriented pseudo-static image and the pure stomach VOI (voxels assumed to contain only stomach uptake) was defined in the LV-reference frame but then transformed back into the transaxial frame (section 4.2.3). Coefficients for each structure (myocardium, LV, RV and stomach) were then produced for each voxel in the interference-correction region by fitting the TAC from the corresponding dixel to a linear combination of the basis functions. Stomach coefficients for voxels inside the pure stomach VOI were set to one and omitted from fitting. Fitting was performed using linear least squares. The corrected pseudo-static image was produced by multiplying each voxel in the region of the image to be corrected with the summation of its myocardium, LV and RV coefficients (i.e. omitting the stomach coefficient) and then transforming the image volume into the LV-reference frame for display. Similarly, images of the eliminated stomach intensity were produced by multiplying transaxially-oriented images by stomach coefficients within the

correction region and then transforming the image volumes into the LV-reference frame.

4.2.2 Image acquisition and reconstruction

The dynamic image series used in this chapter are derived from 3D list-mode format data acquired 0 - 8 minutes post-injection and binned into 15 sinograms based on acquisition time. The sinogram frame durations are, sequentially: 9x 10 s, 3x 30 s, 1x 60 s and 2x 120 s. Frame lengths are those used in our clinical dynamic cardiac ^{82}Rb PET protocol and are chosen to capture tracer kinetics and ensure sufficient coincidence events per frame. Images are produced from 3D sinograms using either FORE-FBP reconstruction (Wernick and Aarsvold 2004) with 24 subsets, 4 iterations and a 12 mm cut-off post-reconstruction Hann filter or OSEM iterative ViewPointHD reconstruction (GE-Healthcare 2008) with 24 subsets, 4 iterations and an 8 mm Hann filter but only reconstructing the first 14 sinograms (0 – 6 minutes). The difference in reconstruction is due to the differences in algorithms available at the time of image acquisition.

FlowQuant software was used to locate and re-orient the LV myocardium. Pseudo-static images were created by summing all dynamic frames falling within the static acquisition period: frames 12 – 15 (FBP), frames 12 - 14 (iterative).

4.2.3 Estimation of Basis Functions

Manual VOI TAC examples

TACs for the LV blood, RV blood, myocardium and stomach were obtained by manually delineating ROIs on multiple transaxial image slices and then calculating the mean of all voxels within the resulting VOI. The RV blood region was defined on a summed image

from the first 3 dynamic frames. The LV blood region was defined on the sum of dynamic frames 4 - 6 and the myocardium and stomach regions were defined on the pseudo-static images (summation of frames ≥ 12). ROIs were kept within the highest uptake regions of the structures and were sampled for three scans: one with no interference but well separated, high uptake stomach and two scans with ECI in their reference images, one with mild interference and one with severe. The VOI TACs derived from these examples were only used to assess the potential of this approach and confirm the biodistribution data (Hunter 2010), they were not used as basis functions for fitting coefficients and producing corrected images.

FAMIS factors as basis functions and structures as coefficients

Six scans with visible stomach uptake were selected to test the hypothesis that FADS with minimum-spatial overlap (MSO), implemented using FAMIS, could generate factors representative of separate physiologic basis functions for the myocardium and stomach. These basis functions would then provide distinct structures for the stomach and myocardium. Two of the six scans did not have ECI in their reference images but had elevated and proximal stomach uptake and the remaining 4 scans had severe interference in their reference images. The automated method used by FAMIS to define a VOI first selects out a rectangular region from a transaxially-oriented image which includes contiguous voxels with high summed dynamic voxel uptake. A fraction of the maximum summed dynamic voxel uptake is then used as a threshold to determine which voxels from within the rectangular region are included in the final VOI. The default threshold value used is 30% of the maximum summed dynamic voxel uptake. When the

dynamic image series for each of the six scans was input to FAMIS, the VOI was automatically determined and then expanded to include stomach by both manually increasing the inferior axial extent of the rectangular region and reducing the threshold of maximum summed dynamic voxel uptake. FAMIS was then run allowing the number of factors to be automatically selected (Klein 2010). The results were examined for physiologically realistic basis function shapes and structures that separated stomach and myocardium. Following this, the FAMIS input parameters were varied to determine the best possible solution for each scan. The input parameters investigated were: the number of factors to resolve, the method of constraint (MSO versus minimum temporal overlap, (MTO)), the VOI (via threshold value) and the number of temporal frames included.

FAMIS myocardium and blood basis functions and VOI-TAC stomach basis function

The VOI automatically determined by FAMIS was then manually cropped in the inferior axial dimension to exclude the stomach and regions of myocardium with ECI. FAMIS with MSO was run using 3 factors, aiming to consistently obtain physiologically realistic shapes for the RV blood, LV blood, and myocardium basis functions.

The stomach basis function was then determined by placing a VOI in the stomach. To obtain a pure stomach VOI, a search region was first defined on the LV-oriented pseudo-static image that contained only stomach intensity. The search region was defined manually on the pseudo-static image by selecting a range of SA slices and radial extent, followed by angular extent on each SA slice. Generally, the search region corresponded well with the interference-search region defined in Chapter 2's detection and severity

correction (DSC) algorithm with the radial range shifted outwards of the interference region, to approximately 25 mm – 55 mm outside the FlowQuant-defined myocardium location. The pure stomach VOI was then defined as voxels in the search region that were also inside the contour representing 70% of the maximum voxel uptake inside the search region. The stomach basis function was defined as the mean of the TAC normalized to the area under the curve (AUC) in each voxel of the VOI.

This procedure was performed on the 6 scans from section 4.2.3 above, on scans from the development dataset (section 4.2.6), and on scans from the evaluation dataset (section 4.2.7). The number of scans from the development dataset, for which physiologically realistic shaped basis functions were obtained, was recorded.

Reducing noise in basis functions

Despite efforts to establish a robust method for consistently producing physiologically representative basis functions, some scans still exhibited small non-physiological variations. To reduce noise and correct for non-physiological variations, the FADS-derived basis functions were fit with functions whose shapes represent the underlying physiology. The physiological shape of RV and LV blood functions was assumed to follow a gamma variate model (Madsen 1992, Thompson *et al* 1964). The 1-compartment model, which is frequently used for MBF quantification with ^{82}Rb uptake (Klein *et al* 2010a), was used to define the myocardial function and was also applied to model extra-cardiac uptake, similar to Sitek *et al* (Sitek *et al* 2002a).

Four methods for modifying the basis functions were investigated. In the first ‘original’ method, only the VOI-TAC stomach basis function was fit with a 1-compartment model

while the blood and myocardium basis functions derived from FAMIS were taken directly. In the 'fitFADS' method, blood basis functions derived from FAMIS were fit with gamma variate models. The myocardium basis function, derived from FAMIS, and the VOI-TAC-derived stomach basis function were fit to separate 1-compartment models. Following this, in the 'oneMyo' method, the blood input to the myocardium 1-compartment model was required to be consistent with the blood gamma-variate functions. Finally, in the 'subtrMyo' method, the consistent myocardium fitting was repeated but the fraction of myocardium signal found contaminating the blood gamma variate basis functions was subtracted, which should leave pure blood basis functions.

Using a kinetic model to define mean and variance of blood-free myocardial and stomach basis functions

Analysis of dynamic image series within FlowQuant uses a 1-compartment kinetic model (KM) which assumes that TACs are composed solely of myocardial and blood signals and therefore the sum of the fraction attributable to the myocardium, the recovery coefficient (RC), and the fraction attributable to blood, the total blood volume (TBV), is one (Klein *et al* 2010b). If regions input to this model exclude ECI, the model can be accurately applied to the myocardium or to the stomach to define voxel-based, blood-free myocardial or stomach basis functions. By grouping a number of input myocardium or stomach voxels, the mean and variance of blood-free basis functions can then be evaluated. The interference-free, high-uptake myocardium and interference-free stomach were evaluated for blood-free basis function mean and variance for the three scans used to demonstrate manual VOI-TACs. FlowQuant was used to determine the

myocardium and blood VOIs and then the DSC algorithm used to omit regions of myocardium where interference was detected. The stomach VOI was that used to find the manual stomach VOI-TAC. Predicted tissue and blood functions, and their uncertainties, produced by the FlowQuant KM were then AUC normalized to produce basis functions. The shapes and uncertainties of the blood-free myocardium and stomach basis functions were compared. The basis functions derived from these examples were not used for fitting coefficients and producing corrected images.

4.2.4 Estimation of coefficients

Coefficient fitting was performed using FAMIS myocardium and blood basis functions and the VOI-TAC stomach basis function, for all methods of reducing noise in basis functions. Fitting used linear least squares and was first performed independently for each voxel in the correction region. Assuming voxels used in the VOI-TAC to define the stomach basis function should be purely stomach, these voxels' stomach coefficients were set to one.

Stomach coefficient fall-off and the threshold for pure stomach volume

If the VOI used to define the stomach basis function is assumed to include, or be contiguous with, pure stomach voxels then it can also be assumed that stomach coefficients of voxels outside this volume can be constrained to values equal to or less than those of their neighbouring voxels that are spatially closer to voxels in the pure stomach volume. Six methods for constraining stomach coefficient fall-off were investigated: no constraint and \leq maximum, \leq mean, \leq minimum, \leq pc25, and \leq pc10 of neighbouring voxels closer to pure stomach, where pc25/pc10 denotes the upper

quartile/highest 10%. In addition, two values were investigated for the fraction of maximal stomach uptake used as the threshold to define pure stomach voxels: 0.7 and 0.4. Regardless of the fraction of maximal stomach uptake used as a threshold, the pure stomach volume was always confined to be within the radial and angular boundaries used during stomach VOI-TAC definition and the stomach VOI-TAC was always defined using the volume corresponding to the threshold of $0.7 \times \text{maximal stomach uptake}$.

4.2.5 Interference-free normal databases

Normal databases (NDBs) quantify the amount of variation expected in normal myocardium and, as such, can help estimate the degree of change in myocardial image intensity that has a clinical impact, i.e. is clinically relevant. When evaluating changes in myocardial image intensity caused by the correction algorithm, the variation expected in normal myocardium can be used as an indicator of when changes are large enough to have an impact or small compared to normal variability.

40 studies contributing to the clinical rest and stress NDBs were identified, with the aim of reproducing the clinical NDB in an accessible format outside of the 4DM (Invia) software that is used in our clinic. However, when these studies were reviewed, a number of the images were found to contain ECI (stress (26/40): 19 mild, 3 mod, 4 severe; rest (32/40): 19 mild, 2 mod, 11 severe). In addition, the clinical NDB used a cut-off of $SSS \leq 4$ and did not implement a cut-off value for SRS. The cut-off of $SSS \leq 4$ is a typical value (Iskandrian 1999, Kaster *et al* 2012); however, in previous studies which

were interested in characterizing smaller differences in apparent perfusion, a more strict criterion of $SSS \leq 2$ has been implemented (Ali *et al* 2009).

To express algorithm development and evaluation measures relative to *interference-free* physiologically normal variability, a rest/stress normal database was created using 30 studies whose reference rest and stress images were free of interference, as determined by the DSC algorithm, and exhibited normal perfusion relative to the clinical rest and stress NDBs. Normal perfusion was evaluated with 4DM software, using the following criteria: $SSS \& SRS \leq 2$; $TID < 1.2$ and rest and stress $LVEF > 0.4$; and using clinical NDB defect score cut-offs (Kaster *et al* 2012). This new pair of rest/stress databases was created using FlowQuant LV-processing of the reference images, with additional off-line Matlab code to generate 17 segment polarmaps. The new databases are referred to as interference-free NDBs, $NDB_{INT-free}$, with segmental mean and standard deviation values denoted $\mu_{NDB, INT-free}$ and $\sigma_{NDB, INT-free}$. While scans were selected for the development and evaluation datasets based on 4DM assessment of normal perfusion relative to the clinical NDBs, measures of myocardial perfusion used in algorithm development and evaluation to compare uncorrected and corrected images, used the interference-free NDBs. Although not always explicitly stated in the sections below, rest scans are always compared to the rest NDB and stress scans compared to the stress NDB.

4.2.6 Correction algorithm development

Correction algorithm development involved assessment of the overall failure rate of the algorithm and comparison of the methods for reducing noise in the basis functions, stomach coefficient fall-off and threshold for pure stomach VOI definition. The

development process identified the most promising combination of these methods which was then implemented for algorithm evaluation (section 4.2.7). An independent measure of true myocardial perfusion, e.g. from invasive coronary angiography (CA) or an alternative form of MPI, was not available for the ^{82}Rb PET MPI studies used in this work and as a result, the accuracy of correction algorithm results could not be directly, quantitatively assessed. To move forward without an independent measure of truth, the correction algorithm was developed and evaluated based on its performance when applied to different categories of scans.

Dataset and scan categories

The correction algorithm was developed in the context of three different categories of scans (A-C). The development dataset was composed of 16 scans and included 5, 6, and 5 scans from categories A, B and C, respectively. Scans in categories A and B aim to demonstrate preservation of myocardial perfusion while scans in category C aim to demonstrate the ability to reduce or remove interference. Scans in category A have reference images that show normal myocardial perfusion without ECI but show elevated and proximal stomach uptake. Similarly, category B scans have reference images without ECI but with elevated and proximal stomach uptake; however, the reference images from these scans show abnormal myocardial perfusion in the interference search region. Category C includes the rest scans from studies having stress reference images that show normal myocardial perfusion without ECI and rest reference images with ECI. This category comes as close as possible to having an independent measure of true myocardial perfusion underlying ECI since normal perfusion in stress images

indicates that the rest image perfusion should also be normal after interference correction.

Presence versus absence of ECI was determined using the DSC algorithm and presence of elevated and proximal stomach uptake was determined visually by display of MMI-normalized, SA image slices with a 10-step colour-scale. Normalcy of myocardial perfusion was determined by comparison to the clinical normal databases using 4DM software. The criteria for normal perfusion used to select scans for the development dataset based on their reference images were: $SSS \leq 4$, $TID < 1.2$ and $LVEF$ at both rest and stress > 0.4 . Abnormal perfusion for category B scans required a perfusion defect in the region facing stomach uptake, showing a reduction of $\geq 30\%$ MMI.

Measures

The measure used to reflect preservation of myocardial uptake for scans in categories A and B was the difference in summed defect score, after versus before image correction, (ΔSS). Segmental defect scores were evaluated using 17-segment polarmaps from FlowQuant LV-processed images and comparing them to $NDB_{INT-free}$ using $(\mu_{NDB, INT-free} - \mu_{seg}) \geq n * 1.5\sigma_{NDB, INT-free}$ to give a segmental defect score of n. All 17 segments were included in the summed defect score. A positive difference in summed defect score indicates increased perfusion defect after correction; a summed defect score difference of zero indicates preservation of myocardial perfusion. The measures used for category C were the difference in interference severity before versus after correction, as evaluated by the DSC algorithm; and the difference in summed defect score, as well as visual examination of myocardial perfusion post-correction.

4.2.7 Correction algorithm evaluation

Dataset and scan categories

Evaluation of the correction algorithm was performed using scans from categories A-C (defined in algorithm development above) and as well an additional category D. Like category C, category D aims to demonstrate the ability to remove ECI. Category D scans are those whose reference images have moderate to severe ECI. This category was added as the scans in category C typically have low levels of interference while images from category D scans require substantially more correction. However, normalcy of myocardial perfusion is not known in regions affected by ECI for scans in this category as the both rest and stress images contained ECI.

The evaluation dataset was independent of the development dataset and was composed of 23 (10 rest, 13 stress), 16 (7 rest, 9 stress), 15 (all rest) and 22 (13 rest, 9 stress) scans, respectively from categories A, B, C and D. Scans from the truth dataset (Chapter 2) were reviewed first and those which met inclusion criteria, were not used in the development dataset, and whose DSC algorithm-defined interference severity matched the known truth interference severity for the reference image, were selected. This resulted in 7, 2, 2, and 22 scans from the truth dataset in categories A, B, C and D, respectively, where the DSC algorithm is known to be accurate. The additional scans came from review of the Jan 2011 – Dec 2012 dataset with the goal of obtaining a minimum of 15 scans per category. To include scans in the evaluation dataset, the reference image interference severity was again determined by the DSC algorithm and normal perfusion determined by comparison to the clinical rest/stress NDB using 4DM

software and clinical NDB defect score cut-offs. The criteria for normal perfusion, however, were more stringent for scans in the evaluation dataset compared to the development dataset and required: $SSS \leq 2$ for stress scans and $SSS \leq 2$ and $SRS \leq 2$ for rest scans, in addition to $TID < 1.2$ and $LVEF$ at both rest and stress > 0.4 for all scans. Measures used for algorithm evaluation are only assessed in the potential interference (PI) segments of the 17 segment polarmap: those segments where, when the interference search region of the DSC algorithm is projected onto the 17 segment polarmap, $> 50\%$ of their area occupied by the interference search region. This was done to avoid dilution of results by inclusion of segments where the effect of ECI is limited. Using this definition, the five PI segments are: [4, 5, 10, 11 and 15] (Figure 1-10c) and correspond to the basal inferior, basal inferior-lateral, mid inferior, mid inferior-lateral and the apical inferior segments, respectively. Abnormal perfusion for scans included in category B of the evaluation dataset were required to have a summed score > 2 with a defect score ≥ 1 in a least one of the PI segments.

Measures

With the exception of interference severity, all measures used for algorithm evaluation focus on normalcy or the amount of change in myocardial intensity caused by the correction algorithm. The amount of change in myocardial intensity caused by the correction algorithm was quantified as the difference, *delta*, in the myocardial segment value after minus before correction. Mean delta values were expressed in units of interference-free NDB standard deviations, $\sigma_{NDB,INT-free}$, and were evaluated for the five PI segments, for each image category. In order to determine if changes produced by the

correction algorithm were on the scale of clinically relevant changes to the myocardial intensity, it was assumed that a change of $\mu_{\text{CRC}} = -0.5\sigma_{\text{NDB, INT-free}}$ would be needed to be clinically relevant. This value was estimated by assuming segmental values in the NDB follow a Gaussian distribution and determining amount by which this distribution would need to shift in order to double the number of normal segments that, by chance, result in a defect score ≥ 1 when the cut-off of $-1.5\sigma_{\text{NDB}}$ for defect scoring is used. Measures of myocardial intensity were quantified using non-directional Student's t-tests, performed on a segment-by-segment basis for each of the five PI segments at a $p \leq 0.05$ level, Bonferroni-corrected for 5 segments, leading to $p \leq 0.01$. Normalcy of myocardial intensity and comparison of delta values between categories was performed using unpaired t-tests assuming unequal variance.

Measures prior to correction

Because inclusion criteria identified scans using reference images relative to the clinical NDB, normal myocardial perfusion in PI segments from category A, B and C reference and pseudo-static images was evaluated before correction relative to $\text{NDB}_{\text{INT-free}}$ to demonstrate any changes in normalcy caused by the different NDBs or differences between reference and pseudo-static images. Scans in categories A and B were divided into rest and stress groups to allow use of the appropriate $\text{NDB}_{\text{INT-free}}$ state (rest/stress). The reference and pseudo-static images from stress scans paired with the category C (all rest) scans were also tested versus the $\text{NDB}_{\text{INT-free}}$. The DSC algorithm was applied to the pseudo-static images for all categories to measure any changes in interference severity relative to the reference images.

Measures post-correction

After correction, category A images were tested for normalcy versus $NDB_{INT-free}$ and their delta values tested versus zero and μ_{CRC} . Delta values for category B images were tested versus zero, μ_{CRC} and category A delta values. After correction, category C (rest) images were tested for normalcy versus $NDB_{INT-free}$ and their delta values tested versus zero, μ_{CRC} , category A and category B delta values. Delta values for category D images were tested versus zero, μ_{CRC} category A, B and C delta values. Interference severity after correction was also evaluated for category C and D images, via the DSC algorithm, and the proportion of scans with reduced and eliminated interference recorded.

4.3 Results

4.3.1 Manual VOI TACs

Figure 4-2 shows mean +/- standard deviation of TACs from manually sampled, well separated VOIs in the RV blood, LV blood, myocardium and stomach from 3 scans (1 with no interference but visible stomach, 1 with mild interference, and 1 with severe interference). Each scan shows significantly earlier uptake in the myocardium compared to the stomach, and blood TACs that have a much more rapid rise and fall in uptake compared to the myocardium and stomach; the RV blood peaks earlier than the LV blood.

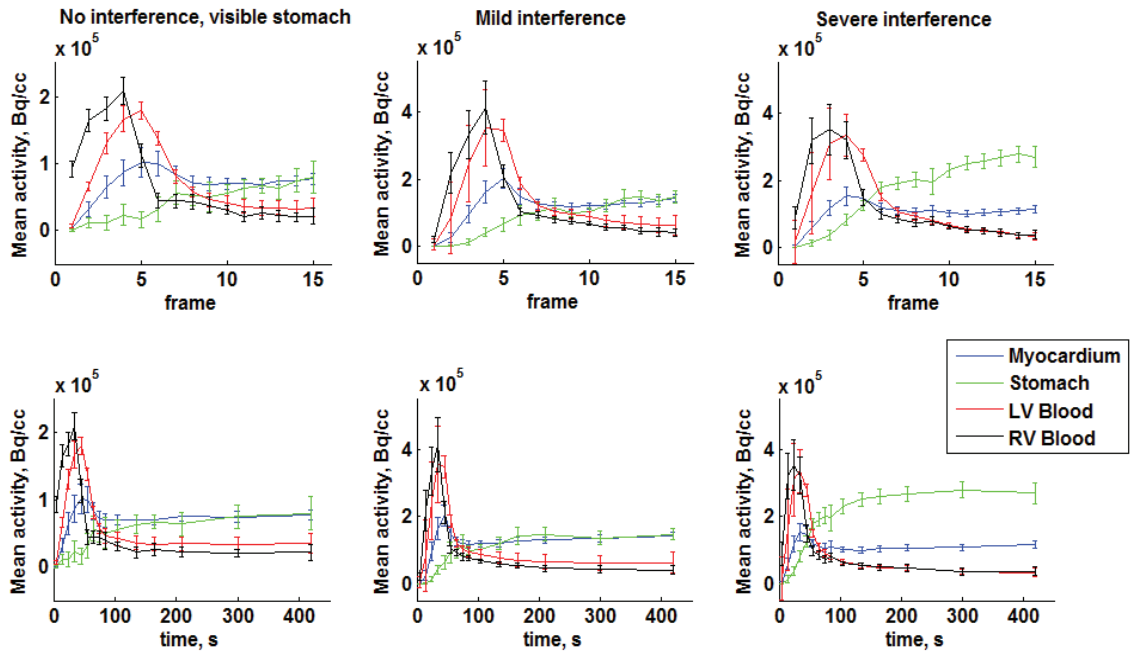


Figure 4-2. Manually sampled region of interest (VOI)-based time activity curves (TACs) for 3 example dynamic image series, all with visible stomach uptake. In the upper row, TACs are expressed as a function of dynamic frame number; in the lower row, as a function of the frame's central acquisition time. LV = left ventricle; RV = right ventricle.

4.3.2 FAMIS factors as basis functions and structures as coefficients

Figure 4-3 shows the results of applying FAMIS-MSO with an automatically selected number of factors to 6 example scans. The VOI is shown in the first column, outlined on pseudo-static SA image slices. The images following columns S1-S3 are the product of the pseudo-static images and the structures corresponding to the factor curves (F1-F3) shown in the far right column. The first scan was iteratively reconstructed, leading to one less time frame in factor curves. FAMIS resolved 2 factors in 3 of the six scans and 3 factors in the remaining 3 scans. When 2 factors were resolved, factor curves appeared

representative of blood/myocardial physiologic basis functions and the stomach is fully included in the same structure as the myocardium. When 3 factors were resolved, one factor curve appears consistently representative of physiologic blood (F3); while the remaining two factors curves appear to mix LV myocardium and stomach (F1) and RV myocardium and stomach (F2). This method of implementing FAMIS did not sufficiently isolate stomach intensity into a separate structure in any of the six scans.

When the FAMIS input parameters were varied, it was found that the best solutions were consistently reached when FAMIS was forced to resolve four factors using MSO and a FAMIS VOI threshold slightly lower than that which tightly encompassed the stomach, applied to all temporal frames. Figure 4-4 shows the best possible solutions for the examples of Figure 4-3. The second column of Figure 4-4 shows corrected images: the product of the pseudo-static image and the sum of all structures except that showing the greatest amount of isolated stomach, denoted by an asterisk (*). The remaining columns show structure images and factor curves.

None of the investigated variations in FAMIS input parameters was able to provide completely separate myocardial and stomach structures and physiologically realistic shapes for the basis functions of any of the six example scans. Although stomach could be partially isolated using FAMIS with four factors, none of the structures from the six example scans includes all stomach and excludes all myocardium and the factor curve shapes were not representative of independent myocardial/blood/stomach physiological basis functions and shapes suggested by the manual TACs.

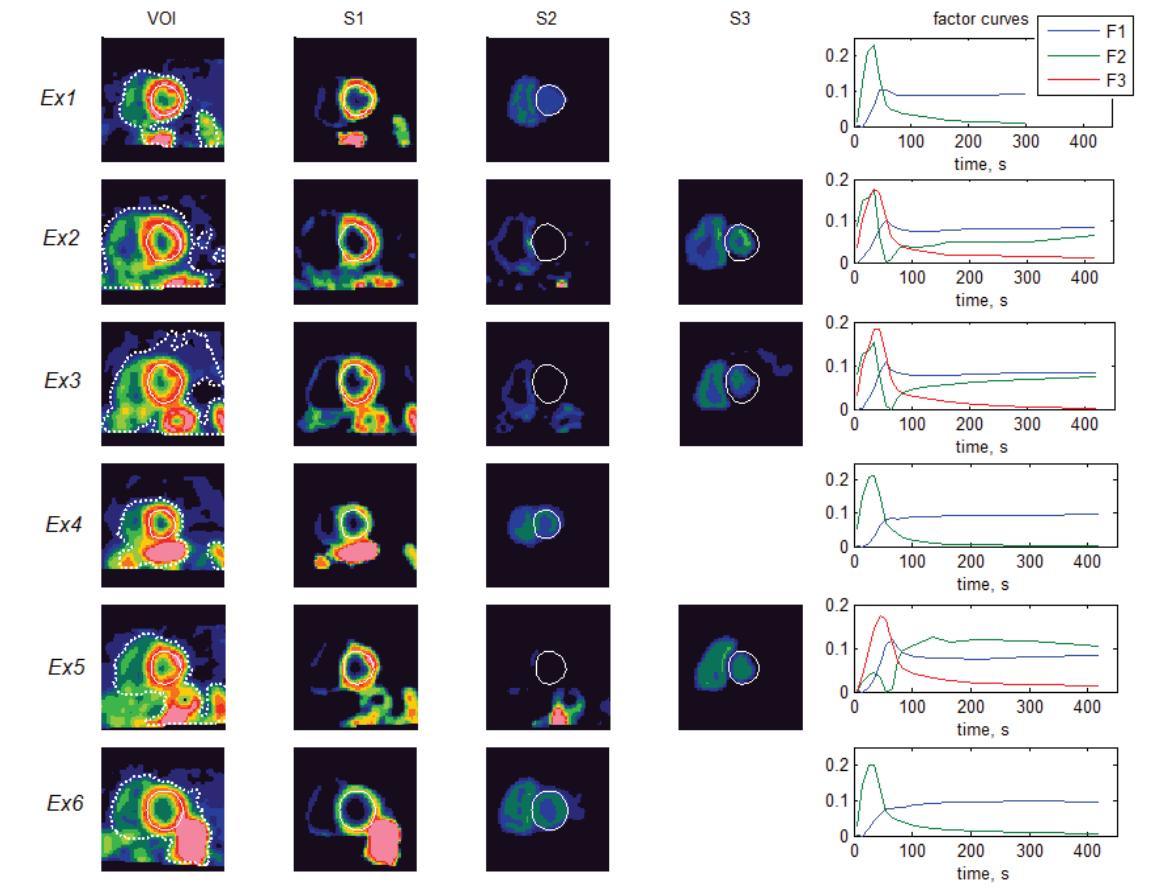


Figure 4-3. Implementation of FAMIS-MSO with an automatically determined number of factors on six example scans with visible stomach uptake. The first column shows the FAMIS VOI on pseudo-static SA image slices; columns 2 – 4 show the product of the pseudo-static images and structures, {S1, S2 and S3}, corresponding to the factor curves, {F1, F2 and F3}, shown in column 5. Ex2 and Ex6 are the no-interference, visible stomach and severe interference scans shown in Figure 4-2, respectively.

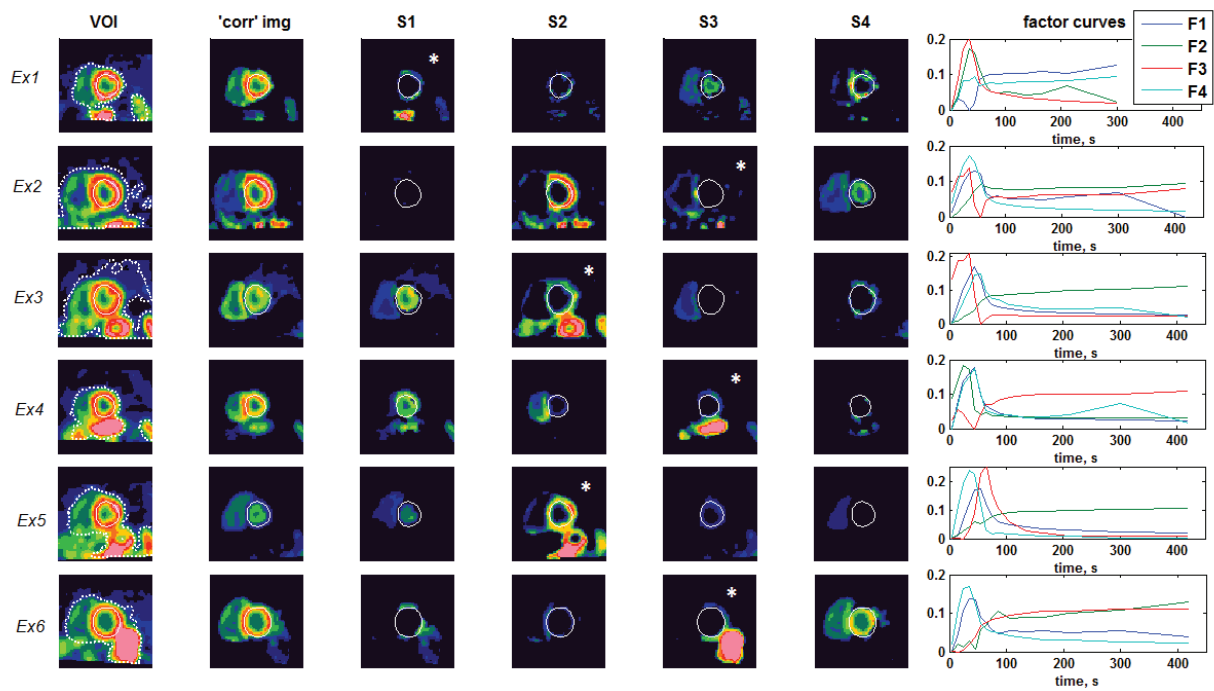


Figure 4-4. Implementation of FAMIS-MSO with four factors on example scans of Figure 4-3. The first column shows the FAMIS VOI on pseudo-static SA image slices; column 2 shows the 'corrected image': the product of the pseudo-static images and the sum of all structures except that attributed to the stomach (denoted *); columns 3 – 6 show the product of the pseudo-static images and structures, {S1, S2, S3 and S4}, corresponding to the factor curves, {F1, F2, F3 and F4}, plotted in column 5.

4.3.3 FAMIS myocardium and blood basis functions and VOI-TAC stomach basis function

Figure 4-5 shows FAMIS results on the Figure 4-3 example scans, limiting the VOI to exclude stomach and requiring resolution of 3 factors. This method shows consistent separation of LV blood, RV blood and myocardium into the 3 structures and the 3 factor curve shapes are physiological, with the exception of a small amount of noise in Example 2's myocardial factor curve. Of the 16 development scans, 10 produced physiologically realistic blood and myocardium shaped factor curves by this method. All 16 scans had sufficient stomach extent and imaging FOV to enable definition of interference-free, pure stomach VOIs for generating TACs.

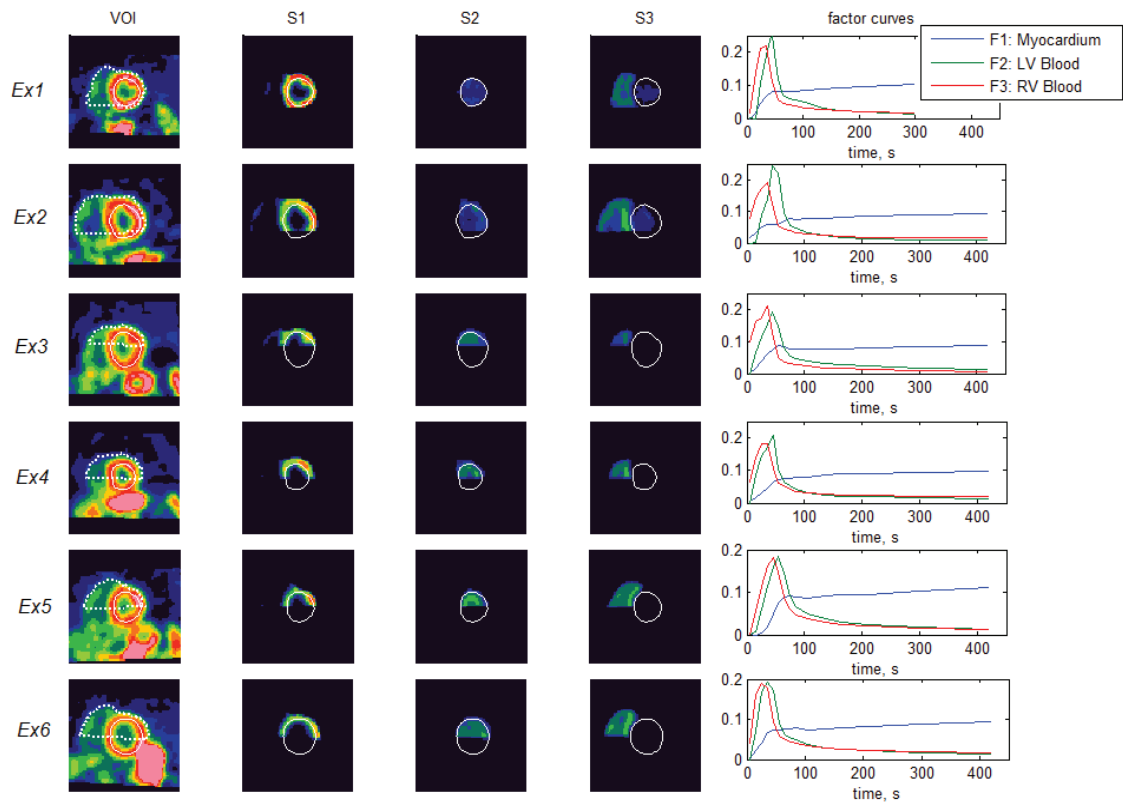


Figure 4-5. Application of FAMIS-MSO with 3 factors and a VOI excluding the stomach and interference regions to Figure 4-3 example scans. Pseudo-static SA image slices with the VOI delineated are shown in column 1, followed by structure images (columns 2 – 4) and corresponding factor curves (column 5).

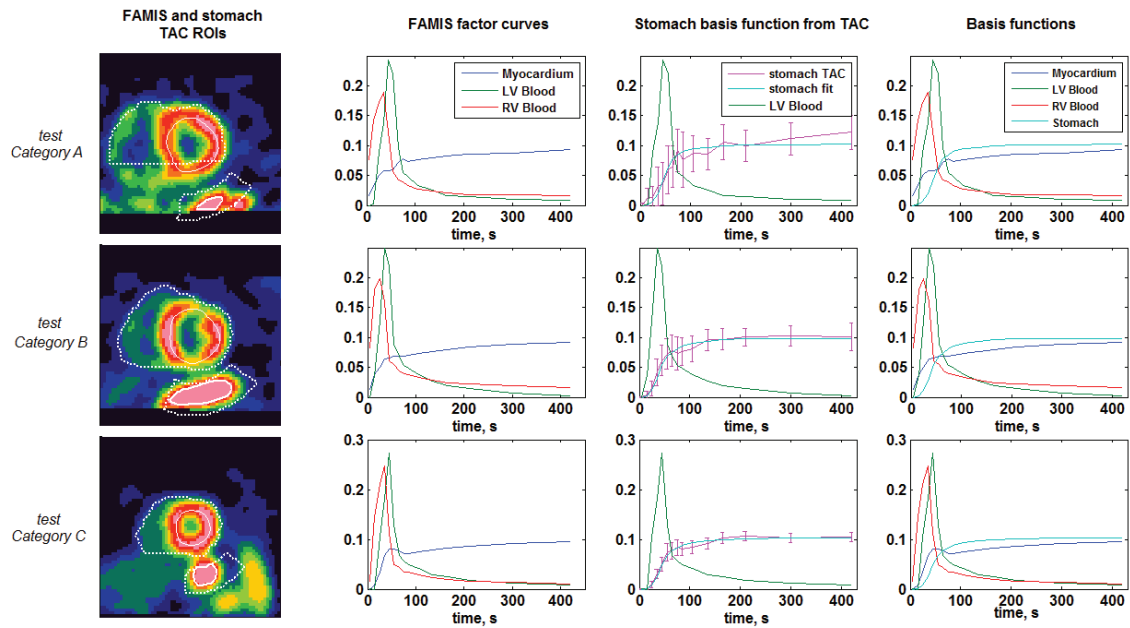


Figure 4-6. Basis functions derived using a combination of FAMIS with 3-factors and a VOI excluding stomach and VOI-TAC derived stomach basis function, shown for examples from the categories A, B and C development images. Column 1 shows pseudo-static SA image slices with the FAMIS VOI excluding stomach (upper dotted), the stomach search region (solid) and the stomach TAC-VOI delineated (lower dotted); column 2, myocardium, LV and RV blood factor curves from application of FAMIS-MSO with 3 factors and the VOI from column 1. Column 3 shows stomach VOI-TACs and TACs fit with a 1-compartment model using the LV blood factor curve and column 4 shows all four basis functions together. The category A and category C examples are the no interference, visible stomach and mild interference scans shown in Figure 4-2, respectively.

4.3.4 Reducing noise in basis functions

Figure 4-7 demonstrates the four methods of fitting factor curves and the stomach TAC-derived basis function to remove noise and produce more physiologically realistic basis function shapes. When blood curves were fit with gamma-variate functions, and

myocardium and stomach curves fit with 1-compartment models, realistic basis function shapes could be recovered for all 16 development scans.

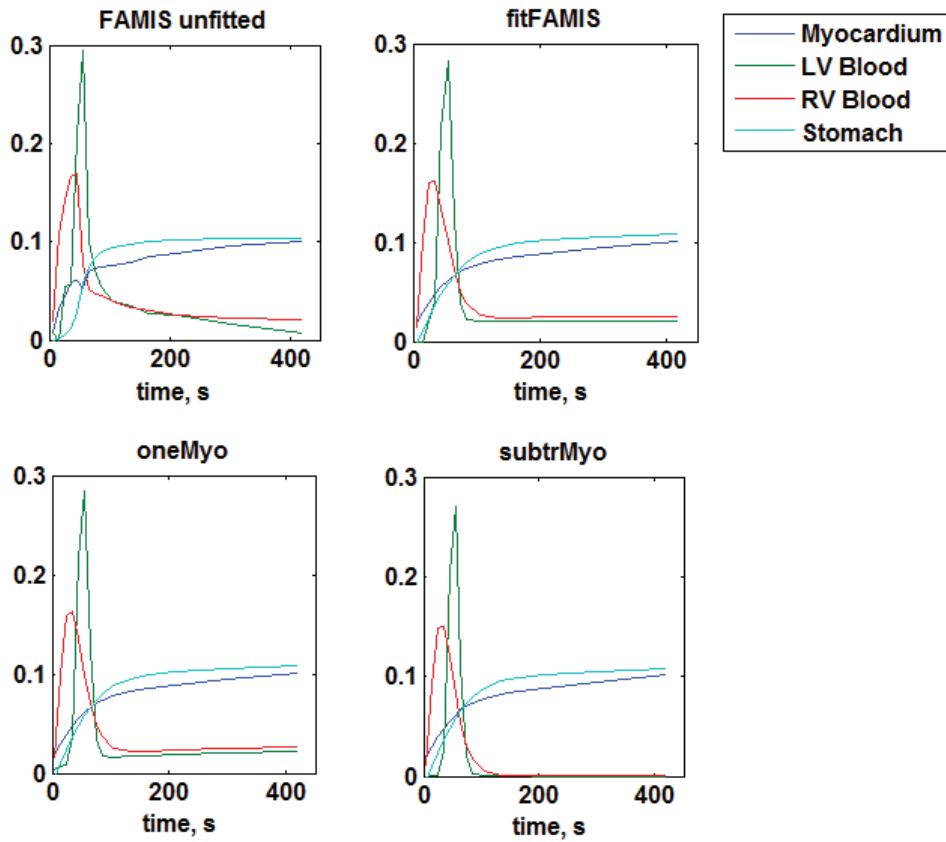


Figure 4-7. The four methods of fitting factor curves and the TAC-derived stomach function to remove noise and produce physiologically realistic basis functions.

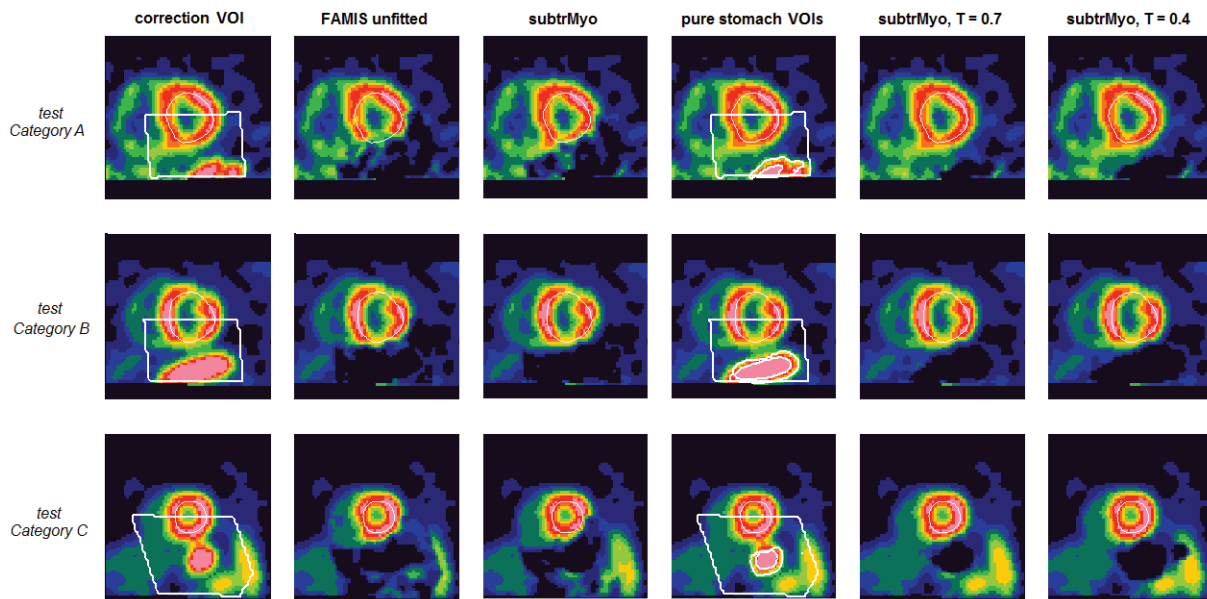


Figure 4-8. The results of four variations in the correction method for the three development image examples of Figure 4-6. The VOIs in column 1 show the area of the image selected for correction; the two additional VOIs in column 4 show the pure stomach region for the $T = 0.7$ and $T = 0.4$ thresholds. The correction methods which produced images in columns 2 and 3 did not constrain stomach fall-off and used the basis function fitting methods given; the correction methods which produced images in columns 5 and 6 constrained stomach fall-off to $\leq pc10$ (less than or equal to the upper 10% of coefficients of voxels closer to pure stomach) and used the basis function fitting and pure stomach threshold values given.

4.3.5 Evaluation of stomach fall-off conditions

Figure 4-8 demonstrates images corrected using the FAMIS unfitted and subtrMyo methods of basis function fitting without a stomach fall-off constraint (columns 2 and 3) as well as images corrected using the \leq pc10 fall-off constraint and subtrMyo basis function fitting, using two threshold levels for defining pure stomach, (columns 5 and 6; threshold values 0.7 and 0.4 of max stomach uptake respectively).

4.3.6 Interference-free normal databases

Figure 4-9 shows 17-segment polarmaps of the mean and standard deviation for $NDB_{INT-free}$. The standard deviation values for $NDB_{INT-free}$ are less than the clinical NDB (Kaster *et al* 2012) due to the combination of eliminating interference and using more strict summed score cut-off values for $NDB_{INT-free}$ (SSS and SRS \leq 2) versus clinical NDB (SSS \leq 4).

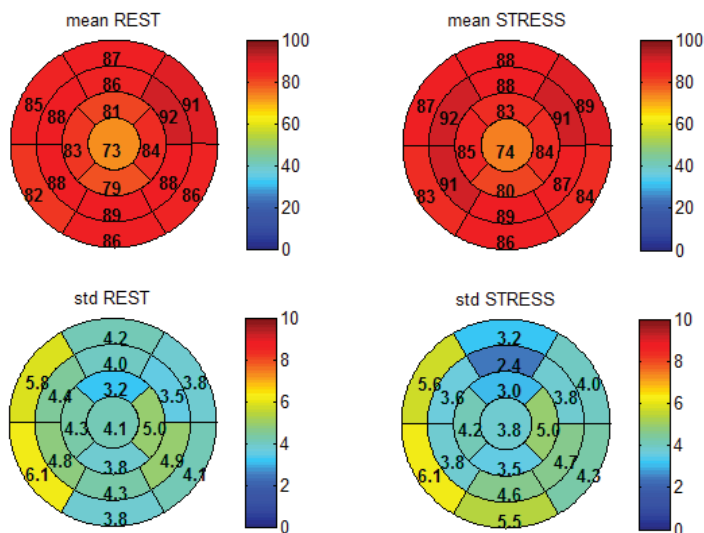


Figure 4-9. Interference-free physiological normal perfusion rest and stress databases, $NDB_{INT-free}$; units are maximum myocardial intensity, MMI.

4.3.7 Correction algorithm development

Without constraining stomach coefficient fall-off, all of the basis function fitting methods were found to eliminate interference from all development category C images. However, they were also found to increase perfusion defect severity in category A and B images and, in correcting Category C images, produced defect severities equivalent to abnormal perfusion. Columns 2 and 3 of Figure 4-8 show the result of correction using unfitted and subtrMyo-fitted basis functions without a stomach fall-off constraint.

Incorrect removal of myocardial intensity is especially apparent in category A, where the stomach does not cause interference and therefore myocardial intensity should remain unchanged.

When the stomach coefficient fall-off was constrained to less than the maximum or the mean of voxels closer to the pure stomach, increased perfusion defect severity was still found for the majority of category A and B images, as well as abnormal post-correction perfusion in the majority of category C images. Interference was eliminated from all category C images. When the stomach coefficient fall-off was constrained to the minimum, no increases in perfusion defect severity were found in category A or B images and post-correction perfusion in all category C images was normal; however, interference was reduced (eliminated) in only 4/5 (3/5) category C images.

When the stomach coefficient fall-off was constrained to less than the upper 25% and upper 10% of voxels closer to pure stomach, the majority of category A images did not show increased perfusion defect severity for any of the basis function fitting methods, while the majority of category B images did not show increased perfusion defect

severity only when the stomach coefficient fall-off was constrained to less than the upper 10%. In category C images, constraining the stomach fall-off to less than the upper 25% eliminated interference in all images when using the original basis functions, and in 4/5 images when using any of the other basis function fitting methods. Abnormal post-correction perfusion occurred in 2/5 or 3/5 images for all basis function fitting methods and interference. If stomach fall-off was constrained to less than the upper 10%, interference was eliminated/reduced in only 3/5 category C images for all basis function fitting methods while post-correction perfusion was not abnormal in any images when using the oneMyo method of basis function fitting, and was only abnormal in 1/5 images using the subtrMyo and original methods.

When a 0.4 threshold for pure stomach was substituted for the previous value of 0.7, constraining stomach fall-off to less than the upper 10% and using oneMyo basis function fitting, it was found that interference could be eliminated in all category C images while maintaining normal post-correction perfusion and, in category A and B images, perfusion defect severity was only increased in 1/6 category B images. Using the same method, but substituting the subtrMyo method for basis function fitting, it was found that interference could also be eliminated in all category C images while maintaining normal post-correction perfusion in all images but one and increased perfusion defect severity could be avoided in all category A and B images. Figure 4-8, column 4 demonstrates the pure stomach VOIs produced when using 0.7 and 0.4 as threshold values. Columns 5 and 6, of the same figure, demonstrate constraining

stomach fall-off to less than the upper 10% for the subtrMyo method of basis function fitting, for the 0.7 and 0.4 thresholds for pure stomach VOI definition, respectively.

In summary, the subtrMyo basis function and stomach fall-off less than the upper 10% methods combined with a 0.4 threshold for pure stomach VOI definition resulted in the best overall performance and were chosen as the final version of the correction algorithm and used for algorithm evaluation.

4.3.8 Correction algorithm evaluation

Normal perfusion in reference images from category A scans was unchanged in the majority of segments by use of pseudo-static images or the interference-free instead of the clinical NDBs: no significant differences were found between the rest and stress interference-free NDBs and rest and stress PI segments of the category A static or pseudo-static images before correction with the exception of segment 4 pseudo-static rest images.

Correction preserved normal myocardial perfusion: after correction, all category A rest and stress pseudo-static image PI segments, that were not significantly different from the interference-free NDBs before correction, remained not significantly different.

Abnormal perfusion was unchanged in the majority of segments from category B scans by use of pseudo-static versus reference images or the interference-free versus clinical NDBs: All category B rest and stress PI segments from reference and pseudo-static images were found significantly different than the rest and stress interference-free NDBs before correction, with the exception of stress segment 5. The frequency of abnormal perfusion in some segments of category B scans was higher than others. Some

segments did not show abnormal perfusion in enough of the scans to differentiate them from normal but still showed lower mean segment values: category B rest and stress PI segments from pseudo-static images were found significantly different than the rest and stress interference-free NDBs before correction in 3/5 segments. The mean category B, PI segment values before correction from both static and pseudo-static images were all lower than the corresponding NDB segment values.

Similar to category A scans, normal perfusion in reference images of category C paired stress scans was unchanged by use of pseudo-static images or the interference-free versus clinical NDBs: none of the PI segments of category C partner stress images, either reference or pseudo-static, were found significantly different than the stress interference-free NDB. The severity of ECI in category C rest scans was not sufficient to make their pseudo-static images differ from normal before correction and correction did not change this: category C rest pseudo-static images were not found significantly different than the rest interference-free NDB before or after correction.

Table 4-1 summarizes the changes in myocardial intensity due to the correction algorithm by giving delta mean \pm standard deviation values for all PI segments and all categories, as well as the results of t-test comparisons to an estimated mean clinically relevant change, $\mu_{\text{CRC}} = -0.5\sigma_{\text{NDB, INT-free}}$, and finally, comparisons between categories. No delta values (all PI segments and all categories) were found significantly different than zero. The correction algorithm was able to preserve both normal and abnormal myocardial intensity on a clinically relevant scale when ECI was not present: category A and B delta values are found significantly different than the mean clinically relevant

change, with mean PI segment delta values all less than μ_{CRC} . When ECI was present but mild, changes made to myocardial intensity by the correction algorithm were smaller than that considered clinically relevant in the majority of segments and were not larger than the changes seen when ECI was not present: category C delta values were found not significantly different than μ_{CRC} in 1 of the 5 segments, while the mean delta in the remaining 4 significantly different segments was less than μ_{CRC} . Category C delta values were also not found significantly different than category A or B differences. When more severe ECI was present, the changes made to myocardial intensity by the correction algorithm were still less than that considered clinically relevant but were larger than the changes seen when ECI was not present. They were not; however, larger than changes seen when ECI was present but mild. Category D delta values were found not significantly different than μ_{CRC} in any PI segments. Category D delta values were found significantly different than category A and B delta values, with the mean delta from category D exceeding categories A and B in all segments. Category D delta values were not found significantly different than category C delta values.

Table 4-1. Comparing the difference in myocardial segment values after minus before correction (delta) for the dynamic-based correction algorithm applied to the evaluation dataset.

Category	delta	segment 4	segment 5	segment 10	segment 11	segment 15
Category A n = 23	$\mu \pm \sigma =$	-0.04 \pm 0.07	-0.01 \pm 0.01	-0.02 \pm 0.04	-0.01 \pm 0.01	-0.01 \pm 0.01
	<u>Comparisons:</u> vs $\mu_{CRC} = -0.5$	p = 0.00* (A < μ_{CRC})				
Category B n = 16	$\mu \pm \sigma =$	-0.06 \pm 0.16	-0.02 \pm 0.02	-0.07 \pm 0.16	-0.02 \pm 0.02	-0.02 \pm 0.03
	<u>Comparisons:</u> vs $\mu_{CRC} = -0.5$	p = 0.00* (B < μ_{CRC})				
	vs μ Category A	p = 0.52	p = 0.37	p = 0.30	p = 0.54	p = 0.45
Category C n = 15	$\mu \pm \sigma =$	-0.08 \pm 0.17	-0.02 \pm 0.03	-0.05 \pm 0.11	-0.01 \pm 0.02	-0.02 \pm 0.05
	<u>Comparisons:</u> vs $\mu_{CRC} = -0.5$	p = 0.03	p = 0.00* (C < μ_{CRC})			
	vs μ Category A	p = 0.38	p = 0.74	p = 0.32	p = 0.96	p = 0.42
	vs μ Category B	p = 0.82	p = 0.73	p = 0.80	p = 0.68	p = 0.76
Category D n = 22	$\mu \pm \sigma =$	-0.27 \pm 0.66	-0.19 \pm 0.64	-0.28 \pm 0.90	-0.18 \pm 0.70	-0.25 \pm 1.05
	<u>Comparisons:</u> vs $\mu_{CRC} = -0.5$	p = 0.74	p = 0.64	p = 0.81	p = 0.66	p = 0.81
	vs μ Category A	p = 0.00* (D > A)				
	vs μ Category B	p = 0.00* (D > B)				
	vs μ Category C	p = 0.19	p = 0.22	p = 0.26	p = 0.28	p = 0.33

Histograms (Figure 4-10) of category D segmental delta values showed that the vast majority of category D scans showed little to no change in myocardial intensity as a function of correction with the exception of a single set of segmental delta values.

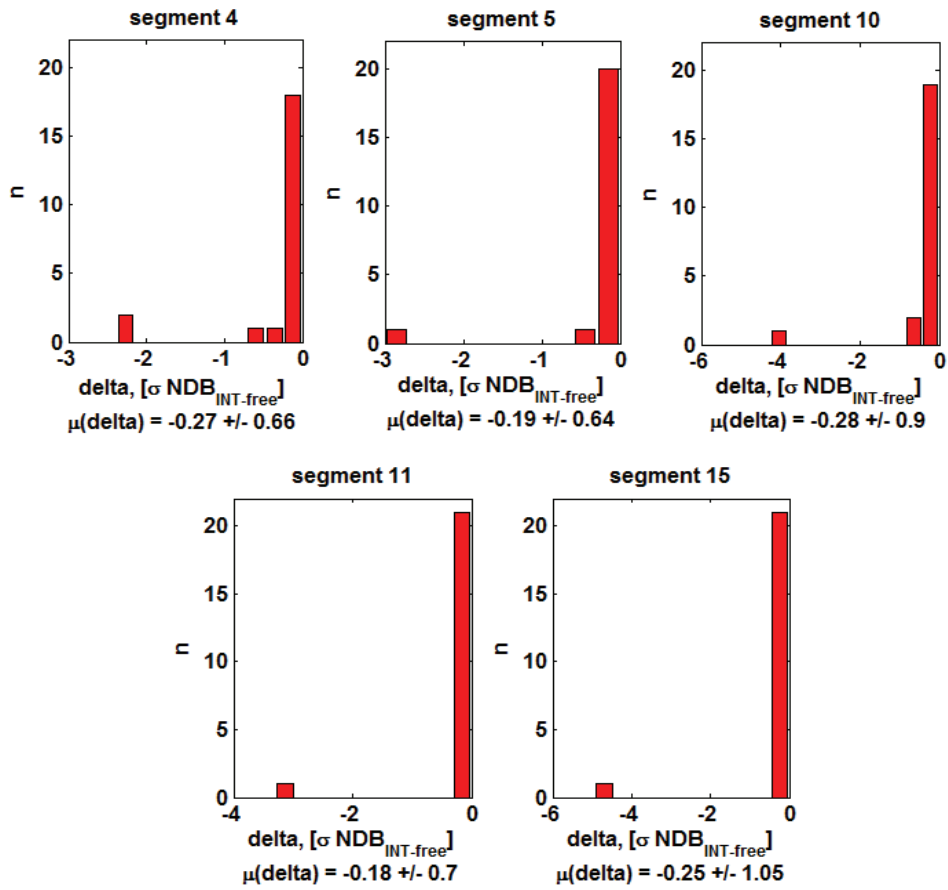


Figure 4-10. Histograms of delta values for the N = 22 category D evaluation dataset scans.

Visual examination of corrected images for all categories demonstrated that while the algorithm appeared to perform well in cases where little to no change in myocardial intensity was likely, (categories A, B and C); in cases of moderate – severe interference (category D), the algorithm was observed to terminate the stomach subtraction

prematurely in the majority of cases, Figure 4-11a. The set of large category D segmental delta values were found to originate from a single outlier scan, whose myocardial basis function was non-physical (did not pass through the origin at time zero), Figure 4-11b. Review of all other category D scan basis functions revealed this was an isolated case and Table 4-2 gives revised evaluation category D delta results when this scan was removed from the dataset.

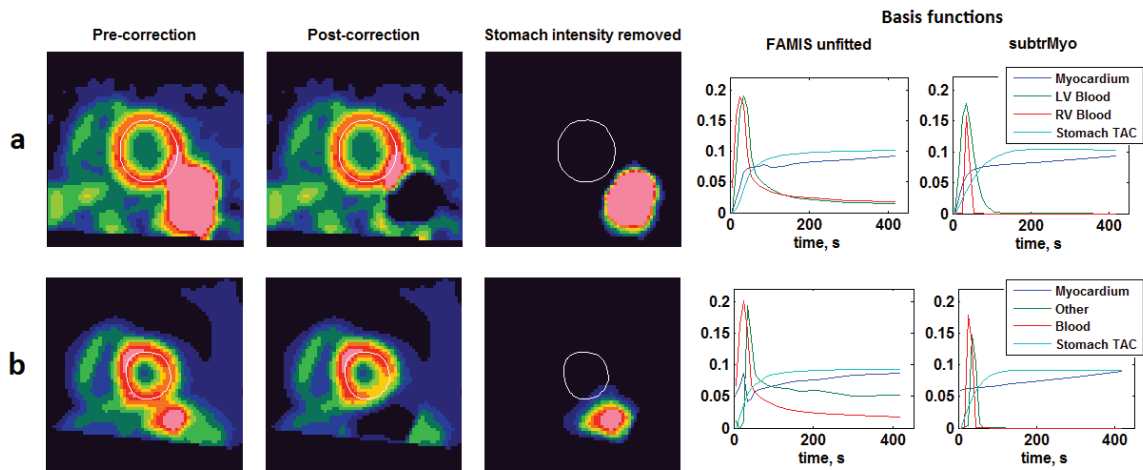


Figure 4-11. Examples demonstrating the two types of correction algorithm failure on category D images. Type (a), first row, is the more common failure where factor curves appear physiologically realistic but myocardial intensity is unchanged by correction; while type (b), second row, is the isolated case where factor curves and resulting basis function fits are non-physiologic and myocardial intensity is greatly reduced by correction.

Once the population was revised by removal of the outlier scan, application of the correction algorithm to scans with more severe ECI was found to produce changes in myocardial intensity less than the clinically relevant change and no larger than changes

seen when ECI was present but mild, or not present. The revised category D delta values were now found significantly different than μ_{CRC} in all PI segments except one and all mean category D delta values were less than μ_{CRC} . Revised category D delta values were no longer found significantly different than category A and B delta values. Revised category D delta values remained not significantly different than category C delta values.

Table 4-2. Revised category D delta values and comparisons for the dynamic-based correction algorithm applied to the evaluation dataset after exclusion of one category D scan exhibiting a non-physiologic myocardial basis function.

Category	delta	segment 4	segment 5	segment 10	segment 11	segment 15
Category D n = 21	$\mu \pm \sigma =$	-0.17 \pm 0.47	-0.05 \pm 0.09	-0.09 \pm 0.15	-0.03 \pm 0.05	-0.02 \pm 0.05
	<u>Comparisons:</u>					
	vs $\mu_{CRC} = -0.5$	p = 0.50	p = 0.00* (D < μ_{CRC})	p = 0.01* (D < μ_{CRC})	p = 0.00* (D < μ_{CRC})	p = 0.00* (D < μ_{CRC})
	vs $\mu_{Category A}$	p = 0.20	p = 0.07	p = 0.06	p = 0.15	p = 0.38
	vs $\mu_{Category B}$	p = 0.33	p = 0.12	p = 0.67	p = 0.27	p = 0.84
	vs $\mu_{Category C}$	p = 0.40	p = 0.09	p = 0.42	p = 0.19	p = 0.90

4.3.9 Using a kinetic model to define mean and variance of blood-free myocardial and stomach basis functions

Figure 4-12 demonstrates the mean voxel measured TACs input to FlowQuant's 1-compartment kinetic model and the corresponding KM-predicted blood, myocardial, and stomach TACs that result. TACs and AUC-normalized basis functions are shown for the three dynamic image series used initially to find the manual TACs in Figure 4-2. The

AUC-normalized KM-predicted basis functions show there is actually no significant difference between the blood-free myocardium and stomach curve shapes when the variance is taken into account.

4.4 Discussion

The study by Sitek et al. (Sitek *et al* 2002a) suggested that the differences in temporal uptake between myocardium and extra-cardiac uptake (liver) in ^{99m}Tc -teboroxime SPECT MPI were large enough for factor analysis of dynamic sequences penalized by minimal spatial overlap (PLS-FADS, or FAMIS MSO) to correct extra-cardiac interference by resolving the majority of myocardium and extra-cardiac uptake into separate basis functions. When VOI-based TACs were manually sampled from ^{82}Rb PET MPI, the observed differences in temporal uptake between myocardium and extra-cardiac uptake (stomach) were of similar magnitude to those shown in Sitek et al. However, when FAMIS-MSO was applied to ^{82}Rb PET, it was found that this method alone could not separate myocardium and stomach into separate factor curves/structures or reliably produce factor curves with shapes representative of the four known underlying physiological structures. By excluding stomach and ECI-affected myocardium from the FAMIS VOI, myocardium and blood factor curves could be reliably defined via FAMIS-MSO and all images examined were found to have sufficient inferior FOV that pure-stomach VOIs and TACs could be produced.

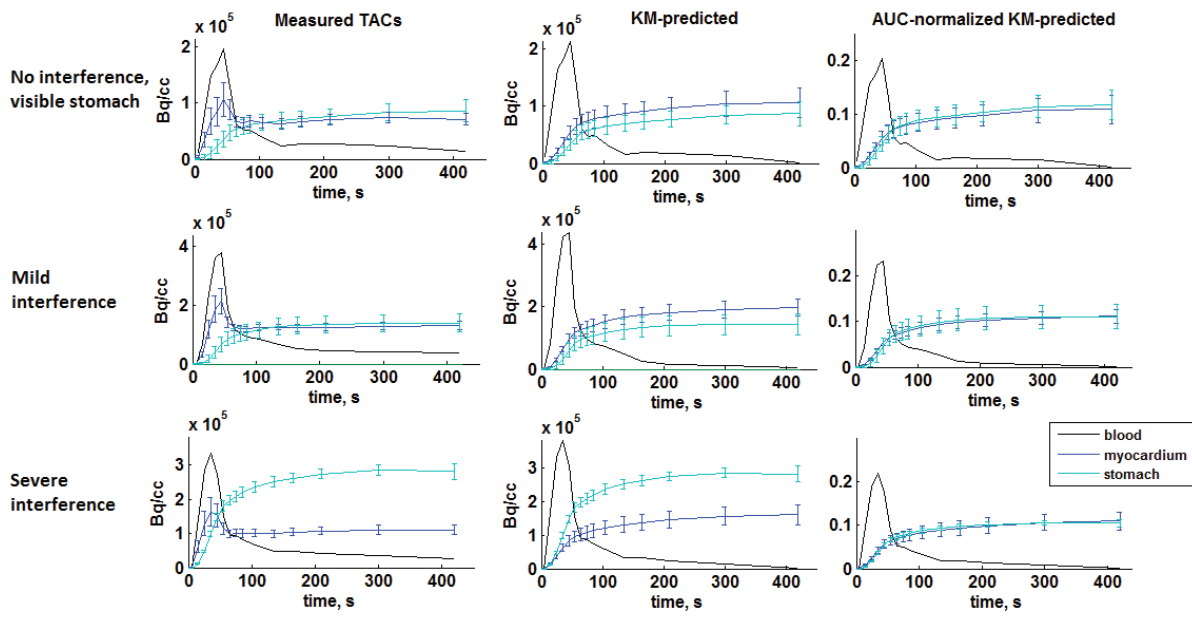


Figure 4-12. FlowQuant (Klein *et al* 2006) voxel-based 1-compartment kinetic modeling of measured TACs to evaluate uncertainty on resulting basis functions (AUC-normalized KM-predicted curves). The examples shown are the {No interference, visible stomach; mild interference; and severe interference} scans from Figure 4-2.

By converting the stomach TAC to a pseudo-factor curve via AUC normalization and reducing noise in factor curves with fits to known physiologically shaped functions, four separate basis functions could be produced representing the blood (RV and LV), myocardium and stomach. However, when voxel-based TACs from the region of the image suffering from interference were fit as a linear combination of these four basis functions and corrected images produced as the sum of structures excluding the extra-cardiac uptake (stomach), summed defect scores were increased in images which did not exhibit interference prior to correction. Myocardial intensity was reduced in images where this was not expected. As a result, additional information was incorporated into fitting the basis function coefficients: the region of the image known to be purely occupied by stomach was identified and the value of stomach basis function coefficients required to fall-off (decrease) with distance from this region.

To compare results of images corrected using multiple methods for fitting basis functions and constraining stomach coefficient fall-off, a framework was created for developing and evaluating the results of correction, based on testing the ability of the algorithm to preserve myocardial intensity in the absence of interference and to change myocardial intensity, on a potentially clinically relevant scale, when correcting interference. It was found that despite the ability to define factor curves with apparent differences between the myocardium and stomach, none of the investigated methods for combined basis function fitting and stomach fall-off constraint could simultaneously correct images with all levels of interference severity and minimize increases in image defect severity for images without interference prior to correction.

By using a full 1-compartment kinetic model, incorporating correction for partial voxel occupancy and spill-over, blood-free myocardium and stomach basis functions with uncertainties were examined and it was demonstrated that, without blood contamination in the myocardium, there was no significant difference between the two. Comparison to the FAMIS MSO factor curves and VOI-based TACs showed that the blood contamination in the myocardium TACs and factor curves is likely the source of the apparent difference between the dynamic myocardium and extra-cardiac uptake signals.

Examining Sitek et al. (Sitek *et al* 2002a) more closely, it is hypothesized that their myocardial factor also contains some blood, that their extra-cardiac (liver) factor contains some myocardium and that it is the magnitude of blood contamination in the myocardium factor that preserves the myocardium. Sitek et al. do not show the factor curves produced by PLS-FADS, only the structure images in which the mixing is not clear; however, the hypotheses are motivated by the fact that they report conserving myocardial uniformity not uptake for normal myocardium and also report increased contrast for abnormal myocardium. Abnormal myocardium is likely to experience reduced perfusion resulting in lower structure values for the myocardium-blood mixed factor and higher structure values for the stomach-myocardium mixed factor. Because of the relative reduction in blood in abnormal versus normal myocardial areas, more image intensity is attributed to the stomach-myocardium mixed structure and therefore subtracted, increasing contrast.

Regardless of factor mixing, we were unable to find an implementation of FAMIS-MSO that separated the majority of uptake and, visually, maintained myocardial uniformity to replicate the results of Sitek et al. (Figure 4-4). It is possible that this is due to differences in the FAMIS VOIs input to factor analysis; factor analysis is known to be highly dependent on initialization conditions. However, it is also possible that the technique of Sitek et al. may not generalize accurately to a larger patient population, as they reported results for only one canine and two patient scans.

By adjusting the FAMIS method used to define the VOI, it may be possible to replicate Sitek's results with FAMIS-MSO and ^{82}Rb PET MPI, but it is important to note that the meaning of intensity in the resulting images is likely not the same as the original MPI and is more reflective of the overall amount of blood signal co-located with myocardium than the amount of tracer taken up from the blood into the myocardial cells. In addition, it is expected that noise in the remaining fractional myocardial signal may be amplified to the point of causing apparent mild defects. Lack of blood in the stomach factor is explained by the combination of spatial separation from large vasculature (heart cavities and aorta), minimizing image resolution-based spillover, and the fact that the stomach does not have the same level of vasculature as the myocardium, minimizing partial voxel occupancy.

A useful correction algorithm needs to be accurate, robust and reliable, i.e. applicable to the population at large. Evaluating accuracy requires an independent measurement of true myocardial perfusion. The gold standard for evaluating cardiac perfusion is invasive coronary angiography, (CA); however, CA is not currently available for the scans used in

this work. Simulation is an alternative often employed when clinical measures of truth are lacking but is most useful only when all aspects with significant impact on the problem at hand can be quantified and replicated. If this is not the case, there is a risk of developing a solution that is not applicable to the population. Simulation was not employed in this thesis since some of the most important components contributing to extra-cardiac interference (stomach shape, size, location, motion) were unknown; decreasing the likelihood that this method would produce a solution widely applicable to clinical images. As a result, this chapter builds a body of evidence which, although not capable of providing a direct, quantitative measure of accuracy, produces a solid foundation for directing and evaluating correction algorithms based on their performance in selected datasets. The behaviours expected of an ECI correction algorithm are: the ability to reduce/eliminate interference, as well as to preserve and to change myocardial intensity when appropriate, for both normally and abnormally perfused myocardium. The remaining, unavailable measure is the ability to change myocardial intensity by the correct amount. Chapter 6 discusses the type of prospective study that would allow quantitative validation of ECI correction algorithm accuracy. The results of this chapter demonstrate that differences between physiologic time-dependent uptake of ^{82}Rb in pure stomach and pure myocardium are insufficient to allow differentiation between the two. Results further demonstrate that previous methodology likely relied on blood contamination in the PLS-FADS derived myocardial factor to preserve the fraction of the myocardial image intensity in proportion to the local blood fraction.

4.5 Conclusion

When uncorrected for blood contamination, myocardial and extra-cardiac uptake kinetics, found either by manual VOI-based TACs or by minimum-spatial overlap factor analysis, can be shown to produce different TACs and factor curves for ^{82}Rb PET MPI scans. Extra-cardiac signal from the stomach appears to have a significantly later rise time than the myocardial signal. However, using kinetic modeling with a 1-compartment model and RC/TBV correction, it was found that this apparent difference is likely due to contamination of the myocardial signal with blood. When physiologically realistic, independent basis functions (where myocardium is blood-free) are fit for voxel-based coefficients, the myocardial-stomach factor differences are insufficient to both remove ECI when present and avoid increasing defect severity in images without ECI prior to correction. An alternate approach to interference correction is, therefore, required.

5 Chapter: 1D convolution-based correction

5.1 Introduction

This chapter proposes a correction algorithm that works directly on the static ^{82}Rb PET images used for MPI interpretation. The algorithm considers the 3D image as a series of independent SA slices and, like the PVE correction proposed by Gambhir (1992)(section 1.4.1), models the structures in the image (myocardium and stomach) by fitting a series of 1D radial profiles, extracted from the SA slice image, to the convolution of rectangular functions with a 1D Gaussian function. The rectangular functions represent the myocardium and stomach and the Gaussian function represents the combination of the scanner PSF and the effects of motion. By removing the fitted stomach rectangular function, a corrected image can be recovered. This method's potential is demonstrated on a set of clinical images and is shown to preserve myocardial uptake where appropriate, be able to change myocardial activity by a clinically relevant amount when correcting moderate-severe ECI and provide a visually acceptable correction in >90% of the 37 cases of ECI examined.

Extra-cardiac interference can be considered mixing of the signals from two different sources. Unlike the blood and the myocardium, the source of ECI (the stomach) is physically separated from the myocardium. Thus, in the absence of motion, the interference is caused by the limited spatial resolution of the camera. The point-spread function (PSF) of the PET camera can be approximated by a simple Gaussian function. Periodic motion (such as from cardiac and respiratory motion) blurs the distribution of

activity and the effects of this motion can also be approximated by a convolution with a Gaussian function. Therefore, it may be possible to model the PET myocardial image as distinct myocardium and stomach activity which has been blurred together through convolution with a Gaussian kernel.

We hypothesize that ECI can be corrected in static ^{82}Rb PET images by fitting radial profiles through the myocardium to a simple 1D model that is convolved with a 1D Gaussian PSF, where the fit is guided by information from interference-free regions of the image. Corrections for PVE and spillover using simple models of the underlying activity distribution and modulation transfer function, i.e. 1D rectangular functions convolved with 1D Gaussian blurring kernels, have been applied previously to recover myocardial activity in the presence of LV blood pool and low, uniform background (Gambhir 1990, Porenta *et al* 1995, Dumouchel 2011). In this chapter we propose expanding this approach to include a second rectangular function which models stomach activity in 1D radial profiles extracted from static ^{82}Rb SA image slices. A within-slice model of the interference-free myocardial wall is developed and incorporated to improve initialization and apply constraints to the model fitting.

5.2 Methods and materials

5.2.1 Scan acquisition, image reconstruction, LV processing and 1D profile extraction

The static reference images that were acquired and reconstructed as described in section 2.2.1 are used as the starting point for this approach. They were re-oriented to the LV reference frame and the LV located using FlowQuant software. 1D profiles were then extracted from the 2D SA slices of the LV-oriented images using 2D interpolation at 1 pixel-width increments along lines extending radially out from the LV axis. Profiles were generated at five degree intervals. Two angular regions were defined for profile sampling: an interference-free region in the anterior/anterior-lateral myocardial wall, from 0° - 90° CW (where 0° = mid-anterior), and the interference-search region defined in Chapter 2 (section 2.3.2) from 90° - 200° CW, Figure 5-1. The location of the LV myocardium, determined by FlowQuant, and the LV radius (equal to the radial distance between the LV axis and myocardium) were used, respectively, to initiate profile sampling (place the origin) and to set the profile extent to 1.5x(LV radius) inward and twice the LV radius outward (for profiles in the interference-free region) or 40mm outward (for profiles in the interference-search region)(Figure 5-1). The inwards extent of the profile was chosen to be greater than the LV radius to ensure the blood pool minimum was included during the initialization phase of the algorithm and the location of the LV myocardium was used as the origin (reference point) of the profile instead of the LV axis since LV radii were not equal for all angles.

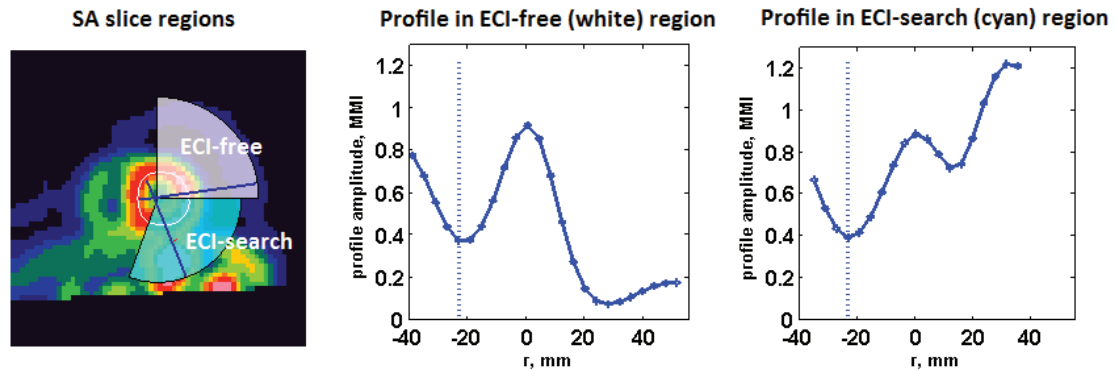


Figure 5-1. The interference-free (ECI-free) and interference-search (ECI-search) regions along with example 1D profiles as extracted from each region. The vertical line on the profiles demonstrates the inwards extent where profiles will be truncated during initialization prior to modeling (section 5.2.4).

5.2.2 Datasets

The same datasets were used for algorithm development and evaluation as were used in Chapter 4 (sections 4.2.6 and 4.2.7). In addition, to determine the algorithm’s failure rate and execution time, an additional dataset of 150 scans with interference was chosen from the Jan 2011 – Dec 2012 dataset. Scans were evenly distributed between rest and stress states, as well as mild, moderate and severe interference severity, as determined by the DSC algorithm.

5.2.3 Algorithm summary

The correction algorithm treats each 2D SA slice separately and each profile extracted from the image was fit independently. The *myocardium-only* model was used to fit all 1D profiles from the interference-free region. This model has 6 parameters that describe a single rectangular function bounded by two separate backgrounds, convolved with a 1D Gaussian function (Figure 5-2). Once all profiles from the interference-free region of

a SA slice were fit, the mean and 95% confidence interval for each parameter of the myocardium-only model was determined, characterizing the myocardium, in the absence of ECI, for that slice (Figure 5-3). Only parameter values from profiles which successfully completed fitting with goodness-of-fit ($R^2 \geq 0.97$) were included in this calculation.

For each profile from the interference-search region, an attempt to fit the myocardium-only model is first used as a method for determining whether or not extra-cardiac uptake exists at this angle. When fitting a profile from the interference-search region with the myocardium-only model, the mean and 95% confidence intervals on the model parameters, derived from the interference-free region, are used to initialize and constrain (via upper and lower bounds) the fit. If optimization fails or if the goodness-of-fit R^2 is ≤ 0.94 then the profile is passed to a second model: the *myocardium-stomach* model.

The myocardium-stomach model adds a second rectangular function to the myocardium-only model to represent the stomach. This adds three parameters to the six pre-existing myocardium-only model parameters (Figure 5-4). When fitting the myocardium-stomach model, the myocardium-only model parameters remain initialized and constrained by the interference-free region-derived mean and 95% confidence intervals. Two goodness-of-fit criteria are used to evaluate the results of the myocardium-stomach model. For a profile to show an acceptable fit the myocardium-stomach model fit was required to have an $R^2 \geq 0.8$ and the maximum difference between the measured and fit values inside the myocardium region was not permitted

to exceed 7.5%. All fitting was done using non-linear least squares. Profiles which failed during initialization, execution of the fitting routine, or by the fit not meeting goodness-of-fit criteria, were marked as having failed.

Once parameter values were fit for all of the interference search region profiles, the profiles fit with the myocardium-stomach model were used to identify the (angular) regions of the SA slice requiring interference correction. Parameter values from all interference search region profile fits were then smoothed using a (normalized) $1/\text{distance}^2$ -weighted 5-point filter to eliminate abrupt, non-physical transitions and cope with isolated profile fitting failures. For this purpose, the stomach parameters of the profiles fit with a myocardium-only model were set to zero.

To produce the corrected image, model parameter values specific to each voxel in the correction region were determined using a $1/\text{distance}^2$ -weighted average from the 4 closest profiles – 2 on either side of the voxel. The myocardium-only component of the model (i.e. omitting the stomach) was then used to estimate the corrected voxel value based on the radial distance of the voxel from the myocardium. Corrected voxel values were substituted into the SA slice and the process repeated for all voxels within the given slice and then for all slices within the 3D image. To produce an image of the subtracted stomach intensity, the same process was repeated using just the stomach component of the model (i.e. setting myocardial and background amplitude parameters to zero).

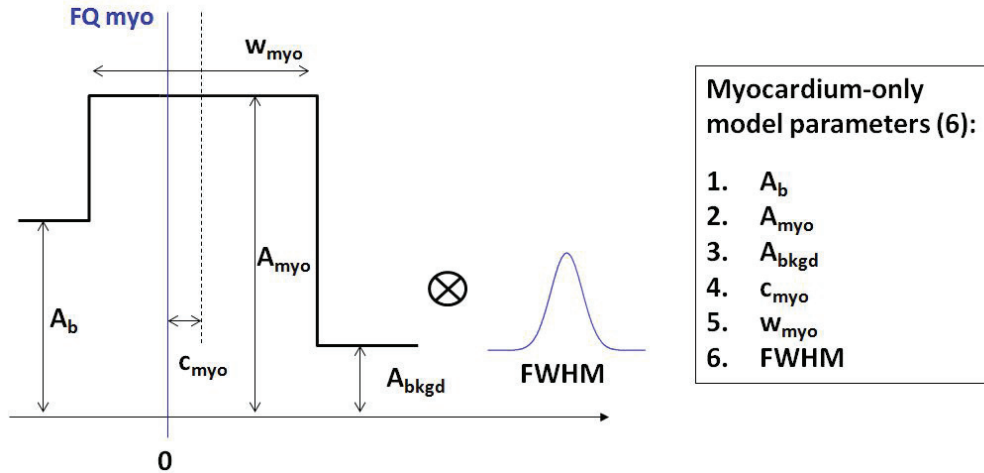


Figure 5-2. Myocardium-only model and parameters, where: A_b , A_{myo} , and A_{bkgd} are the blood, myocardium and background amplitudes, respectively, and c_{myo} and w_{myo} are the myocardium centre location and width and FWHM is the full width at half maximum of a 1D normalized Gaussian PSF.

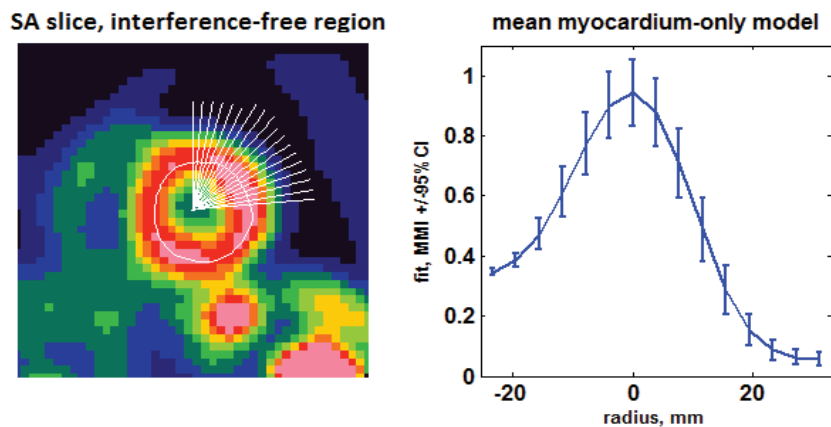


Figure 5-3. Development of the mean and 95% confidence myocardium-only model from the interference-free region of a SA slice: (a) interference-free profiles and (b) mean \pm 95% myocardium-only model.

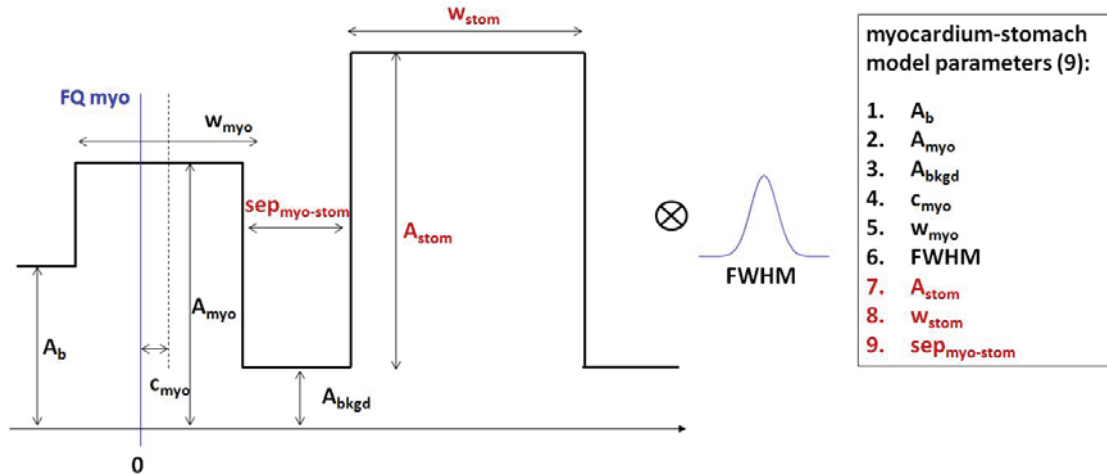


Figure 5-4. Myocardium-stomach model and parameters, where: A_b , A_{myo} , and A_{bkgd} are the blood, myocardium and background amplitudes, c_{myo} and w_{myo} are the myocardium centre location and width, FWHM is the full width at half maximum of a 1D normalized Gaussian PSF, A_{stom} and w_{stom} are the stomach amplitude and width and $sep_{myo-stom}$ is the radial separation/distance between the outer wall of the myocardium and the inner wall of the stomach.

5.2.4 Myocardium-only model in the interference-free region

The six parameters of the myocardium-only model are shown in Figure 5-2. For profiles in the interference-free region, parameter values were initialized and upper and lower bounds set as given in Table 5.1. Following initialization, the inner extent of profiles was truncated at the location of the minimum profile value for radii less than the FlowQuant-defined LV myocardium (location of $A_{b,i}$). Model parameters were then fit for all measured profiles from the interference-free region using a subspace trust-region algorithm based on the interior-reflective Newton method (Coleman and Li 1996, 1994) to evaluate non-linear least squares. The coefficient of determination (R^2) was used as the measure of goodness-of-fit and $R^2 = 0.97$ was used as the minimum acceptable fit.

Table 5-1. Initialization and bounds of myocardial-only model parameters, applied when fitting profiles from the interference-free region. r = profile radial location; $r = 0$ at the FlowQuant-determined LV myocardium, $r < 0$ inwards (blood pool), $r > 0$ outwards.

Model parameter	Initialization value	Lower bound	Upper bound
myocardial amplitude, A_{myo}	$A_{myo,i} = \max(\text{profile})$	0	$2 \times A_{myo,i}$
width of the myocardium, w_{myo}	$w_{myo,i} = 10 \text{ mm}$	0	$\text{length}(\text{profile}) * 3.9 \text{ mm}$
shift of myocardium centre, c_{myo} , relative to FlowQuant-defined location	$c_{myo,i} = 0$	$c_{myo,i} - w_{myo,i}$	$c_{myo,i} + w_{myo,i}$
inner background amplitude, A_b	$A_{b,i} = \min(\text{profile}(r < 0))$	0	$A_{myo,i}$
outer background amplitude, A_{bkgd}	$A_{bkgd,i} = (\text{profile value of the region outside the myocardium } (r > w_{myo,i}/2) \text{ where the gradient is minimized})$	0	$A_{myo,i}$
Gaussian PSF FWHM	$\text{FWHM}_i = 14 \text{ mm}$	3.9 mm (1 pixel width)	$2 \times \text{FWHM}_i$

5.2.5 Myocardium-only and myocardium-stomach models in the interference search region

Myocardium-only model

When fitting the myocardium-only model to profiles from the interference-search region, all parameter values except A_{myo} and c_{myo} were initialized and upper and lower bounds set to the mean and 95% confidence intervals from the interference-free region.

The myocardial amplitude, A_{myo} , and centre, c_{myo} , were initialized to the profile value and location of the FlowQuant-determined LV myocardium. Their bounds were the same as those used to fit the myocardium-only model in the interference-free region.

The extent of sampled profiles was reduced to the mean inner and outer extent of profiles from the interference-free region prior to fitting. R^2 was used as the goodness-of-fit criterion for the myocardium-only model when applied in the interference-search region. The minimum required R^2 value was determined by visual examination of the fitted model superimposed on the measured profiles from the category A, B and C development images (4.2.6) and was set to $R^2 = 0.94$. For the category C images, profiles passing/failing the R^2 criterion were also displayed on 2D SA image slices showing the result of the DSC algorithm from Chapter 2 to visually evaluate where interference was being detected or rejected by the myocardium-only model R^2 (Figure 5-5).

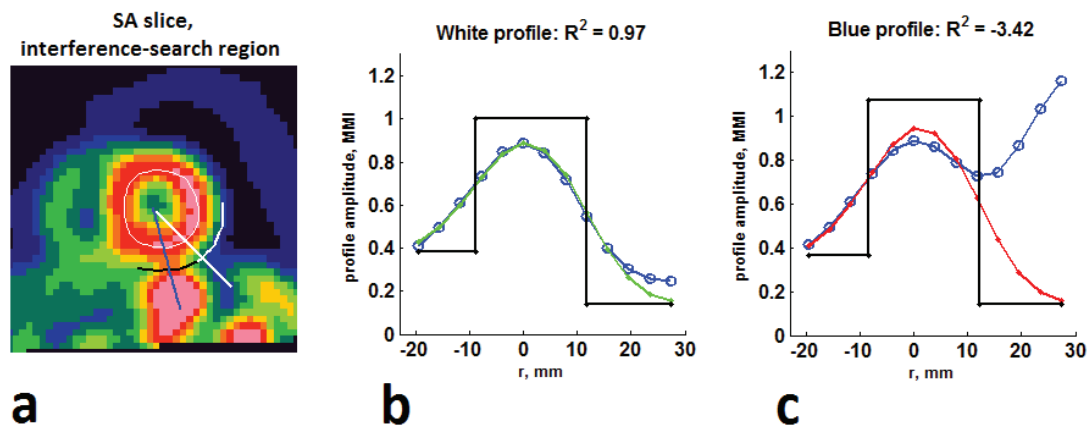


Figure 5-5. Example of information used to visually evaluate the appropriate value for the coefficient of determination (R^2) when the myocardium-only model is applied in the interference-search region. The locations of the two profiles (b, no interference, white profile and c, with interference, blue profile) as well as the results of the DSC algorithm are displayed on the SA slice (a).

Myocardium-stomach model

When fitting the myocardium-stomach model to profiles from the interference-search region, the six myocardium-only parameters were initialized and constrained in the same way as the myocardium-only model. To cope with the variety of profile shapes caused by elevated stomach intensity, a sequential initialization process was required for the remaining stomach parameter values: A_{stom} , w_{stom} and $\text{sep}_{\text{myo-stom}}$. The stomach amplitude, centre location and width are estimated and the centre location and width values are then combined with the myocardium centre location and width to calculate $\text{sep}_{\text{myo-stom}}$. Figure 5-6 illustrates some of the observed profile shapes that must be fit by the myocardium-stomach model and Figure 5-7 gives a flowchart demonstrating the sequential initialization process. Table 5-2 gives the upper and lower bounds used for the stomach parameters.

Initialization method 1 is used for profiles with bi-modal or indistinctly separated, high amplitude stomach (Figure 5-6a&b). The stomach amplitude, $A_{\text{stom},i}$, is set to the maximum profile value outside the initialized location of the outer myocardial wall. The stomach centre, $c_{\text{stom},i}$, is set to the location of A_{stom} and the stomach is estimated to fill the myocardium-stomach separation; stomach width, $w_{\text{stom},i}$, is set to twice the distance between the stomach centre and the myocardium outer wall.

Profiles with insufficient stomach uptake for Initialization method 1 are then tested to determine if a minimum or a break in the smooth decline of the profile slope occurs outside the outer wall of the myocardium. A transition from negative to positive values,

in the third derivative of the profile amplitude, is used for this since a negative (positive) third derivative means the slope of the profile is becoming less (more) steep.

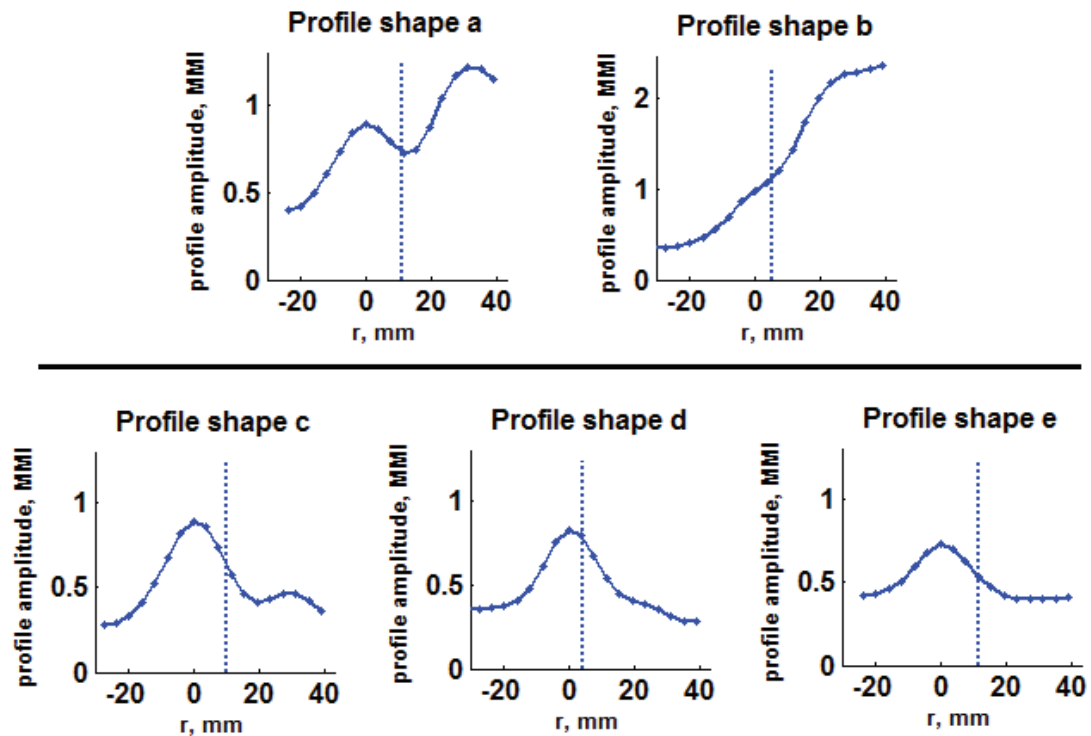


Figure 5-6. A selection of the observed profile shapes that must be fit by the myocardium-stomach model: (a) bi-modal with high stomach amplitude; (b) indistinct separation with high stomach amplitude; (c) bimodal with low stomach amplitude; (d) indistinct separation with gradually decreasing but detectable, low amplitude stomach; (e) constant, low amplitude background. Note the difference in vertical scale used in (b); the vertical dotted line on each plot marks the outer boundary of the myocardium. For initialization of the stomach parameters, profile values outside (right) of this boundary are considered.

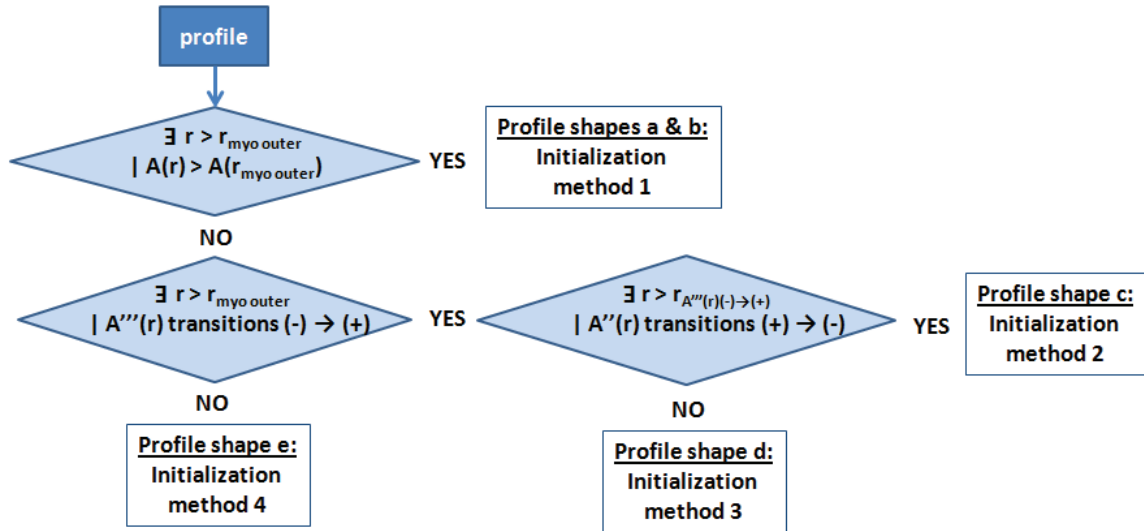


Figure 5-7. Sequential process used to decide the initialization method used for stomach parameters based on characteristics of the profile shape. Profile shapes are illustrated in Figure 5-6; A is the amplitude of the profile and r is the radial coordinates of A . $r_{\text{myo outer}}$ is the location of the outer myocardial wall, \exists indicates ‘there exists’, $|$ indicates ‘such that’ and Lagrange’s notation is used to represent derivatives.

If a minimum or a break in decline of the profile slope is detected, a transition in the second derivative from positive to negative is used to differentiate between a secondary, low amplitude maximum outside the myocardium (bimodal with low stomach amplitude) and an indistinctly separated, gradually decreasing but detectable, low amplitude stomach. Initialization method 2 is used for profiles that are bimodal with low stomach amplitude (Figure 5-6c). $A_{\text{stom},i}$ and $c_{\text{stom},i}$ are set to the value and location, respectively, of the profile at the secondary, low amplitude maximum. $w_{\text{stom},i}$ is then set to twice the distance between the inflection point (zero in the third derivative) prior to secondary, low amplitude maximum and its centre. Initialization method 2 is used for profiles with indistinctly separated and gradually decreasing but detectable, low

amplitude stomach (Figure 5-6d). $A_{stom,i}$ and $c_{stom,i}$ are set to the value and location, respectively, of the profile at the interpolated location of the zero in the third derivative at the negative to positive transition; allowing them to correspond to the centre of the ‘bump’ or break in decline of the profile slope. $w_{stom,i}$ is then set to twice the distance between $c_{stom,i}$ and the initialized location of the outer myocardial wall.

Table 5-2. Bounds of myocardial-stomach model parameters. N_i is used to denote the initialization value of the parameter N ; r = profile radial location; $r = 0$ at the FlowQuant-determined LV myocardium, $r < 0$ inwards (blood pool), $r > 0$ outwards.

Model parameter	Lower bound	Upper bound
w_{myo} , c_{myo} , A_b , A_{bkgd} , FWHM	$\max([0, \text{lower bound of 95\% confidence interval on myocardium-only model fit from interference-free region}])$	Upper bound of 95% confidence interval on myocardium-only model fit from interference-free region
stomach amplitude, A_{stom}	$\max([\text{small positive number } 2xA_{stom,i} - A_{bkgd,i}]])$	$\max([2xA_{stom,i} \quad 2xA_{myo,i}])$
width of the stomach, w_{stom}	0	$\max(r) - (c_{myo} - w_{myo} + lb(w_{myo})/2)$ (the maximum possible width where the stomach occupies all of the profile outwards of the most inwards possible location and minimum width of the myocardium)
separation between the myocardium and stomach, $sep_{myo-stom}$	0	$\max(r) - (c_{myo} - w_{myo} + lb(w_{myo})/2)$ (the maximum possible separation where the stomach is located at the outwards end of profile with the most inwards possible location and minimum width of the myocardium)

Finally, if the profile amplitude outside the myocardial wall is low but a minimum or a break in decline of the profile slope cannot be detected (e.g. Figure 5-6e), initialization method 4 is used for rough but inclusive initialization. Initialization method 4 sets $A_{stom,i}$ and $c_{stom,i}$ to the maximum value and location, respectively, of the profile an extra half-

width of the myocardium outside the initialized location of the outer myocardial wall and $w_{\text{stom},i}$ is estimated as twice the distance $c_{\text{stom},i}$ and the initialized location of the outer myocardial wall.

The stomach parameter initialization method was developed based on the ability to successfully initialize all parameters for all profiles from a single SA image slice selected out of each of the development images (section 4.2.6). This was accompanied by visual examination of model initialization, fit and model boundaries superimposed on measured profiles for the development images, as well as model boundaries before convolution on 2D SA slices, Figure 5-8. The R^2 goodness-of-fit criterion was found insufficient to describe an acceptable fit on its own due to variable amplitude at the outer extent of some profiles despite acceptable results in the region proximal to the myocardium. As such, a second measure of fit was incorporated.

This measure (d_{maxmyo}) was defined as the maximum allowable difference between the measured and fit profile values inside the model-defined myocardium region.

d_{maxmyo} was set to 0.075 MMI, and the minimum acceptable R^2 goodness-of-fit value, as determined by visual evaluation similar to the approach used for the myocardium-only model in the interference-search region, was set to $R^2 = 0.80$.

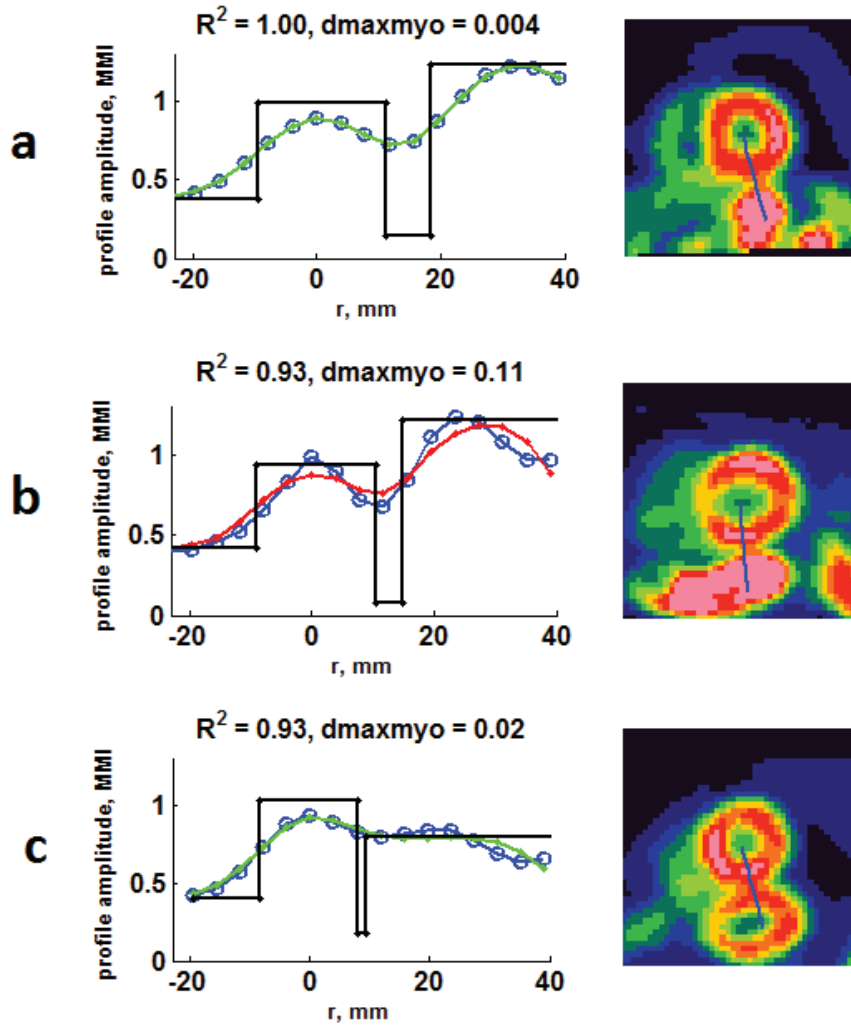


Figure 5-8. Examples of the information used to visually evaluate the appropriate values for the coefficient of determination (R^2) and maximum allowable difference between measured and fit profiles values, d_{maxmyo} , when the myocardium-stomach model is applied in the interference-search region. (a) shows successful fitting; (b) shows failure and (c) shows success due to incorporation of d_{maxmyo} and relaxing R^2 .

5.2.6 Parameter smoothing, voxel-specific interpolation and corrected images

To remove abrupt transitions in parameter values and to handle isolated profile failures, a smoothing filter was applied to parameters across interference-search region profiles for each SA image slice. A 5-pt $1/\text{distance}^2$ -weighted average filter was used, where parameter values for failed profiles were filled in from their neighboring values for up to two sequential failed profiles. The maximum radial and angular extent of interference-search region profiles fit with the myocardium-stomach model was used to define the region of the SA image slice requiring correction. Voxels with the majority of their area inside this region were identified and their values corrected. Profiles within a 2-pixel neighborhood of the voxel were identified and the orthogonal distance from the voxel to each profile determined. Parameter values specific to the voxel were calculated using $1/\text{distance}^2$ weighted averages. The voxel's radial distance from the myocardium was determined and, finally, the corrected voxel value estimated from the myocardium-only model parameters at the voxel's radial distance (i.e. setting the stomach amplitude in the model to zero).

5.2.7 Correction algorithm evaluation

The method for algorithm evaluation described in section 4.2.7 was used to quantitatively evaluate the behaviour of the algorithm. The comparisons described for each category of images were performed and additionally, for images from category C and D scans, the magnitude of the 1D convolution-based correction was compared to that of the dynamic-based correction (paired, non-directional, t-test, $p < 0.05$ Bonferroni corrected to $p < 0.01$).

5.2.8 Failure criteria, population failure rate and algorithm execution time

The correction algorithm was considered to have failed if, within any of the SA slices within the image, an insufficient fraction (<50%) of the interference-free region contributed to the mean/95% CI values for the myocardium-only model. The correction algorithm was also considered to have failed if, within any of the SA slices within the image, > 2 adjacent profiles from the interference-search region were marked as failed. Profiles could fail during initialization or execution of the fitting routine, or by not meeting their respective goodness-of-fit criterion/criteria (unacceptable fit). The failure rate during algorithm execution (due to initialization or execution of the fitting routine), failure due to unacceptable fit and overall failure rate were evaluated. Failed scans were visually reviewed to identify common causes of failure.

5.3 Results

5.3.1 Algorithm evaluation

The correction algorithm was found to preserve normal myocardial perfusion: no significant differences were found between the rest and stress interference-free NDBs and category A rest and stress PI segments, respectively, either before or after correction. The frequency of abnormal perfusion was high enough in the majority of segments of category B scans to differentiate them from normal perfusion and mean segment values were all lower than normal: all category B rest and stress PI segments were found significantly different than the rest and stress interference-free NDBs before correction, with the exception of stress segment 5. The mean category B, PI segment

values before correction were all lower than the corresponding NDB segment values. The correction algorithm preserved abnormal myocardial perfusion: there were no significant differences between category B, PI segment values before versus after correction (paired t-test, $p = 0.05$, Bonferroni corrected to $p = 0.01$). The reference images of category C scans confirmed normal perfusion but the severity of ECI in category C rest scans was not sufficient to make their reference images differ from normal before correction and correction did not change this: None of the PI segments of category C partner stress images, or rest images before or after correction, were found significantly different than the stress or rest interference-free NDBs, respectively. Table 5-3 summarizes the changes in myocardial intensity due to the correction algorithm by giving mean \pm standard deviation of the change in values for all PI segments and all categories, as well as the results of t-test comparisons to an estimated mean clinically relevant change, $\mu_{CRC} = -0.5\sigma_{NDB, INT-free}$, and finally, comparisons between categories. No delta values (all PI segments and all categories) were found significantly different than zero. This may appear surprising for category D images, where removal of moderate-severe ECI is expected to be accompanied by a change in myocardial intensity in at least a fraction of scans. However, since not all segments experience ECI in all scans, variance in delta will increase offers some explanation for why category D delta values were not significantly different than zero.

Table 5-3. Delta values and comparisons for the 1D convolution-based correction algorithm (Ch5) applied to the evaluation dataset, including additional comparisons to the dynamic-based algorithm (Ch4) in categories C and D. Delta is the difference in myocardial segment values after minus before correction.

Category	delta	segment 4	segment 5	segment 10	segment 11	segment 15
Category A n = 23	$\mu \pm \sigma =$	-0.10 \pm 0.12	-0.03 \pm 0.08	-0.12 \pm 0.11	-0.02 \pm 0.03	-0.07 \pm 0.11
	<u>Comparisons:</u> vs $\mu_{CRC} = -0.5$	p = 0.00* (A < μ_{CRC})				
Category B n = 16	$\mu \pm \sigma =$	-0.07 \pm 0.11	-0.04 \pm 0.05	-0.06 \pm 0.08	-0.02 \pm 0.04	-0.02 \pm 0.04
	<u>Comparisons:</u> vs $\mu_{CRC} = -0.5$	p = 0.00* (B < μ_{CRC})				
	vs $\mu_{Category A}$	p = 0.47	p = 0.81	p = 0.05	p = 0.86	p = 0.05
Category C n = 15	$\mu \pm \sigma =$	-0.34 \pm 0.55	-0.08 \pm 0.07	-0.31 \pm 0.44	-0.04 \pm 0.05	-0.23 \pm 0.41
	<u>Comparisons:</u> vs $\mu_{CRC} = -0.5$	p = 0.78	p = 0.00* (C < μ_{CRC})	p = 0.69	p = 0.00* (C < μ_{CRC})	p = 0.53
	vs $\mu_{Category A}$	p = 0.11	p = 0.06	p = 0.12	p = 0.19	p = 0.16
	vs $\mu_{Category B}$	p = 0.08	p = 0.06	p = 0.04	p = 0.20	p = 0.07
	vs $\mu_{Category C, Ch 4}$	p = 0.11	p = 0.00* (Ch5 > Ch4)	p = 0.05	p = 0.09	p = 0.08
Category D n = 22	$\mu \pm \sigma =$	-0.53 \pm 0.26	-0.45 \pm 0.50	-0.64 \pm 0.39	-0.44 \pm 0.48	-0.36 \pm 0.40
	<u>Comparisons:</u> vs $\mu_{CRC} = -0.5$	p = 0.91	p = 0.92	p = 0.72	p = 0.91	p = 0.74
	vs $\mu_{Category A}$	p = 0.00* (D > A)				
	vs $\mu_{Category B}$	p = 0.00* (D > B)				
	vs $\mu_{Category C}$	p = 0.23	p = 0.00* (D > C)	p = 0.03	p = 0.00* (D > C)	p = 0.32
	vs $\mu_{Category D, Ch 4}$	p = 0.06	p = 0.13	p = 0.08	p = 0.15	p = 0.63
	$\sigma \mu_{Category D, Ch 4}$ vs Ch5	p = 0.00* (Ch5 < Ch4)	p = 0.29	p = 0.00* (Ch5 < Ch4)	p = 0.09	p = 0.00* (Ch5 < Ch4)

The correction algorithm was able to preserve both normal and abnormal myocardial intensity on a clinically relevant scale when ECI was not present: category A and B delta

values are found significantly different than the mean clinically relevant change, with mean PI segment delta values all less than μ_{CRC} . When ECI was present but mild, changes made to myocardial intensity by the correction algorithm were of the order considered clinically relevant in the majority of segments but were not larger than the changes seen when ECI was not present: Category C delta values were found not significantly different than μ_{CRC} in 3/5 segments, while the mean delta in the remaining 2 significantly different segments was less than μ_{CRC} . Category C delta values were also not found significantly different than category A or B delta values. The final row of category C comparisons shows that for a single segment, the change in myocardial intensity, delta, made by the 1D convolution-based algorithm (Ch 5) was significantly greater than that made by the dynamic-based algorithm (Ch 4).

When more severe ECI was present, the changes made to myocardial intensity by the correction algorithm were of the order considered clinically relevant, and were larger than the changes seen when ECI was not present, in all segments. The changes were larger than those seen when ECI was present but mild, in some but not all segments. Category D delta values were found not significantly different than μ_{CRC} in all PI segments. Category D delta values were found significantly different than category A and B delta values, with the mean delta from category D exceeding those of categories A and B in all segments. Category D delta values were found significantly different than category C delta values, in 2/5 segments and all mean delta values from Category D were greater than those from category C.

For scans with more severe ECI (category D), the changes made to myocardial intensity by the 1D convolution-based correction algorithm were not found different than those made by the dynamic-based correction algorithm, when all category D scans were considered: the second to last row of category D comparisons shows that no segments exhibited a significant difference between the 1D convolution-based algorithm (Ch 5) and the dynamic-based algorithm (Ch 4) for this category.

However, as in section 4.3.8, if the category D dataset is revised to exclude the outlier (the scan whose myocardial basis function was found to be non-physical), the changes made to myocardial intensity by the 1D convolution-based correction algorithm were now found to exceed those made by the dynamic-based correction algorithm in all segments. While, for the dynamic correction algorithm, excluding this scan changed the results of comparisons between category D and other scan categories, as well as comparison to clinically relevant change, the same was not true for the 1D convolution-based correction algorithm: the results of all of these comparisons remained unchanged. Table 5-4 demonstrates that much more significant differences are evident between the two algorithms. Using the revised category D dataset does not change the significance of comparisons to μ_{CRC} or category A, B or C delta values; however, the paired comparison to category D, Chapter 4 delta values becomes significant for all PI segments and in all segments the mean delta values from the 1D convolution-based algorithm (Ch5) exceed those of the dynamic-based algorithm (Ch4). Histograms of category D segmental delta values for the 1D convolution-based correction algorithm showed values were grouped together with no evidence of outliers.

Table 5-4. Revised category D delta values and comparisons for the 1D convolution-based correction algorithm applied to the evaluation dataset, after exclusion of the category D scan exhibiting a non-physiologic myocardial basis function in Chapter 4.

Category	delta	segment 4	segment 5	segment 10	segment 11	segment 15

Category D n = 21	$\mu \pm \sigma =$	-0.53±0.26	-0.43±0.51	-0.64±0.40	-0.44±0.49	-0.36±0.41
	<u>Comparisons:</u>					
	vs $\mu_{CRC} = -0.5$	p = 0.92	p = 0.90	p = 0.74	p = 0.90	p = 0.75
	vs μ Category A	p = 0.00* (D>A)	p = 0.00* (D>A)	p = 0.00* (D>A)	p = 0.00* (D>A)	p = 0.00* (D>A)
	vs μ Category B	p = 0.00* (D>B)	p = 0.00* (D>B)	p = 0.00* (D>B)	p = 0.00* (D>B)	p = 0.00* (D>B)
	vs μ Category C	p = 0.24	p = 0.01* (D>C)	p = 0.03	p = 0.00* (D>C)	p = 0.33
vs μ Category D, Ch 4	p = 0.00* (Ch5>Ch4)					

To evaluate how often the correction algorithm failed, the category C and D scans were visually reviewed. It was seen that 7% (1/15) of category C scans had a SA slice where excess myocardial intensity was removed and 9% (2/22) of category D scans had 1 – 3 SA slices where excess myocardial intensity was removed (1 scan) or obvious ECI remained (1 scan). Excess myocardial intensity was removed where the thickness of the myocardium caused it to be seen by the algorithm as partially stomach and obvious ECI remained where the (hollow) stomach shape was seen by the algorithm as myocardium. Examples of these two types of failures are shown in Figure 9. Figure 5-10 demonstrates the results of the 1D convolution-based algorithm on images from the same three development category scans as in Figure 4-9. Figure 5-11 shows two category D examples demonstrating where the 1D convolution-based algorithm produced much more reasonable corrections than the dynamic-based algorithm, with respect to preserving myocardial uptake and removing visible interference.

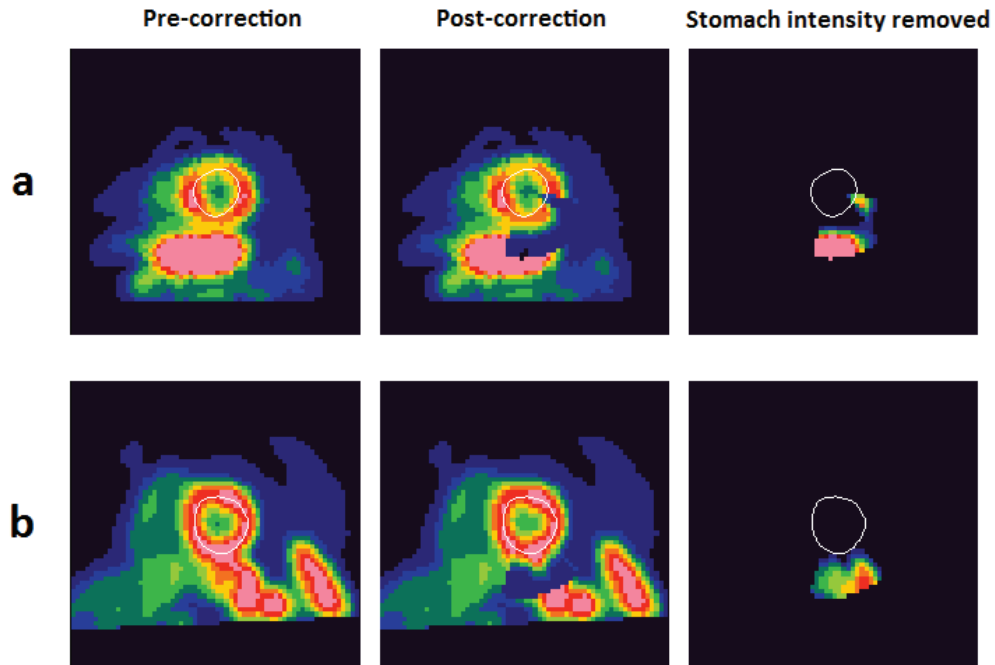


Figure 5-9. Examples of the two types of incorrect myocardial intensity found during visual review of corrected images from the evaluation dataset: (a) shows where excess myocardial intensity was removed and (b) shows where insufficient stomach was removed.

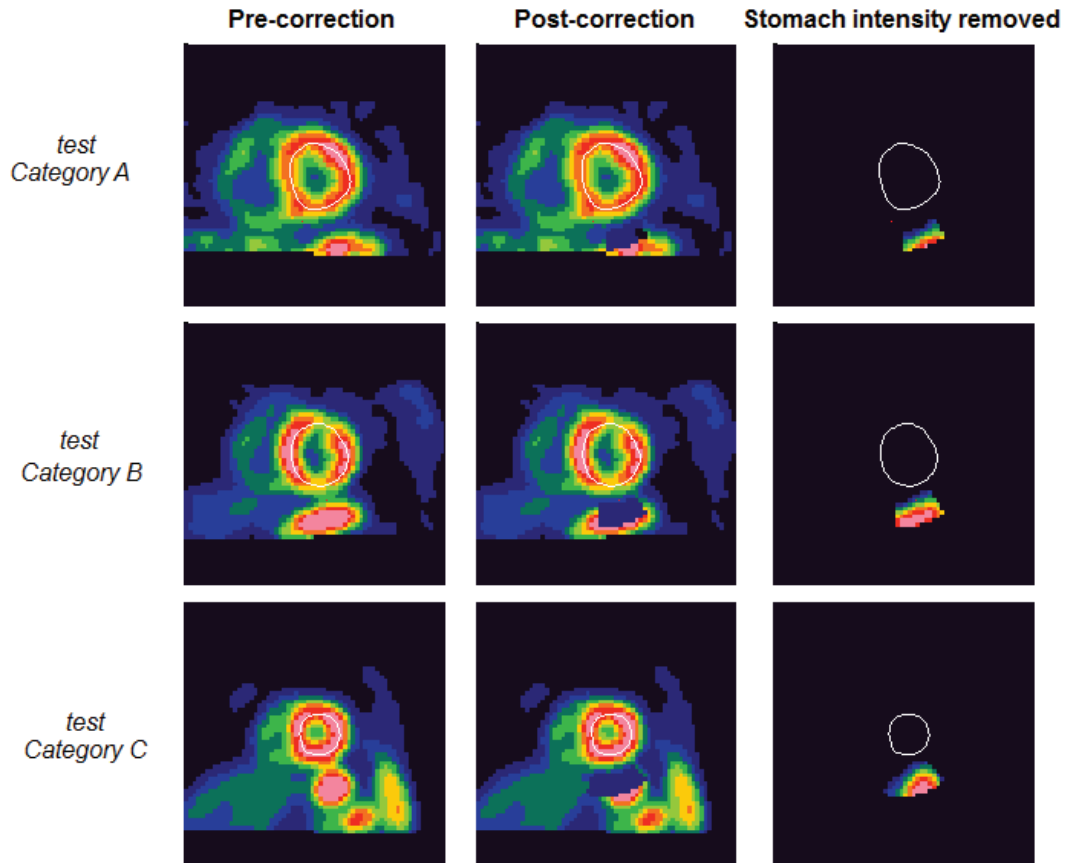
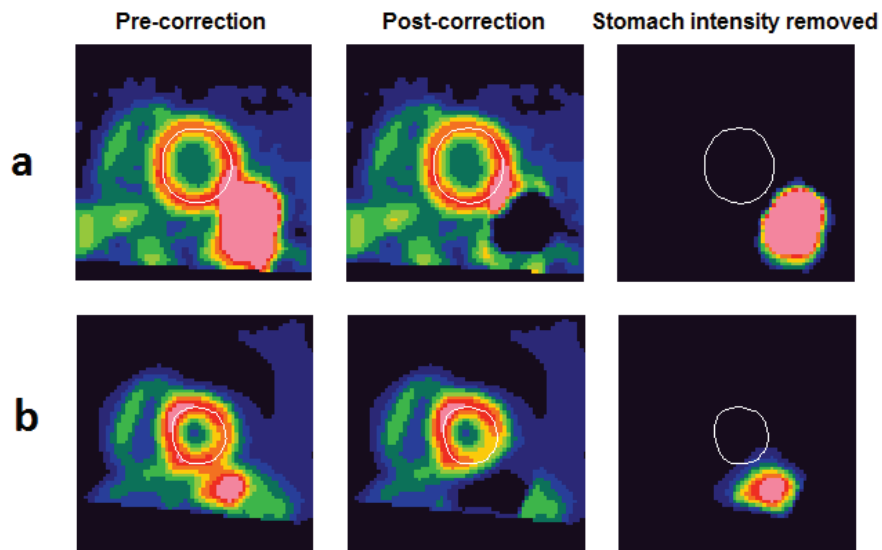


Figure 5-10. Demonstration of the 1D convolution-based correction algorithm results on an image from each category in the algorithm development dataset. Scans are the same as those used in Figure 4-9.

dynamic-based correction



1D convolution-based correction

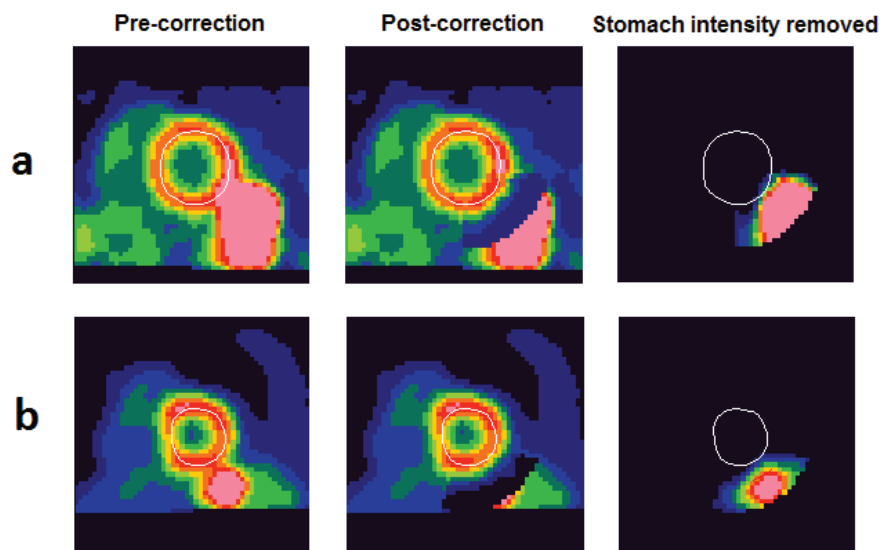


Figure 5-11. The difference between correction algorithm results for the dynamic-based versus the 1D convolution-based algorithm , on the two scans used in Figure 4-11 to demonstrate failure of the dynamic-based algorithm in category D images.

5.3.2 Population failure rate and algorithm execution time

The algorithm's overall failure rate was 7.3% (11/150 scans); 4.7% (7/150) scans failed during algorithm execution (3 at initialization and 4 during execution of the fitting routine) and 2.7% (4/150) scans failed due to unacceptable fit in >2 sequential profiles. The 4 scans which failed during execution of the fitting routine, occurred in images that were observed to have limited inferior FOV. Figure 5-8b gives an example of failure due to an unacceptable fit which is caused by the shape of the stomach and the outer radial sampling limit of interference-search region profiles. The execution time for the algorithm was 10.3 ± 0.4 minutes, in addition to FlowQuant LV-processing using MATLAB version 7.12.0 (R2011a) running on a 1.86 GHz Intel® Core™ 2 CPU, 6300 processor with 2.00 GB RAM. Apart from the potential requirement for manual intervention during FlowQuant processing, the 1D convolution-based correction algorithm is fully automated.

5.4 Discussion

The 1D convolution-based correction algorithm has been shown to preserve myocardial intensity for cases of both normal and abnormal perfusion, in images where the stomach uptake is elevated but well separated from the myocardium. It has also been shown to remove interference and be capable of changing the myocardial intensity by a clinically relevant amount in cases of moderate to severe interference. Although no independent measure of true myocardial perfusion was available, mild – moderate interference was removed from a population of 15 rest images known to have normal

perfusion via their paired stress image and, after correction, the rest image population was found not significantly different than the interference-free normal database. When images from scans that had ECI prior to correction, were visually reviewed, less than 10% showed evidence of incorrect myocardial intensity after correction.

While initialization of myocardium-only model parameters in the interference-free region was simple and fitting was found to be robust to initialization values, this was not the case in the interference-search region. Initialization in the interference-search region was made more robust by first determining if the profile could be adequately fit with the constrained myocardium-only model. For those profiles which could not be fit to the myocardium-only model, initializing the myocardium amplitude to its FlowQuant value, and the remaining 5 myocardium components of the myocardium-stomach model with the mean and 95% confidence intervals values from the interference-free region greatly increased the frequency of successful fits. Although this provided a means of initializing the myocardial components, appropriate initialization of the three remaining stomach parameters was still not simple and the fitting process was found to be sensitive to these values, suggesting an optimization space with local minima. At this point, information is not shared between adjacent profiles during initialization or fitting. Incorporating constraints into initialization and fitting that require 2D or 3D continuity of parameters is likely to make the algorithm more robust.

As the mean and 95% confidence intervals on the myocardium-only model parameters (from the interference-free region) influence fitting in the interference-search region, the variation in these values and the number of scans failing, as a function of the R^2

goodness-of-fit cutoff for the interference-free profiles, was briefly investigated using the development dataset. The mean and 95% confidence intervals were found to be slowly varying functions of R^2 up to a value of $R^2 > 0.99$ where the number of failing scans increased rapidly. $R^2 > 0.97$ was chosen as an intermediate value that did not cause any of the development scans to fail during this step of the algorithm. It may be possible to relax this R^2 cut-off further; however, this is unlikely to improve algorithm performance because, during assessment of failure rate, it was not found to be a dominant cause of failure.

The images were only corrected in the interference-search region where it was not possible to fit a myocardium-only profile. A second R^2 goodness-of-fit cutoff was used on the myocardium-only profiles to determine the extent of this correction region. A threshold of $R^2 > 0.94$ was chosen based on visual assessment of the development dataset images. In images where all extra-cardiac activity results in ECI, the sectors identified by the DSC algorithm as containing interference should cover the same extent as this correction region and numerical optimization could have been used to determine the R^2 cut-off based on concordance of the interference algorithm with the DSC results. However, this approach was intentionally not taken and instead, the DSC algorithm results were used as only a guide since, at this time, the correction algorithm aims to identify and remove *all* stomach detected in the extracted profiles, i.e. both that which does and does not cause ECI. This feature of the correction algorithm was implemented to allow assessment of algorithm's ability to preserve myocardial intensity in category A and B scans, i.e. those without ECI but which still had stomach to remove.

In the final step of fitting profiles with the myocardium-stomach model, goodness-of-fit criteria R^2 and $d_{\max\text{myo}}$ are used. These goodness-of-fit criteria, in conjunction with the width of the neighbourhood over which isolated profile failures could be smoothed, were used to differentiate when the algorithm would cause correct versus incorrect myocardial intensity in the corrected image. Initially, this decision was based solely on R^2 ; however, in many of the images with inappropriate correction, it was found that inaccuracies were being introduced because of profiles that failed only in the portion of the profile distal to the myocardium. Due to failed profiles, the values in these regions were being corrected based on interpolation from adjacent regions, rather than using the data present in those areas. As the myocardium is the organ of interest in ^{82}Rb PET MPI, it is the fit closest to the region occupied by the myocardium which is most important. Errors that occur in the extra-cardiac portion of the fit that are distal to the myocardium are less likely to influence the myocardial values. Therefore, the algorithm was adjusted to allow a less accurate fit distal to the myocardium by relaxing the overall fit criteria, as long as the fit in the myocardium region remains accurate. This could potentially result in an inaccurate fit to the activity causing interference, and thus an inaccurate correction. While this was not observed in the datasets evaluated, it is a potential source of error that would need to be investigated with more extensive studies where the true myocardial uptake was known.

Upon review of the dataset, one cause of failure was found to be a hollow stomach structure where either both the proximal and distal stomach walls were within the profile range or the distal wall caused the profile to plateau above the background (Figure 5-8b). To accurately model this scenario, a method would first need to be implemented for recognizing profiles of this type and then the radial range of the profile would need to be reduced or an additional rectangular function incorporated into the myocardium-stomach model. Another cause of failure is where myocardium thickness is truly greater in the interference-search region than in the interference-free region, seen most often when the RV insertion falls within the interference-search region. One type of image that can result in false correction, unidentified by the algorithm, is severe overlap of thin hollow stomach wall that cannot be differentiated from thick myocardium without interference. All of these cases would benefit from constraints that require 2D or 3D continuity.

Previous applications of the 1D convolution-based method for PVE correction (Gambhir 1990, Dumouchel 2011) have not derived the PSF from the images themselves as was done with the ECI correction algorithm. The previous methods used pre-determined PSFs derived from phantom experiments which reduces the number of degrees of freedom during fitting relative to that in the ECI correction method developed here (Gambhir 1990, Dumouchel 2011)(Gambhir 1990, Dumouchel 2011)(Gambhir 1990, Dumouchel 2011)(Gambhir 1990, Dumouchel 2011). In order to use pre-determined PSFs on in-vivo data, the effects of motion on the image PSF must be minimized since the amplitude of in-vivo motion varies spatially within the image and is subject specific.

The PVE correction approaches resolve this problem by using cardiac-gated image frames to minimize motion (and ignoring other forms of motion such as respiration). These approaches also use tracers which provide higher count acquisitions compared to ^{82}Rb so that the increased noise in the gated image frames did not create a problem. Because the PSF is fit to the images in the ECI correction approach, it is able to work well on static reference images with large post-reconstruction filtering (optimized for visual clinical evaluation) and does not require pre-correction for motion (the resolution loss due to motion is incorporated within the fitted PSF). The PSF of an image depends on the image processing steps used to produce it: reconstruction, filtering, TOF information and gating. Since the PSF used in the correction algorithm model is determined from the image itself, no modifications are inherently required to apply the algorithm to any of these forms of images. One factor that needs to be taken into consideration, however, is that the initialization routines for the algorithm were developed for profiles exhibiting little noise. Using the algorithm on images with reduced counts (i.e. gated image frames) may necessitate the application of a profile smoothing filter to aid in the initialization. It is possible that improving the spatial resolution of the input images, through motion correction or reduced filtering, could improve the quality of the ECI correction by reducing the amount of interference that needs to be removed from the myocardial image; however, this is also likely to increase noise and so further studies would be required to optimize the input images.

5.5 Conclusion

The 1D convolution-based correction algorithm provides a fully automated correction in 93% of ^{82}Rb PET cardiac images that had detectable interference; the remaining 7% may be resolvable and the robustness of the algorithm improved by expanding the fitting procedure to enforce smoothness in 2D or 3D. Based on the evaluation images that had interference, the algorithm produced a visually acceptable correction in >90% of scans.

6 Chapter: **Summary and future directions**

6.1 Introduction

This thesis developed two automated algorithms which aimed to solve the problem of ECI in ^{82}Rb PET MPI. The first algorithm detects ECI with high sensitivity and specificity and ranks the severity of ECI. This algorithm was applied to sets of clinical ^{82}Rb PET MPI images to determine: the prevalence of ECI, the variation of ECI in images produced using modified forms of image processing (gating, filtering and TOF reconstruction) as well as the algorithm failure rate and execution time. The second algorithm corrects ECI by fitting a 1D convolution model of the stomach and myocardium to the measured data. The performance of this algorithm was evaluated with a select set of clinical ^{82}Rb PET MPI images and shows considerable promise. During development of the algorithms a number of modifications were identified which have the potential to further enhance performance. Clinical implementation requires further validation the correction algorithm and migration of the research code to a clinical platform. By providing clinics with software-based ECI detection and correction, the work from this thesis can be used to better the quality of care derived from ^{82}Rb PET MPI.

6.2 Directions for improving algorithm performance

6.2.1 Expanding 1D convolution algorithm to 2D/3D

The structures in PET MPI are three dimensional, as are the PSF of the system and the filtering which is applied post-reconstruction. The use of a 1D model ignores the correlations inherent in the images in the other two dimensions. Expanding the

algorithm to take this into account would enhance the quality of the fit and may provide a more accurate estimate of the underlying tracer distribution. There are two main obstacles to expanding the algorithm to higher dimensions. The first is a method to describe the 3D shape of the stomach as it is much more irregular than the myocardium. Parameterization would be inefficient and this obstacle is potentially best overcome by using codependent constraints on fits within neighbourhoods to ensure surface smoothness. The second obstacle is increased computational complexity caused by increasing the number of parameters integrated into simultaneous fitting. Without modifications to processing methods, algorithm execution time increases with computational complexity and, beyond a practical limit, will restrict implementation of the algorithm. The 1D convolution algorithm is currently implemented in Matlab and has an execution time of 10 minutes which is considered clinically acceptable. Computational efficiency can be improved by translating the Matlab-based code into a language with less overhead (i.e. C++) and/or by adapting programming to allow for parallel execution.

6.2.2 Optimizing the input to the convolution algorithm

In image processing, just like most scientific experiments, the quality of the system output is dependent on the quality of the system input (colloquially known as the GIGO concept: 'garbage in, garbage out', (Lidwell *et al* 2010)) but it is also important to recognise that the definition of quality is specific to the system and can vary depending on the task at hand. The imaging protocol which produces principle images used for MPI interpretation has been optimized for the task of visually interpreting perfusion and not

the task of software-based quantitative and accurate removal of ECI. As demonstrated in chapter 3, the severity of ECI can be reduced by using alternate forms of image processing. Correspondingly, the 1D convolution correction algorithm may be able to benefit from increased spatial resolution afforded by gating and reduced filtering and may also be able to handle higher noise levels than are acceptable for visual interpretation. Investigation of fitting methods specific to high noise scenarios may also be useful.

6.2.3 Defining scan-specific interference search region

A small but potentially important improvement to the detection and correction algorithms is the ability to estimate the scan-specific position of the inferior RV insertion since, from the stand point of both algorithms, the elevated image intensity due to the RV is only distinguished from ECI in terms of position. If, in the detection algorithm, the septal limit of the interference search region includes the RV insertion, false positives can result. In the correction algorithm, inclusion of the RV insertion provides a geometry that is particularly difficult for the algorithm to handle. The insertion is seen as a gradual increase in myocardial wall thickness up to a point beyond which it becomes separated into thin myocardium directly adjacent to a thin, high uptake extra-cardiac structure and small variations in intensity and width can cause oscillation between the two results.

The ability to model the RV has been recently developed for FlowQuant (Takobana *et al* 2013) and, after assessing the accuracy of this model in the presence of ECI, incorporating its estimate of the inferior RV insertion location into the ECI algorithms is expected to prove beneficial. In addition to this improvement, the detection algorithm is

also expected to benefit from incorporation of the interference-free wall modeling technique, developed for the 1D convolution correction algorithm, to produce scan-specific lateral interference search limits and radial sampling distances.

6.3 Impact on the quality of care derived from ^{82}Rb PET MPI

6.3.1 Clinical implementation of ECI correction

Software migration

The ECI detection and correction algorithms are currently executed on a research workstation, using a combination of FlowQuant processing and independent Matlab code. FlowQuant is also currently installed on technician's workstations in our clinic and used to produce myocardial blood flow quantification as part of the standard data supplied to clinicians for MPI interpretation. Since FlowQuant code is Matlab-based, the ECI algorithms could easily be incorporated into the version of FlowQuant used by technicians. Detection is quick (<7s) and could therefore be executed as a standard procedure generating a flag. If ECI is flagged, the technician could choose to execute the, more time consuming, correction algorithm thus producing and exporting an additional set of corrected images. These images would then be incorporated into the standard data supplied to clinicians for MPI interpretation.

Correction algorithm validation

The correction algorithm evaluation procedure, described in section 4.2.7 and used in both chapters 4 and 5, demonstrated basic properties of algorithm behaviour. However, for images where myocardial intensity was most likely to be modified by correction

(those with moderate to severe interference), no independent measure of true myocardial perfusion was available. Multiple independent measures have been used in previous work to assess the accuracy of myocardial perfusion imaging: coronary angiography (CA) (Beller and Zaret 2000), fractional flow reserve (FFR) (Takx *et al* 2015), repeat imaging (Klein *et al* 2010b) and alternate forms of MPI (Bateman *et al* 2006). While CA is frequently used as a means of evaluating MPI and MPI exams can lead to CA clinically, CA provides anatomical (percent occlusion of arteries) not functional information and because it requires catheterization (an invasive procedure with additional associated risk) the population who receive CA is biased towards those with perfusion defects (Beller and Zaret 2000). FFR is another catheterization-based technique that does provide an indication of hemodynamically significant disease but adds additional expense to simple CA and is not performed frequently at our centre. Patients are often imaged multiple times for a variety of reasons and so images from similar tests may be able to provide insight as to the true state of the myocardium. Alternate forms of MPI performed at our centre include ^{99m}Tc -tetrofosmin SPECT and ^{13}N -NH₃ (ammonia) PET. To determine if retrospective data for independent measures of true myocardial perfusion was available through repeat ^{82}Rb imaging or these alternate forms of MPI, the ^{82}Rb , ^{13}N -NH₃ and ^{99m}Tc -tetrofosmin SPECT clinical databases from our centre were cross referenced for the 2 year time period between January 2011 and December 2012. Unfortunately, there were no cases with repeated or alternate forms of MPI acquired within a timeframe where progression of disease was unlikely ($\Delta t < 3$ months) which didn't also have intervention (PCI or stenting) in the

interim or co-located ECI in both scans (repeat ^{82}Rb). Therefore, minimal data are available at our centre to retrospectively evaluate the correction algorithm and a prospective study would be needed for validation.

To perform a prospective validation of the detection algorithm, we would first integrate it into the standard image processing performed by the technicians on all ^{82}Rb PET MPI studies. Patients whose ^{82}Rb PET MPI scans exhibit ECI would be approached to request that they return, within a short time period, for a $^{13}\text{N-NH}_3$ PET MPI study. Images from the $^{13}\text{N-NH}_3$ PET MPI scans would then be used as the independent measure of 'true' myocardial perfusion for comparison with the ^{82}Rb PET MPI images before and after correction. Selection of patients for $^{13}\text{N-NH}_3$ PET MPI scanning could be limited to those whose ^{82}Rb PET MPI scan(s) exhibit moderate-severe ECI and/or those whose ^{82}Rb PET MPI stress scans exhibit ECI to increase the likelihood of ECI being clinically relevant (section 6.3.2). ECI may also be present in $^{13}\text{N-NH}_3$ PET MPI; however, the extra-cardiac organ with elevated uptake differs (liver as opposed to stomach) and therefore, if myocardial perfusion is obscured by ECI in $^{13}\text{N-NH}_3$ PET, it is less likely to be co-located with the ECI in the ^{82}Rb PET (section 6.4). A study design of this type would allow an evaluation of the accuracy of the correction and also provide images which could be used to assess the impact of the correction on clinical interpretation by having physicians perform the interpretation with and without the corrected ^{82}Rb images.

Phantom studies and simulations

Physical phantom studies and computer simulations are two additional approaches that could be used to evaluate correction algorithm accuracy. Quantitative underlying truth

for the activity distribution and concentration are inherently known in phantom studies, as they are designed and input by the scientist. Comparing measured myocardial activity in the corrected image would indicate the accuracy of the correction method. However, the value of a phantom study relies heavily on the degree to which the input information is able to reflect the true, clinical situation. At the outset of this project, the theoretical causes of ECI were known but there was very little objective information characterizing the clinically representative case of ECI or information on the clinical variability. Development of the DSC algorithm in chapter 2 provided information regarding the relative myocardial: stomach intensity and the LV surface area of involvement that is identified clinically as ECI. In chapter 3, further information was gained regarding the relative contributions of respiratory and cardiac motion, as well as post-reconstruction filtering. In chapter 5, the correction algorithm provides an estimate of the myocardium: stomach separation values. Although, strict parameter values and their ranges were not quantified in this work, a set of scans has been identified for which these measurements could be made. To perform a physical phantom study to assess accuracy of the correction algorithm, a phantom such as the DataSpectrum Anthropomorphic Torso Phantom with the cardiac insert (DataSpectrum Corporation), could be used. The phantom could be modified to accommodate extra-cardiac activity by attaching, for example, a saline bag to the side of the cardiac insert. A deformable, approximately water-equivalent material (e.g. paraffin) could then be used to mould a variable thickness spacer, to be placed between the cardiac insert and the extra-cardiac activity reservoir. The difficulties associated with ^{82}Rb 's short half-life could be

overcome by substituting ^{18}F as the tracer but ensuring the clinical image processing protocol for ^{82}Rb MPI is used (in particular matching post-reconstruction filter width). By performing acquisitions at multiple levels of cardiac: extra-cardiac activity concentration, ECI of multiple severity classes could be simulated. An image with no extra-cardiac activity would provide a true no-interference image. A limitation of this approach is that motion and positron range are not incorporated into this first-order model and, indeed to accomplish this, computer simulations using digital phantoms (e.g. the NCAT phantom, (Segars *et al* 2007)) may prove more efficient.

6.3.2 Clinically relevant versus physical ECI

As briefly discussed in section 2.4, not all ECI influences clinical interpretation of MPI studies, e.g. the category C rest images from the correction algorithm evaluation procedure were known to have normal perfusion despite the presence of ECI since their paired stress images were free of ECI and exhibited normal perfusion. Therefore scans with clinically relevant ECI are a subset of those with physical ECI. The clinician's evaluation of the truth dataset in chapter 2 estimated 35% of physical interference is clinically relevant and, although not strictly correlated, the probability of clinical relevance increases with ECI severity and is higher if ECI is present in the stress scan. The current detection algorithm allows rapid identification of physical interference. If the execution time of the correction algorithm is not prohibitive, and the risk of falsely altering myocardial perfusion is small, then the correction could simply be applied to all scans with physical ECI which, by default, would ensure that all scans with clinically relevant ECI were also corrected. Expansion of the detection algorithm to identify

clinically relevant ECI is not a simple task. It requires methods to predict what would change diagnosis and prognosis and therefore requires incorporating all other relevant information available to clinicians upon interpretation. This information includes patient history, previous test results, comparison of rest versus stress perfusion, and measures of localized wall motion. Some studies have investigated methods for performing this type of integration (Slomka *et al* 2004, Nakazato *et al* 2012), but an approach such as this would require considerable development and validation.

6.3.3 Clinical impact of ECI

The current accuracy (sensitivity and specificity) of ^{82}Rb PET-CT MPI for detecting the presence of ischemic heart disease is high (87.8% sensitivity and 95.7% specificity, (Yoshinaga *et al* 2010, Beanlands *et al* 2007)); indicating that the impact of ECI on accuracy is likely to be limited. However, the impact of ECI on interpretation of the severity and extent of perfusion defects and on clinician confidence, particularly in low-volume clinics, may be significant, as discussed in section 2.4. The severity and extent of perfusion defects are used to direct treatment (Hachamovitch *et al* 2003) and increased clinician confidence might reduce the frequency of downstream testing. Assessment of clinical impact is one instance where differentiating between physical and clinically relevant ECI may prove beneficial as inclusion of only clinically relevant ECI would prevent dilution of results otherwise caused by a population with a large fraction of clinically irrelevant ECI.

6.4 Extended application

Although the algorithms within this thesis were developed specifically for ^{82}Rb PET MPI, alternate forms of MPI also suffer from ECI and therefore may also benefit from this work. ^{13}N -NH₃ PET MPI and $^{99\text{m}}\text{Tc}$ - tetrafosmin and sestamibi SPECT MPI suffer from ECI due to elevated liver uptake. ECI has been shown to be problematic in up to half of $^{99\text{m}}\text{Tc}$ sestamibi SPECT MPI studies (Bateman *et al* 2006). Differences in tracer properties and scanner technology result in some differences between ^{82}Rb PET images and those produced by these alternate forms of MPI.

^{13}N has a lower positron range and longer half life than ^{82}Rb resulting in longer acquisition times (20 versus 8 minutes), better count statistics (noise levels) and better spatial resolution compared to ^{82}Rb PET. SPECT MPI studies with $^{99\text{m}}\text{Tc}$ tracers generally have intermediate acquisition time (15 minutes) but worse noise and spatial resolution than do PET studies. Longer acquisition times increase the probability of significant patient motion which may prove detrimental for both alternate forms of MPI compared to ^{82}Rb . Both algorithms within this thesis break down at some point as levels of image noise increase (through production of invalid results by the detection algorithm (chapter 3) or through failure of the correction algorithm initialization routines (chapter 5)).

While increasing the degree of filtering can exchange spatial resolution for decreased noise in images, as filter width increases, smoothing progressively reduces the image's information content. Higher levels of image noise and lower spatial resolution in SPECT MPI will make these studies more susceptible to algorithm failure than ^{82}Rb or ^{13}N -NH₃ PET MPI. The liver is a solid organ whose structure is expected to be less variable than

that of the stomach and whose position relative to the myocardium is more septal than that of the stomach. The solid and more consistent shape of the liver may facilitate application of the correction algorithm; however, its position will likely cause more frequent and more severe overlap between liver-induced ECI and the RV insertion than seen with stomach-induced ECI in ^{82}Rb PET MPI. Increased overlap between ECI and the RV insertion is expected to cause the accuracy of the ECI algorithms to rely more heavily on the development of scan-specific estimates for the septal limit of the interference search region (section 6.2.3).

Differences between images, from ^{82}Rb PET MPI versus those from $^{13}\text{N-NH}_3$ PET MPI and SPECT MPI studies with $^{99\text{m}}\text{Tc}$ tracers, will necessitate tracer-specific validation of the algorithms. Despite these differences, it is expected that application of the detection and correction algorithms can successfully be extended to these alternate forms of MPI.

6.5 Conclusion

Ischemic heart disease affects a large fraction of the population and can be effectively managed if detected early. ^{82}Rb PET MPI is a highly accurate tool for diagnosis and prognosis of IHD but interpretation of perfusion in the inferior myocardial wall of the heart's left ventricle can be compromised by ECI. To date, the problem of ECI has received little attention and no software-based solutions are currently clinically available. The automated detection method developed in this thesis was used to demonstrate that the prevalence of ECI may be higher than previously estimated and that simple modifications to image processing are insufficient to eliminate ECI. A simple,

fully automated, convolution-based method for ECI correction has been produced which, when evaluated in a small set of clinical studies, has been shown to have considerable promise.

Appendices

Appendix A Permission for use of material from Medical Physics

This appendix consists of the letter providing permission for inclusion of the published article:

E.J. Orton, I. Al-Harbi, R. Klein, R.S. Beanlands, R.A. deKemp and R.G. Wells, "Detection and severity classification of extra-cardiac interference in ^{82}Rb PET myocardial perfusion imaging", *Med. Phys.* **41**, 102501 (2014)

as Chapter 2 of this PhD thesis granted by the journal Medical Physics. It is provided on the page following this (page 220).



American Association of Physicists in Medicine

One Physics Ellipse
College Park, MD 20740-3846
(301) 209-3350
Fax (301) 209-0862
<http://www.aapm.org>

Office of the Executive Director

Angela R. Keyser
Phone: 301-209-3385 Fax: 301-209-0862
E-mail: akeyser@aapm.org

DATE OF REQUEST: 04 March 2015

FROM:

Elizabeth J Orton, University of Ottawa Heart Institute, 40 Ruskin Street, Ottawa, Ontario K1Y 4W7, Canada

EMAIL ADDRESS: eorton@physics.carleton.ca

1. Permission is granted to:

Elizabeth J Orton / Carleton University

2. Permission is requested to use the following material:

Detection and severity classification of extracardiac interference in ^{82}Rb PET myocardial perfusion imaging.

Elizabeth J. Orton, Ibraheem Al Harbi, Ran Klein, Rob S. B. Beanlands, Robert A. deKemp, and R. Glenn Wells.

Medical Physics 41, 102501 (2014); doi: 10.1118/1.4893501

3. For what purpose:

Reformatted article for inclusion as chapter in PhD thesis.

Authors seeking permission must also notify the first author of the article from which permission is being sought.

Permission is hereby granted: _____
Signature

03/17/15

Date

Appendix B Ottawa Health Research Ethics Board (OHREB) Application

This appendix contains correspondence with the Ottawa Health Research Ethics Board that was necessary to gain access to the clinical scans data used in this thesis. It consists of four sub-appendices:

- B.1 OHREB Approval Letter (p. 222)
- B.2 PhD Supervisory Committee Approval (p. 223)
- B.3 Annual Renewal Report (pp. 224-225)
- B.4 OHREB ethics protocol, final version 8 May 2013 (pp. 226-230)



Ottawa Hospital Research Ethics Boards / Conseils d'éthique en recherches

725 Parkdale Avenue, Box 411, Ottawa, Ontario K1Y 4E9 613-798-5555 ext. 14902 Fax: 613-761-4311
<http://www.ohri.ca/ohreb>

May 28, 2013

Dr. Glenn Wells
Division of Cardiac Imaging,
University of Ottawa Heart Institute
40 Ruskin Street H 2103
Ottawa, ON K1Y 4W7

Dear Dr. Wells:

**Re: Protocol # 20130268-01H Characterization of image artifacts due to extra-cardiac uptake in 82-rubidium (Rb-82) positron emission tomography (PET) myocardial perfusion imaging (MPI)
(Sub-study of Rb ARMI HI Protocol #200987)**

Protocol approval valid until - May 27, 2014

I am pleased to inform you that your Application for Chart Review underwent expedited review by the Research Ethics Board (HREB), and is approved. No changes, amendments or addenda may be made to the protocol without the REB's review and approval.

The Thesis Board approval letter should be provided to the REB office, prior to starting the study.

The HREB has approved Research Protocol, Version 1, dated May 8, 2013.

If the study is to continue beyond the expiry date noted above, a Renewal Form should be submitted to the REB approximately six weeks prior to the current expiry date. If the study has been completed by this date, a Termination Report should be submitted.

The Human Research Ethics Board is constituted in accordance with, and operates in compliance with the requirements of the Tri-Council Policy Statement: Ethical Conduct for Research Involving Humans; Health Canada Good Clinical Practice: Consolidated Guideline; Part C Division 5 of the Food and Drug Regulations of Health Canada; and the provisions of the Ontario Health Information Protection Act 2004 and its applicable Regulations.

Yours sincerely,

Jim Robblee M.D.
Vice-Chairman
Human Research Ethics Board

JR/dw



UNIVERSITY OF OTTAWA
HEART INSTITUTE
INSTITUT DE CARDIOLOGIE
DE L'UNIVERSITÉ D'OTTAWA

11 April 2013

Research Ethics Review Board
The Ottawa Hospital
Ottawa, Ontario

RE: PhD Supervisory Committee Approval for
Characterization of image artifacts due to extra-cardiac uptake in ^{82}Rb PET MPI
Sub-study of: ^{82}Rb - An Alternative Radiopharmaceutical for Myocardial Imaging

Dear Sir/Madam,

I am writing on behalf of the PhD Supervisory Committee for Ms. Elizabeth Orton. We are aware and approve of the protocol entitled "Characterization of image artifacts due to extra-cardiac uptake in ^{82}Rb PET MPI Sub-study of: ^{82}Rb - An Alternative Radiopharmaceutical for Myocardial Imaging". This research will form part of Ms Orton's PhD research project and be included as part of her PhD thesis.



R. Glenn Wells
Associate Professor, Dept. of Medicine (Cardiology),
Adjunct Professor, Dept. of Physics, Carleton University

University of Ottawa Heart Institute
40 Ruskin St., Ottawa, ON

Cc: Xiaoyi Bao, University of Ottawa
Dave Rogers, Carleton University
Ran Klein, University of Ottawa Heart Institute



**Ottawa Health Science Network Research Ethics Board/ Réseau des sciences de la santé
d'Ottawa Conseil d'éthique de la recherche**

Civic Box 411 725 Parkdale Avenue, Ottawa, Ontario K1Y 4E9 613-798-5555 ext. 14902 Fax : 613-761-4311
<http://www.ohri.ca/ohsn-reb>

ANNUAL RENEWAL REPORT

1. REPORT DATE:	24 June 2014	
2a. Protocol Number:	20130268-01H	
2b. Protocol Title:	Characterization of image artifacts due to extra-cardiac uptake in 82-rubidium (Rb-82) positron emission tomography (PET) myocardial perfusion imaging (MPI); Sub-study of Rb ARMI HI Protocol #200987	
3. Principal Investigator at The Ottawa Hospital:	Dr. Glenn Wells	
4a. Co-Investigators:	Elizabeth Orton	Dr. Rob deKemp
4b. Have any co-investigators been added or removed since the last approval? <input type="checkbox"/> Yes <input checked="" type="checkbox"/> No If new investigators have been added, include a letter or Amendment Report with the Additional Co-Investigator page http://www.ohri.ca/ohreb/forms/additional_co.doc with their original signature.		
5a. Most recent approval 'expiry date':	May 27, 2014	
5b. Number of research participants who have provided consent AND enrolled into the study locally, since initial approval (if this is the first renewal for this study) OR last renewal report date (if this is the 2 nd /subsequent renewal for this study) :	0	
5c. Total number of research participants who have provided consent AND enrolled at this site since <u>initial OHREB approval</u> (if this number exceeds the currently approved sample size, then refer to Section 7):	2533	
5d. Number of local withdrawals since initial OHREB approval (if this is the first renewal for this study) OR last renewal report date (if this is the 2 nd /subsequent renewal for this study):	0	
5e. Total number of withdrawals at this site since <u>initial OHREB approval</u> :	0	
5f. Reason for withdrawals:	n/a	
6. Projected date of study completion (this should reflect the information provided in the initial application and/or the information provided in Section 7)	May 2015	

ANSWER ALL OF THE FOLLOWING QUESTIONS:

- 7a. Yes No Has there been a departure from previously approved research. If yes, please specify:
- Completion date change/sample size increase Yes No or decrease?
 - Inclusion/exclusion criteria? Yes No
 - Source of subject (participant) population? Yes No
 - Source of volunteer population (if applicable)? Yes No
 - Other? Describe: Yes No

[Empty box]

- 7b. Yes No An amendment form has been submitted to the OHREB for review of any of the above changes?
If yes, date approved:
- 7c. Yes No Have any unexpected side effects, adverse events, or findings been noted since last approval? Has the OHREB been informed of these?
 Yes No If yes, date submitted:
- 7d. Yes No Has any information appeared in the literature, or evolved from this or other similar ongoing studies, since the date of last approval that might affect the OHREB's or the research participant's perception of the risks and benefits of the study? (If yes, provide this information and your assessment of it in the section on progress of the study). Has the OHREB been informed of these? Yes No If yes, date submitted:
- 7e. Yes No Has the consent form been modified since last approval? Has the OHREB been informed of these changes? Yes No If yes, date approved:
- 7f. Yes No WRITTEN INFORMED CONSENT has been obtained and will continue to be obtained from all research participants, or their next-of-kin/legal representative.

NOTE:

Attach an **ORIGINAL COPY** of the most recently **APPROVED** consent forms, if no changes have been made. (If recruitment is closed, the OHREB does not require a copy of the consent form)

If the Patient Information Sheets and/or Consent Forms are being revised, attach a copy of the revised documents with **ALL CHANGES HIGHLIGHTED**; and a clean, final version of the **REVISED** documents printed **ON ORIGINAL LETTERHEAD**.

Consent Forms and the study are approved for a maximum duration of one year only and must be validated by the board annually.

8. In the space below, briefly describe the progress of the study to date. Renewals cannot be considered **if this section is not complete.**

PLEASE TYPE OR PRINT CLEARLY

An automated algorithm has been developed, validated and applied retrospectively to 4920 images, producing estimates for prevalence and severity classification of extra-cardiac interference artefacts due to stomach uptake in 82-rubidium PET MPI. This work is currently under consideration for publication. The correlation of extra-cardiac interference artefact presence and severity on the frequency of downstream testing and associated costs remains to be completed. There have been no changes (no additions and no exclusions) to the set of images/patients from the original application.



Original Signature of Principal Investigator

24 Jun 2014

Date

PLEASE NOTE: You must keep a copy of this form for your study file.

Protocol: Characterization of image artifacts due to extra-cardiac uptake in ^{82}Rb PET MPI
Sub-study of: ^{82}Rb - An Alternative Radiopharmaceutical for Myocardial Imaging

Background

Heart disease is one of the three leading causes of death in Canada and coronary artery disease represents the most common form of heart disease. The coronary arteries supply blood to the heart muscle (myocardium); therefore myocardial perfusion imaging, MPI, is an effective tool in the diagnosis of coronary artery disease.

This protocol is a sub-study of the Rb-ARMI Trial (summarized below). The aim of this protocol is to characterize a type of image artifact appearing in a subset of the ^{82}Rb PET MPI population and to then determine how this artifact affects overall accuracy and cost efficiency of ^{82}Rb PET MPI.

Brief summary of the Rb-ARMI Trial:

Rubidium-82 - An Alternative Radiopharmaceutical for Myocardial Imaging
HI Protocol # 2009872-01H; ClinicalTrials.gov identifier: NCT01128023

The objective of this Canadian multicentre trial is to demonstrate that, in a large population with respect to MPI for the identification of coronary artery disease, positron emission tomography, PET, with the radiopharmaceutical rubidium-82, ^{82}Rb , provides an accurate and cost effective alternative to single photon emission computed tomography, SPECT, with technetium-99m, $^{99\text{m}}\text{Tc}$.

This comparison is motivated by the fact that $^{99\text{m}}\text{Tc}$ -SPECT is the current standard for MPI; however, $^{99\text{m}}\text{Tc}$ is a reactor-produced radiopharmaceutical which experienced a significant shortage during the Chalk River NRU reactor shutdown, while ^{82}Rb is a non-reactor produced radiopharmaceutical that could potentially serve as an alternative. The Rb-ARMI trial involves 10 Canadian sites and its start date, estimated completion date and estimated enrollment are: April 2010, June 2015 and 7500 cases, respectively. The University of Ottawa Heart Institute, UOHI, serves as the core centre for the Rb-ARMI trial.

Extra-cardiac uptake artifacts in ^{82}Rb PET MPI

MPI involves injection of a radiopharmaceutical, followed by imaging of the cardiac distribution of radiopharmaceutical accumulation, or 'uptake', using the PET scanner. While ^{82}Rb accumulates relatively selectively in the myocardium; in a large fraction of patients, the stomach wall and spleen also exhibit comparably high levels of ^{82}Rb accumulation. Due to a combination of organ motion (cardiac & respiratory) and limited PET spatial resolution, high levels of extra-cardiac ^{82}Rb in close proximity to the heart can degrade the quality of the output images.

Currently, the solution to this problem is repeat imaging which incurs additional patient, staff and equipment time and cost, as well as additional radiation dose to the patient and does not guarantee improved images. In recognition of the problem, imaging protocols have been adapted to include drinking and eating prior to imaging in the hopes of

weighing the stomach down away from the heart or drinking carbonated beverages, hoping that gas will distend the stomach. In 2010, ~200 'no water' ^{82}Rb PET studies were collected in the Rb-ARMI trial at UOHI, after which the imaging protocol was adapted to include drinking water or carbonated water prior to scanning. Even after these adaptations, image artifacts are seen to remain in an estimated 10% of PET MPI studies. As a side note in their 2006 comparison of ^{82}Rb PET versus $^{99\text{m}}\text{Tc}$ SPECT MPI, Bateman et al. are the only study found in the literature to report on this problem. 1%, 5%, and 4% of 112 ^{82}Rb PET MPI studies are indicated as suffering from Major, Significant and Minor artifacts respectively; however, given the small number of studies relative to the low artifact prevalence, Bateman et al.'s numbers come with a large uncertainty, prevalence of artifacts was not separated from artifacts impacting interpretation, and no analysis of water's effect on artifact prevalence, of pre-test probability of artifact based on patient demographics, or of downstream imaging costs were reported. The aims of this protocol, as a sub-study of the Rb-ARMI trial, are to fill these gaps in the literature and to then use the identified group of artifact-exhibiting studies to develop and test a robust, reproducible software solution to the problem.

Research Questions

What are the prevalence and severity of extra-cardiac ^{82}Rb accumulation-based image artifacts in the University of Ottawa Heart Institute's 2010 – 2012 Rb-ARMI population? What is the resulting effect on nuclear cardiologist diagnostic confidence, as measured by image quality and overall interpretation? Does administration of water pre-scanning reduce the prevalence and/or severity of artifacts? Are there demographics (basic information) that significantly influence the pre-test probability of this artifact? Is there a significant difference in the downstream imaging cost of patients with versus without accumulation-based image artifacts?

The hypotheses of this study are that the prevalence and severity of artifacts will be similar to those reported by Bateman et al. (2006); that nuclear cardiologist diagnostic confidence will decrease with increasing artifact severity; that administration of water will decrease artifact prevalence and body mass index will be a positive pre-test predictor of artifact. The final hypothesis is that downstream patient imaging costs will increase in cases of image quality and confidence-limiting artifacts.

Participants

The University of Ottawa Heart Institute, UOHI, is the core site for Rb-ARMI trial and between May 2010 and December 2012 ~2800 ^{82}Rb PET studies with complete ARMI consent were collected. All UOHI studies with complete Rb-ARMI consent and having successfully completed the rest/stress ^{82}Rb PET MPI protocol will be included. UOHI studies without complete consent or without successful ^{82}Rb PET MPI will be excluded. From the above population, the 200 'no water' studies acquired between May and August 2010, will be identified for comparison to a sample of 200 demographically matched 'water' studies.

For cost analysis, permission (pending ethics approval) has been obtained to cross-reference patient identifiers (MRNs) and imaging study dates from responsible parties holding the UOHI's NH₃ PET, nuclear medicine (SPECT), cardiac CT, catheterization, and echocardiogram databases. Under the Rb-ARMI consent Group A (defined here as 'complete consent'), participants have agreed to use of their imaging results, basic information and information on 6-month follow-up tests that their doctor orders. Details are demonstrated in **Patient Information and Consent Form Rb-ARMI, Group A** (uploaded in Additional documents).

Proposed Method

Prevalence and severity of extra-cardiac ⁸²Rb accumulation-based image artifacts

Automated artifact detection:

Based on discussions with an experienced nuclear imaging cardiologist and simulations, automated software has been developed that scores the degree of extra-cardiac accumulation-based image artifact in (static) ⁸²Rb PET MPI images. The software is based on FlowQuant, an in-house program for detection and quantitative myocardium blood flow analysis (maintained by Dr. Ran Klein at UOHI). Once the myocardium is detected, the software searches the exterior edge of the heart for regions where the uptake does not decrease as expected. Artifact and patient-specific normal uptake is modeled on a short axis slice basis and artifact occurs where, at the exterior edge of the myocardium:

- 1) uptake is >50% higher than expected and
- 1) the slope of uptake fall-off is < 50% as steep as expected.

Cardiologist classification:

100 studies will be classified for artifact presence/severity by a cardiologist trained in nuclear imaging as: absent, mild, moderate or severe. These studies will then be scored using the software and a receiver operating curve analysis performed to determine the scoring thresholds corresponding to the cardiologist's classification with maximal sensitivity and optimal specificity.

Once the software is calibrated against the cardiologist, it will be applied to all studies from the Rb-ARMI trial to provide artifact classification for each scan. Prevalence at each level of severity can then be calculated.

Impact, Image Quality and Overall Interpretation

The same 100 studies used for classification will also be rated for the impact of artifacts on clinical decision making, using the following classes: no artifact, artifact not affecting interpretation, artifact probably affecting interpretation or artifact affecting interpretation. Similarly, as part of the Rb-ARMI trial, the image quality and overall interpretation of all studies have been evaluated by trained nuclear imaging cardiologists.

Demographics

A summary of patient demographics will be recorded for the purpose of sharing findings. Demographics will be recorded in aggregate form and will include: age, gender, body mass index (BMI), diabetes mellitus, smoker, hypertension, and hyperlipidemia, family

history of heart disease, typical angina, previous MI, previous PCI, & stress agent (persantine or dobutamine). Only aggregate form demographic statistics will be reported/published from this work; individual data will not be reported.

Cost analysis

For cost analysis, permission (pending ethics approval) has been obtained to cross-reference patient identifiers (MRNs) and imaging study dates from responsible parties holding the UOHI's NH₃ PET, nuclear medicine (SPECT), cardiac CT, catheterization, and echocardiogram databases. The prevalence, and related cost, of each type of follow-up test will be evaluated with respect to presence and severity of extra-cardiac ⁸²Rb accumulation-based image artifacts, and their impact on image quality and overall interpretation.

Data Security

Upon electronic retrieval of PET MPI studies from the database, an alpha-numeric code will be assigned to replace all patient identifying information and study datasets | anonymized de-identified. A file linking the alpha-numeric codes to patient name/MRN will be maintained securely (password protected) on the institution network, separately from the data analysis computer where study datasets will be kept. This file will be the only possible method to track the data back to the patient MRN. The data analysis computer is password protected and kept in a locked office.

For the purpose of cost analysis, image quality and overall interpretation, and pre-test probability analysis, the file linking the alpha-numeric codes to patient name/MRN will be used to cross-list the artifact severity scores with patient information in the Rb-ARMI database and study dates in the follow-up imaging databases.

Secondary use of data

The requested access to the Rb-ARMI ⁸²Rb PET MPI studies and study dates of NH₃ PET, nuclear medicine (SPECT), cardiac CT, catheterization, and echocardiograms is for secondary use of data: 'other research evaluations' in the **Patient Information and Consent Form Rb-ARMI, Group A** (uploaded in Additional documents). The following specific conditions are met by this study: the research involves no more than minimal risk to the participants and the research does not involve a therapeutic intervention, or other clinical or diagnostic interventions.

Dissemination

Results from this study will be published in a peer-reviewed nuclear medicine/medical imaging journal and used to guide development of a software correction method for extra-cardiac uptake based artifacts.

Contact Information

Principle Investigator:

Dr. R. Glenn Wells
Division of Cardiac Imaging,
Room H02-1-32
University of Ottawa Heart Institute
40 Ruskin Street
Ottawa, ON K1Y 4W7
tel: 613-798-5555 x 18175
email: gwells@ottawaheart.ca

Co-Investigator:

Elizabeth Orton, PhD Candidate
Division of Cardiac Imaging
Room H-2285
University of Ottawa Heart Institute
40 Ruskin Street
Ottawa, ON, K1Y 4W7
tel: 613-798-5555 x 19744
email: eorton@ottawaheart.ca

Co-Investigator:

Dr. Rob deKemp
Division of Cardiac Imaging
Room H-2285
University of Ottawa Heart Institute
40 Ruskin Street
Ottawa, ON, K1Y 4W7
tel: 613-798-5555 x 19744
email: eorton@ottawaheart.ca

References:

Bateman TM, Heller GV, McGhie AI, Friedman JD, Case JA, Bryngelson JR, et al. Diagnostic accuracy of rest/stress ECG-gated Rb-82 myocardial perfusion PET: comparison with ECG-gated Tc-99m sestamibi SPECT. J Nucl Cardiol 2006;13:24-33.

References

- Abidov A, Germano G, Hachamovitch R, Slomka P and Berman D S 2006 Gated SPECT in assessment of regional and global left ventricular function: An update *J. Nucl. Cardiol.* **13** 261–79
- Abraham A, Kass M, Ruddy T D, DeKemp R A, Lee A K Y, Ling M C, Ha A, Beanlands R S and Chow B J W 2010 Right and left ventricular uptake with Rb-82 PET myocardial perfusion imaging: markers of left main or 3 vessel disease. *J. Nucl. Cardiol.* **17** 52–60 Online: <http://www.ncbi.nlm.nih.gov/pubmed/19826892>
- Ali I, Ruddy T D, Almgrahi A, Anstett F G and Wells R G 2009 Half-Time SPECT Myocardial Perfusion Imaging with Attenuation Correction *J. Nucl. Med.* **50** 554–62
- Bailey D L, Antoch G, Bartenstein P, Barthel H, Beer a. J, Bisdas S, Bluemke D a., Boellaard R, Claussen C D, Franzius C, Hacker M, Hricak H, la Fougère C, Gückel B, Nekolla S G, Pichler B J, Purz S, Quick H H, Sabri O, Sattler B, Schäfer J, Schmidt H, van den Hoff J, Voss S, Weber W, Wehrl H F and Beyer T 2015 Combined PET/MR: The Real Work Has Just Started. Summary Report of the Third International Workshop on PET/MR Imaging; February 17–21, 2014, Tübingen, Germany *Mol. Imaging Biol.* **17** 297–312 Online: <http://link.springer.com/10.1007/s11307-014-0818-0>
- Bailey D L, Townsend D W, Valk P E and Maisey M N 2005 *Positron Emission Tomography: Basic Sciences* (Springer Science & Business Media) Online: <https://books.google.com/books?id=qxEoHsMglgoC&pgis=1>
- Barber D C 1980 The use of principal components in the quantitative analysis of gamma camera dynamic studies *Phys. Med. Biol.* **25** 283–92
- Bartlett M L, Buvat I, Vaquero J J, Mok D, Dilsizian V and Bacharach S L 1996 Measurement of myocardial wall thickening from PET/SPECT images: comparison of two methods. *J. Comput. Assist. Tomogr.* **20** 473–81 Online: <http://www.ncbi.nlm.nih.gov/pubmed/8626916>
- Bateman T M, Heller G V, McGhie a I, Friedman J D, Case J a, Bryngelson J R, Hertenstein G K, Moutray K L, Reid K and Cullom S J 2006 Diagnostic accuracy of rest/stress ECG-gated Rb-82 myocardial perfusion PET: comparison with ECG-gated Tc-99m sestamibi SPECT. *J. Nucl. Cardiol.* **13** 24–33 Online: <http://www.ncbi.nlm.nih.gov/pubmed/16464714>

- Beanlands R S B, Chow B J W, Dick A, Friedrich M G, Gulenchyn K Y, Kiess M, Leong-Poi H, Miller R M, Nichol G, Freeman M, Bogaty P, Honos G, Hudon G, Wisenberg G, Van Berkom J, Williams K, Yoshinaga K and Graham J 2007 CCS/CAR/CANM/CNCS/CanSCMR joint position statement on advanced noninvasive cardiac imaging using positron emission tomography, magnetic resonance imaging and multidetector computed tomographic angiography in the diagnosis and evaluation of ischemic heart *Can. J. Cardiol.* **23** 107–19 Online: <http://www.pubmedcentral.nih.gov/articlerender.fcgi?artid=2650646&tool=pmcentrez&rendertype=abstract>
- Beanlands R S B and Youssef G 2010 Diagnosis and prognosis of coronary artery disease: PET is superior to SPECT: *Pro. J. Nucl. Cardiol.* **17** 683–95 Online: <http://www.ncbi.nlm.nih.gov/pubmed/20589487>
- Beller G A and Zaret B L 2000 Contributions of Nuclear Cardiology to Diagnosis and Prognosis of Patients With Coronary Artery Disease *Circulation* **101** 1465–78 Online: <http://circ.ahajournals.org/cgi/doi/10.1161/01.CIR.101.12.1465>
- Bengel F M, Higuchi T, Javadi M S and Lautamäki R 2009 Cardiac Positron Emission Tomography *J. Am. Coll. Cardiol.* **54** 1–15 Online: <http://dx.doi.org/10.1016/j.jacc.2009.02.065>
- Berger M J, Hubbell J H, Seltzer S M, Chang J, Coursey J S, Sukumar R, Zucker D S and Olsen K 2010 XCOM: Photon Cross Section Database (version 1.5)[Online] Online: <http://physics.nist.gov/xcom>
- Bettinardi V, Presotto L, Rapisarda E, Picchio M, Gianolli L and Gilardi M C 2011 Physical Performance of the new hybrid PET *690 Med. Phys.* **38** 5394
- Bourque J M and Beller G A 2011 Stress myocardial perfusion imaging for assessing prognosis: an update. *JACC. Cardiovasc. Imaging* **4** 1305–19 Online: <http://www.ncbi.nlm.nih.gov/pubmed/22172788>
- Branswell H 2013 Unplanned shutdown triggers isotope shortage; hospitals warned to use cautiously *Can. Press* Online: <http://www.citynews.ca/2013/11/23/unplanned-shutdown-triggers-isotope-shortage-hospitals-warned-to-use-cautiously/>
- Bruesewitz M, Yu L, Vrieze T, Kofler J and McCollough C 2008 Smart mA: Automatic Exposure Control (AEC)—Physics Principles and Practical Hints *Annual Meeting of the Radiological Society of North America* (Chicago IL) Online: <http://archive.rsna.org/2008/6021555.html>
- Cerqueira M D, Weissman N J, Dilsizian V, Jacobs A K, Kaul S, Laskey W K, Pennell D J, Rumberger J a., Ryan T and Verani M S 2002 Standardized myocardial

- segmentation and nomenclature for tomographic imaging of the heart: A statement for healthcare professionals from the Cardiac Imaging Committee of the Council on Clinical Cardiology of the American Heart Association *J. Nucl. Cardiol.* **9** 240–5
- Cervino L I, Gupta S, Rose M A, Yashar C and Jiang S B 2009 Using surface imaging and visual coaching to improve the reproducibility and stability of deep-inspiration breath hold for left-breast-cancer radiotherapy *Phys. Med. Biol.* **54** 6853–65
- Chawla N V 2005 Chapter 40 DATA MINING FOR IMBALANCED DATASETS : AN OVERVIEW *Data Mining and Knowledge Discovery Handbook* (Springer) pp 853–67
- Cherry S R and Dahlbom M 2006 *PET: Physics, Instrumentation, and Scanners*
- Cherry S R, Sorenson J A and Phelps M E 2012 *Physics in Nuclear Medicine* (Elsevier Health Sciences) Online:
<http://www.sciencedirect.com/science/article/pii/B9781416051985000344>
- Chung S, Breton E, Mannelli L and Axel L 2011 Liver stiffness assessment by tagged MRI of cardiac-induced liver motion *Magn. Reson. Med.* **65** 949–55
- Cohen J 1960 A coefficient of agreement of nominal scales *Educ. Psychol. Meas.* **20** 37–46 Online: <http://epm.sagepub.com/cgi/doi/10.1177/001316446002000104>
- Coleman T F and Li Y 1996 An Interior, Trust Region Approach for Nonlinear Minimization Subject to Bounds *SIAM J. Optim.* **6** 418–45
- Coleman T F and Li Y 1994 On the Convergence of Reflective Newton Methods for Large-Scale Nonlinear Minimization Subject to Bounds *Math. Program.* **67** 189–224
- Conti M 2009 State of the art and challenges of time-of-flight PET *Phys. Medica* **25** 1–11 Online: <http://dx.doi.org/10.1016/j.ejmp.2008.10.001>
- Conti M 2011 Why is TOF PET reconstruction a more robust method in the presence of inconsistent data? *Phys. Med. Biol.* **56** 155–68
- deKemp, Robert A 2013 *Research proposal: Rb PET - An Alternative Radiopharmaceutical for Myocardial Imaging (Rb-ARMI)* (Ottawa)
- Dilsizian V, Bacharach S L, Beanlands R S, Bergmann S R, Delbeke D, Gropler R J, Knuuti J, Schelbert H R and Travin M I 2009 PET myocardial perfusion and metabolism clinical imaging. *J. Nucl. Cardiol.* **16** 651

- Dumouchel T 2011 *Partial Volume Correction of Cardiac Mouse Positron Emission Tomography Images* (Carleton University)
- Erlandsson K, Buvat I, Pretorius P H, Thomas B a and Hutton B F 2012 A review of partial volume correction techniques for emission tomography and their applications in neurology, cardiology and oncology *Phys. Med. Biol.* **57** R119–59
- El Fakhri G, Sitek A, Gu erin B, Kijewski M F, Di Carli M F and Moore S C 2005 Quantitative dynamic cardiac ⁸²Rb PET using generalized factor and compartment analyses. *J. Nucl. Med.* **46** 1264–71
- Finegold J a., Asaria P and Francis D P 2013 Mortality from ischaemic heart disease by country, region, and age: Statistics from World Health Organisation and United Nations *Int. J. Cardiol.* **168** 934–45 Online: <http://dx.doi.org/10.1016/j.ijcard.2012.10.046>
- Frouin F, Bazin J, Paola M Di, Jolivet O and Paola R Di 1992 FAMIS ☐: A SOFTWARE
PACKAGE FOR FUNCTIONAL FEATURE EXTRACTION FROM BIOMEDICAL
MULTIDIMENSIONAL IMAGES FredCrique Frouin *Comput. Med. Imaging Graph.* **16**
81–91
- Gambhir S S 1990 *Quantitation of the physical factors affecting the tracer kinetic modeling of cardiac positron emission tomography data* (University of California)
- GE-Healthcare 2009 *Clinical Implementation of VUE Point FX* (GE Healthcare) Online: www.gehealthcare.com
- GE-Healthcare 2008 *VUE Point HD: Bringing accuracy to PET reconstruction* Online: www.gehealthcare.com
- Goodsell D S 2009 SODIUM-POTASSIUM PUMP RCSB *Protien Bank Mol. Mon.* 2–3
Online: www.pdb.org
- Gould K L, Johnson N P, Bateman T M, Beanlands R S, Bengel F M, Bober R, Camici P G, Cerqueira M D, Chow B J W, Di Carli M F, Dorbala S, Gewirtz H, Gropler R J, Kaufmann P A, Knaapen P, Knuuti J, Merhige M E, Rentrop K P, Ruddy T D, Schelbert H R, Schindler T H, Schwaiger M, Sdringola S, Vitarello J, Williams K A, Gordon D, Dilsizian V and Narula J 2013 Anatomic versus physiologic assessment of coronary artery disease. Role of coronary flow reserve, fractional flow reserve, and positron emission tomography imaging in revascularization decision-making. *J. Am. Coll. Cardiol.* **62** 1639–53 Online: <http://www.ncbi.nlm.nih.gov/pubmed/23954338>
- Gould K L, Pan T, Loghin C, Johnson N P, Guha A and Sdringola S 2007 Frequent Diagnostic Errors in Cardiac PET / CT Due to Misregistration of CT Attenuation and

- Hachamovitch R, Hayes S W, Friedman J D, Cohen I and Berman D S 2003 Comparison of the Short-Term Survival Benefit Associated With Revascularization Compared With Medical Therapy in Patients With No Prior Coronary Artery Disease Undergoing Stress Myocardial Perfusion Single Photon Emission Computed Tomography *Circulation* **107** 2900–7
- Heller G V, Mann A and Hendel R C 2009 *Nuclear Cardiology: Technical Applications* (McGraw-Hill Companies, Inc.)
- Houston A S 1984 The effect of apex-finding errors on factor images obtained from factor analysis and oblique transformation. *Phys. Med. Biol.* **29** 1109–16 Online: <http://www.ncbi.nlm.nih.gov/pubmed/6483975>
- Hudson H M and Larkin R S 1994 Accelerated image reconstruction using ordered subsets of projection data. *IEEE Trans. Med. Imaging* **13** 601–9 Online: <http://www.ncbi.nlm.nih.gov/pubmed/18218538>
- Hunter C 2010 *The Internal Dosimetry of Rubidium-82 based on Dynamic PET/CT Imaging in Humans* (Carleton University)
- ICRP 2002 Basic Anatomical and Physiological Data for Use in Radiological Protection Reference Values *Ann. ICRP* **32** 3–4
- Iskandrian A E 1999 Risk assessment of stable patients (panel III) *J. Nucl. Cardiol.* 93
- Johnson N P, Sdringola S and Gould K L 2011 Partial volume correction incorporating Rb-82 positron range for quantitative myocardial perfusion PET based on systolic-diastolic activity ratios and phantom measurements *J. Nucl. Cardiol.* **18** 247–58
- Kaster T, Mylonas I, Renaud J M, Wells G a, Beanlands R S B and deKemp R a 2012 Accuracy of low-dose rubidium-82 myocardial perfusion imaging for detection of coronary artery disease using 3D PET and normal database interpretation. *J. Nucl. Cardiol.* **19** 1135–45 Online: <http://www.ncbi.nlm.nih.gov/pubmed/22996831>
- Kaul S, Wismer G L, Brady T J, Johnston D L, Weyman a. E, Okada R D and Dinsmore R E 1986 Measurement of normal left heart dimensions using optimally oriented MR images *Am. J. Roentgenol.* **146** 75–9
- Kereiakes D J, Teirstein P S, Sarembock I J, Holmes D R, Krucoff M W, O'Neill W W, Waksman R, Williams D O, Popma J J, Buchbinder M, Mehran R, Meredith I T, Moses J W and Stone G W 2007 The truth and consequences of the COURAGE trial.

J. Am. Coll. Cardiol. **50** 1598–603 Online:
<http://www.ncbi.nlm.nih.gov/pubmed/17936161>

Khorsand A, Graf S, Frank H, Kletter K, Sochor H, Maurer G, Schuster E, Globits S, Dudczak R and Porenta G 2003 Model-based analysis of electrocardiography-gated cardiac (18)F-FDG PET images to assess left ventricular geometry and contractile function. *J. Nucl. Med.* **44** 1741–6 Online:
<http://www.ncbi.nlm.nih.gov/pubmed/14602854>

Kinahan P E, Hasegawa B H and Beyer T 2003 X-Ray-Based Attenuation Correction for Positron Emission Tomography/Computed Tomography Scanners *Semin. Nucl. Sci.* **XXXIII** 166–79

King M A, Dey J, Johnson K, Dasari P, Mukherjee J M, McNamara J E, Konik A, Lindsay C, Zheng S and Coughlin D 2013 Use of MRI to assess the prediction of heart motion with gross body motion in myocardial perfusion imaging by stereotracking of markers on the body surface Use of MRI to assess the prediction of heart motion with gross body motion in myocardial perfusion *Med. Phys.* **40** 112504–1 – 112504–14

Klein R 2010 *Kinetic Model Based Factor Analysis of Cardiac ⁸²Rb PET Images for Improved Accuracy of Quantitative Myocardial Blood Flow Measurement* (University of Ottawa)

Klein R, Adler A, Beanlands R S and A R 2007 Precision-controlled elution of a ⁸²Sr / ⁸²Rb generator for cardiac perfusion imaging with positron emission tomography *Phys. Med. Biol.* **52** 659–73

Klein R, Beanlands R S B and DeKemp R A 2010a Quantification of myocardial blood flow and flow reserve : Technical aspects *J. Nucl. Cardiol.* **17** 555–70

Klein R, Hunter C, Beanlands R and deKemp R 2011 Prevalence of patient motion in dynamic PET *J. Nucl. Med.* **52** 2105 – Online:
http://jnm.snmjournals.org/content/52/supplement_1/2105.abstract?sid=1286d890-3d88-43d3-8c12-42cdca624e74

Klein R, Lortie M, Adler A, Beanlands R S and DeKemp R 2006 Fully Automated Software for Polar-Map Registration and Sampling from PET Images *IEEE Nuclear Science Symposium Conference Record* vol 6 pp 3185–8

Klein R, Renaud J M, Ziadi M C, Thorn S L, Adler A, Beanlands R S and DeKemp R A 2010b Intra-and inter-operator repeatability of myocardial blood flow and myocardial flow reserve measurements using rubidium-82 pet and a highly automated analysis program *J. Nucl. Cardiol.* **17** 600–16

- Kohavi R 1995 A Study of Cross-Validation and Bootstrap for Accuracy Estimation and Model Selection
- Lecomte R 2009 Novel detector technology for clinical PET *Eur. J. Nucl. Med. Mol. Imaging* **36** S69–85
- Lecomte R 2004 Technology challenges in small animal PET imaging *Nucl. Instruments Methods Phys. Res.* **527** 157–65
- Lertsburapa K, Ahlberg a, Bateman T, Katten D, Volker L, Cullom S and Heller G 2008 Independent and incremental prognostic value of left ventricular ejection fraction determined by stress gated rubidium 82 PET imaging in patients with known or suspected coronary artery disease *J. Nucl. Cardiol.* **15** 745–53
- Levin C S and Hoffman E J 1999 Calculation of positron range and its effect on the fundamental limit of positron emission tomography system spatial resolution. *Phys. Med. Biol.* **44** 781–99
- Lidwell W, Holden K and Butler J 2010 Garbage In-Garbage out *Universal Principles of Design* (Massachusetts: Rockport Publishers) pp 112–3
- Loong C Y and Anagnostopoulos C 2004 Diagnosis of coronary artery disease by radionuclide myocardial perfusion imaging. *Heart* **90 Suppl 5** v2–9 Online: <http://www.pubmedcentral.nih.gov/articlerender.fcgi?artid=1876323&tool=pmcentrez&rendertype=abstract>
- Lynch P J (medical illustrator) 2006 Heart anatomy and circulation diagram 128px – Heart_circulation_diagram.svg.png Online: https://upload.wikimedia.org/wikipedia/commons/7/73/Heart_circulation_diagram.svg
- Machac J, Bacharach S L, Bateman T M, Bax J J, Beanlands R, Bengel F, Bergmann S R, Brunken R C, Case J, Delbeke D, Dicarli M F, Garcia E V, Goldstein R A, Gropler R J, Travin M, Patterson R and Schelbert H R 2006 Positron emission tomography myocardial perfusion and glucose metabolism imaging *J. Nucl. Cardiol.* **13** 121–51
- Madsen M T 1992 A simplified formulation of the gamma variate function *Phys. Med. Biol.* **37** 1597–600
- Marieb E N 2012 The cardiovascular system *The Essentials of human anatomy and physiology* (San Fransico, California: Pearson Education) p 357
- McCollough C H, Bruesewitz M R and Kofler J M 2006 CT dose reduction and dose management tools: overview of available options. *Radiographics* **26** 503–12

- Morrison A 2010 The Global Impact of Technetium-99m Supply Disruptions *Ottawa Can. Agency Drugs Technol. Heal. Environ. Scan.* 1–9 Online:
http://www.rsna.org/Publications/rsnanews/July-2010/isotope_feature.cfm
- Moses W W 2011 Fundamental Limits of Spatial Resolution in PET *Nucl. Instruments Methods Phys. Res.* **648** 1–14
- Moses W W and Derenzo E S 1993 Empirical observation of resolution degradation in positron emission tomographs utilizing block detectors *Journal of nuclear medicine* p 101P
- Mukherjee J M, Hutton B F, Johnson K L, Pretorius P H and King M A 2013 An evaluation of data-driven motion estimation in comparison to the usage of external-surrogates in cardiac SPECT imaging **58** 7625–46
- Mullani N A, Goldstein R A, Gould K L, Marani S K, Fisher D J, O'Brien H A and Loberg M D 1983 Myocardial Perfusion with Rubidium-82 . 1. Measurement of Extraction Fraction and Flow with External Detectors *J. Nucl. Med.* **24** 898–906
- Murray C J L, Vos T, Lozano R, Naghavi M, Flaxman A D, Michaud C, Ezzati M, Shibuya K, Salomon J a, Abdalla S, Aboyans V, Abraham J, Ackerman I, Aggarwal R, Ahn S Y, Ali M K, Alvarado M, Anderson H R, Anderson L M, Andrews K G, Atkinson C, Baddour L M, Bahalim A N, Barker-Collo S, Barrero L H, Bartels D H, Basáñez M-G, Baxter A, Bell M L, Benjamin E J, Bennett D, Bernabé E, Bhalla K, Bhandari B, Bikbov B, Bin Abdulhak A, Birbeck G, Black J a, Blencowe H, Blore J D, Blyth F, Bolliger I, Bonaventure A, Boufous S, Bourne R, Boussinesq M, Braithwaite T, Brayne C, Bridgett L, Brooker S, Brooks P, Brugha T S, Bryan-Hancock C, Bucello C, Buchbinder R, Buckle G, Budke C M, Burch M, Burney P, Burstein R, Calabria B, Campbell B, Canter C E, Carabin H, Carapetis J, Carmona L, Cella C, Charlson F, Chen H, Cheng A T-A, Chou D, Chugh S S, Coffeng L E, Colan S D, Colquhoun S, Colson K E, Condon J, Connor M D, Cooper L T, Corriere M, Cortinovis M, de Vacarro K C, Couser W, Cowie B C, Criqui M H, Cross M, Dabhadkar K C, Dahiya M, Dahodwala N, Damsere-Derry J, Danaei G, Davis A, De Leo D, Degenhardt L, Dellavalle R, Delossantos A, Denenberg J, Derrett S, et al 2012 Disability-adjusted life years (DALYs) for 291 diseases and injuries in 21 regions, 1990-2010: a systematic analysis for the Global Burden of Disease Study 2010. *Lancet* **380** 2197–223 Online:
[http://www.thelancet.com/journals/a/article/PIIS0140-6736\(12\)61689-4/fulltext](http://www.thelancet.com/journals/a/article/PIIS0140-6736(12)61689-4/fulltext)
- Murthy V L, Lee B C, Sitek a., Naya M, Moody J, Polavarapu V, Ficaro E P and Di Carli M F 2014 Comparison and Prognostic Validation of Multiple Methods of Quantification of Myocardial Blood Flow with ⁸²Rb PET *J. Nucl. Med.* **55** 1952–8 Online:
<http://jnm.snmjournals.org/cgi/doi/10.2967/jnumed.114.145342>

- Nakazato R, Berman D S, Dey D, Le Meunier L, Hayes S W, Fermin J S, Cheng V Y, Thomson L E J, Friedman J D, Germano G and Slomka P J 2012 Automated quantitative Rb-82 3D PET/CT myocardial perfusion imaging: Normal limits and correlation with invasive coronary angiography *J. Nucl. Cardiol.* **19** 265–76
- Ollinger J M 1996 Model-based scatter correction for fully 3D PET *Phys. Med. Biol.* **41** 153–76
- Paola R Di, Bazin J P, Aubry F, Aurengo A, Cavailloles F, Herry J Y and Kahn E 1982 Handling of Dynamic Sequences in Nuclear Medicine *IEEE Trans. Nucl. Sci.* **NS-29** 1310–21
- Pepin C M, Bérard P, Perrot A L, Pépin C, Houde D, Lecomte R, Melcher C L and Dautet H 2004 Properties of LYSO and recent LSO scintillators for phoswich PET detectors *IEEE Trans. Nucl. Sci.* **51** 789–95
- Phelps M E 2004 *PET: Molecular Imaging and Its Biological Applications* (Springer Science & Business Media) Online: <https://books.google.com/books?hl=en&lr=&id=YmejMRneO90C&pgis=1>
- Pickhardt P J and Asher D B 2003 Wall Thickening of the Gastric Antrum as a Normal Finding: Multidetector CT with Cadaveric Comparison *Am. J. Radiol.* **181** 973–9
- Polycarpou I, Thielemans K, Manjeshwar R, Aguiar P, Marsden P K and Tsoumpas C 2011 Comparative evaluation of scatter correction in 3D PET using different scatter-level approximations *Ann. Nucl. Med.* **25** 643–9
- Porenta G, Kuhie W, Sinha S, Krivokapich J, Czernin J, Gambhir S S, Phelps M E and Schelbert H R 1995 Parameter Estimation of Cardiac Geometry by ECG-Gated PET Imaging: Validation Using Magnetic Resonance Imaging and Echocardiography *J. Nucl. Med.* **36** 1123–30
- Qi J and Leahy R M 2006 Iterative reconstruction techniques in emission computed tomography. *Phys. Med. Biol.* **51** R541–78 Online: http://iopscience.iop.org/0031-9155/51/15/R01/pdf/0031-9155_51_15_R01.pdf
- Radon J and Parks P C (translator) 1986 On the Determination of Functions from Their Integral Values along Certain Manifolds. *IEEE Trans. Med. Imaging* **5** 170–6 Online: <http://ieeexplore.ieee.org/articleDetails.jsp?arnumber=4307775>
- Renaud J M, Mylonas I, McArdle B, Dowsley T, Yip K, Turcotte E, Guimond J, Trottier M, Pibarot P, Maguire C, Lalonde L, Gulenchyn K, Wisenberg G, Wells R G, Ruddy T, Chow B, Beanlands R S B and Dekemp R A 2014 Clinical Interpretation Standards

- and Quality Assurance for the Multicenter PET/CT Trial Rubidium-ARMI. *J. Nucl. Med.* **55** 58–64 Online: <http://www.ncbi.nlm.nih.gov/pubmed/24249797>
- Riordan M M and Kovács S J 2006 Relationship of pulmonary vein flow to left ventricular short-axis epicardial displacement in diastole : model-based prediction with in vivo validation Relationship of pulmonary vein flow to left ventricular short-axis epicardial displacement in diastole *Am J Physiol Hear. Circ Physiol* **291** H1210–5
- Rousset O, Rahmim A, Alavi A and Zaidi H 2007 Partial Volume Correction Strategies in PET *PET Clin.* **2** 235–49
- Rummel R J 1988 *Applied Factor Analysis* (Northwestern University Press)
- Segars W P, Mori S, Chen G T Y and Tsui B M W 2007 Modeling Respiratory Motion Variations in the 4D NCAT Phantom *IEEE Nuclear Science Symposium Conference Record* pp 2677–9
- Segars W P, Sturgeon G, Mendonca S, Grimes J and Tsui B M W 2010 4D XCAT phantom for multimodality imaging research *Med. Phys.* **37** 4902–15
- Senthamizchelvan S, Bravo P E, Esaias C, Lodge M a, Merrill J, Hobbs R F, Sgouros G and Bengel F M 2010 Human biodistribution and radiation dosimetry of ⁸²Rb. *J. Nucl. Med.* **51** 1592–9 Online: <http://www.pubmedcentral.nih.gov/articlerender.fcgi?artid=3172678&tool=pmcentrez&rendertype=abstract>
- Shepp L A and Vardi Y 1982 Maximum Likelihood Reconstruction for Emission Tomography *IEEE Trans. Med. Imaging* **MI-1** 113–21
- Shkvorets M, deKemp R A and Wells R G 2007 Respiratory-Motion Errors in Quantitative Myocardial Perfusion with PET/CT *IEEE Nuclear Science Symposium Conference Record* pp 3946–50
- Sitek a, Di Bella E V R and Gullberg G T 2000 Factor analysis with a priori knowledge - application in dynamic cardiac SPECT *Phys Med Biol* **45** 2619–38 Online: <Go to ISI>://WOS:000089438900018
- Sitek A, Di Bella E V R, Gullberg G T and Huesman R H 2002a Removal of liver activity contamination in teboroxime dynamic cardiac SPECT imaging with the use of factor analysis *J. Nucl. Cardiol.* **9** 197–205 Online: <http://link.springer.com/10.1067/mnc.2002.120362>

- Sitek A, Gullberg G T and Huesman R H 2002b Correction for Ambiguous Solutions in Factor Analysis Using a Penalized Least Squares Objective *IEEE Trans. Med. Imaging* **21** 216–25
- Slomka P J, Nishina H, Berman D S, Kang X, Friedman J D, Hayes S W, Aladl U E and Germano G 2004 Automatic quantification of myocardial perfusion stress-rest change: a new measure of ischemia. *J. Nucl. Med.* **45** 183–91
- Statistics Canada 2011 *Mortality, summary list of causes 2008* Online: <http://www.statcan.gc.ca/pub/84f0209x/84f0209x2008000-eng.pdf>
- Takobana S, Klein R, Adler A, deKemp R, Beanlands R and Mielniczuk L 2013 A spline model for RV myocardium sampling from cardiac PET images *Soc. Nucl. Med. Annu. Meet. Abstr.* **54** 1646 Online: http://jnumedmtg.snmjournals.org/cgi/content/meeting_abstract/54/2_MeetingAbstracts/1646?maxtoshow=&hits=10&RESULTFORMAT=&author1=Takobana&andorexactfulltext=and&searchid=1&FIRSTINDEX=0&sortspec=relevance&resourcetype=HWCIT
- Takx R a, Blomberg B a, El Aidi H, Habets J, de Jong P a, Nagel E, Hoffmann U and Leiner T 2015 Diagnostic accuracy of stress myocardial perfusion imaging compared to invasive coronary angiography with fractional flow reserve meta-analysis *Circ Cardiovasc Imaging* **8** Online: <http://www.ncbi.nlm.nih.gov/pubmed/25596143>
- Tarantola G, Zito F and Gerundini P 2003 PET Instrumentation and Reconstruction Algorithms in Whole-Body Applications * *J. Nucl. Med.* **44** 756–69
- Teras M, Tolvanen T, Johansson J J, Williams J J and Knutti J 2007 Performance of the new generation of whole-body PET/CT scanners : Discovery STE and Discovery VCT *Eur. J. Nucl. Med. Mol. Imaging* **34** 1683–92
- Thompson H K, Starmer C F, Whalen R E and McIntosh H D 1964 Indicator Transit Time Considered as a Gamma Variate *Circulation* **14** 502–15
- Thompson R C 2008 The problem of radiotracer abdominal activity in myocardial perfusion imaging studies. *J. Nucl. Cardiol.* **15** 159–61 Online: <http://www.ncbi.nlm.nih.gov/pubmed/18371585>
- Ueki J, De Bruin P F and Pride N B 1995 In vivo assessment of diaphragm contraction by ultrasound in normal subjects. *Thorax* **50** 1157–61
- Wang W, Hu Z, Gualtieri E E, Parma M J, Walsh E S, Sebok D, Hsieh Y, Tung C, Griesmer J J, Kolthammer J A, Popescu L M, Werner M, Karp J S and Gagnon D 2006 Systematic

and Distributed Time-of-Flight List Mode PET Reconstruction *IEEE Nuclear Science Symposium Conference Record* pp 1715–22

- Watson C, Newport D and Casey M 1996 A single scatter simulation technique for scatter correction in 3D PET ed P Grangeat and J-L Amans *3D Image Reconstr. Radiol. Nucl. Med.* **4** 255–68 Online: <http://link.springer.com/10.1007/978-94-015-8749-5>
- Weiss G M and Provost F 2003 Learning when training data are costly: The effect of class distribution on tree induction *J. Artif. Intell. Res.* **19** 315–54
- Wells R G, Ruddy T D, deKemp R A, DaSilva J N and Beanlands R S B 2010 Single-Phase CT Aligned to Gated PET for Respiratory Motion Correction in Cardiac *J. Nucl. Med.* **51** 1182–90
- Wernick M N and Aarsvold J N 2004 *Emission Tomography: The Fundamentals of PET and SPECT* (Academic Press) Online: https://books.google.com/books?id=R5slur_hdfEC&pgis=1
- Wollenweber S D 2002 Parameterization of a Model-Based 3-D PET Scatter Correction *IEEE Trans. Nucl. Sci.* **49** 722–7
- Yoshinaga K, Chow B J W, Williams K, Chen L, deKemp R a, Garrard L, Lok-Tin Szeto A, Aung M, Davies R a, Ruddy T D and Beanlands R S B 2006 What is the prognostic value of myocardial perfusion imaging using rubidium-82 positron emission tomography? *J. Am. Coll. Cardiol.* **48** 1029–39 Online: <http://www.ncbi.nlm.nih.gov/pubmed/16949498>
- Yoshinaga K, Klein R and Tamaki N 2010 Generator-produced rubidium-82 positron emission tomography myocardial perfusion imaging-From basic aspects to clinical applications *J. Cardiol.* **55** 163–73
- Zaidi H 2000 Comparative evaluation of scatter correction techniques in 3D positron emission tomography *Eur. J. Nucl. Med.* **27** 1813–26
- Zellweger M J, Hachamovitch R, Kang X, Hayes S W, Friedman J D, Germano G and Berman D S 2009 Threshold, incidence, and predictors of prognostically high-risk silent ischemia in asymptomatic patients without prior diagnosis of coronary artery disease *J. Nucl. Cardiol.* **16** 193–200

